NUI MAYNOOTH

Ollscoil na hÉireann Má Nuad

Modal Analysis of Millimetre-wave and Terahertz Imaging Systems

Presented by

Ronan John Mahon, B.Sc. (Hons.)

A thesis submitted for the Degree of

Doctor of Philosophy

Department of Experimental Physics, NUI Maynooth,
Co. Kildare, Ireland

Thesis Supervisor: Prof. J. Anthony Murphy

Acting Head of Department: Dr. Créidhe O'Sullivan

August 2011

Abstract

This thesis presents the theory and applications of electromagnetic field calculation using orthogonal Gaussian beam modes within the context of far-infrared imaging systems. Laguerre and Hermite-Gaussian modes have been frequently reported in the analysis of paraxial millimetre-wave propagation in astronomical optical systems. Here the method of Gaussian beam mode analysis (GBMA) is extended to fields of optical research that have until recently been associated with wavelengths in the visible band.

Using recently derived expressions for the non-paraxial diffraction of Hermite-Gaussian modes, the author demonstrates the modal calculation of far-field intensity distributions with less angular restriction on the accuracy of the method compared to the conventional paraxial description of orthogonal Gaussian modes. This method shows excellent agreement with predictions from more rigourous full-wave numerical methods such as the finite-difference time-domain algorithm, which is also described as a software tool in the modelling of horn and lens antennas.

The properties of diffraction limited Bessel beams is described using the Laguerre-Gaussian expansion of conical lenses, and experimental measurements of a conical lens is presented to explore the validity of the use of these optical elements as horn coupled devices in millimetre wave imaging systems.

A study of diffractive Fresnel lenses has been undertaken with a comparison of experimentally measured fields with those predicted by the modal techniques. The effects of such lenses on ultrashort paraxial pulses are also investigated using a novel numerical description of few-cycle fields as a superposition of pulsed Laguerre-Gaussian modes.

The application of digital holography in the far-infra red band has the prospect of diffraction limited imaging systems without creating distortions and aberrations which is a common problem in conventional techniques using lenses and mirrors. The author presents results from a simple proof-of-concept system which exhibits the potential of this technique for application in, for example, mm-wave security imaging.

Acknowledgements

Prof. Anthony Murphy has been an excellent supervisor of this work. Conversations with him on the behaviour of light were always informative but more importantly they were also very enjoyable. My appreciation of his patience cannot be emphasised enough.

I must also extend my gratitude to all the lecturers in the Physics department, and especially to the senior members of the mm-wave group: Dr. Marcin Gradziel, Dr. Bill Lanigan, Dr. Créidhe O'Sullivan, Dr. Neil Trappe and Mr. Tully Peacocke whose doors were always open for students with silly questions.

I enjoyed working with Mr. Ian McAuley on digital holography measurements and I greatly benefited from the expert work of Mr. David Watson in the manufacture of the binary lens and the conical lens described in this thesis, amongst other work. Mr. John Kelly was always available to help with computer problems no matter how trivial they were, and I always learned a lot looking over his shoulder.

Special thanks to Ms. Gráinne Roche who was always on hand to help students with their problems, as was Mr. Derek Gleeson and Dr. Niall McKeith.

Thanks to all the postgraduate students of the Experimental Physics department past and present especially Dr. Tim Finn, Dr. John Lavelle, and Dr. Robert May for several nonsensical but useful conversations over the years. Many thanks also to Ms. Mairéad Bevan and Mr. Brian McLaughlin for putting up with me in their office.

I am very grateful to Mr. Darragh McCarthy and Mr. Paul McLaughlin who carried out the measurements of the diffractive lens described in Chapter 5.

I greatly appreciated the financial support of the Irish Research Council for Science, Engineering, and Technology.

Thanks to Paul and the Walsh family for their help and friendship over the last twenty years.

Finally, I would like to thank my family Eithne, Ray, Ewa, and Michael for their support, but most of all my parents Seán and Mary for never losing faith in me.

Dedicated to my parents

Chapter One

Millimetre-wave and terahertz radiation

1.1 - Introduction

The study of light in all its forms is one of the major endeavours in Physics research and has great influence on the interaction of humans and their environment. In everyday life it is very simple to witness the variation in the behaviour of light of different wavelengths and the effects created by its interaction with the world around us, from the generation of a blue sky by Rayleigh scattering in the atmosphere to the refraction of light in water, electromagnetic (EM) radiation is subject to a broad range of phenomenon through its interaction with matter. The position of a certain form of radiation in the EM spectrum is defined by its wavelength λ (or associated frequency ν), and this parameter greatly affects the magnitude of effects it is subject to. See Figure 1.

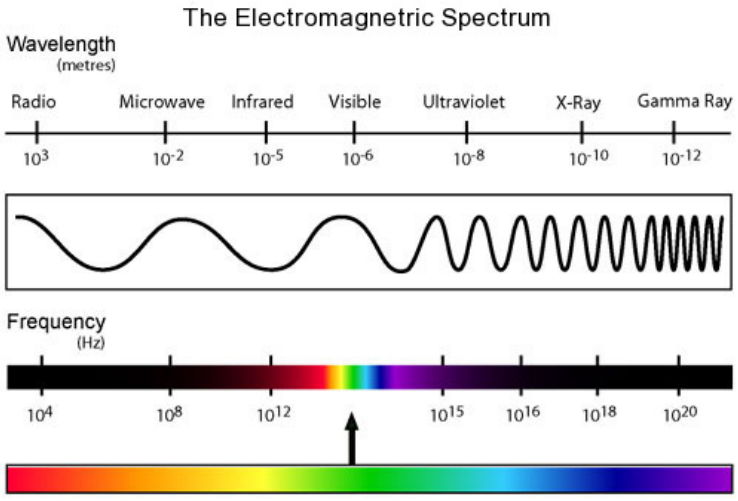

Figure 1.1 - The electromagnetic spectrum.

It can be said that light was the catalyst for the huge advancement in Physics during the twentieth century. Einstein's theory of the photoelectric effect and the development of the idea of the photon as a quantum mechanical entity was a massive step forward in understanding nature. For centuries, the most basic comprehension of the behaviour of EM radiation was obtained from the study of light within the visible region, an obvious endeavour as the retina in our eyes are sensitive only to light within

that relatively narrow section of the spectrum, with wavelengths within the approximate range of 380nm to 770nm.

Isaac Newton predicted, and gave evidence for, the fundamental ideas relating to the colour of light, while it was James Clerk Maxwell and the equations that bear his name that unified the theories of light with the observed behaviour of electric and magnetic fields. These important equations are one of the cornerstones of modern physics, and importantly showed that the properties of light of all wavelengths are based on the same physical principles. The work of Heinrich Hertz was central in the study of radio waves, while Wilhelm Röntgen discovered X-rays. In between the extreme wavelengths associated with these latter forms of radiation lies a region of the EM spectrum that, in comparison with other common forms of radiation, has not been applied to everyday life applications to the same level. This is the terahertz (THz) and millimetre wave regime.

It can be said THz/mm-wave radiation is where electromagnetics cross over into optics. At radio frequencies, fields are described in terms of electromagnetic properties like polarisation and electrical impedance, whereas at shorter wavelengths in the infra-red and optical regions the field is measured by phase and the irradiance, directly related to the photon flux. Also, microwave laboratory systems have traditionally relied on the transmission of radiation by waveguides, whereas with THz and mm-wave research the free-space propagation of field variations can be a more convenient, and less costly, alternative. The success and progression in recent years of terahertz imaging has, in part, been due to the borrowing of ideas from optical studies relating to both long and short wavelengths without any need to reinvent existing ideas relating to the manipulation or measurement of radiation.

1.2 Application of terahertz / sub-millimetre waves

There is no official standard definition for the limits of the terahertz and mm-wave regime, with the two terms often used interchangeably. Siegel admits to submitting to a “popular culture” in the use of the word terahertz in the title of an article, despite the content relating primarily to properties of millimetre waves with frequencies of 300 GHz - 3 THz [SIE86]. Although the experimental measurements in this thesis are performed at 100 GHz, outside the range of this loose classification, we shall utilise “terahertz” to include this frequency.

In the last decade terahertz technology was greatly publicised by the general media through the publication of journal articles relating to research in medical and biological applications [WOO02], [PIC04]. The energy levels at terahertz frequencies, for example $h\times$(300 GHz) = 1.2 meV, are significantly low which makes such radiation non-ionising, an important fact in the use of such radiation in medical and biological scenarios. The dangers of X-ray radiation in medical imaging are well known, thus any alternative to this high energy technique would be a beneficial addition. However, the plot below exhibits an obstacle to the development of medical applications utilising relatively long wavelengths, the absorption of terahertz and millimetre-wave radiation by water, an important compound in any biological sample [QUE91].

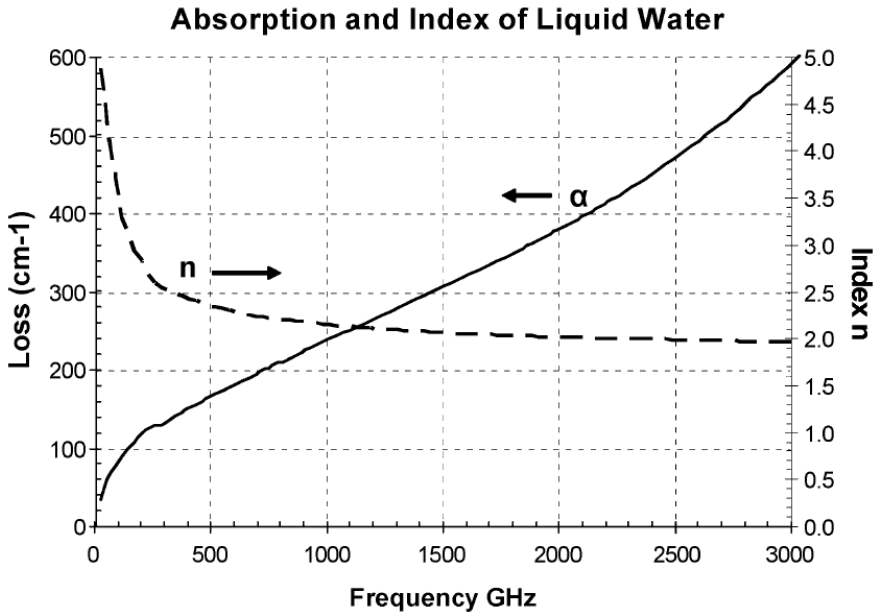

Figure 1.2 – Absorption α (left axis) and refractive index n of deionised water in the terahertz regime. Reproduced from [BER96].

Terahertz radiation, or "*T-rays*", was, and sometimes continues to be, represented by the print media as an alternative to X-rays. However the difference in the behaviour of both forms of radiation in a biological context is immense. Figure 1.2 shows the loss associated with H_2O, with α quantifying the exponential decay of a field within the material, given by Beer's law $\exp(-\alpha z)$, where z is the distance of propagation. The data presented in the plot shows a big disadvantage for the application of terahertz/mm-wave radiation to medical imaging or diagnosis. The water content of animal tissue is very large, thus any penetration like that achieved with X-ray radiation, is very limited if not

impossible. However, the field has found some interesting applications, for example, Dr. Duncan Robertson at the University of St. Andrews has developed a mm-wave imaging system for the monitoring of wounds which would normally be obscured by bandaging, allowing for examination of the progression of healing [ROB04].

The resolution of any diffraction limited image is proportional to the wavelength of radiation being used. Thus, the application of a sub millimetre wave technique with λ = 0.1mm to 3mm will have restricted medical applications, where the dimensions of features of interest can be on the same scale as the wavelength or even smaller. At millimetre wavelengths, the primary application of imaging has been targeted to the area of security scanning, with particular emphasis on counter-terrorism applications. In the 2000's continuous progress was made in the commercialisation of mm-wave scanners and recently such technology has begun to be used in many international airports. A unique property of mm-waves is their ability to pass through several forms of material that are opaque in the visible and near-IR range of the spectrum, such as plastics, clothing, glass, and paper. Thus this form of radiation is very suitable for the detection and imaging of items concealed by clothes, or by using terahertz pulses to identify objects through comparison of their spectral signature.

Below is an example of the kind of images and applications possible at millimetre wavelengths

Figure 1.3 - An image of a large concealed knife in a briefcase. Reproduced from Karpowicz (2005). The system employed a continuous wave (cw) source operating at 200 GHz (λ=1.5mm). The use of cw radiation is evident from the appearance of standing waves across the image.

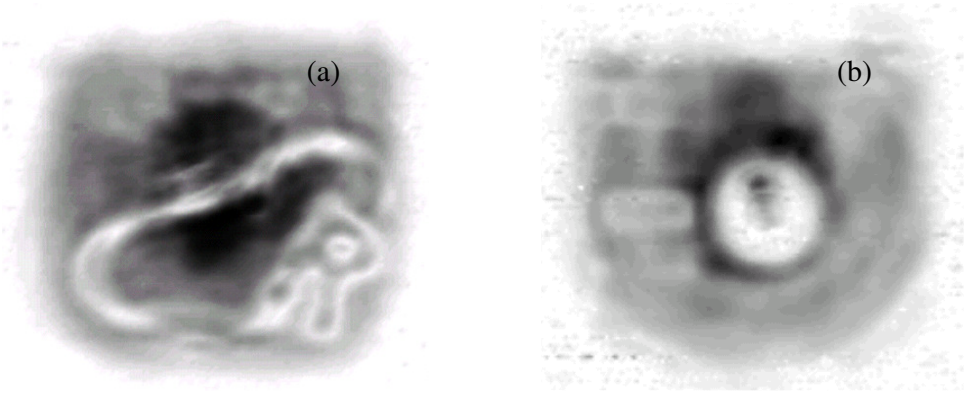

Figure 1.4 – (a) 100 GHz image of an envelope concealing an elastic band, an 'R' shaped piece of Teflon, and (b) image of a 3½" floppy disc. Measured by the author with a scanning Schottky diode detector in the near-field of the objects.

Figure 1.4 shows mm-wave images obtained by near field *active* imaging, whereby the system contains a radiation source to generate the fields used to illuminate the object. However, all objects radiate energy and *passive* mm-wave imaging is based solely on the detection and focusing of naturally occurring long wavelength radiation.

A good example of such imaging that does not require any artificial illumination is that applied in a system developed at the National Institute of Standards and Technology [GRO10]. The engineering involved in this arrangement is predominantly based on complex sensitive detection technology requiring intricate clean room development, and the use of motorised optical systems. An example image obtained with this system is given in Figure 1.5.

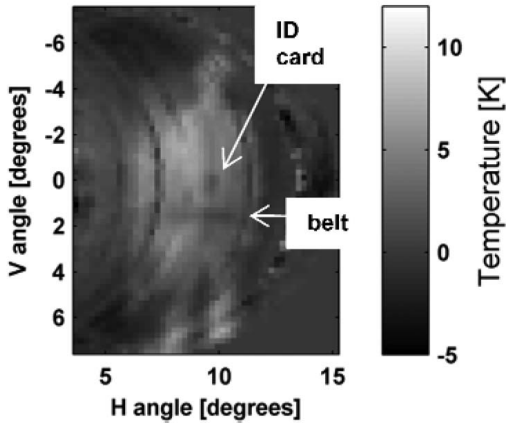

Figure 1.5 - MM-wave image of a human body. Reproduced from [GRO10].

The results in Figure 1.5 are measured on a 8×8 array of microbolometers, and measure the variation in temperature of an object, within a distance of 8m, from the temperature of some reference object. The images are also produced in real time which is a necessity for the application of the technology in security operations.

While mm-wave systems are most often carried out on a laboratory scale, the study of that specific band of the spectrum has been growing in large-scale applications such fields as remote sensing. Although water is strongly absorbent in the millimeter-wave regime, there are propagation windows at 35, 94, 140, and 220 GHz, where the attenuation is relatively modest in both clear air and fog. This may allow for imaging of, for example, land surfaces that are concealed by clouds or fog. In fact, millimetre-wave radiation can be attenuated several orders of magnitude less in clouds, fog, smoke and snow, than visual or IR radiation. For this reason, the use of millimetre wave radiation in airport traffic control has been studied [SHO93]. An example of similar work is shown in Figure 1.6

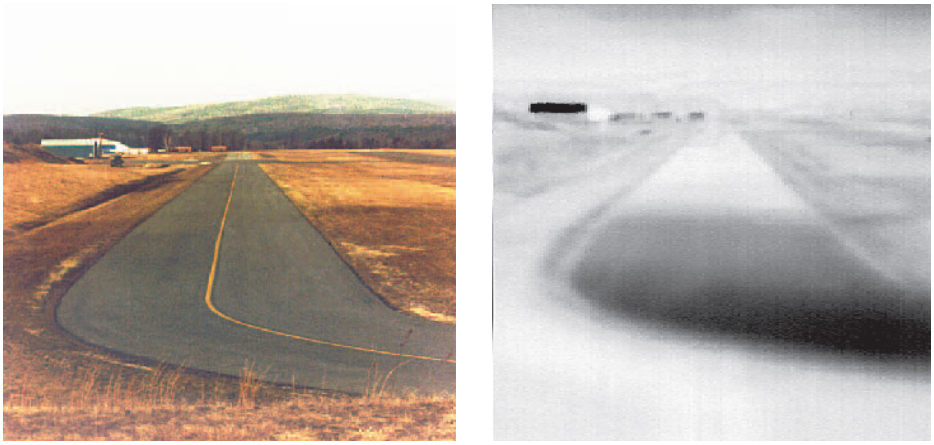

Figure 1.6 – (a) Visible image of airport runway, and (b) the same scene measured by detection of 94GHz radiation. Reproduced from [YUJ03].

1.3 - Sources of terahertz radiation

Research into the behaviour of electromagnetic waves, of any wavelength, could be divided into three subgroups: generation, propagation, and detection. This thesis is primarily concerned with the propagation of electromagnetic waves, and numerical techniques used to describe such. But to deal with mm-wave radiation and not mention the various technologies involved would be an incomplete summary of the field.

The surge of interest in terahertz radiation in the past two decades or so has been primarily due to the increase in availability and decrease in cost of radiation sources.

Previous attempts at far-IR imaging in the 1970's lacked continuity due to the expense of such technology, [HAR76].

1.3.1 - Gunn diode oscillator

At millimetre wavelengths the most commonly used, and least expensive, radiation source is known as a Gunn diode. Historically, this form of device was used primarily as a source of lower frequency radio waves, 500MHz-50GHz, but advances such as the use of gallium arsenide GaAs and gallium nitride GaN materials have allowed the generation of radiation with frequencies well into the terahertz range.

Gunn diodes are created from a single section of n-type semiconducting material with a variation of the doping across the material creating three regions with two heavily doped n (n+) regions surrounding a lesser doped n region. The densely doped regions can act as conductive terminals for connection of a device to the Gunn diode.

The active region of the diode is the central region which, because it is especially thin, will be subject to a large electric field when a voltage is applied across it. When the voltage in the central region exceeds a certain level the properties of the middle layer change and a current is induced and moves across this active region. While a current exists the potential gradient falls thus preventing any further current pulses to be generated, this is sometimes referred to as negative differential resistance see Figure 1.7. The voltage across the active layer will only increase again when the current reaches the far-side of the central region.

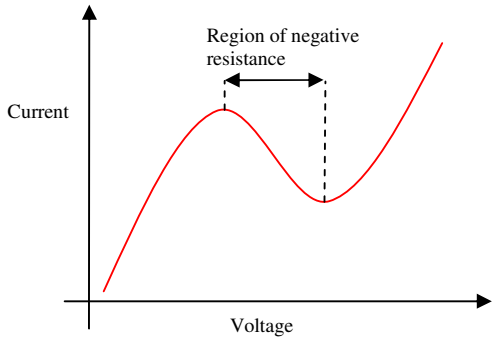

Figure 1.7 – Behaviour of current as a function of voltage in the middle layer of a Gunn diode.

When combined with an oscillator circuit, by adjusting the bias voltage across the diode, the negative resistance of the Gunn diode can be used to counteract the AC

resistance of the circuit, and oscillations can be maintained indefinitely thus generating EM radiation. See Figure 1.8.

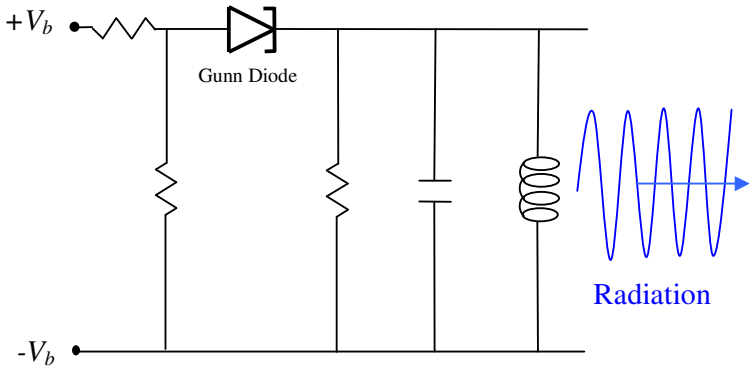

Figure 1.8 – Schematic of a basic microwave oscillator circuit employing a Gunn diode [LEE09].

In practice, a Gunn diode is normally mounted in a waveguide system with the whole assembly acting as a resonant cavity, see Figure 1.9. In such an arrangement the frequency of operation of a Gunn diode can be modified by mechanical tuning of the waveguide dimensions.

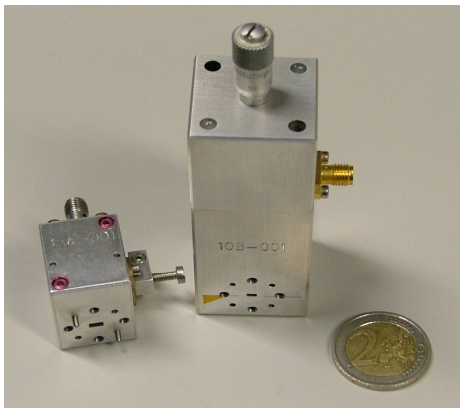

Figure 1.9 – Two examples of W-band Gunn-diode resonators.

Generally, such sources can be considered monochromatic with the bandwidth often less than a fraction of a percentage of the designated frequency.

1.3.2 - Free electron laser (FEL)

The operation of the free-electron laser is similar to that of a conventional laser, but whereas a gas laser uses excited electrons in a bound state, the FEL uses a beam of free electrons as the lasing medium. To generate a radiative action from the free particles, an electron beam with relativistic speeds is targeted between the poles of

magnets with alternating north and south poles, generally known as an undulator. The path of the electrons is defined by the Lorentz force $F=v\times B$ and results in a sinusoidal trajectory. Bremsstrahlung radiation is then emitted when the electrons undergo rapid acceleration at the crests and troughs of the electron path. Coherence is achieved as the oscillations of the electrons are in phase with the generated light. Note that in the descriptive figure below the waves are representative of oscillations that in reality would be polarised in the vertical direction (i.e. out of the page). A magnet is then used to direct the electron beam away from the direction of propagation of the coherent output radiation.

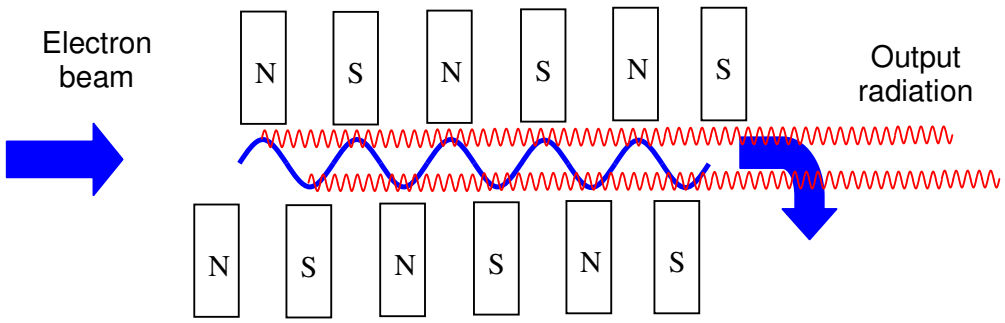

Figure 1.10 - Illustration of the production of EM fields by a free-electron laser.

In the last ten years, increasing numbers of publications have been devoted to the application of free-electron lasers in terahertz imaging, and the use of holography as an imaging technique using these sources has been suggested [CHE05]. Shown below is an example of images obtained by the illumination of a leaf with a free-electron laser, from [JEO05].

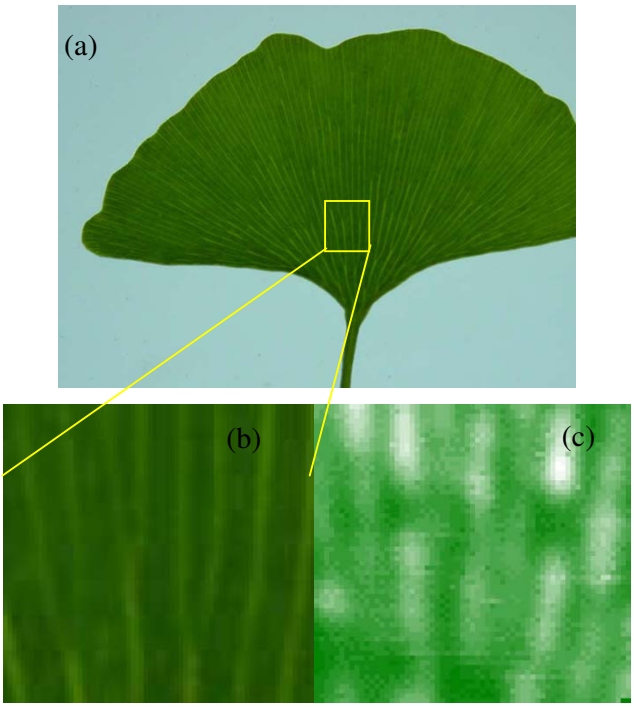

Figure 1.11 – Imaging using a free electron laser, reproduced from Jeong et. al. [JEO05]. (a) Sample of leaf to be imaged. (b) Visible image, (c) THz image using FEL.

The FEL is, however, not a portable or commercially available device. The length of the undulator can be several metres in length, depending on the desired power output, and the strength of the static magnetic field is required to be extremely large.

1.4 - Waveguides and Horn antennas

After generation of radiation within a Gunn diode, manipulation of the output field is often desired to provide effects such as attenuation, shifting of the phase of the wave, or indeed aiming of the beam in a desired direction. The components used to achieve such field alterations can be mounted to the output of the source as part of a waveguide system. Waveguides are effectively a one-piece transmission line which is tubular and most commonly has a circular or rectangular cross section. There are numerous possible field structures that can exist within a waveguide structure, represented by the transverse electric modes, TE_{mn} and transverse magnetic modes TM_{mn}, where, in simple terms, m and n represent the number of oscillations along the x and y direction respectively. The actual modes that will be generated within a waveguide cavity are dependant on the temporal excitation frequency of the EM field and the dimensions of the cavity [HUA08].

In a rectangular symmetric system, the propagation of a wave within a waveguide can be described by

$$E = E_0 \exp\left(i\left(k_x x + k_y y + k_z z - \omega t\right)\right)$$

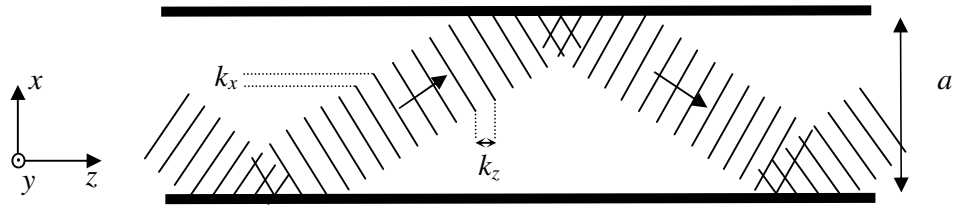

Figure 1.12 – Illustration of wave propagation within a waveguide.

The boundary conditions of a conductor define the allowable values of the transverse wavenumbers k_x and k_y of the normal E field which must have zero magnitude at the interior wall of the waveguide. Thus,

$$k_x = \frac{m\pi}{a}, \text{ and } k_y = \frac{n\pi}{b},$$

where m and n are integers. The length of the waveguide is assumed to be infinite thus the restrictions placed on k_x and k_y do not apply to k_z. However, for propagation along the z axis it is essential that the value of k_z must remain real, otherwise the wave will decay exponentially in that direction and there will be no transfer of electrical energy.

The *dispersion relation* of the waveguide is given by

$$\frac{\omega^2}{c^2} = \left(\frac{m\pi}{a}\right)^2 + \left(\frac{n\pi}{b}\right)^2 + k_z^2.$$

Thus, to allow for lossless propagation within the cavity $k_z^2 > 0$, this gives the minimum allowable, or cut-off, frequency within the waveguide as

$$\nu_c = \frac{c}{2}\sqrt{\left(\frac{m}{a}\right)^2 + \left(\frac{n}{b}\right)^2}\ .$$

which for the fundamental (m = 1, n = 1) mode

$$\nu_c = \frac{c}{2a}.$$

For circular waveguides of radius a, where the allowed modes are described in terms of Bessel functions, the cut-off frequency is given by

$$\nu_c = c\frac{1.81}{2\pi a}.$$

These values determine the minimum frequency at which radiation can propagate within the cavity of the antenna. The waveguides generally used in the laboratory at NUI Maynooth are the WR10 type which are designated for use at frequencies between 75GHz and 110GHz, and with dimensions of 2.54mm×1.27mm, the cut-off frequency for the TE_{10} mode is ~59 GHz. Shown below, in Figure 1.13, is a simple example of the propagation of fields within a WR10 waveguide calculated by solving Maxwell's curl equations using the Finite-Difference Time-Domain method. The field is derived from a 100 GHz source (λ = 3mm), resulting in a waveguide wavelength λ_g of

$$\lambda_g = \frac{\lambda}{\sqrt{1-\left(\frac{\lambda}{\lambda_c}\right)^2}} \approx 3.7mm.$$

In the case of a one-dimensional depiction of waveguide propagation, the components of the electric field, excited in the fundamental mode, are given by

$$E_y = E_0 \sin\left(\pi \frac{x}{a}\right) \exp\left(i\left(k_z z - \omega t\right)\right),$$

$$E_x = E_z = 0,$$

while the magnetic field components are given by

$$H_x = H_1 \sin\left(\pi \frac{x}{a}\right) \exp\left(i\left(k_z z - \omega t\right)\right),$$

$$H_y = 0,$$

$$H_z = H_2 \cos\left(\pi \frac{x}{a}\right) \exp\left(i\left(k_z z - \omega t\right)\right),$$

where E_0, H_1, and H_2 are constants.

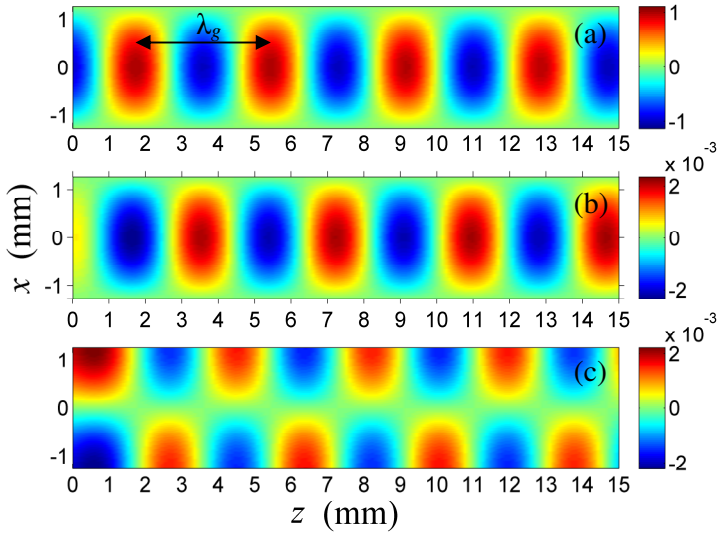

Figure 1.13 - The propagation of the fundamental mode of a 100 GHz field within a WR10 waveguide. (a) E_y, (b) H_x, (c) H_z. The waveguide wavelength, marked λ_g, shows an increase from the free space wavelength of 3mm.

The images shown in Figure 1.13 are an example of the importance of numerical simulation in mm-wave and terahertz optics. Although the field structures in the waveguide are relatively straightforward the technique used to derive those structures, FDTD, is not trivial. In the case of more complicated mode propagation this numerical method has significant potential in mm-wave applications, and will be discussed in more detail in Chapter 2.

Waveguides are used to "carry" the wave from the radiation source, such as a Gunn-diode, to a desired point in an optical arrangement, but the similarity in the dimensions of the waveguide to the radiation wavelength means that upon entering free-space from the waveguide, the EM field spreads out (diffracts) very rapidly which is not desired in a compact or indeed a large optical system. To allow for a more controlled and directed propagation, horn antennas are used to limit the angular spread of the radiation in free-space. The size, shape, and symmetry of such antennas have a huge variance, and the definition of whether a horn has a smooth or corrugated interior wall is an important factor in predicting its output. Cylindrically symmetric flared horn antennas are one of the most popular forms of horn antenna, while another frequently used form is a rectangular smooth-walled flared horn, see Figure 1.14.

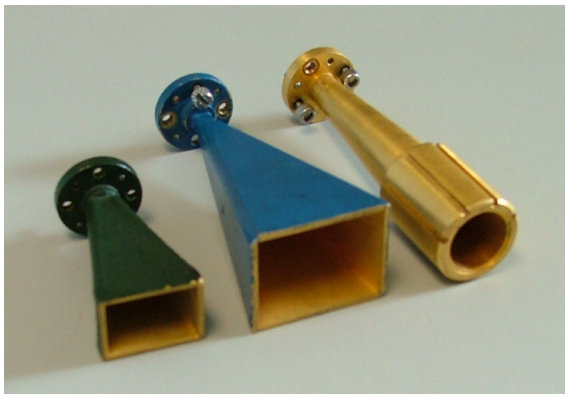

Figure 1.14 – Examples of horn antennas for the millimetre wave band. The two horns on the left are rectangular horns with WR15 (3.76mm×1.88mm) and WR10 (2.54mm×1.27mm) waveguide flanges, and on the right a WR10 corrugated circular horn.

The following plots illustrate the advantage of using a horn antenna. The simulations are based on a two-dimensional model, so the horn antennas in Figure 1.15 can be considered to be approximations to a sectoral horn. The value in the use of horn antennas in conserving the directionality of a propagating field is illustrated in the following Figure 1.15 (a) and (b).

The data in Figure 1.15 was generated by the author with an intensive electromagnetic computational technique finite-difference time-domain (FDTD), but more generally, the field at the mouth of a sectoral horn of diameter d can be represented as

$$E(x) = E_0 \cos(\pi x / d) \exp\left(i \frac{k x^2}{2L} \right),$$

where L is the slant length of the interior wall of the horn.

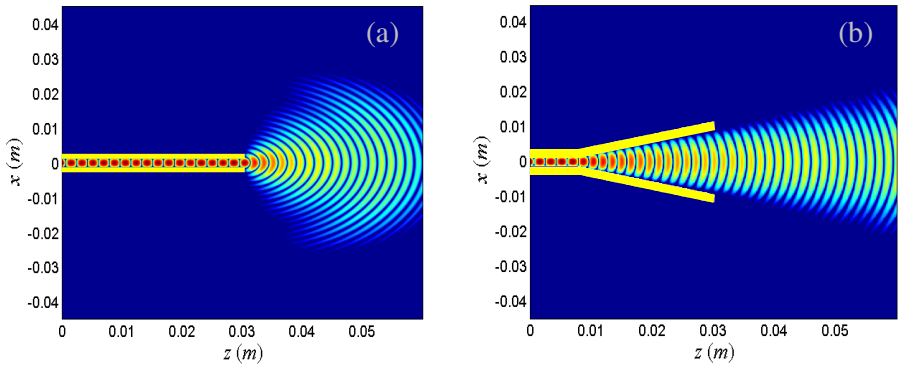

Figure 1.15 - Propagation of a 100 GHz field, shown as $|E_y|$, from (a) a bare waveguide, (b) a rectangular pyramidal horn with flare angle of 20º. Both plots are "clipped" at -30 dB. The electric field is polarised along the vertical axis (out of page). The structures of the fields in these plots were calculated by the author using the finite-difference time-domain method (FDTD).

The radiation generated by rectangular horn antennas is not uniform in that there are components of the field which are polarised orthogonally to the desired co-polarisation axis. Detectors, such as those with a waveguide receiver, are sensitive to the polarisation of the field, so to minimise power loss due to the generation of cross polarisation by the antenna the internal wall of the horn may be designed to have a corrugated profile.

The electric field in a conical cylindrical horn is dominated by an electric field with components having the form

$$E_x = A_1 J_0(k_r r) - \frac{(Z-Y)}{k_0 a} A_2 J_2(k_r r)\cos(2\theta)$$

$$E_y = \frac{(Z-Y)}{k_0 a} A_2 J_2(k_r r)\sin(2\theta)$$

where a is the maximum radius of the horn, k_r and k_0 are the transverse and free-space wavenumbers, A_1 and A_2 are amplitude coefficients, and Z and Y are the impedance and admittance, with

$$Z = -i\frac{E_\theta}{H_z} y_0 \text{ and } Y = -i\frac{H_\theta}{E_z} y_0 .$$

Cross polarisation is eliminated in this situation by exclusion of the angular variation present in E_x and E_y as $\cos(2\theta)$ and $\sin(2\theta)$, which can be done by equating Z and Y or their value being zero. H_θ, and consequently Y, is nullified by the reduction of currents in the axial z direction which is done when the corrugations in the wall of the antenna

are one quarter of a wavelength deep, thus the currents interfere destructively to cancel any angular variation of the fields. With a sufficient number of corrugations, E_θ will tend to zero and as the cross polarisation is very low in these instances, vector representation of the field can be unnecessary, thus such horns are sometimes referred to as being *scalar* horns, [CLA84].

In the laboratories at NUIM the standard method of detection is through the use of planar Schottky barrier diode detectors. Schottky diodes have a metal-semiconductor junction and exhibit a low voltage drop which allows for better efficiency and faster switching times.

1.5 - Chapter outline

This chapter has briefly introduced some of the applications and appliances in use today within the ever growing research field of terahertz and millimetre-wave technology. The author will describe methods for the calculation of electromagnetic fields in the mm-wave bands, and discuss their novel application in the modelling of imaging systems, namely, digital holography, ultrashort pulse behaviour, and diffractive optical components.

The thesis is divided into chapters as follows

Chapter 2

This section gives a description of the behaviour of electromagnetic fields due to diffraction, with emphasis on the paraxial description of radiation whereby it is assumed that the angular spreading of the beam is limited to shallow angles relative to the optical axes. In particular, we discuss the Gaussian beam mode method which will be shown to give an accurate, and computationally swift, description of paraxially propagating fields such as those that occur in terahertz optics.

Accounts are given of two methods used in the description of fields without any restriction to the angle of their diffractive spread, the finite-difference time-domain (FDTD) method, and a new form of GBM analysis using more recent expressions for the propagation of Hermite-Gaussian modes allowing for efficient and accurate non-paraxial calculations of far-field diffraction patterns.

Chapter 3

A description of a 100 GHz digital holographic system is presented for the measurement of phase by simple means. This is a good example of how techniques developed for the visible band may be applied to the terahertz/mm-wave band. This method relies on digital post-processing for imaging rather than physical manipulation of optical fields. The method has the potential to eliminate aberrations or other effects that may occur when relying on lenses or mirrors for the formation of images.

The author describes the numerical reconstruction of images using the Hermite-Gaussian expansion, which is completely independent from the Fourier theory that is the standard procedure in visible band hologram processing.

Chapter 4

The ideas presented in Chapter 2 are applied to the calculation of diffraction effects in fields that have time-dependent amplitudes, i.e. pulses. Knowledge of the behaviour of such waves has increased importance in the analysis of terahertz time-domain imaging and spectroscopy which is becoming a more widely used technique.

Here, pulsed fields diffracted by an aperture are calculated using the Gaussian beam mode approach, by superimposing individual pulsed Gaussian beam modes with suitable weightings to determine the overall effect of an aperture on the behaviour of pulses. Individually, the pulsed modes exhibit interesting properties, and we highlight how these effects manifest themselves in the diffraction of a plane wave pulses by apertures.

Chapter 5

A study of the optical properties of diffractive lenses was undertaken using the Laguerre-Gaussian mode analysis for both continuous and pulsed wave fields. A binary lens was designed by the author for operation at 100GHz and measured in a millimetre wave system. The modulation of optical pulses, near the visible band, by diffractive optical components was simulated, and an analysis of the focusing properties of these elements was performed.

Chapter 6

Bessel beams are solutions to the complete wave equation that, like an ideal plane wave, show complete resistance to diffraction. While they are also theoretical

field distributions, approximations to amplitude structures defined by a Bessel function can be generated using a conical lens, otherwise known as an axicon. The fields generated by these elements generate relatively long focal lines which may have advantages when incorporated onto THz and mm-wave imaging systems. We present a description of such fields using Gaussian beam mode analysis, along with experimental results measuring the intensity distribution of such an element.

Chapter 7 Summarises the main contributions and results of the work undertaken.

Chapter Two

Methods for Numerical Simulation of Far-Infrared Electromagnetic Fields

2.1 – Introduction

The branch of Physics known generally as Optics sets out to explain the myriad of phenomena associated with the propagation, reflection, absorption, scattering and other effects related to electromagnetic (EM) waves. From the formation of images by mirrors, to the transmission of radio signals, the study of how radiation interacts with its surrounding environment is one of the most important aspects of modern Physics. Like most phenomena in the physical sciences there are several theories with varying levels of complexity and accuracy that can be used to account for observed optical effects. In a broad categorisation, four theoretical formulations are used to describe the propagation of EM radiation and its interaction with matter, namely geometrical, scalar, physical, and quantum optics:

Geometrical optics provides the simplest description of the propagation of light. The theory assumes that the wavelength λ of the radiation to be described tends towards zero, $\lambda \longrightarrow 0$, thus allowing all free space diffraction effects to be neglected. In this instance, a beam, or the edge of a beam, is represented as an infinitesimal linear ray described by its angular components of propagation, which are altered only by refractive or reflective interactions with optical components resulting in deviations in its path. This form of optics allows for explanation of such effects as reflection and image formation and has been mainly used for visible wavelengths, but loses much of its usefulness in the millimetre wave band of the spectrum, although some diffractive behaviour in that regime can be represented as a linear effect, such as the far-field diffraction angle of a beam from a truncating obstacle.

Physical optics: This theory represents the oscillatory nature of light, and incorporates the description of light's electric and magnetic effects from Maxwell's equations. Light is described as a wave vector, thus calculation of the polarization of the field is allowed by such a formulation. Physical electromagnetic calculations are based

on the determination of the reflected fields generated by the current distribution created by the incident radiation on a conducting reflector. Such computations, depending on the scenario, can be very intensive and are often carried out with dedicated commercial software, such as Grasp™ a program developed by Ticra research corporation. At NUIM such software is used frequently in the analysis of long wavelength radio telescope systems, [OSU02].

Quantum optics: The quantum theory of matter requires a theory that can allow for the quantisation of the electromagnetic radiation to permit the atomic energy transitions predicted by the atomic theory. In this case EM fields are represented as a photonic quanta of energy $E = h\nu$, and enables prediction of the effects such as absorption caused by materials on radiation of different frequencies. This theory is rarely used in the applied optics that we discuss in this thesis, but is required, for example, in laser design, [LOU73].

Scalar Wave Optics: The wave nature of light has been recognised since the seminal work of Huygens, Fresnel, and Young, to name but a few. It is however; mainly due to the mathematical foundations laid by Joseph Fourier that scalar wave optics has become one of the most commonly used methods in the description of macroscopic optical effects. The Fourier theory of optics has allowed for the prediction of diffractive effects from complex wave interactions, and work on the theory in recent years has allowed for such calculations to be performed quickly by digital computers. In this formulation, an electromagnetic field can be represented through the amplitude and phase of the dominant polarization component within the field. The amplitude represents the magnitude of the electric field while the phase tends to be the dominating effect in the variation of beams' characteristics by propagation from its source.

One feature of electromagnetic wave propagation at long wavelengths that has the utmost importance is *diffraction*, defined in simple terms as the spreading or bending of waves as they pass through an aperture or round the edge of a barrier. Diffraction has been rigorously studied since the 18th century, and many theories and simplifications of theories have been presented. Here, the effect will be discussed with application to millimetre wave optics through the Fresnel theory [GOO05], and the Gaussian beam mode approximations [GOL98]. These are scalar paraxial techniques

and some aspects of the true vectorial nature of the fields are lost, for instance, a description of the field's polarisation.

Diffraction is an important subject in far-infrared optics due to the long wavelengths which are usually the same order of magnitude as the entrance pupil diameters of the optical systems through which the radiation propagates. If we use a simple formula for the angular spread of a beam from a circular truncating aperture of diameter D the angle of divergence is defined as $\theta = 1.22\ \lambda\ /\ D$, where λ is the wavelength of radiation, one can see that any similarity in magnitude between wavelength and aperture dimensions would give a large angular spread, thus one can not treat such situations with geometrical optics as is commonly performed with visible wavelengths.

This thesis is concerned with the scalar theory of optical diffraction and its analysis through mathematical techniques involving solutions to the paraxial form of the wave equation described by orthonormal wavefunctions more commonly associated with solutions of the Schrödinger equation in quantum mechanics. The form of diffraction calculation to be discussed is notably different, although physically related, to the far more frequently used method of the Fresnel diffraction integral to which thousands of scientific publications have been devoted since its derivation.

2.2 - The Fresnel diffraction integral

Christian Huygens postulated that the diffraction of a wave is due to every infinitesimal point on the wavefront being a source of secondary wavelets which recombine to form a subsequent wavefront. In the cases of ideal spherical and plane zwaves a description can be applied to their behaviour in all free space. However, when such waves encounter an obstacle causing dislocations in their ideal wavefront, discrepancies occur in the arrangement of the wavefront, as shown schematically in Figure 2.1, causing the phenomenon of diffraction.

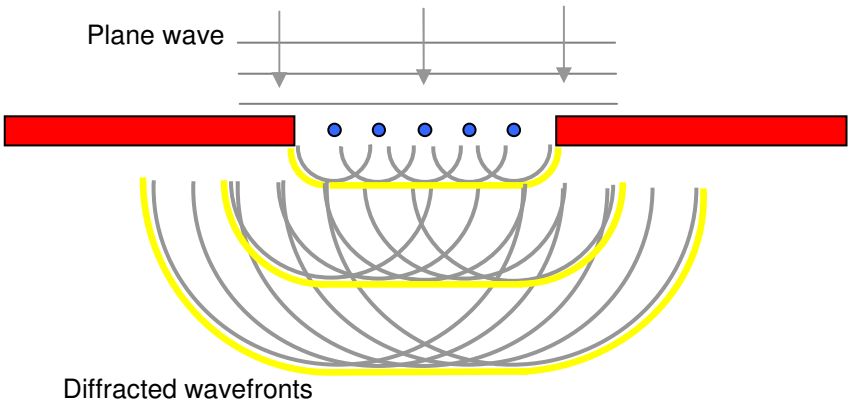

Figure 2.1 – Graphical depiction of Huygen's principle - the diffraction of a wave as a superposition of secondary spherical wavelets from each point on the wavefront.

The superposition of each spherical wave is defined through the Huygens-Fresnel principle and is represented mathematically as

$$E(x, y, z) = \frac{1}{i\lambda}\iint_A E_0(x_0, y_0, z_0)\cos\theta\,\frac{e^{ikr}}{r}\,dA \tag{2.1}$$

where the wavelength λ is the distance between the crests of the monochromatic field, and the wavenumber k gives the change in phase of the field in a unit distance, also related to $k = \omega/c$ with angular frequency ω and speed of light c. In eq. (2.1), x, y, and z represent the horizontal, vertical, and longitudinal Cartesian coordinates respectively in the region beyond the aperture $z > z_0$. x_0, y_0, and z_0 symbolise the coordinates at the aperture plane, where it is assumed that the aperture lies on a flat plane at $z = z_0$, which unless otherwise stated will be assigned the value zero for convenience without any loss of generality. r corresponds to the distance between a point in the diffraction plane (x,y,z) and a point on the aperture plane (x_0,y_0,z_0), and the obliquity factor (which prevents back-propagation of the field) has the form [GOO05]

$$\cos\theta = \frac{z}{r} = \frac{z}{\sqrt{(x-x_0)+(y-y_0)+(z-z_0)^2}}$$

and therefore

$$E(x, y, z) = \frac{z}{i\lambda}\iint_A E_0(x, y, z)\frac{e^{ikr}}{r^2}\,dA$$

Like most mathematical models of physical phenomenon, simplifications of this equation can be used to enable swifter calculations. The distance r is given by

$$r = \sqrt{z^2 + (x-x_0)^2 + (y-y_0)^2}$$

and it is known that if a quantity |γ| is less than unity then the binomial series predicts

$$\sqrt{1+\gamma} = 1 + \frac{\gamma}{2} + \frac{\gamma^2}{8} + \ldots$$

Rewriting r in the correct form for application of the expansion to the above integrals

$$r = z\sqrt{1 + \left(\frac{x - x_0}{z}\right)^2 + \left(\frac{x - y_0}{z}\right)^2}$$

which, when we take the first two terms of the binomial expansion, produces

$$r \cong z\left(1 + \frac{1}{2}\left(\frac{x - x_0}{z}\right)^2 + \frac{1}{2}\left(\frac{y - y_0}{z}\right)^2\right).$$

This is one form of the paraxial approximation and gives the Fresnel diffraction integral in Cartesian coordinate frame as

$$E(x, y, z) = \frac{i\exp(-i\,k\,z)}{\lambda z}\exp\left(-i\frac{k\left(x^2 + y^2\right)}{2z}\right)$$

$$\times\iint_A E_0(x_0, y_0)\exp\left(-i\frac{k\left(x_0^2 + y_0^2\right)}{2z}\right)\exp\left(-i\frac{k\,(x\,x_0 + y\,y_0)}{z}\right)dx_0 dy_0. \qquad (2.2)$$

Diffraction effects calculated using the above integral show frequent changes of the diffracted intensity structure in regions near the aperture. However, when the field is calculated at $z >> z_0$, successive measurement planes show similar intensity patterns, albeit with differing intensity and transverse scaling. This allows for further simplifications in the diffraction integral. A condition known as the Fraunhofer approximation is given by [GOO05] as being valid if

$$z >> \frac{k\left(x_0^2 + y_0^2\right)_{\max}}{2}$$

which if applied to the Fresnel integral eq.(2.2) yields the *Fraunhofer* diffraction integral

$$E(x, y, z) = \frac{i\exp(-i\,k\,z)}{\lambda z}\exp\left(-i\frac{k\left(x^2 + y^2\right)}{2z}\right)\iint_{x_0, y_0} E_0(x_0, y_0)\exp\left(-i\frac{k\left(x\,x_0 + y\,y_0\right)}{z}\right)dx_0 dy_0 \qquad (2.3)$$

The structure of this integral now allows for direct comparison with the Fourier transform, which, with modern algorithms, enables swift calculation of diffraction integrals. The Fourier transform, or spectral composition, $F(k_x)$ of a function $f(x)$ is given as

$$F(k_x) = \int_{-\infty}^{\infty} f(x)\exp(-ik_x x)dx$$

and its inverse is calculable from

$$f(x) = \frac{1}{\sqrt{2\pi}} \int_{-\infty}^{\infty} F(k_x)\exp(ik_x x)dx \ .$$

Shown below is the diffractive effect of a square aperture on a plane wave calculated by the fast Fourier transform (FFT) algorithm, and shows the amplitude of a wave very far from the aperture.

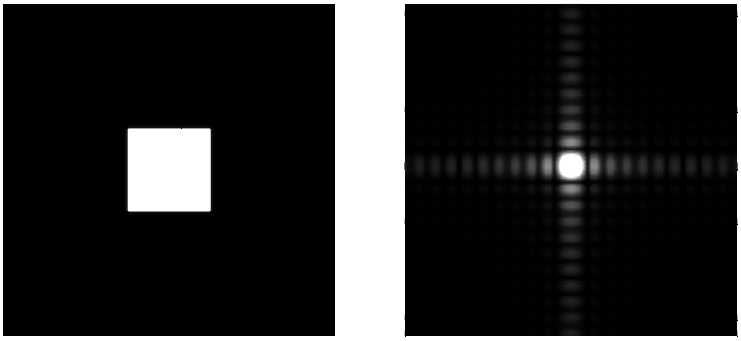

Figure 2.2 – A square aperture and its Fraunhofer diffraction pattern as calculated using the Fourier transform.

The main application of the Fourier transform is to derive a frequency-space representation of a function through elementary cosine and sine functions, and is an essential application in signal processing. It has also revolutionised the computational study of optics. The Fourier transform will be applied in later chapters, in the description of optical pulses and in image formation by digital holography.

The binomial approximation used previously is the basis of the paraxial theory of optics. In essence it is the representation of a spherical wavefront by a similar parabolic function, and is also associated with the trigonometric approximation $\theta \approx \sin\theta \approx \tan\theta$ where θ is the diffraction angle of the wavefront. Theories that employ this estimate are therefore valid only at points within relatively shallow angles to the optical axis where a sphere and a representative paraboloid deviate insignificantly. The angular region within which the paraxial method is valid, is ambiguous. The parabolic approximation of a spherical surface breaks down gradually at distances from its centre. Generally, and somewhat arbitrarily, fields within angles of 12° to the optical axes are considered valid within the literature. Despite these approximations, the diffraction

integrals obtained from (2.2) and (2.3) have become the standard mathematical procedure for analysis of many forms of optical fields.

2.3 - Gaussian beam diffraction

We have presented the general Fresnel diffraction integral for a general field without any reference to the form of the field $E_0(r_0)$. One important form of amplitude variation, particularly in coherent radiation fields, is the circularly symmetric Gaussian beam. These beams are, in theory, infinitely wide fields characterized by the variation

$$E(r) = \exp\left(-\frac{r^2}{w^2}\right) \tag{2.4}$$

where w is a real number known as the width parameter. With infinite extent, the ideal Gaussian beam is not realized in practice, but because of the rapid off-axis decrease in energy, approximations can be produced by coherent light sources such as Lasers and horn antennas like the conical corrugated horns discussed in [GOL98], and [LES90].

With the Fresnel diffraction integral the propagation of an ideal Gaussian field can be characterized by simple formulaic means. There are a few occasions when the Fresnel integral can be solved to give a complete simple analytical description of the diffracted field, and these usually involve integration of fields over an infinite range, which is valid here given the extent of the Gaussian function.

The field of a circularly symmetric field beam at a plane z can be calculated using the Fresnel integral from

$$E(r,z) = i\frac{k}{z}\exp\left(-ikz - i\frac{kr^2}{2z}\right)\int_0^\infty E_0(r_0)J_0\left(\frac{krr_0}{z}\right)\exp\left(-i\frac{kr_0^2}{2z}\right)r_0 dr_0 \tag{2.5}$$

which is the analogue of eq. (2.2) in cylindrical coordinates, with the zeroth order Bessel function J_0 arising from the substitution of angular coordinates in equation (2.2). With $E_0(r_0)=\exp(-r_0^2/w_0^2)$, the integral in equation (2.5) has an appropriate form to be compared with the integral from [GRA07],

$$\int_0^\infty \exp\left(-\frac{1}{2}\gamma r^2\right)J_0(\delta r)r\,dr = \frac{\exp\left(-\frac{\delta^2}{2\gamma}\right)}{\gamma}$$

and both equations have the same form if

$$2\gamma = \frac{2ik}{z} - \frac{4}{w_0^2},\ \delta = \frac{kr_0}{z}, \text{ and } \frac{1}{2\gamma} = \frac{zw_0^2}{2ikw_0^2 - 4z}\ .$$

With some algebraic manipulation the diffraction of an ideal fundamental Gaussian beam ψ_0 is given by the equation

$$\psi_0(r,z) = \sqrt{\frac{2}{\pi\, w(z)^2}} \exp\left(-\frac{r^2}{w^2(z)}\right) \exp\left(i(k\,z - \omega t)\right) \exp\left(i\frac{kr^2}{2R(z)}\right) \exp\left(-i\tan^{-1}\left(\frac{2z}{k\,w_0^2}\right)\right) \tag{2.6}$$

where the subscript in ψ_0 indicates that this form of field is the basic form of a family of similar solutions. The functions w and R are given by

$$w^2(z) = w_0^2\left(1 + \left(\frac{2z}{k\,w_0^2}\right)^2\right), \tag{2.7}$$

$$R(z) = z\left(1 + \left(\frac{k\,w_0^2}{2z}\right)^2\right). \tag{2.8}$$

These parameters $w(z)$ and $R(z)$ have paramount importance in the modeling of long wavelength optical systems. $w(z)$ represents the transverse broadening of the field due to diffraction with increasing distance from the source, while $R(z)$ determines the variation in the radius of curvature of the wavefront of the field.

The propagation equation of a Gaussian beam, eq. (2.6), can be divided into three distinct parts. Firstly, the parameter $\sqrt{2/\pi\, w(z)^2}$ normalizes the amplitude value of the beam such that the energy present in the field at any plane, i.e. $\int_0^\infty |\psi|^2 2\pi\, r\, dr$, is a constant. The second real exponential term defines the transverse variation of the field amplitude envelope which is seen to always possess the form of a Gaussian function but varies with increasing z according to $w(z)$. The final three complex exponential terms combine to define the phase of the beam. The direction of the wavefront can be considered to be the normal to the surfaces of equal phase of this function which are flat at the plane $z = 0$ due to the convergence of $R(z = 0) \rightarrow \infty$, and at larger distances the increasing spherical variation of the field increases causing the beam to diverge from the optical axis and become wider with increasing z.

A useful parameter in describing Gaussian beam propagation is the *confocal distance*

$$Z_c = \frac{\pi\, w_0^2}{\lambda} = \frac{k\, w_0^2}{2}. \tag{2.9}$$

Its value can be informally regarded as the distance at which a diffracted Gaussian beam mode no longer represents an image of the original field at $z = 0$, and gives the distance at which the width parameter $w(z)$ is equal to $\sqrt{2}w_0$ or as the plane at which the area of the beam becomes twice that at the source. $w(z)$ increases approximately linear when $z >> Z_c$, and the effective radius $w(z)$ of each Gaussian beam diverges at an angle of

$$\theta_{FF} \approx \tan\theta \approx \frac{\lambda}{\pi w_0} \tag{2.10}$$

while at the same distances the radius of curvature of the wavefront converges to the relationship $R(z) \approx z$. Figure 2.3 depicts the propagation of a Gaussian beam according to equation (2.6).

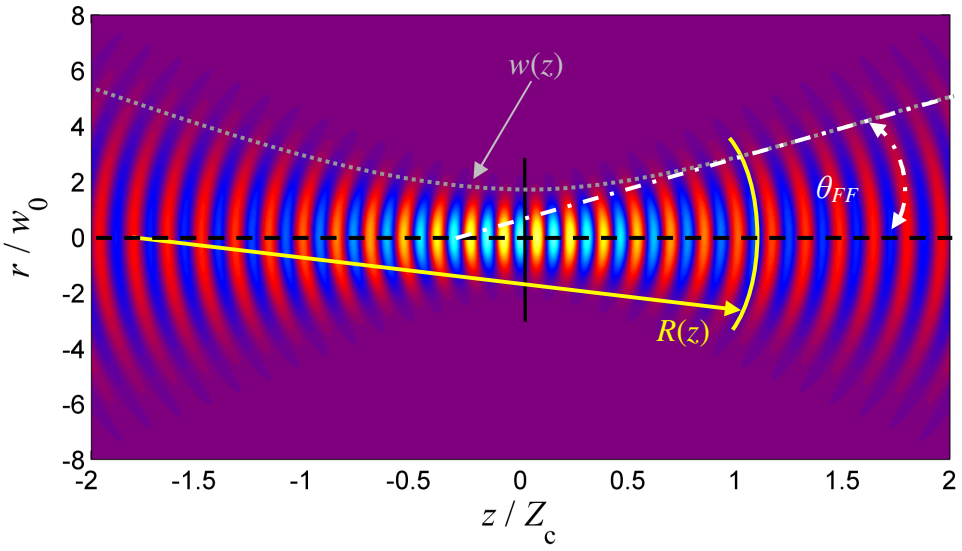

Figure 2.3 - The propagation of a fundamental Gaussian beam.

The final term of equation (2.6) is an important term known as the *Gouy phase shift*. This factor represents a deviation of the Gaussian beam's phase from the ideal plane wave due to off-axis diffractive spreading. The variation of this phase difference is shown below.

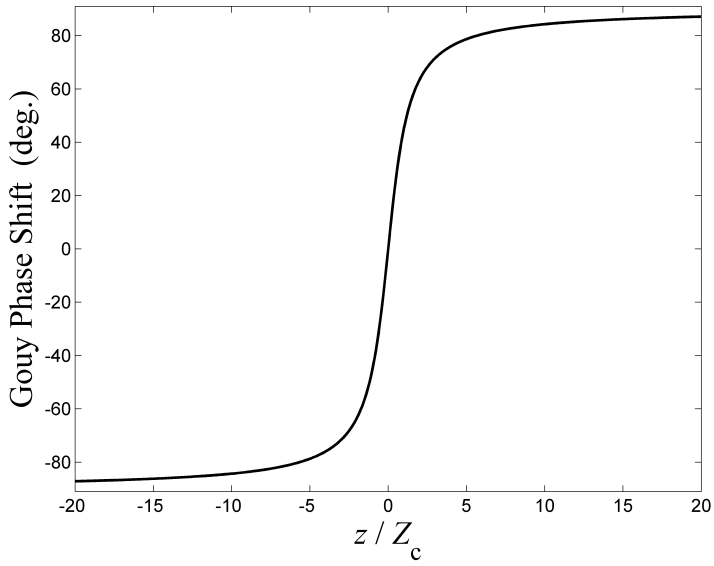

Figure 2.4 - The on-axis Gouy phase shift for a fundamental Gaussian beam.

The phase converges, for the fundamental Gaussian beam, to $\pi/2$, and has important consequences on the behaviour of Gaussian beams. This will play an important role in the study of pulses subject to this phase shift to be described in chapter 4.

2.4 - Ray transfer matrices

The lens, and its effect on the propagation of a radiation field, is a very important aspect of optics, it being the most widely used optical element in all areas of optical research, and indeed in everyday life. The most basic and a frequently used method of describing the effect of a lens on a field is the application of ray-transfer matrices, or, as they are commonly known, *ABCD* matrices. The basis for this technique is the representation of an optical system by a product of matrices, by which each individual matrix represents the effect of an optical element on a ray of light, be it due to refraction, reflection, or propagation through a medium, such as a vacuum or glass.

In the case of the traversal of free space by a ray of light the corresponding ABCD matrix maps the original spatial and angular direction co-ordinates, relative to the optical axis, to the new position and angle, as in Figure 2.5

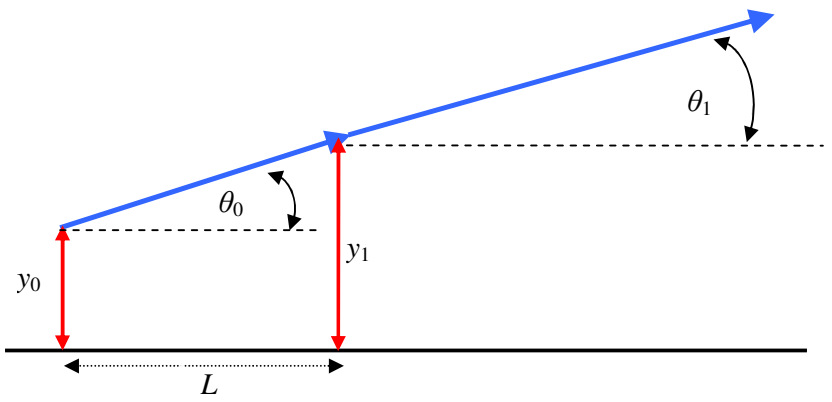

Figure 2.5 - The translation of a ray of light (blue) over a medium of regular refractive index

Given a medium of constant optical density of unit value it should be obvious that $\theta_0 = \theta_1$ and $y_1 = y_0 + L \tan\theta_0$. The matrix notation that represents these equations is [PED93]

$$\begin{pmatrix} y_1 \\ \theta_1 \end{pmatrix} = \begin{pmatrix} 1 & L \\ 0 & 1 \end{pmatrix} \begin{pmatrix} y_0 \\ \theta_0 \end{pmatrix},$$

using the approximation $\theta = \tan\theta$. Thus, the transfer matrix associated with free-space propagation is given by

$$\begin{pmatrix} 1 & L \\ 0 & 1 \end{pmatrix}$$

The most common occurrence of ABCD matrices in optics is in the transmission of a beam through a spherical surface that acts as an interface between two media of refractive indices n_1 and n_2 as, for example, in a thick lens with a surface curvature of R. In that case, using a paraxial form of Snell's law $n_1\theta_1 = n_2\theta_2$ (valid under the paraxial assumption $\sin\theta \approx \theta$), the appropriate transfer matrix becomes

$$\begin{pmatrix} y_2 \\ \theta_2 \end{pmatrix} = \begin{pmatrix} 1 & 0 \\ \frac{1}{R}\left(\frac{n_1}{n_2} - 1\right) & \frac{n_1}{n_2} \end{pmatrix}$$

One can show that the transfer matrix of a beam entering a medium of refractive index n_2 at a plane interface is given by

$$\begin{pmatrix} 1 & 0 \\ 0 & \frac{n_1}{n_2} \end{pmatrix}$$

because a flat surface has a radius of curvature $R \to \infty$. Most common simple surfaces can have their effects on a light ray represented in an ABCD matrix. Other examples of transfer matrices are:

For a thin lens

$$\begin{pmatrix} 1 & 0 \\ \frac{-1}{f} & 1 \end{pmatrix}$$

and for a spherical mirror

$$\begin{pmatrix} 1 & 0 \\ 2/R & 1 \end{pmatrix}$$

where the sign of the mirror curvature R depends on the mirror being concave or convex.

In millimetre wave optics, the propagation of Gaussian beams through an optical system can be determined by use of a complex beam parameter q

$$\frac{1}{q(z)} = \frac{1}{R(z)} - i\left(\frac{\lambda}{\pi w^2(z)}\right).$$

With representation of an optical system through an ABCD matrix the q parameter will vary according to the change in values of R(z) and $w(z)$ as defined by eqs. (2.7) and (2.8). With definition of the radius of curvature and width of a Gaussian beam at the entrance of an optical system, the value of q at an output plane can be determined from

$$q_{out} = \frac{Aq_{in} + B}{Cq_{in} + D}$$

and the beam parameters R and w can be calculated as

$$\frac{1}{R_{out}} = \mathrm{Re}\left\{\frac{1}{q_{out}}\right\} \text{ and } \frac{\lambda}{\pi w_{out}^2} = \mathrm{Im}\left\{\frac{1}{q_{out}}\right\}.$$

While very simple to use, ray transfer matrices are often not adequate for a complete description of a beam. This is so when the paraxial approximation breaks down or when the phase distribution of a beam at the face of a lens or medium is not spherical, or aberrations are present and the effect of the optical component is more complicated and therefore requiring the lens to be represented by a complex exponential phase term in, for example, the Fresnel diffraction integral. Goodman [GOO05] describes a variation of the spherical wavefront imposed by a lens on a beam as a parabolic/quadratic function for the situation of fields with only weak divergence in

relation to the optical axis. It should be noted however that this is still an approximation, valid only in the paraxial regime of diffraction.

If the total thickness of the lens at the coordinates x and y is given by Δ, the phase transformation imposed by a lens is given by

$$\exp(i\phi_{lens}) = \exp(i\,k\,(n-1)\Delta(x,y))$$

The total thickness function of the lens Δ is taken to be the sum of the depth of three individual sections of the lens $\Delta=\Delta_1+\Delta_2+\Delta_3$, see Figure 2.6.

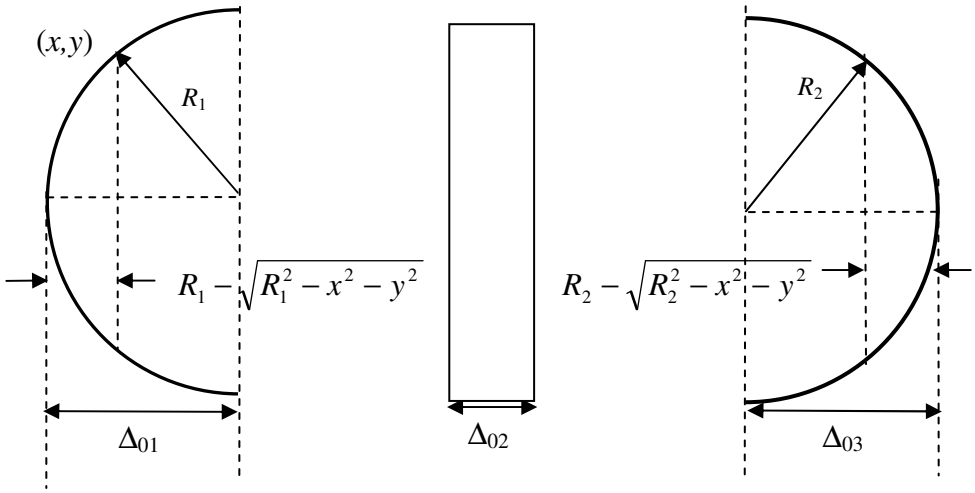

Figure 2.6 – Layout for simplification of the structure of a thin lens.

We can see from the figure above,

$$\Delta_1(x,y) = \Delta_{01} - R_1 - \sqrt{R_1^{\,2} - x^2 - y^2}\,.$$

and, calculating in the same manner

$$\Delta_3(x,y) = \Delta_{03} - R_2 - \sqrt{R_2^2 - x^2 - y^2}\,.$$

Thus, total thickness at (x,y) becomes

$$\Delta(x,y) = \Delta_0 - R_1\left(1 - \sqrt{1 - \frac{x^2+y^2}{R_1^2}}\right) - R_2\left(1 - \sqrt{1 - \frac{x^2+y^2}{R_2^2}}\right).$$

Using the binomial approximation we now define a transformation function for the lens as

$$\phi_{lens}(x,y) = \exp\left(i\,k\,\frac{(x^2+y^2)}{2f}\right) \tag{2.11}$$

where

$$\frac{1}{f} = (n-1)\left(\frac{1}{R_1} - \frac{1}{R_2}\right) \tag{2.12}$$

f being the *focal length* of the lens. The phase distribution described in eq. (2.11) is akin to the definition of the curved wavefront of a Gaussian beam, and thus the effect of such transformation is to alter the radius of curvature of a Gaussian wavefront incident on the lens. This form of approximation is commonly used in the paraxial regime of diffraction analysis in estimating field divergence.

Equation (2.12) is often referred to in optics and quasi-optics as the "*Lens-makers formula*", as it allows for a quick calculation of the parameters required for a desired lens.

2.5 - Orthogonal beam modes

Fourier analysis is a fundamental technique used in the physical sciences for the expansion of an arbitrary function as a series of fundamental harmonic sinusoids. There are several functions like the sine and cosine functions that allow for a similar formulation of arbitrary functions.

Two functions $f_i(x)$ and $f_j(x)$ are said to be orthogonal if they satisfy the condition

$$C\int_{-\infty}^{\infty} \Pi(x) f_i(x) f_j(x)\, dx = \delta_{ij}$$

where δ_{mn} is the Kronecker delta function, given as

$$\delta_{ij} = \begin{cases} 0, & i \neq j \\ 1, & i = j \end{cases}.$$

$\Pi(x)$ is known as a weighting function, and C is a constant. Other examples of such orthogonal functions include the Legendre polynomials, and the Laguerre and Hermite polynomials. A Gaussian modulation of the latter two functions provides two important solutions to the paraxial wave equation, arising in optical theory as free-space modes, or as modes within a Laser cavity [SIE86, MUR93, PED93]. The orthogonality of the Hermite and Laguerre-Gaussian beam modes is the characteristic of the functions that make them so useful in the context of far-infrared applications.

Suppose we wish to describe the Fraunhofer diffraction from an obstacle which consists of two rectangular slits parallel to each other. It would be correct to insert the

entire aperture function into the diffraction integral and integrate over the entire area surrounding the two slits to obtain a solution. However a much simpler method would be to define the overall transmittance as the superposition of two independently diffracting rectangular apertures, for which the Fraunhofer calculation is widely known. The characterisation of a beam diffracted by an aperture of transmittance E_0 can only be directly expressed analytically for a certain number of aperture functions, usually with infinite extent. If, however, an irregular transmittance can be described in terms of constituent beams for which the diffraction characteristics are known, we can then describe the total diffractive behaviour of the aperture through the summation of the independently propagating fields. This is the basic reasoning behind Gaussian beam mode analysis (GBMA), whereby the unknown characteristics of a field diffracted by an obstacle are calculated by a weighted sum of field modes whose properties can be well described.

2.5.1 – Higher-order paraxial Gaussian beams

The propagation of the fundamental Gaussian beam in the previous section has been studied intensively for decades. The beam is often used as a first order approximation of fields with similar structures, such as a laser output field or the beam derived from a cylindrical horn antenna which may be useful in preliminary analyses of optical systems. There are, however, other similar solutions that can observe similar propagation laws to those for the Gaussian beam, and it turns out that the form of Gaussian beam described previously is a fundamental form of a complete family of beam modes.

An alternative description of paraxial propagation involves a reduction of the wave equation. Electromagnetic fields are generally defined in the general form of harmonic waves given by

$$E(x,y,z)=\psi(x,y,z)\exp(i\,(k\,z - \omega t)) \tag{2.13}$$

where the quantity ψ is assumed to be a slowly varying time-independent function, i.e. the wave is monochromatic. In this case the wave equation can be rewritten as the *Helmholtz equation*

$$\nabla^2\psi + k^2\psi = 0\,. \tag{2.14}$$

Defining a paraxial field as one for which the longitudinal (on-axis) variation is less than the order of a wavelength, this can be represented as the paraxial

assumption $\frac{\partial \psi}{\partial z} << k\psi$, then $\frac{\partial^2 \psi}{\partial z^2} << \frac{\partial^2 \psi}{\partial x^2} + \frac{\partial^2 \psi}{\partial y^2}$, which further reduces the above equation to the *paraxial wave equation*, given in the Cartesian co-ordinate frame as

$$\frac{\partial^2 \psi}{\partial x^2} + \frac{\partial^2 \psi}{\partial y^2} - 2\,i\,k\frac{\partial \psi}{\partial z} = 0\,. \tag{2.15}$$

Up to this, only the propagation of the fundamental Gaussian beam has been discussed. However, the paraxial wave equation gives rise to several other forms of more complicated solutions, but which display similar diffraction characteristics. These are they Hermite-Gaussian and Laguerre-Gaussian beam modes.

2.5.2 - Hermite-Gaussian beam modes

In the Cartesian frame of the paraxial wave equation the solutions obtained were found to be the Hermite-Gaussian (HG) functions, which were applied in Quantum theory as the solutions for the wave-functions of a harmonic oscillator. These polynomials satisfy Hermite's differential equation [WEI02] and as solutions to the paraxial wave equation (PWE) take the two-dimensional form $H_l(ax)H_m(by)$ where l and m are integers, and a and b are constants related to the scaling of the modes in a coordinate system defined by x and y. The first few Hermite polynomials are easily obtained from its generating function, and for low values of the mode index we obtain

$$H_0(s) = 1,\ H_1(s) = 2s, H_2(s) = 4s^2\text{-}2,\ H_3(s) = 8s^3\text{-}12s.$$

The Hermite polynomials of order m are m^{th} order polynomials thus each mode has m roots of $H_m(s) = 0$. Texts on mathematical techniques commonly give the following integral

$$\int_{-\infty}^{\infty} e^{-s^2} H_m(s)\,ds = 2^m\,m!\,\sqrt{\pi}\,\delta_m\,.$$

Here we will present the same equation as (where $s = \sqrt{2}\,x/w$)

$$\int_{-\infty}^{\infty} H_m\left(\sqrt{2}\,\frac{x}{w_0}\right)\exp\left(-\frac{x^2}{w_0^2}\right)dx = 2^{m-1/2}\,m!\sqrt{\pi\,w_0^2}$$

which allows for the waist parameter and Gaussian envelope to be more easily recognised.

Thus, the one-dimensional normalised Hermite-Gaussian mode is given by

$$\psi_m^H = \frac{1}{\sqrt{2^{m-1/2}\, m! \sqrt{\pi\, w_0^2}}} H_m\left(\sqrt{2}\,\frac{x}{w_0}\right) \exp\left(-\frac{x^2}{w_0^2}\right). \tag{2.16}$$

The orthogonal properties of Hermite-Gaussian functions are extremely convenient and result in their frequent application in the physical and mathematical sciences. In particular, image processing is one such area that has used Hermite-Gaussian functions in, for example, forensic fingerprint analysis [WANG07a], seismic image analysis [WANG07b], and other image processing functions such as edge detection [SHE95]. Figure 2.7 shows the one-dimensional structure of the Hermite-Gaussian modes.

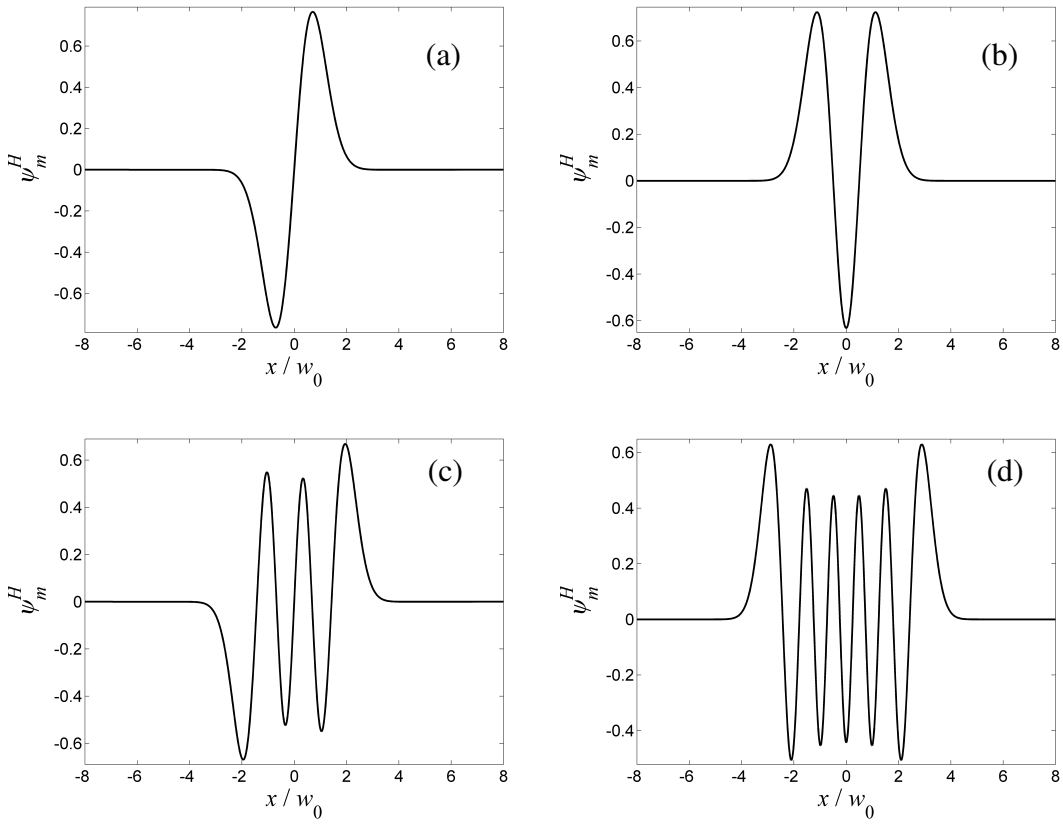

Figure 2.7- The Hermite-Gaussian functions (a) $m = 1$, (b) $m = 2$, (c) $m = 3$, (d) $m = 10$.

As solutions of the complete PWE in Cartesian systems the HG modes appear as $\psi_l\psi_m$. Examples of these two-dimensional Hermite-Gaussian distributions are shown in Figure 2.8.

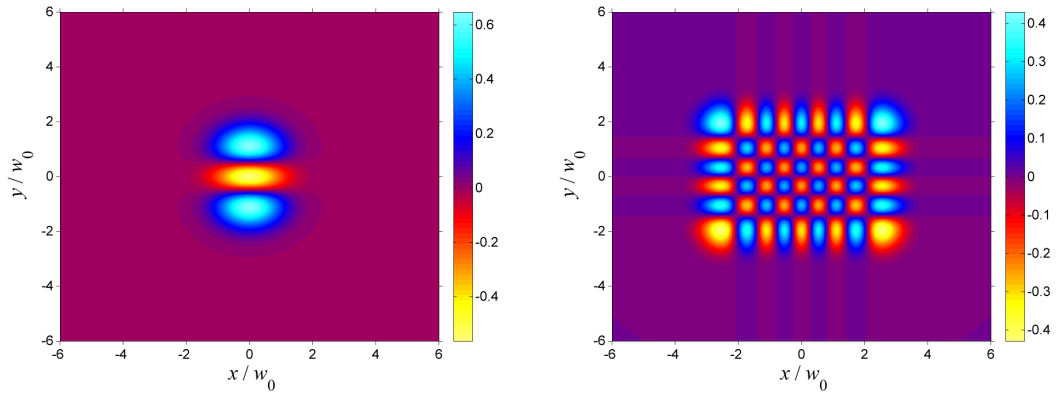

Figure 2.8 - Two dimensional Hermite-Gaussian beam modes for (*l*,*m*)= (a) (0,2) (b) (8,5).

The propagation of the HG beam modes can be defined from the Fresnel diffraction integral in Cartesian coordinates for $z > 0$ and their field is defined as [MUR93]

$$\psi_{l,m}^{H}(x,y,z) = C_l C_m H_l\left(\sqrt{2}\,\frac{x}{w_x(z)}\right) H_m\left(\sqrt{2}\,\frac{y}{w_y(z)}\right) \exp\left(-\frac{x^2}{w_x^2(z)} - \frac{y^2}{w_x^2(z)}\right)$$
$$\times \exp(i\,k\,z) \exp\left(i\,\frac{k\,x^2}{2R_x(z)} + i\,\frac{k\,y^2}{2R_y(z)}\right)$$
$$\times \exp\left(-i(l+m+1)\tan^{-1}\left(\frac{\lambda z}{\pi w_0^2}\right)\right), \qquad (2.17)$$

where w and R have the same meaning as defined earlier in this chapter, eqs. (2.7) and (2.8), but here subscripts of x and y indicate that there may be a difference in the beam parameters in the horizontal and vertical directions due to asymmetry in the definition of the propagation space. C_m is the normalization constant

$$C_m = \frac{1}{\sqrt{2^{m-1/2}\,m!\,\sqrt{\pi w^2}}} \qquad (2.18)$$

used to maintain a constant energy at each z plane. Figure 2.9 depicts the propagation of the $m = 5$ HG beam mode.

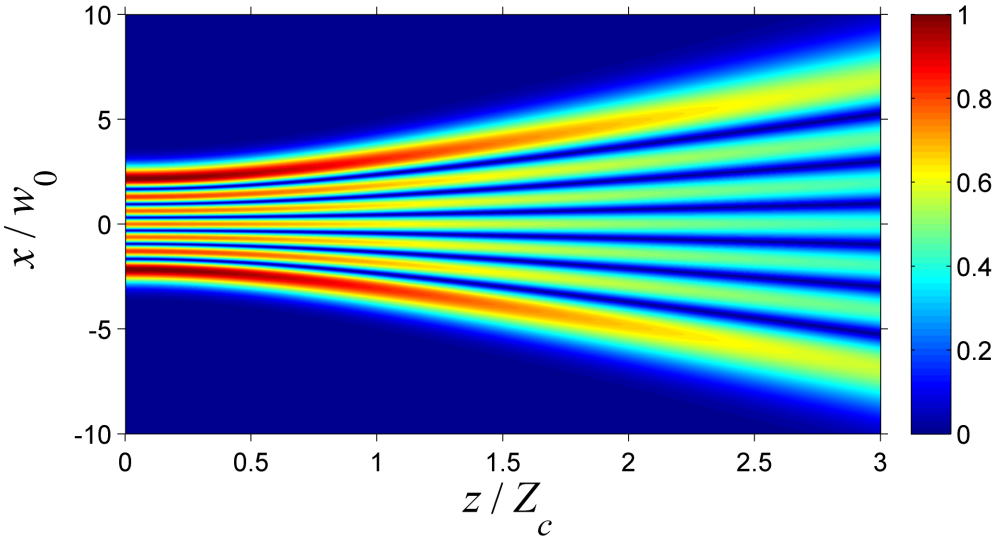

Figure 2.9 - The propagation of the one-dimensional m = 6 Hermite-Gaussian beam mode, $\left|\psi_6^H\right|$. The field values have been normalised to the maximum amplitude.

The behaviour of the phase of the Hermite-Gaussian fields is similar to that of the fundamental Gaussian mode, but for the higher order modes the Gouy phase term includes a factor of the beam mode index, with the phase shift now converging on $(l+m+1)\,\pi / 2$ in the far-field.

2.5.3 - Synthesis of functions using Hermite-Gaussian modes

In many real applications in long wave optics, the composition of functions with the appropriate orthogonal Hermite-Gaussian mode set has a high rate of convergence with an increasing number of modes. Like Fourier analysis, observation can allow for exclusion of certain modes, for example, those with the same symmetry as the field being considered.

The synthesis of a one-dimensional function using HG modes involves the calculation of an *overlap integral* between each mode and the desired field $E_0(x)$ given in eq. (2.19)

$$A_m = \frac{1}{\sqrt{2^{m-1/2}\, m!\, \sqrt{\pi\, w_0^2}}} \int_{-\infty}^{\infty} E_0(x) H_m\left(\sqrt{2}\,\frac{x_0}{w_0}\right) \exp\left(-\frac{x_0^2}{w_0^2}\right) dx_0 \ . \qquad (2.19)$$

This equation defines the *mode coefficient* A_m, similar to the coefficients used in Fourier analysis, and represents a correlation between each mode and the function $E_0(x)$. With knowledge of the coefficients the synthetic function can be constructed

with a summation over a finite number of M modes which will closely approximate $E_0(x_0)$, i.e.

$$E_0(x_0) \cong \frac{1}{\sqrt{2^{m-1/2}\, m! \sqrt{\pi\, w_0^2}}} \sum_{m=0}^{M} A_m H_m\left(\sqrt{2}\,\frac{x_0}{w_0}\right) \exp\left(-\frac{x_0^2}{w_0^2}\right) \tag{2.20}$$

where the superscript denotes a truncated series expansion. In Figure 2.10 we show the HG synthesis of a *rect* function given as

$$rect\left(\frac{x_0}{a}\right) = \begin{cases} 1, & |x_0| \le a \\ 0, & |x_0| > a \end{cases} \tag{2.21}$$

We can expand this function within the range $x_0 = \{-a,a\}$ without any loss of information as $E(x_0) = 0$ beyond these points.

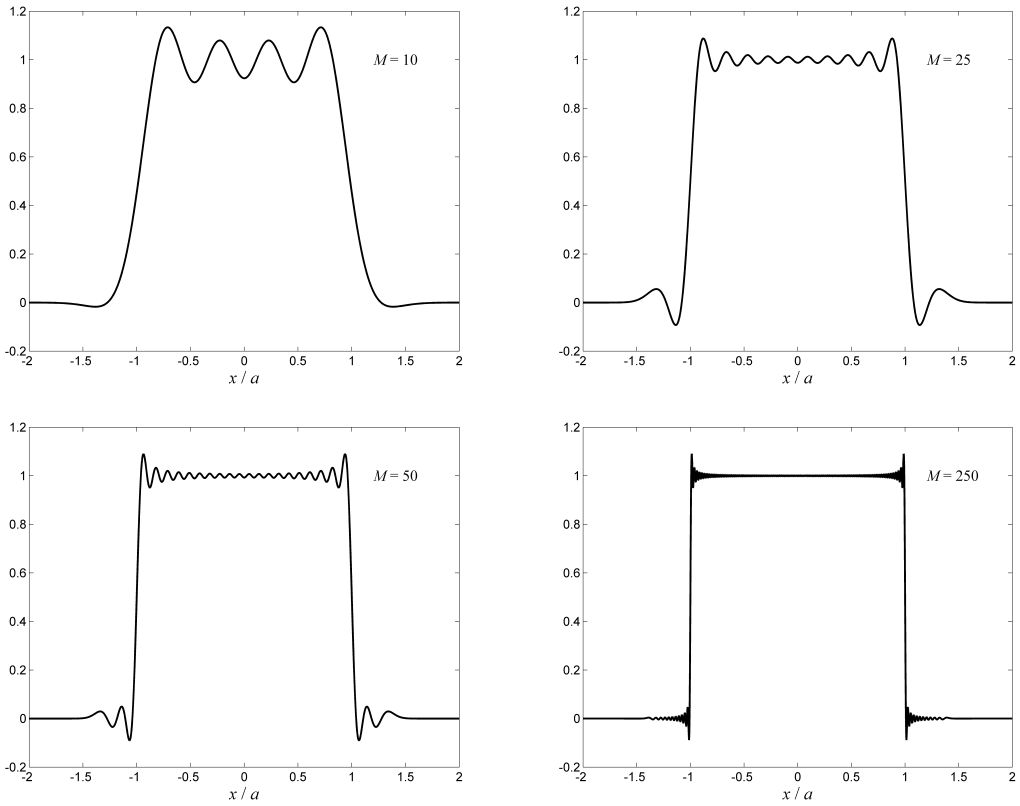

Figure 2.10 - The convergence of a HG synthesis towards a desired top hat signal.

There are an infinite number of mode sets that can be achieved from successive overlap integrals, and this is because the Hermite-Gaussian modes are orthonormal for all values of the width parameter w_0. w_0 affects the extent of the Gaussian envelope of the mode, and therefore any integration over a finite region will create a reduction of the mode coefficients for larger values of m as those modes will be truncated more

significantly by the aperture function. *Carter* has defined the effective extent σ_m^H of a Hermite-Gaussian mode to be [CAR80]

$$\sigma_m^H = w\sqrt{m+1/2} \tag{2.22}$$

We can numerically show that for synthesis of a real function using a maximum mode number M, there is an ideal waist value w allowing for the optimum field synthesis related to the value of σ_m^H. To quantify the accuracy of the Hermite-Gaussian mode synthesis E the error can be calculated through its deviation from the ideal function E_0 by the root mean squared error (rms), given as

$$\Delta_{rms} = \sqrt{\int_{-\infty}^{\infty} |E_0(x_0) - E(x_0)|^2 \, dx} \,. \tag{2.23}$$

Like Fourier analysis, it is found that the HG modal sum converges to $E_0(x)$ in smoothly varying continuous regions, and in regions of discontinuity the synthesis tends to the mean of the two values of $E_0(x_0)$ either side of the dislocation, which for a *rect* function is 0.5. Figure 2.11 shows the deviation of the rms errors for the aperture synthesis shown in Figure 2.10.

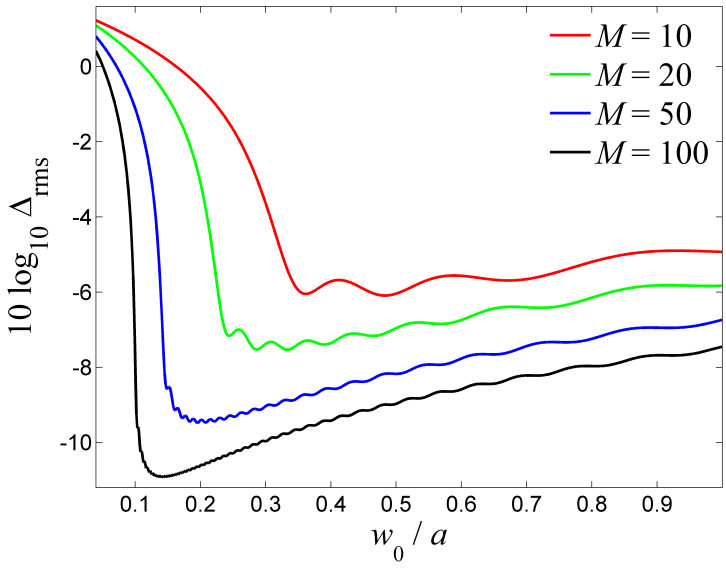

Figure 2.11– The rms error for various values of M, in a Hermite-Gaussian expansion of the "top-hat" function. w_0 is given as a fractions of the aperture semi-width. See also [LIU06]

From the above analysis it can be found that, in general, the optimum parameter for HG synthesis of a function with abrupt truncation at a, such as the *rect* function, is

$$w_0 = \sqrt{2}\,\frac{a}{\sqrt{M}} \tag{2.24}$$

which is an expression given in [LIU06], but is modified here as the definition of mode structure varies amongst the literature.

2.5.4 – Laguerre-Gaussian beam modes

The paraxial wave equation, in a symmetric cylindrical frame of reference, is given as

$$\frac{1}{r}\frac{\partial}{\partial r}\left(r\frac{\partial \psi}{\partial r}\right)-2ik\frac{\partial \psi}{\partial z}=0. \tag{2.25}$$

Solutions of this equation, the Laguerre-Gaussian functions, have the form [GOL98, MUR93)]

$$\psi_m^L=\sqrt{\frac{2}{\pi w_0^2}}L_m\left(2\frac{r^2}{w_0^2}\right)\exp\left(-\frac{r^2}{w_0^2}\right). \tag{2.26}$$

Examples of the structure of these functions are shown in Figure 2.12.

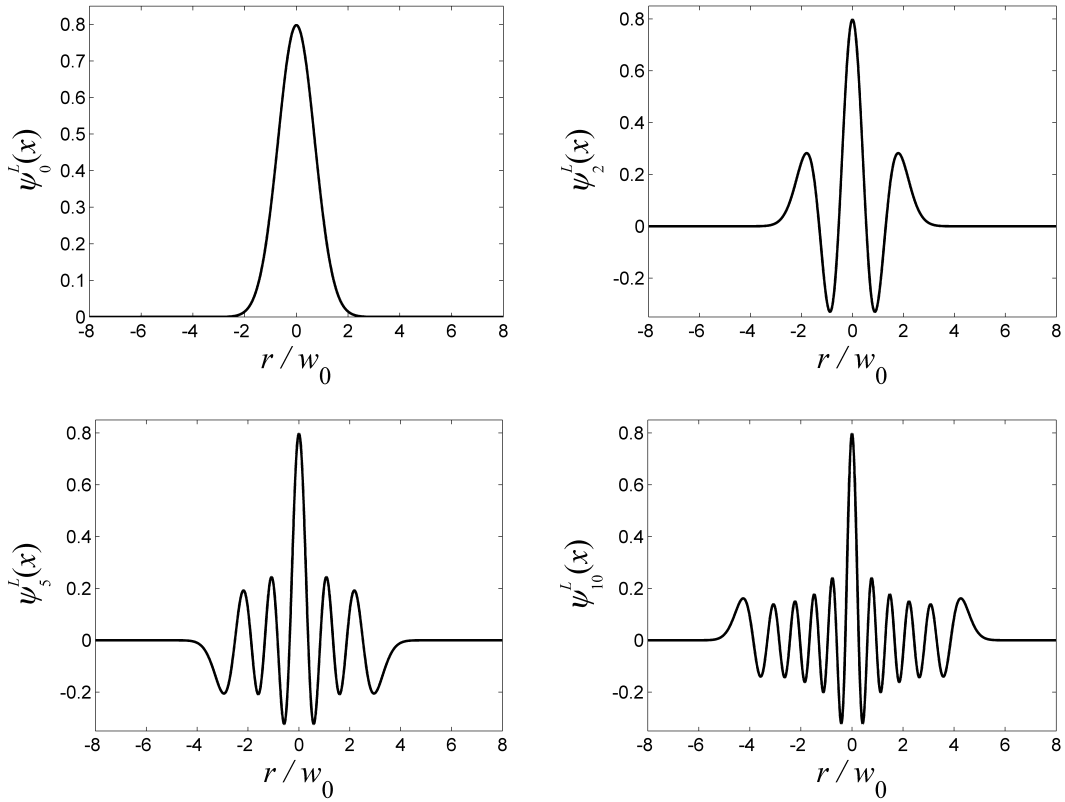

Figure 2.12 - The structure of the Laguerre-Gaussian beam modes.

In a cylindrically symmetric coordinate frame the Laguerre-Gaussian beam modes propagate according to

$$\psi_m^L(r,z) = \sqrt{\frac{2}{\pi w^2(z)}} L_m\left(2\frac{r^2}{w^2(z)}\right)\exp\left(-\frac{r^2}{w^2(z)}\right)$$

$$\times\exp\left(i\,k\,z + i\frac{k\,r^2}{2R(z)} - i(2m+1)\tan^{-1}\left(\frac{\lambda z}{\pi w_0^2}\right)\right) \tag{2.27}$$

and like the Hermite functions the Laguerre forms in eq. (2.27) are orthogonal with a Gaussian weighting, and a radially symmetric function $E_0(r_0)$ can be represented as

$$E_0(r_0) \cong \sqrt{\frac{2}{\pi\, w_0^2}} \sum_{m=0}^{M} A_m L_m\left(2\frac{r_0^2}{w_0^2}\right)\exp\left(-\frac{r_0^2}{w_0^2}\right) \tag{2.28}$$

where M is the index of the highest order mode used and the mode coefficients A_m are determined from

$$A_m = \sqrt{\frac{2}{\pi\, w_0^2}} \int_0^a E_0(r_0\,) L_m\left(2\frac{r_0^2}{w_0^2}\right)\exp\left(-\frac{r_0^2}{w_0^2}\right) 2\pi\, r_0\, dr_0\ . \tag{2.29}$$

An asymptotic variation of an LG function is given as [GRA07]

$$L_m(s) = \frac{1}{\sqrt{\pi}} e^{\frac{s}{2}} s^{-\frac{1}{4}} m^{-\frac{1}{4}} \cos\left(2\sqrt{m\,s} - \frac{\pi}{4}\right) + O\left(m^{-\frac{1}{4}}\right)$$

for large values of m, where O represents the order of magnitude of the argument. When $2r^2/w^2$ is substituted into the *LG* expression and the Gaussian function envelope of the corresponding argument is included, the asymptotic behaviour becomes

$$L_m\left(2\frac{r^2}{w^2}\right)\exp\left(-\frac{r^2}{w^2}\right) = \frac{m^{-1/4}}{\sqrt{\pi\, r}} \cos\left(2\sqrt{2m}\,\frac{r}{w} - \frac{\pi}{4}\right)\exp\left(-\frac{r^2}{w^2}\right) + O\left(m^{-1/4}\right).$$

While this representation of the LG polynomials is valid only for small values of $r > 0$, equating the argument of the cosine term to π / 2, the occurrence of the first zero-crossing, ρ_1, is found to approximately be

$$\rho_1 = \frac{3\pi\, w_0}{8\sqrt{2m}}. \tag{2.30}$$

For indices of m greater than approximately ten, this gives a relatively accurate estimate of the radius of the central lobe, but is not accurate in predicting the roots over the entire mode function. *Phillips and Andrews* [PHI83] defined the "spot size" of a Laguerre-Gaussian beam as

$$\sigma_m^L = w\sqrt{2m+1} \tag{2.31}$$

in the same manner as the effective extent was determined by [CAR80] for the Hermite-Gaussian modes in eq.(2.22). This value will also have importance in the convergence of the modal synthesis to the desired function.

The *circ* function is the analogue of the *rect* function in the cylindrical frame and is defined as

$$circ\left(\frac{r_0}{a}\right)=\begin{cases}1, r_0 \le a\\ 0, r_0 > a\end{cases} . \tag{2.32}$$

The error analysis of synthesis of the circ function using the Laguerre-Gaussian formulism was studied by [BORG96], and show very similar convergence as seen in synthesis with Hermite-Gaussian functions, as shown in Figure 2.13 (a). Figure 2.13 (b) shows the rms errors for the LG synthesis of the function $\exp(-r^{12}/a^{12})$ known as a super-Gaussian distribution.

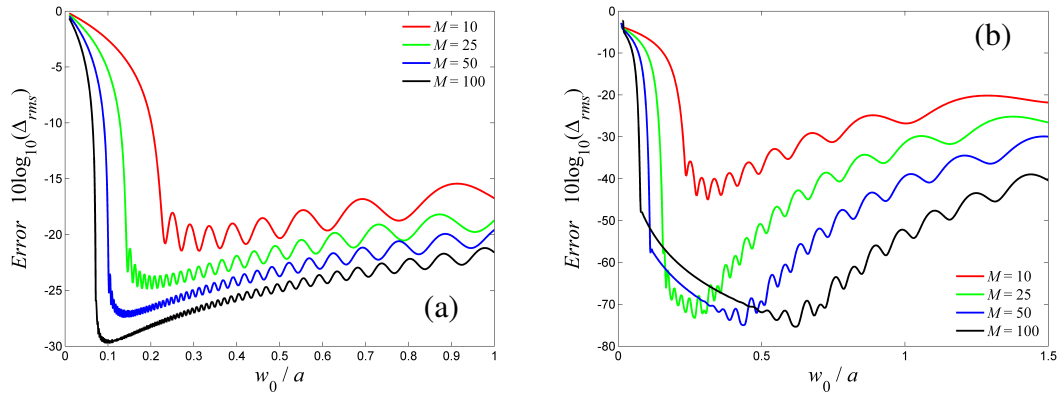

Figure 2.13 - The root mean squared errors in the Laguerre-Gaussian synthesis of the functions (a) circ(r_0/a), and (b) the super-Gaussian function $\exp(-r_0^{12}/a^{12})$.

With such error analysis, it can be found from the data in Figure 2.13 that the most efficient value of w_0 for synthesis of the circ function (hard aperture) is that given by [BORG96] as

$$w_0 = a/\sqrt{M} . \tag{2.33}$$

In Figure 2.13 (b), the super-Gaussian function is truncated at a lower value (0.37) than in the case of the circ function which has a unit value at $r_0 = a$, thus the rms errors in Figure 2.13 (b) show significantly lower values. In the case of (*a*) the larger values of Δ_{rms} must be attributed to the difficulty in reconstructing the dislocation at the radius $r_0 = a$.

2.6 - Applications of Gaussian beam modes in classical optics

Now, we can apply the knowledge of the propagation of higher order Gaussian beam modes in calculating the diffraction effects in an optical scenario by reconstructing an arbitrary field as a superposition of several modes. Due to the

orthogonality of the Laguerre and Hermite Polynomials, we know that we can synthesise accurate representations of functions, and as the propagation of each individual mode is known we can determine the field in the plane $z > 0$ diffracted by a cylindrically symmetric aperture as

$$E(r,z) = \sum_{m=0}^{M} A_m \psi_m^L(x,y,z) \qquad (2.34\ (a))$$

or for an aperture in a two-dimensional Cartesian space

$$E(x,y,z) = \sum_{l=0}^{L}\sum_{m=0}^{M} A_{lm} \psi_{lm}^H(x,y,z) \qquad (2.34\ (b))$$

where ψ is the Laguerre-Gaussian and Hermite-Gaussian mode structures defined in (2.17) and (2.27), with the usage of these forms of mode depending on the symmetry of the defined situation. Eq. 2.34 (a) and (b) are the basis for the modal calculations of diffraction used through out this thesis.

In the Fourier theory of optical diffraction, the calculation of an intensity pattern is a one-step process, requiring only the computation of the Fourier coefficients and converting the extent of frequency space into spatial coordinates. In the case of diffraction analysis using Gaussian beam modes the calculation of the HG or LG mode coefficients is only the first procedure in depicting the diffraction effects, the second being the summation of the modes according to the weights defined by the mode coefficients.

While expressions above may have defined the amplitude of the electric field of diffracted beams, these fields will oscillate rapidly with a phase angle of ωt, a property which is not detectable with conventional radiation detectors. CCD cameras and millimetre wave diode detectors conventionally measure the time averaged intensity of a field which is represented as

$$I(r,z,t) = \frac{1}{T}\int_0^T \left|E(r,z,t)\right|^2 dt$$

where T is the duration of the field measurement at that point. In the case of a continuous wave described by a complex exponential term in the form $E(r,z,t)\exp(i\phi(r,z,t))$, the time averaged intensity is given merely as $|E(r,z)|^2$. For other methods in computational optics that rely on computation of the physical electric field only, determining the time-averaged intensity requires a less direct calculation.

In examples of diffraction analysis in this thesis it should be assumed, unless stated otherwise, that apertures or optical elements are illuminated by plane waves with constant unit transverse amplitude.

2.6.1 – Diffraction of a Gaussian beam at a circular aperture

Propagation of fields truncated by circular apertures is one of the most studied scenarios in optics, as it is the basis for all diffraction effects within circularly symmetric systems, and has relevance in mm-wave research in, for example, the propagation of horn antenna fields. To generalise the simulations of diffraction the optical system can be described in terms of the Fresnel number N_F which relates the wavelength, measurement distance, and aperture dimensions through

$$N_F = \frac{a^2}{\lambda z} \tag{2.35}$$

Figure 2.14 describes the optical arrangement used in this discussion.

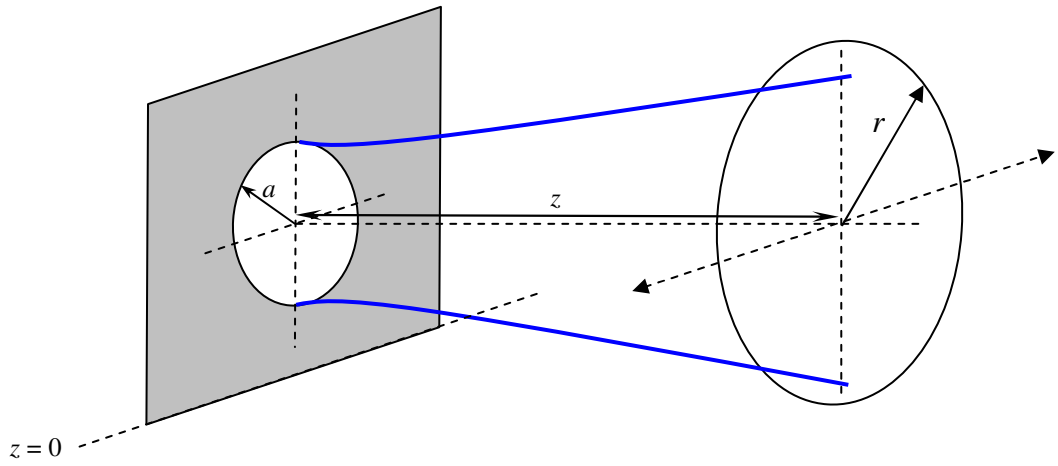

Figure 2.14 – Layout for calculation of diffraction by a circular aperture.

A complete analytical expression for the intensity pattern caused by a circular obstacle cannot be obtained directly from the diffraction integral in the near-field as the field is rapidly evolving, although using the Fresnel integral the Fraunhofer diffraction pattern can be calculated analytically for distances in the far-field where the field profile remains constant, but with a transverse varying scale. The Fraunhofer diffraction caused by an aperture defined by a circ function $E_0(r_0) = circ(r_0/a)$ is the described by

$$E(r) = \frac{i \exp\left(-i\left(k z + \frac{k r^2}{2z}\right)\right)}{\lambda z} F\{E_0(r_0)\}$$

$$F\left\{circ\left(\frac{r_0}{a}\right)\right\} = \pi a^2 \frac{J_1(2\pi ar)}{\pi ar}$$

where J_1 is the first order Bessel function of the first kind, and $F\{\}$ represents a Fourier transformation. Hence the intensity distribution is given as

$$I(r) = \left(\frac{\pi a^2}{\lambda z}\right)^2 \left(\frac{2J_1\left(\frac{kar}{z}\right)z}{kar}\right)^2 . \tag{2.36}$$

The *LG* mode coefficients relating to a circular aperture of radius a, illuminated by an on-axis Gaussian beam of waist radius w_{in}, and with a flat wavefront, are given by

$$A_m = \sqrt{\frac{8\pi}{w_0^2}} \int_0^a L_m\left(2\frac{r_0^2}{w_0^2}\right) \exp\left(-\frac{r_0^2}{w_0^2} - \frac{r_0^2}{w_{in}^2}\right) r_0 \, dr_0 .$$

Conventionally, this form of integral is calculated numerically without any difficulty, but in this situation analytical expressions for the lowest order mode coefficient values could be written. However, higher order modes must be determined numerically. It is now relevant to introduce the use of recurrence relations in the LG decomposition of circularly symmetric fields which can be used to simplify the calculation of mode coefficients. Akin to most special functions derived from the study of higher order differential equations, such as Bessel functions or Legendre Polynomials, there are well-known recurrence relations defining polynomials of a desired index m through those of a lower value of m-1. There are three common recurrence relations for the simple Laguerre polynomials given in standard texts relating to the subject of special functions and from these the pure recurrence relation is obtained,

$$L_{m+1}(s) = \frac{1}{m+1}\left((2m+1-s)\,L_m(s) - s\,L_{m-1}(s)\right)$$

This recurrence relation can be used to determine mode coefficients for certain aperture functions from the values of A_0 and A_1 without need for numerical integration. For the truncation of a Gaussian beam with waist radius w_{in} at an annular aperture of outer radius a and inner radius a_0 this relation allows for derivation of the propagation of a field from a circularly symmetric aperture with Gaussian illumination as

$$A_m = \frac{\sqrt{2\pi w_0^2}\, L_{m-1}\left(2\frac{r_0^2}{w_0^2}\right)\exp\left(-r_0^2\left(\frac{1}{w_0^2}+\frac{1}{w_{in}^2}\right)\right)\Big|_{r_0=a_0}^{r_0=a} - \sqrt{2\pi w_0^2}\, L_m\left(2\frac{r_0^2}{w_0^2}\right)\exp\left(-r_0^2\left(\frac{1}{w_0^2}+\frac{1}{w_{in}^2}\right)\right)\Big|_{r_0=a_0^2}^{r_0=a^2} + \left(\frac{w_0^2}{w_{in}^2}-1\right)A_{m-1}}{\left(\frac{w_0^2}{w_{in}^2}+1\right)}$$

(2.37)

Presented in Figure 2.15 are the mode coefficients for a plane wave illuminated circular aperture, calculated using the above recursive equation eq.(2.37) with $a_0 = 0$.

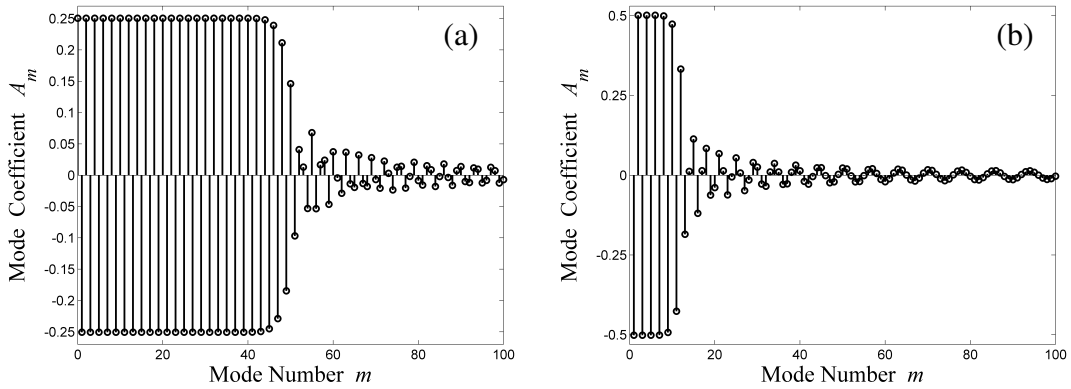

Figure 2.15 - The coefficients of a M=100 LG mode set for $circ(r_0 / a)$ with plane wave illumination, w_{in}=∞, (a) $w_0 = 0.1a$ (optimum value in this case), (b) $w_0 = 0.2a$.

The plots of Figure 2.15 show that the mode set that gives the more accurate reconstruction, shown in (a) with $w_0 = a/\sqrt{M}$, has a more balanced distribution between coefficients of modes that are truncated significantly and therefore negligible values of A_m and those that have large mode coefficients. It can be said that the reconstruction of the gross structure, $E(r_0<a) = 1$, is performed with modes with $m < M / 2$, while the dislocation at the edge of the aperture is represented more closely by the modes with higher spatial frequencies $m \geq M/2$. To calculate the diffraction effects caused by an aperture, the sum of the LG beam modes with weightings defined by A_m and with desired propagations distance z and wavelength λ, is calculated, resulting in the diffraction patterns shown in Figure 2.16.

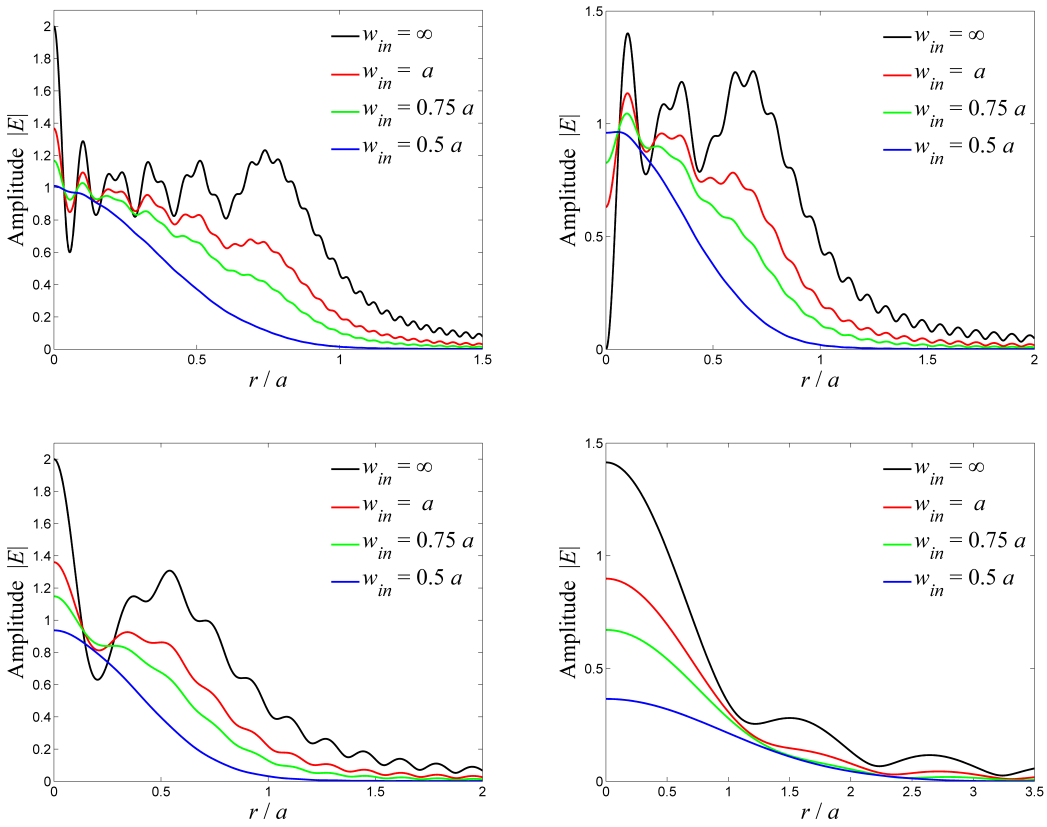

Figure 2.16 - The diffraction patterns from a circular aperture illuminated by a Gaussian beam $\exp(-r^2/w_{in}^2)$, calculated at distances from the aperture given by (a) $z = a^2/11\lambda$, (b) $z = a^2/6\lambda$, (c) $z = a^2/3\lambda$, (d) $2a^2/\lambda$. The fields were calculated using 100 Laguerre-Gaussian modes.

Comparisons with the Fresnel integral calculations are omitted in Figure 2.16 as comparisons show insignificant deviation. The plots show the general characteristics of near-field diffraction at a circular aperture, for example at distances with an even Fresnel number the amplitude pattern has a null at its centre due to the symmetry of the Fresnel zone arrangement with each zone interfering destructively with another at that point. With odd Fresnel numbers a maximum intensity is found at $r = 0$.

The use of Gaussian beam modes has thus far had limited application in optics. Methods such as the Fourier transform technique, of which the mathematical properties has been known since the early nineteenth century, is the standard technique for the calculation of diffracted scalar paraxial fields, accelerated by the use of the fast Fourier transform algorithm. Also, using the Fresnel integral, approximations with certain constraints can allow for the analytical expression of the structure of Fraunhofer diffraction patterns, albeit with limited application. While analytical expressions of the Fresnel integrals are regularly quoted in the literature, they can often only represent a

symbolic reduction of the equation, based on the substitution of an appropriate error function or Fresnel integral, and does not provide any useful increase in computational speed. The advantage of GBMA over Fresnel diffraction integral calculations is that once the mode coefficients of the aperture function have been determined, all information regarding near-field and far-field regions can be obtained, no further numerical integration is necessary with the diffraction calculation relying on finite sums.

The Gaussian beam mode analysis of optical fields provides an asymptotic evaluation of the Fresnel diffraction integral. From eq. (2.31) the effective radius of an LG mode is given by $w(z)\sqrt{2m+1}$, thus we would expect the region over which the finite term LG expansion converges with the result of a Fresnel diffraction calculation is limited by this extent. Shown below is a comparison of the Fresnel-integral method and the GBMA process using an $M = 30$ expansion.

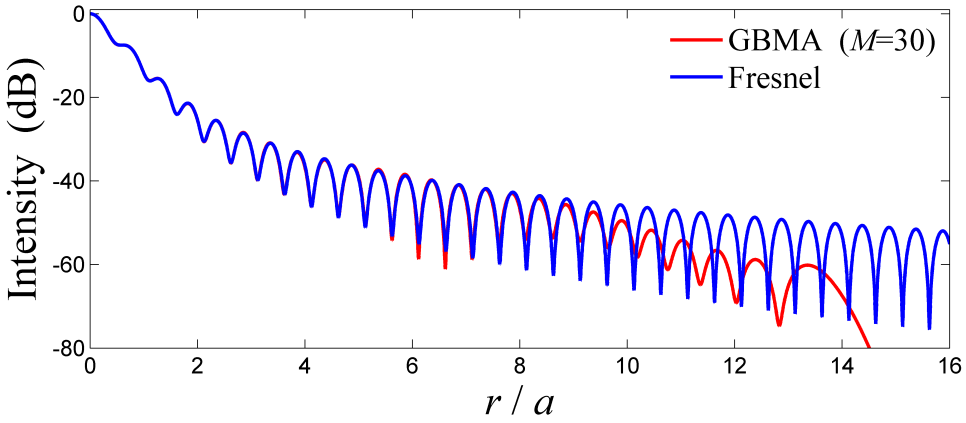

Figure 2.17 - The diffraction pattern of a circular aperture calculated by the Fresnel diffraction integral (blue line) compared with that formed by a 31 term Laguerre-Gaussian series at $z = a^2/\lambda$.

In Figure 2.17 the effective width of the $m = M / 2$ mode is ~8a. Relatively significant discrepancies can be seen to begin to occur between the two methods slightly within this distance as modes with m just less than $M / 2$ begin to be appreciably truncated. However as the number of modes used in this example is relatively low, and the amplitude is comparatively insignificant at this point of deviation, it is foreseeable that the effect will have negligible influence within practical/paraxial distances from the optical axes, particularly when using larger mode sets.

2.6.2 - Modulation of a plane wave by a thin lens

The thin spherical lens is one of the most common and important optical elements in use. Throughout the literature, they are commonly classified through their Fresnel number,

$$N_F = \frac{a^2}{\lambda f} \tag{2.38}$$

a being the pupil diameter and f the focal length of the lens. This factor is often used to represent the focusing ability power of a lens as a single number without having to describe the radius and wavelength. With a larger Fresnel number, the "quality" of the focused beam increased, i.e. it becomes more representative of the ideal convergence of a parabolic wave to an infinitesimal point focus. Another parameter commonly used is the *f*-number or *F#* defined as the ratio of the focal length to the diameter of the lens. To verify the use of GBMA in the modelling of this familiar element, we can briefly examine the variation in the properties of the focus of a lens caused by a variation of its Fresnel number N_F.

The overlap integral required for the calculation of mode coefficients of a spherical thin lens, is given by

$$A_m = \sqrt{\frac{2}{\pi w_0^2}} \int_0^a L_m\left(2\frac{r^2}{w^2}\right) \exp\left(r_0^2\left(\frac{ik f}{2f} - \frac{1}{w_0^2}\right)\right) 2\pi\, r_0\, dr_0 \,.$$

For a circularly symmetric thin lens under plane wave illumination the *LG* mode coefficients can be determined recursively using:

$$A_m = \frac{\sqrt{2\pi w_0^2}\, L_{m-1}\left(2\frac{r}{w_0^2}\right) \exp\left(-\frac{r}{w_0^2}\left(ik\frac{w_{0^2}}{2f} - 1\right)\right)\Big|_{r_1^2}^{r_2^2} - \sqrt{2\pi w_0^2}\, L_m\left(2\frac{r}{w_0^2}\right) \exp\left(-\frac{r}{w_0^2}\left(ik\frac{w_{0^2}}{2f} - 1\right)\right)\Big|_{r_1^2}^{r_2^2} - \left(ik\frac{w_{0^2}}{2f} - 3\right) A_{m-1}}{\left(1 - ik\frac{w_0^2}{2f}\right)}, \tag{2.39}$$

with the mode coefficients now becoming complex. The occurrence of complex terms introduces longitudinal phase shifts in the propagation of the individual modes, causing the interference between the modes to result in an overall curved wavefront just behind the lens. (Note that the recursive equation above can also be used for beams with diverging phase fronts with substitution of $f \rightarrow R$, R being the radius of curvature of the field).

Using w=0.1a, and M=100, mode coefficients were calculated for two lenses of Fresnel number N_F=2 and 5. See Figure 2.18.

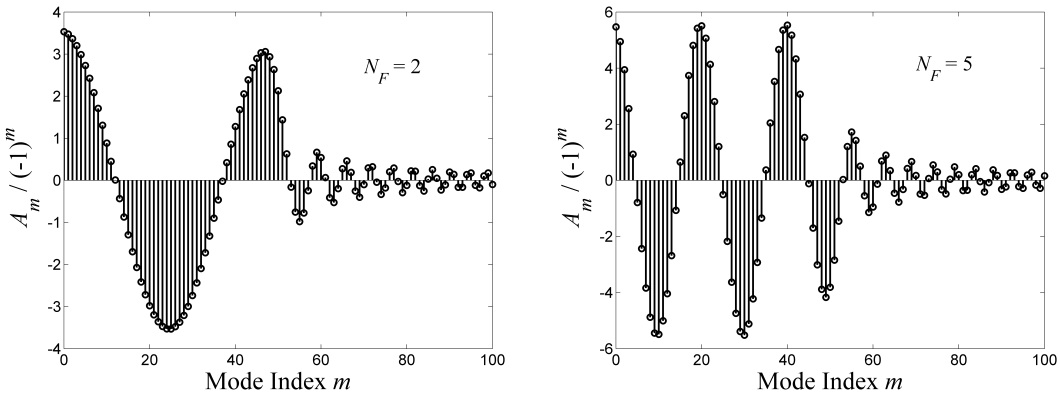

Figure 2.18 – The real part of A_m for a thin spherical lens of N_F = (a) 2, (b) 5.

When the coefficients are examined through the squaring of their absolute values, for low values of N_F the trends show very little difference from the description of a circular aperture. As the coefficients are now complex for a thin lens, inspection of the separate real and imaginary parts shows how the increase in frequency of the lens function causes an increase in oscillation between values of A_m and therefore the complex phase angle of each mode becomes important. Figure 2.19 shows the diffraction of a plane wave modulated by a thin spherical lens.

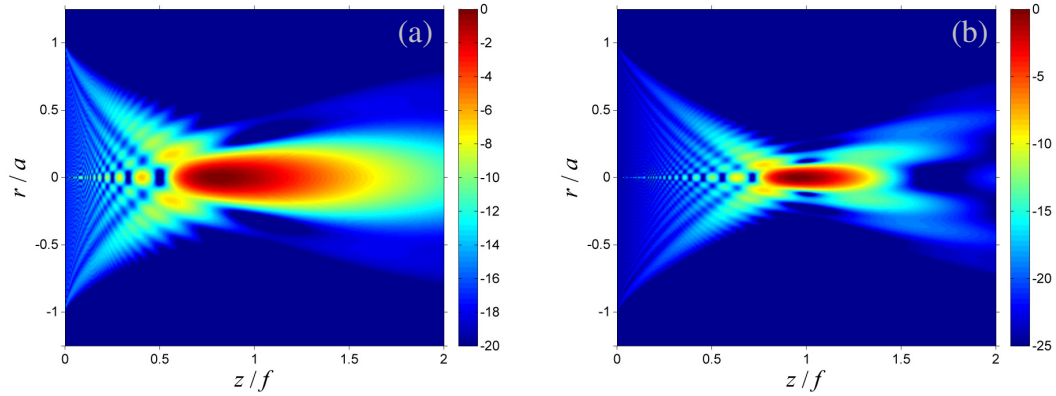

Figure 2.19 - The diffraction half-plane of a thin spherical lens illuminated by a plane wave for (a) N_F = 2, (b) N_F = 5.

In the case of N_F = 2 the focusing effect is seen to be quite limited without any generation of a well-defined narrow focal region, in fact, the output bears little difference from that of a plane wave illuminated circular aperture. With N_F = 5 there is a more obvious concentration of energy towards the focal point, and with increasing Fresnel number there is a decrease in the transverse and longitudinal dimensions of the focal spot.

To compare this GBMA technique to the conventional result, the focal shift phenomena, as examined by [LI81], is illustrated through use of this technique. The focal shift of a lens is the movement of the focus, or more correctly the point of maximum axial intensity, towards the focusing lens as the Fresnel number is reduced, either by reducing the aperture diameter or increasing the wavelength of the illuminating radiation. In either case the Fresnel number of the lens is reduced. Figure 2.20 (a) shows this movement of the point of maximum intensity towards the lens and Figure 2.20 (b) plots this shift as a proportion of the defined focal point as the aperture size is increased.

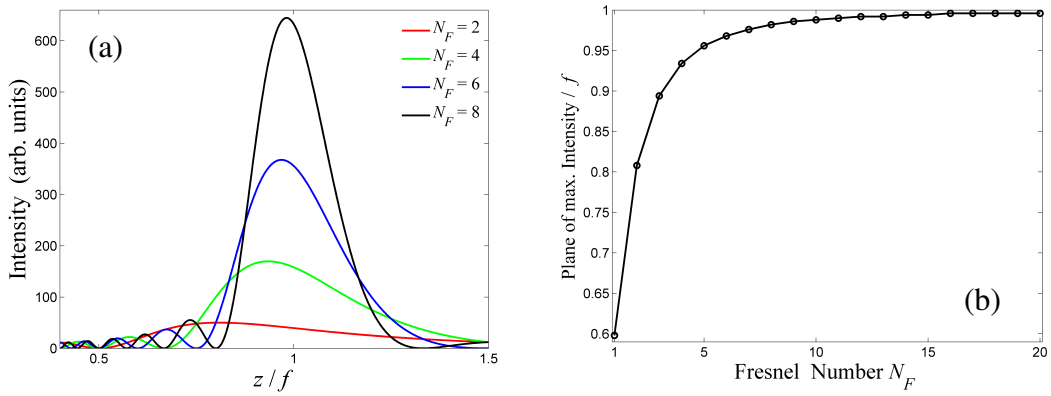

Figure 2.20 – (a) The axial intensity of a thin spherical lens with various Fresnel numbers, under illumination by a plane wave. (b) The variation of plane of maximum intensity of the spherical lens relative to the focal length f for various values of N_F. See [LI81].

2.6.3 - Diffraction of a plane wave at a double slit

For diffraction in Cartesian systems, this effect can be depicted using the Hermite-Gaussian *HG* functions as the applied orthogonal mode set. The overlap integral of any two dimensional function is given by

$$A_{lm} = C_l C_m \int_{-b}^{b}\int_{-a}^{a} H_l\left(\sqrt{2}\frac{x_0}{w_x}\right) H_m\left(\sqrt{2}\frac{y_0}{w_y}\right) \exp\left(-\frac{x_0^2}{w_x^2}\right) \exp\left(-\frac{y_0^2}{w_y^2}\right) E_0(x_0, y_0)\, dx_0\, dy_0$$

However, in the case of the double slit the geometry of the aperture, depicted in Figure 2.21, allows for separation of variables in the overlap integral. i.e.

$$E_0(x,y) = E_{0x}(x)E_{0y}(y).$$

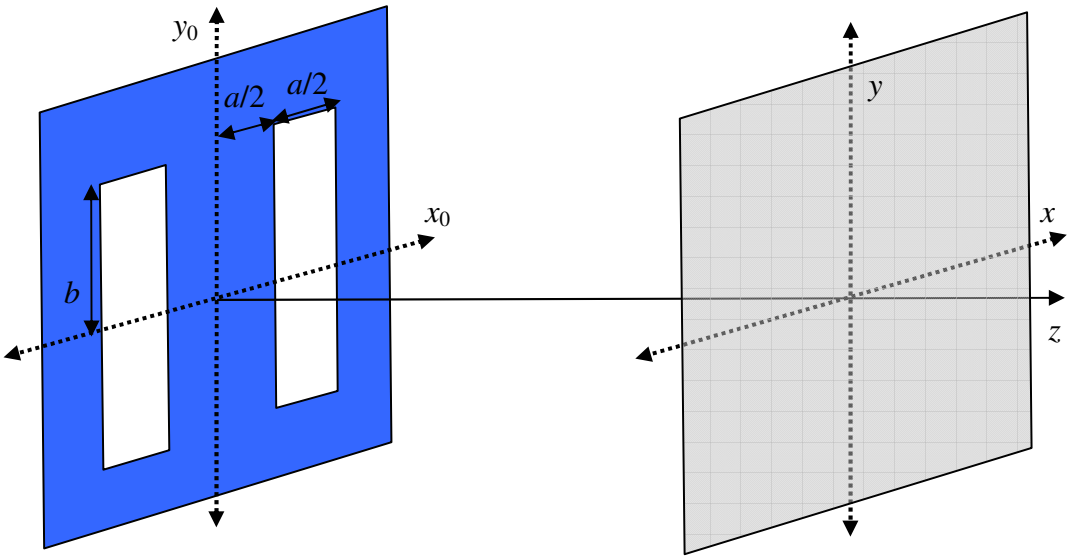

Figure 2.21 - Layout of double slit diffraction.

In this case, the function is symmetric in x_0 and y_0 so only HG modes with even indices are required. The mode coefficient values for this arrangement can also be obtained using recurrence relations for Hermite Polynomials. The "pure" recurrence relation, that involves no derivatives, is given by

$$H_m(x) = 2\,x\,H_{m\text{-}1}(x)\text{-}2\,(m\text{-}1)\,H_{m\text{-}2}(x)$$

and can be used to obtain the following recursive equation, [MUR93], for the calculation of mode coefficients of plane wave truncation by a top-hat aperture of width $2a$ as

$$A_{m+1} = -2\frac{w_0}{\sqrt{m+1}} H_m\left(\sqrt{2}\frac{a}{w_0}\right)\exp\left(-\frac{a^2}{w_0^2}\right) + \sqrt{\frac{m}{m+1}} A_{m-1}\,. \qquad (2.40)$$

With this equation the diffraction of a plane wave illuminated double slit can be easily modelled as two individual slits using an appropriate spatial offset of the HG modes to reconstruct the aperture function along the x direction. The results of a GBMA diffraction calculation for a double slit are shown in Figure 2.22.

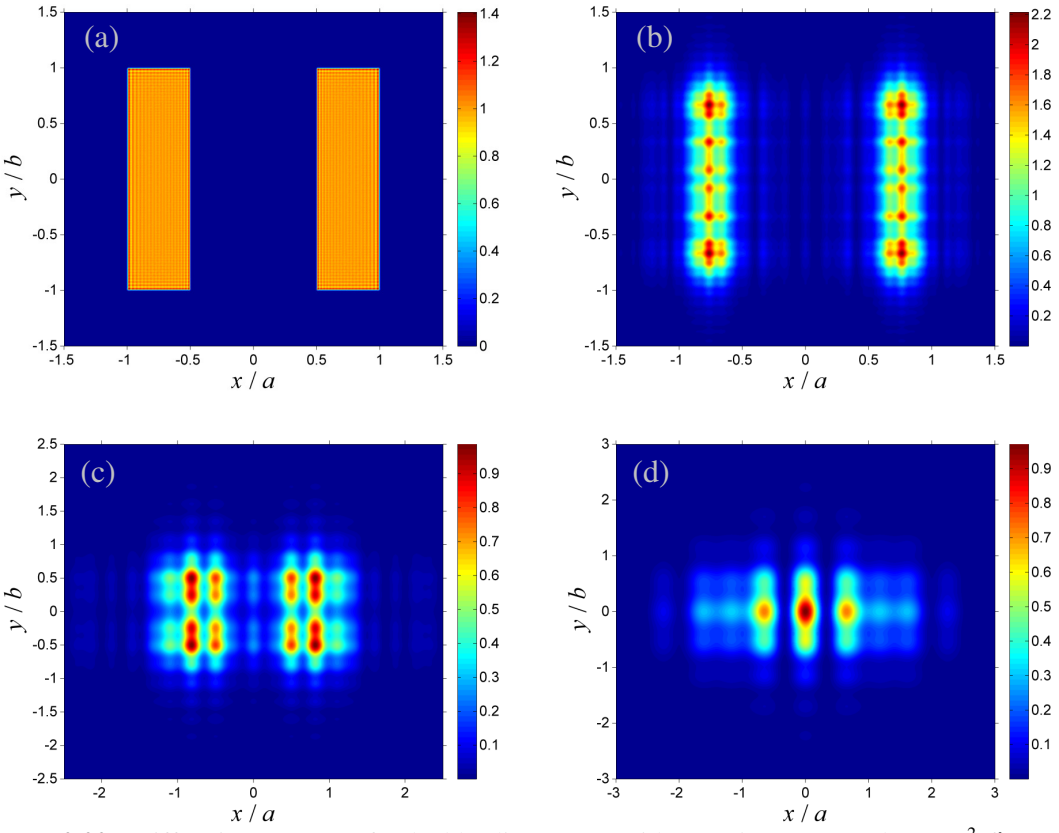

Figure 2.22 - Diffraction patterns of a double slit aperture with $a = 2b$. (a) $z = 0$, (b) $z = a^2/6\lambda$ (c) $a^2/2\lambda$ (d) $z = a^2/\lambda$.

In Mathematica™ the recurrence relations were found, for $M = 150$, to calculate the required one-dimensional overlap integrals in a time of 0.2 seconds compared with a time of approximately one minute using the conventional integration technique.

Although we have only described the recurrence relations as applied to obtaining analytical expressions for the values of the mode coefficients, the relations are also used in the software developed by the author to define the Laguerre and Hermite polynomials themselves. While mathematical software packages such as Mathematica™ and Maple™ provide efficient prewritten functions for the definition of these polynomials, lower level numerical languages such as C or Matlab™ do not include such functions in standard libraries and thus recurrence relations are an efficient method for definition of the higher-order Gaussian beam mode structures.

2.7 - The Wen-Breazeale method

An alternative, but somewhat related, technique to that of GBMA for the calculation of paraxial diffraction effects is that introduced by Wen and Breazeale [WEN87], which defines a diffracted field in terms of fundamental ($m = 0$) Gaussian

beams only. This method was initially reported with applications in acoustic field calculations but it also allows for direct application to optical diffraction with no change of mathematics. An advantage of this technique is that it shows strong convergence with a low number of terms, and with correct analysis has been shown to converge on the desired field more rapidly than a Laguerre-Gaussian synthesis.

The method is based on the field calculation as a summation of paraxial Gaussian beams, described mathematically by ♦

$$E(r,z,A,B) \cong \sum_{m=1}^{M} \frac{i A_m}{\left(1 + i B_m \frac{2z}{ka^2}\right)} \exp\left(- \frac{B_m r^2}{a^2\left(1 + i B_m \frac{2z}{ka^2}\right)} + i k z \right), \qquad (2.41)$$

where A_m and B_m are complex terms that modify the amplitude and phase curvature of the fields. Figure 2.23 shows the amplitude structures of some of these modes (series terms of index m) in relation to the Rayleigh distance $z_R = a^2 / \lambda$.

It can be seen that the constituent modes of this series are merely conventional $m = 0$ Gaussian beams but the complex coefficient B_m creates a variation of the width of each beam along with a deviation of each mode's phase curvature. For example in (c) the mode is a Gaussian beam focused to a waist caused by the complex value of B_{11}.

The disadvantage of the *Wen-Breazeale* diffraction method is the technique by which the values of the coefficients A and B are determined. Because the modes used in this synthesis are not formally orthogonal, a brute force search algorithm is implemented which searches through values of A_m and B_m, and the deviation of the synthesised function from the objective function $E(r_0)$ is measured by

$$Q = \int_0^{\infty} \left(E(r_0, 0, A_m, B_m) - E(r_0) \right)^2 dr_0 \, .$$

♦The form of equation (2.41) given in *Wen and Breazeale* (1987) (as eq. (9) in that paper), has been modified here as typographical errors were found in the original description.

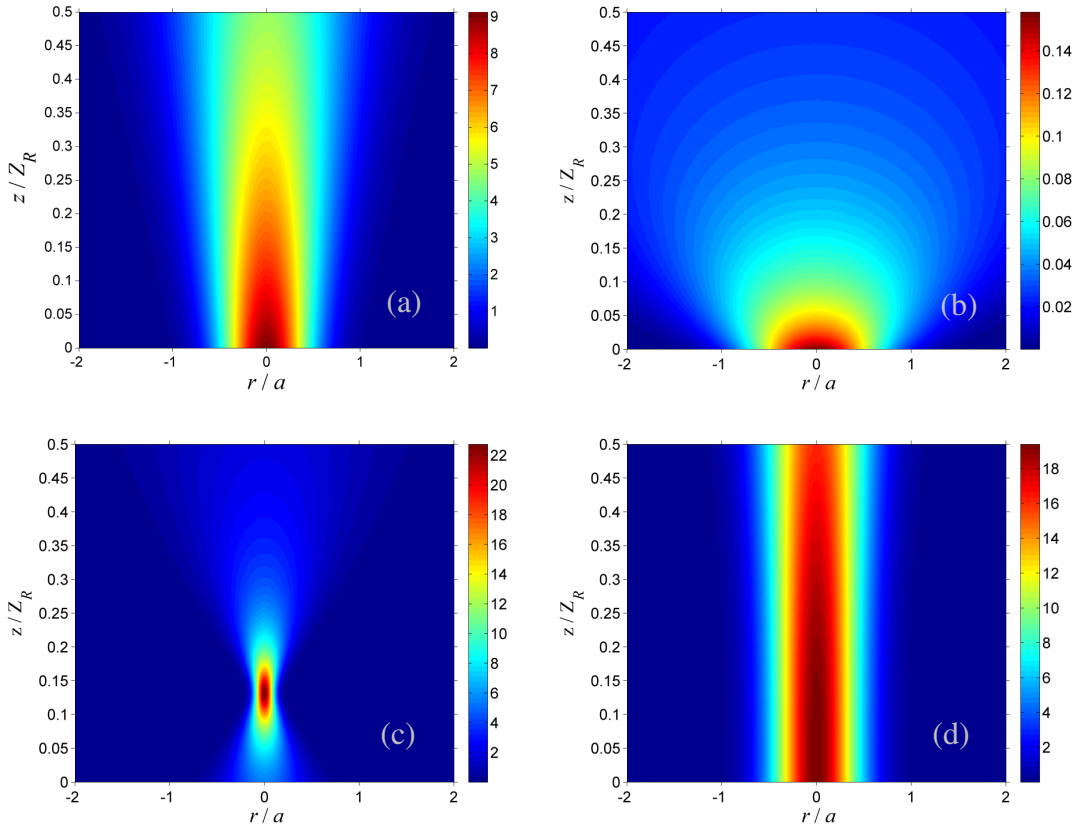

Figure 2.23 - The modes used in the 15 term Wen-Breazeale expansion, eq. (2.41) of the circular aperture with m = (a) 1, (b) 6, (c) 11, (d) 15. $Z_R = a^2 / \lambda$ is the *Rayleigh* distance of the aperture.

The A and B coefficients are then chosen by minimising Q with the conditions

$$\frac{dQ}{dA_m} = \frac{dQ}{dB_m} = 0$$

This is obviously a time consuming computation and does not attract the use of the method in the same manner as LG and HG synthesis which allow for very fast impromptu synthesis of arbitrary functions. However, those authors calculated the coefficients required for analysis of a "radiating piston", which is the acoustic analogue of optical diffraction of a plane wave by a circularly symmetric aperture. Given the importance of that diffraction scenario the data published by the authors is very useful and has been used in the optical literature [YANG07, TAO03]. The coefficients of a circular aperture using 15 terms are shown in table 2.1.

m	A_m	B_m
1	-2.97158 + 8.61871 i	4.18685 – 5.15597 i
2	-3.48107 + 0.96865 i	3.83976 – 10.80037 i
3	-1.39817 - 0.81272 i	3.43551 – 16.35823 i
4	0.07731 - 0.33032 i	2.46175 – 27.71334 i
5	2.87979 + 1.61087 i	5.46993 + 28.63194 i
6	0.12589 - 0.09573 i	1.98326 – 33.28850 i
7	-0.26407 - 0.67225 i	2.93348 – 22.015 i
8	18.01896 + 7.82906 i	6.30351 + 36.77717 i
9	0.05183 + 0.01816 i	1.30459 – 38.46504 i
10	-16.94374 - 9.93841 i	6.58886 + 37.06791 i
11	0.37078 + 5.45223 i	5.55176 + 22.42550 i
12	-6.69285 + 4.07218 i	5.40125 + 16.73262 i
13	-9.36382 - 4.99983 i	5.14975 + 11.12486 i
14	1.58723 - 15.42119 i	4.96645 + 5.68551 i
15	19.00243 + 3.68501 i	4.62955 + 0.30546 i

Table 2.1 - The coefficients, calculated by Wen and Breazeale (1987), for an expansion of a circular aperture using complex Gaussian beams.

In a comparison of a 15 term synthesis using the LG and WB methods, the synthesised circ function using the WB method produced an rms error with a significant reduction from that of the LG expansion. Figure 2.24 compares the two methods.

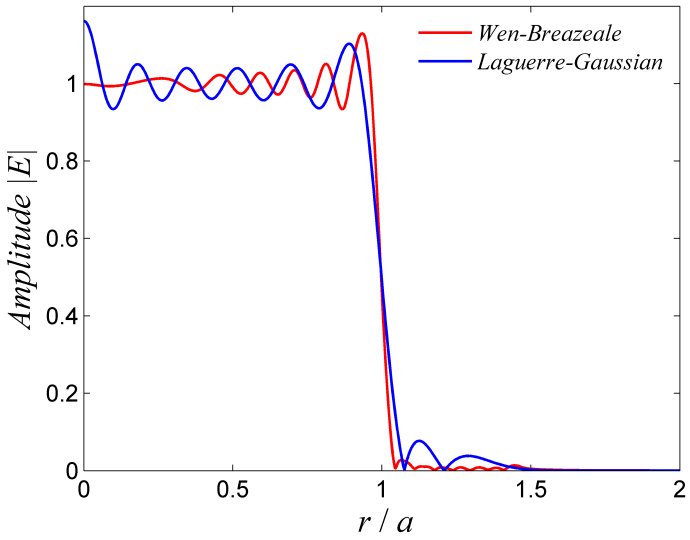

Figure 2.24 - Comparison of the Wen-Breazeale, eq. (2.41), and Laguerre-Gaussian expansion (eq. (2.34a)) methods in the synthesis of the circular aperture using 15 modes.

The Wen-Breazeale method intrinsically reduces the deviation of the synthesis from the desired function, whereas with a truncated LG expansion, an error is inherent in the formulation of the method and is, in the general scheme, inadaptable for a fixed

number of modes and constant waist parameter w_0. Figure 2.25 exhibits the near-field diffraction patterns of a circular aperture calculated using both methods.

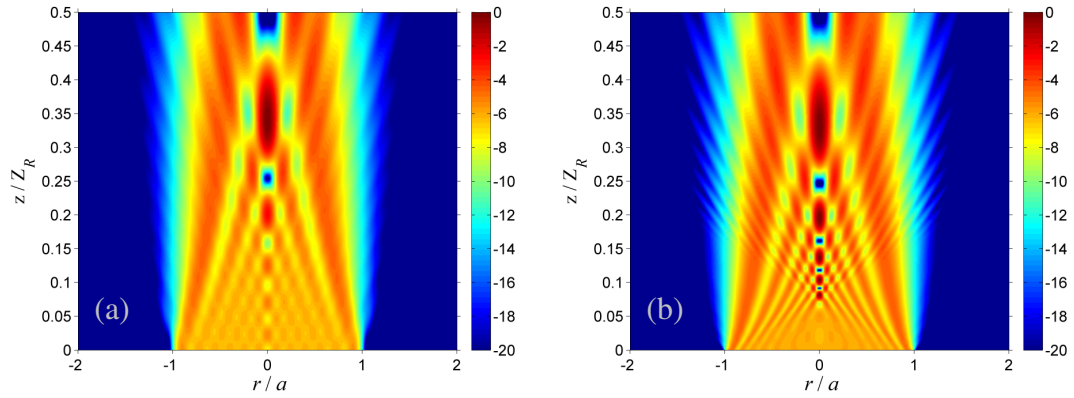

Figure 2.25 - Near-field comparison of (a) the Laguerre-Gaussian expansion and (b) the Wen-Breazeale methods for diffraction of a plane wave at a circular aperture using an expansion series of fifteen terms. Shown with a normalised logarithmic dB scale.

The calculated Fraunhofer diffraction effects show negligible differences between the two methods, but in the near-field, < ~0.2 z_R, it can be seen in Figure 2.25 that there is noticeable inconsistencies between the two methods, with the WB method allowing calculation of the oscillatory field with greater accuracy towards the aperture.

While the complexity associated in calculating the coefficients A and B restricts the use of the method for arbitrary fields, its use could be worthwhile to determine these values for analysis of a diffraction arrangement that a researcher might frequently refer to. In the context of millimetre wave optics, a calculation of the A and B coefficients of a field at the mouth of a circular corrugated horn may be useful, which could allow for swifter calculations than those obtained using a diffraction integral calculation and increased accuracy from a LG expansion with similar number of terms.

2.8 - Propagation outside the paraxial regime

Thus far, we have discussed only the paraxial representation of the electromagnetic fields, the validity of which is limited to weakly diverging wavefronts, as in the diffraction of a field by an aperture with dimensions considerably larger than the wavelength. While generally outside the scope of this thesis, a synopsis of methods used for non-paraxial wave propagation would be useful, particularly in determining the limits of applicability of the approximate paraxial approaches used in this thesis.

The *Rayleigh-Sommerfeld* diffraction integrals quantify the exact diffraction properties of a field and are given by, [BORN97],

$$E_\alpha(r,z) = -\frac{1}{2\pi}\int_{-\infty}^{\infty}\int_{-\infty}^{\infty} E_\alpha(r_0)\frac{\partial G(r,r_0)}{\partial z}dxdy\,, \qquad \alpha = x, y$$
$$E_z(r,z) = -\frac{1}{2\pi}\int_{-\infty}^{\infty}\int_{-\infty}^{\infty}\left[E_x(r_0)\frac{\partial G(r,r_0)}{\partial x} + E_y(r_0)\frac{\partial G(r,r_0)}{\partial y}\right]dxdy \qquad \text{Eq. (2.42)}$$

with the Greens function (a spherical wave) given by

$$G(r,r_0) = \frac{\exp(ik|r-r_0|)}{|r-r_0|}$$

and

$$r = \sqrt{(x-x_0)^2 + (y-y_0)^2 + (z-z_0)^2}$$
$$r_0 = \sqrt{x_0^{\,2} + y_0^{\,2}}$$

with x, y, and z the Cartesian coordinates in an observation plane, and x_0 and y_0 are the coordinates on the aperture plane.

While not universally necessary, these integrals allow for calculation of the total field through the sum of its polarisation components. The dominant reason, assumed by the author, that these integrals are not as commonly used as the Fresnel diffraction integrals in the literature relating to scalar optics is the difficulty associated with deriving analytical expressions of fields structures with them.

2.8.1 - Non-paraxial Gaussian beam mode analysis

The transverse structure of paraxial Hermite-Gaussian beam modes as given by eq. (2.17) remains the same relative to the value of w_0 / λ regardless of whether or not the actual physical propagation of the field obeys the paraxial wave equation. In the true physical forms of these fields, decrease in the value of w_0/λ increases the angle of diffraction of a Gaussian mode beyond the limits of the paraxial description creating deviations from the analytical descriptions. Associated with this are physical evanescent effects that occur when the increased transverse frequency k_x becomes so rapid ($>k$) that forward propagation of the harmonic fields is no longer supported in the mode structure, see Figure 2.26.

In Figure 2.26 (b) one can see that energy is propagated only from the outer extremities of the source field, and closer to $x = 0$ where the amplitude structure becomes more oscillatory the transverse local frequency k_x exceeds k_0 and no longer

supports forward propagation of the wave. In these regions evanescence dominates the field with the longitudinal field structure exhibiting a non-harmonic exponential decrease in amplitude with distance z.

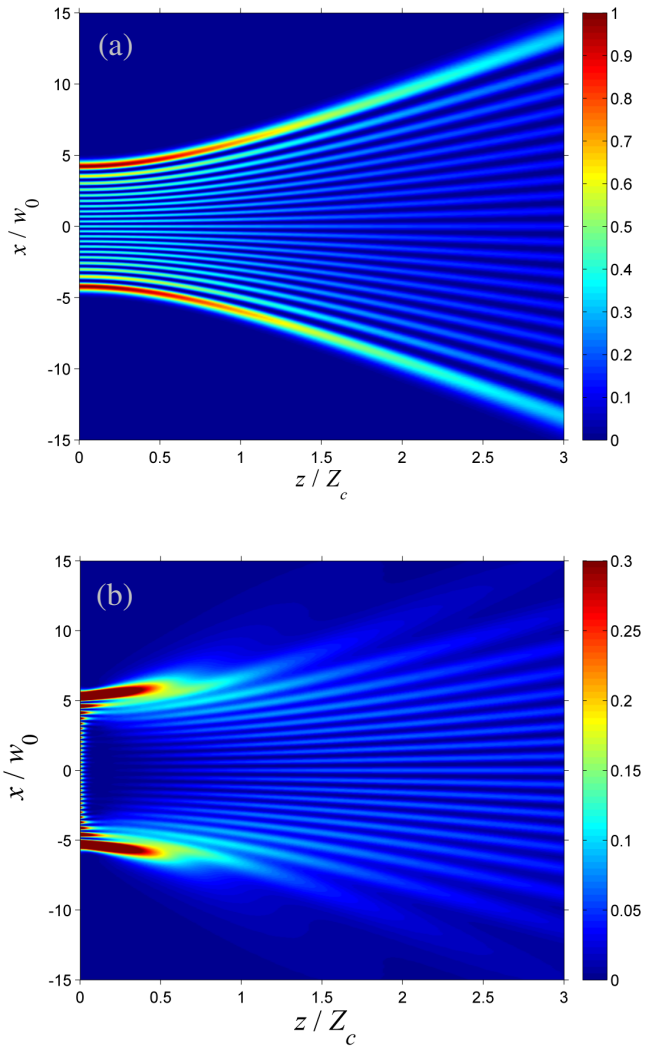

Figure 2.26 – Propagation of the $m = 30$ Hermite-Gaussian field structure (at $z = 0$) with $w_0 = \lambda$ according to (a) the paraxial description given by eq. (2.17), and (b) direct solution of Maxwell's equations using FDTD. The value of $w_0 / \lambda = 1$ creates a diffraction angle of ~18.23°. Fields have been normalised to the maximum intensity value, and the colour scale in (b) is clipped at 0.3 to visually enhance the near-field effects of evanescence.

While this phenomenon does not affect the use of beam modes given by equation (2.17) and equation (2.27) in the approximation of the Fresnel diffraction integral as the modes still obey the diffractive behaviour described by that integral, evanescence limits the applicability of those paraxial descriptions in defining the true physical behaviour of the Gaussian beams with lower values of w_0 / λ. This is especially

true in the case of higher order beam modes with much more extensive ranges of transverse frequency.

The irregular periodicity of the HG functions does not allow one to predict the exact spatial frequency at a specific point in the transverse mode structure. However, adapting equation 7.376.1 of [GRA07] we can define the Fourier spectrum of a un-normalised Hermite-Gaussian function as

$$S(k_x) = \frac{1}{\sqrt{2\pi}} \int_{-\infty}^{\infty} \exp(i k_x x) H_m\left(\sqrt{2}\frac{x}{w_0}\right) \exp\left(-\frac{x^2}{w_0^2}\right) dx = \frac{w_0}{\sqrt{2}} H_m\left(\sqrt{2}\frac{k_x}{\beta}\right) \exp\left(-\frac{k_x^2}{\beta^2}\right) \tag{2.43}$$

which, with $\beta = 2/w_0$, defines the Fourier spectrum also as a Hermite-Gaussian function in frequency space.

The diffraction of a field can be computed using the angular spectrum of plane waves [GOO05], whereby the field is defined as an integration of plane waves with weightings for a specific frequency k_x, defined by the Fourier transform of the field structure at the source of the beam, or any defined plane where the phase and amplitude properties of the field are known. The field can then be computed at any plane as a superposition of plane waves with amplitudes specified by the Fourier transform of a given field such as that given by eq. (2.43). If we quantify the width of the spectrum in equation (2.43) in the same manner that the spatial extent of a HG mode was given by equation (2.22) then the range of frequencies of a HG mode is

$$\Delta k_x = 2\beta\sqrt{m+\frac{1}{2}}\,. \tag{2.44}$$

For propagation of a field structure at the plane $z > 0$ the value of k_x must not exceed the freespace wavenumber k. With values of $\Delta k_x > k$ preventing propagation, we can give a first-order estimate for the proportion of non-evanescent wave-vectors in a physical Hermite-Gaussian mode of order m to be

$$\frac{k}{\Delta k_x} \approx \frac{\pi w_0}{2\lambda\sqrt{m+1/2}}\,. \tag{2.45}$$

Then with even lower values of w_0, propagation of harmonic energy can be almost completely eliminated from the field.

While the Rayleigh-Sommerfeld integrals give exact results, this thesis is concerned with the modal description of diffraction, and for the paraxial Fresnel diffraction integral the eigen-mode solutions are known with completeness, thus we

concentrate our attention on those fields. However, we may also describe an approximate modal formulation of the Rayleigh-Sommerfeld formulation using recently derived expressions for the propagation of Gaussian beam modes with a less restriction on angular divergence.

In [DUAN05], the authors derived very useful expressions for the calculation of diffraction effects in higher order Hermite/Laguerre-Gaussian beam modes with very small values of w_0 / λ, which under the conventional paraxial approximation would give invalid physical results. With low values of w_0 / λ, the divergence of Gaussian fields is much greater than the paraxial descriptions can account for, and in that situation the true physical field of each mode no longer maintains a constant amplitude profile with increasing z.

In [DUAN05] an approximation was introduced allowing for simplification of the Rayleigh-Sommerfield integrals as

$$r - r_0 \approx r + \frac{x_0^2 + y_0^2 - 2x\,x_0 - 2y\,y_0}{2r} \tag{2.46}$$

where $r = \sqrt{x^2 + y^2 + z^2}$ and $r_0 = \sqrt{x_0^2 + y_0^2}$. Dealing with a vertical linearly polarised field, the y component of the field is given by

$$E(x, y, z) = -\frac{i\,z}{\lambda\,r}\frac{\exp(i\,k\,r)}{r}\int_{-\infty}^{\infty}\int_{-\infty}^{\infty} E_y(r_0)\exp\left(i\,k\,\frac{x_0^2 + y_0^2 - 2x\,x_0 - 2y\,y_0}{2r}\right)dx_0 dy_0 \,. \tag{2.47}$$

The x and z polarisation components of a field can be calculated with a similar integral with appropriate change of subscripts, but polarisation effects are omitted here. For a description of the longitudinal and horizontal components of the modes the reader is referred to [DUAN05].

By substituting the previous conventional description of a Hermite-Gaussian mode at the plane $z = 0$, i.e. eq. (2.16), into the Rayleigh-Sommerfeld integral given (eq. 2.42), the propagation of non-paraxial Hermite-Gaussian (NPH) beam modes were then shown in [DUAN05] to be

$$\psi_m^{NPH}(x, z) = -i\,z\sqrt{\frac{2^{1/2-m}\,w(z)}{m!}}\,\frac{B(x,z)\,k\,w_0}{2\pi^{1/4}\left(x^2 + z^2\right)}\exp\left(i\,k\sqrt{x^2 + z^2}\right)\left(1 - 2B(x,z)\right)^{m/2}$$

$$\times H_m\left(\sqrt{2}\,\frac{A(x,z)\,x}{\sqrt{1 - 2B(x,z)}}\right)\exp\left(\frac{A(x,z)^2\,x^2}{B(x,z)}\right) \tag{2.48}$$

with

$$B(x,z) = \frac{2\,i\,A(x,z)\sqrt{x^2 + z^2}}{k\,w_0}\text{, and } A(x,z) = \frac{\left(1 + \frac{2\,i\,\sqrt{x^2+z^2}}{k\,w_0^2}\right)^{-1}}{w_0}\quad .$$

The description given by equation (2.48) differs from that of eq.7 (a) in DUAN05 as that paper described the mode in relation to a unit on-axis amplitude value at the source. This author has included the normalisation terms required for application in a modal field synthesis. Here, although the waist parameter $w(z)$ no longer holds the same obvious relation to the spatial width of the mode, as it did in the paraxial definition of the modes, the normalisation factor of the diffracted mode maintains its form as the energy through each plane must remain a constant (energy loss due to evanescence is not predicted in Duans' expressions).

While eq. (2.48) introduces some invalidity of the mode fields near the source plane due to the approximation used in eq. (2.46), these solutions can be used in an identical procedure as the paraxial beam modes for the synthesis of the beam patterns of fields involving non-paraxial diffraction at planes with lower values of the Fresnel number, i.e. in the far-field, in a similar manner as eq. (2.34).

Duan's definition of the amplitude structure of the non-paraxial modes converge upon the paraxial prediction for large values of w_0 / λ, but with smaller values of this ratio the deviant behaviour of the mode's propagation beyond the paraxial constraints becomes evident, as shown in Figure 2.27. Consistency in the structure of the absolute value of the transverse amplitude pattern was a feature of the paraxial expressions of the Hermite and Laguerre-Gaussian modes. As the modes can now be depicted without the paraxial restriction, the far-field pattern of each mode is no longer represented by the Fraunhofer diffraction integral and therefore is no longer related to the Fourier transform of the field at $z = 0$.

These expressions, eq. (2.48), open up new opportunities for the application of the modal approach of diffraction using a non-paraxial Gaussian beam mode analysis (NPGBMA) of widely diverging fields. Using equation (2.34) with the modes defined by equation (2.48), one can generate a much more accurate prediction of far-fields than was previously described in this chapter, a particularly useful tool for the modelling of sources that are narrow in relation to the field wavelength such as horn antenna bare waveguides.

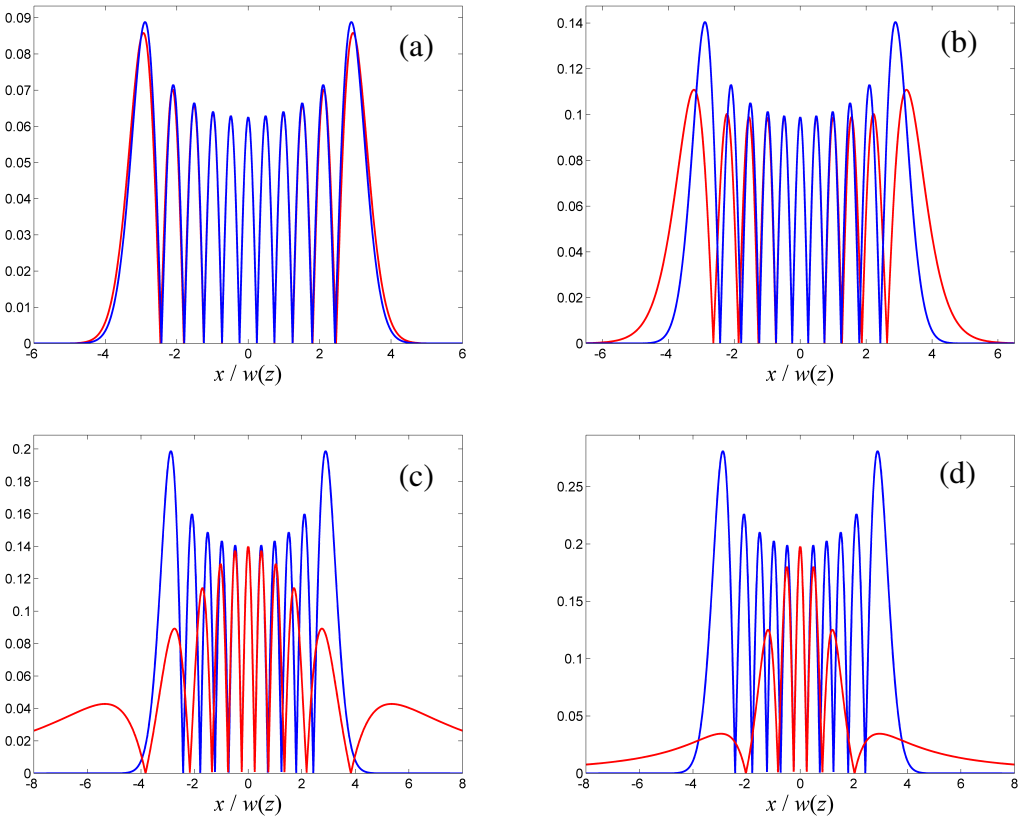

Figure 2.27 – Comparison of the m = 10 non-paraxial Hermite-Gaussian modes given by eq. (2.48) (shown in red) and the conventional form of the paraxial HG mode (blue) from equation (2.17). The mode structures $|\psi_m|$ are calculated at $z = 10\ Z_c$, with w_0/λ = (a) 5, (b) 2, (c) 1, (d) 0.5.

For their application in a field synthesis, at $z = 0$ the non-paraxial beam modes given by (2.48) have the exact structure of the modes discussed previously in this chapter, and calculation of the related mode coefficients A_m for an aperture function is identical for the paraxial and non-paraxial forms. The modal structures deviate from each other only with propagation at $z > 0$.

To demonstrate the practical applications of this new method we describe the diffraction of a plane at a square aperture using the same modal expansion presented earlier in the chapter, and compare the results of the non-paraxial expression of HG mode propagation with the conventional use of the paraxial Hermite-Gaussian modal technique. Calculating the mode coefficients in the conventional manner with equation (2.19), we can now determine the far-field beam structure using the non-paraxial beam modes as a modal sum given by

$$E(x, y, z) \cong \sum_{m=0}^{M} A_m \psi_m^{NPH}(x, y, z) \tag{2.49}$$

The following figures show a comparison of the paraxial and non-paraxial forms of the Gaussian beam mode calculations for a narrow square aperture using eq. (2.49).

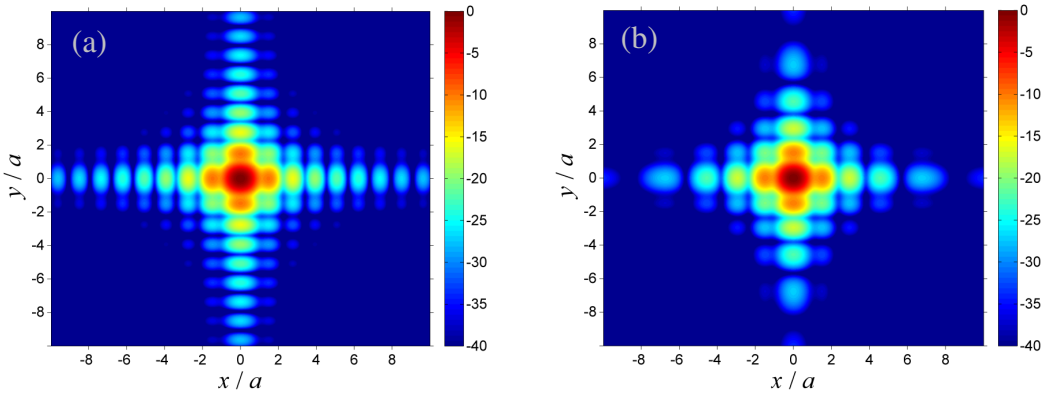

Figure 2.28 – Logarithmic dB scale comparison of the (a) paraxial and (b) non-paraxial forms of the Gaussian beam mode calculation for diffraction of a plane wave at a narrow square aperture of width $2a$ = 6.66λ, predicted at $z = 2.27a^2/\lambda$ using 101 modes.

As the angle of diffraction is dependent on the ratio of the aperture diameter to the radiation's wavelength, with a relatively larger aperture the paraxial approximation has greater validity as depicted in Figure 2.29 (a).

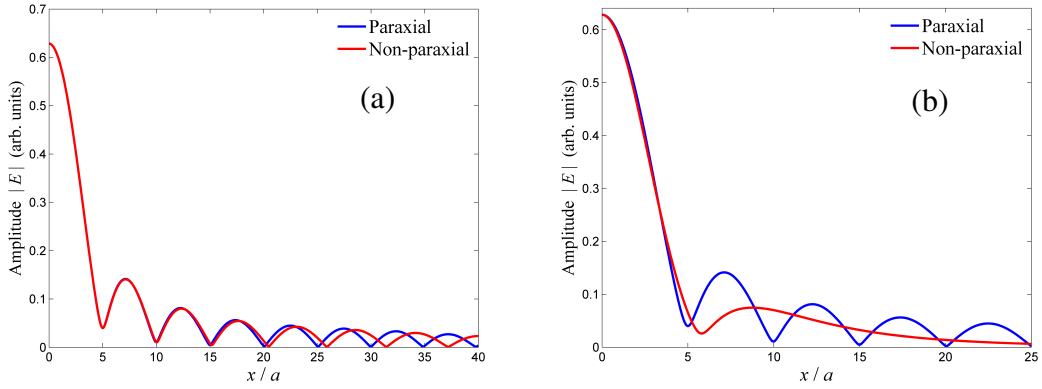

Figure 2.29 – Diffraction patterns of a single slit with semi-width a = (a) 10 λ, and (b) 1 λ, showing the breakdown of the paraxial validity for very narrow apertures under plane wave illumination. The fields were simulated at the plane $z = 10\ a^2 / \lambda$ using the paraxial and non-paraxial forms of the Hermite-Gaussian expansion with $M = 30$.

The deviation inherent in the paraxial calculation is obvious, particularly in Figure 2.29 (b) where the appearance of several off-axis intensity maxima completely diverges from the non-paraxial predictions. At greater offsets, the non-paraxial calculation shows a more rapid fall-off in amplitude away from the origin, while off-axis maxima occur more frequently in the paraxial prediction. However, given these discrepancies in the paraxial method and with relevance to the work in this thesis, the

important aspect to note from these comparisons is the convergence of the paraxial results to the non-paraxial in the case of relatively large apertures like that shown in Figure 2.29 (a).

The non-paraxial GBM method will be further verified in the next section in a comparison between results from it and a numerical algorithm for the direct solution of Maxwell's equations.

2.8.2 - The finite-difference time-domain method

While the paraxial theory of diffraction should be considered an extremely useful tool in the study of electromagnetic and other wave phenomena, it nevertheless has limitations in certain situations as shown in the previous section. As well as the obvious limits placed on the angular spread of the field, a further necessary drawback is the manner in which objects that interact with radiation are defined in a scalar model, creating an inexact description of the matter/component along a flat transverse surface, thus approximations must be employed in the description of non-planar surfaces that neglect diffraction and reflection effects within a thick optically dense component, as was described in the paraxial description of a spherical lens in an earlier section. This is not just the case in paraxial methods, but is also a feature of non-paraxial scalar diffraction techniques such as the Rayleigh-Sommerfeld integrals.

A relatively recent progression in the field of computational electromagnetics was the development of an algorithm known as the finite-difference time-domain (FDTD) technique, first suggested by Kane Yee [YEE66], and gained more attention after a series of publications by Alan Taflove and co-workers [TAF80,TAF82]. The interested reader is referred to the excellent paper by [CHU95] for an introductory but thorough description of the technique. While the algorithm was originally described decades ago it is really only in the last fifteen years that the method has begun to be explored and applied because of the affordability of computers. Referring to literature from the early 1990's, simulations that could now be performed rapidly on the most basic of commercially available computers, then required access to supercomputers [JOS91].

The accuracy of the FDTD solution, based on its direct solution of Maxwell's curl equations, makes it an optimum model of field calculation in terms of precision. However, the number of calculations required for numerical convergence can be a significant disadvantage. Sampling of the field is necessarily high so as to ensure an

accurate approximation of a derivative using finite differences, and the minimum spatial sample rate is conventionally given within the literature as $\lambda / 20$. As the field magnitude is dependent on previous states, in both time and space, calculations of the field far from the source, particularly in three dimensional computations, may require hundreds of hours using a single processor machine, and of course with the large data arrays required for this, computer memory then becomes another issue.

While the Fresnel and Rayleigh Sommerfeld diffraction integrals can be used to describe diffraction by a planar source, the primary advantage of the FDTD technique is the ability to define realistic descriptions for the structures of optical components and media with which a field might interact. Even in its most basic form, reflection and refraction effects are inherently calculated by the method, these are phenomena which would require further significant modification of a diffraction integral technique for similar analysis. The technique has been used most regularly in calculation of EM field structures with radio applications, and with the involvement of wavelengths that are long in comparison to the dimensions of the electrical/optical components it becomes a less extensive calculation in predicting near field effects. At visible or infra-red wavelengths the technique has not gained widespread use, but examples of its use in the modelling of electrically-small low Fresnel number micro-lenses are in the literature [FENG04].

It must be noted that FDTD is not an algorithm with specific uses in electromagnetics, but rather it can be generally adapted to solve any differential wave equation. One discipline that relies on the use of FDTD to the same degree as optics is acoustics where the method is used to model pressure waves of various wavelengths ranging between micrometres (medical ultrasound) [PIN07], to kilometres (earthquakes), [THO07, JAH07].

In numerical techniques used in the analysis of scalar diffraction such as the Fresnel diffraction integral, or its evaluation through the Gaussian beam expansion, the optical properties of a material are represented most commonly by the refractive index, which is a completely macroscopic property and gives little information about the electronic or magnetic behaviour of the substance. In more rigorous electromagnetic calculations, such as FDTD and the finite-element method [RAH95], the refractive index of a medium is defined more relevantly through the characterization of its relationship with the magnetic permeability μ and electric permittivity ε. The permittivity of a material, ε, measured in units of F/m, defines the effect of an applied

electric field E on a material in relation to the electric displacement field generated within the material, i.e. $\varepsilon = D / E$. The permittivity of a vacuum, and therefore a close approximation to the same quantity in air, is given as $\varepsilon_0=1/(c^2\mu_0)$ where μ_0 is the magnetic permeability of free space, describing the relationship between the applied and internal magnetic fields, B and H respectively, as $\mu_0 = B / H$. These two fundamental constants, ε_0 and μ_0 have utmost importance in electromagnetics, for example, ε_0 has a vital role in the effects of the fundamental Coulomb force.

For numerical calculation of electric fields, the shape and composition of the environment, such as the propagation of a wave through an optical component, is defined through the variation in ratio of the local permittivity and permeability, to the free space constants given above (for a coordinate r)

$$\varepsilon_r(\vec{r}) = \frac{\varepsilon(\vec{r})}{\varepsilon_0} \text{ and } \mu_r(\vec{r}) = \frac{\mu(\vec{r})}{\mu_0}$$

which have values of unity in a vacuum. The calculation of the refractive index of a material, and of course it can vary with location, is then

$$n(\vec{r}) = \sqrt{\varepsilon_r(\vec{r})\mu_r(\vec{r})}$$

The current density J within a conducting material is related to the applied electric field through $J = \sigma E$, with the material conductivity σ. One important effect of this is the creation of a exponentially decreasing field amplitude of the EM wave within a conductor.

The FDTD method allows for use of these material parameters in simulations and can therefore be seen to be a much more suitable method for modelling the realistic behaviour of radiation within a material. Recently the algorithm has been applied in the study of meta-materials that exhibit a negative refractive index [WANG08, CHEN10].

2.8.2.1 - Formulation of the FDTD algorithm in Cartesian systems

The fundamental description for behaviour of electromagnetic radiation, is given by the fundamental Maxwell curl equations,

$$\nabla \times \vec{E} = -\mu \frac{\partial \vec{H}}{\partial t} \tag{2.50a}$$

$$\nabla \times \vec{H} = \sigma \vec{E} + \varepsilon \frac{\partial \vec{E}}{\partial t} \tag{2.50b}$$

we can use the common identity

$$\nabla \times \vec{F} = \begin{vmatrix} i & j & k \\ \partial & \partial & \partial \\ \partial x & \partial y & \partial z \\ F_x & F_y & F_z \end{vmatrix},$$

to derive the following six scalar equations

$$\frac{\partial E_x}{\partial t} = \frac{1}{\varepsilon}\left(\frac{\partial H_z}{\partial y} - \frac{\partial H_y}{\partial z} - \sigma E_x\right) \tag{2.51a}$$

$$\frac{\partial E_y}{\partial t} = \frac{1}{\varepsilon}\left(\frac{\partial H_x}{\partial z} - \frac{\partial H_z}{\partial x} - \sigma E_y\right) \tag{2.51b}$$

$$\frac{\partial E_z}{\partial t} = \frac{1}{\varepsilon}\left(\frac{\partial H_y}{\partial x} - \frac{\partial H_x}{\partial y} - \sigma E_z\right) \tag{2.51c}$$

$$\frac{\partial H_x}{\partial t} = \frac{1}{\mu}\left(\frac{\partial E_y}{\partial z} - \frac{\partial E_z}{\partial y}\right) \tag{2.51d}$$

$$\frac{\partial H_y}{\partial t} = \frac{1}{\mu}\left(\frac{\partial E_z}{\partial x} - \frac{\partial E_x}{\partial z}\right) \tag{2.51e}$$

$$\frac{\partial H_z}{\partial t} = \frac{1}{\mu}\left(\frac{\partial E_x}{\partial y} - \frac{\partial E_y}{\partial x}\right) \tag{2.51f}$$

The use of these equations in Yee's method relies on the evaluation of the functions E and H over a discretely sampled space. In such methods a function F is defined by

$$F^n(i,j,k) = F(i\Delta x, j\Delta y, k\Delta z, n\Delta t)$$

The derivatives in discrete form are then given in the spatial and temporal dimensions respectively as the central differences

$$\frac{\partial F^n(i,j,k)}{\partial x} = \frac{F^n(i+1/2,j,k) - F^n(i-1/2,j,k)}{\Delta x} + O(\Delta x^2) \tag{2.52a}$$

$$\frac{\partial F^n(i,j,k)}{\partial t} = \frac{F^{n+1/2}(i,j,k) - F^{n-1/2}(i,j,k)}{\Delta t} + O(\Delta t^2) \tag{2.52b}$$

with, for simplicity, $\delta = \Delta x = \Delta y = \Delta z$. $O(\Delta x^2)$ and $O(\Delta t^2)$ are errors which arise from the approximation of the derivative as a truncated Taylor series, so it is extremely important that Δx and Δt have values that are sufficiently small to minimise these errors to a satisfactory level. The minimum values for these can be determined from the Courant-Friedrichs-Levy condition, [LAK88], which gives the minimum time sampling allowable for accurate convergence of FDTD results:

$$c\,\Delta t \le \sqrt{\frac{1}{\Delta x^2} + \frac{1}{\Delta y^2} + \frac{1}{\Delta z^2}} \tag{2.53}$$

where the refractive index of the medium must be accounted for in the definition of the speed of light c. Also, for calculation of fields with extremely ultrashort durations, the value Δt may have to be decreased significantly.

The space in which the field is to be calculated is sampled with each E and H component defined on a three dimension grid of cubic cells. The H vectors are defined on the faces of the cell and the E fields are determined along its edges. The H value is calculated from the appropriate E components that exist at a previous time of Δt / 2. See Figure 2.30.

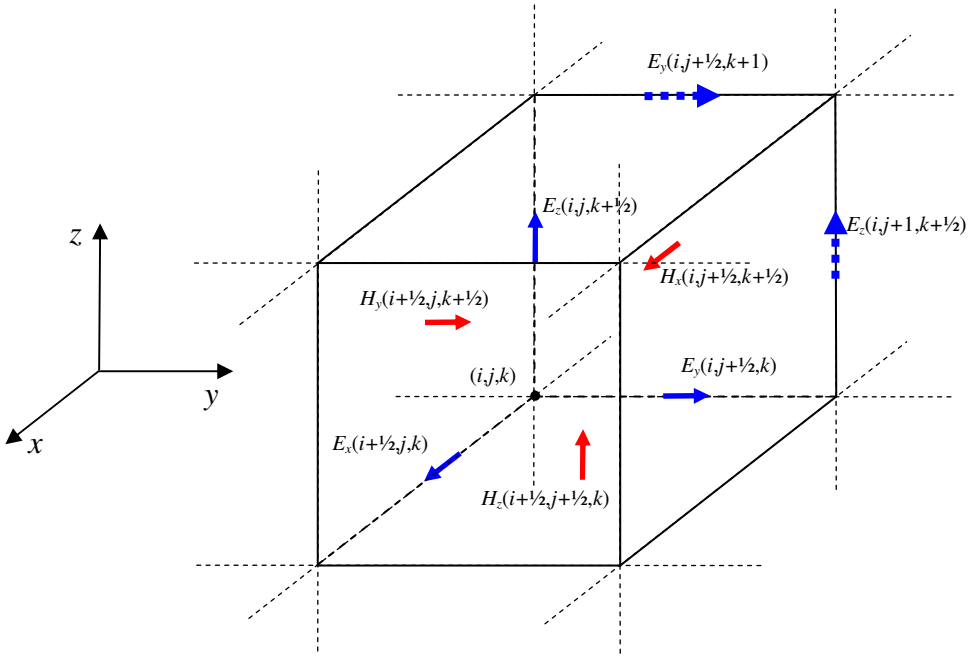

Figure 2.30 – Yee's grid - The geometry used for the FDTD computational solution of Maxwell's equation.

In Figure 2.30 the components $E_y(i,j+½,k+1)$ and $E_z(i,j+1,k+½)$ are related to the neighbouring cells, and are used in calculation of the H_z vector for the cell illustrated.

While their position in the Yee grid cell shown in Figure 2.30 differs, components of the electric field E are defined in the simulation at the same point in space, while each component of the magnetic field vector H has the same position which is defined in the simulation space at distances Δx / 2, Δy / 2, Δz / 2 beyond the E components, along all the respective axis. Their positions in the grid are arranged so as to allow for calculation of the curl of the vector field through comparison of each

component with its analogue in a neighbouring grid cell. Using equations 2.51a-f, the following discrete relations are derived for Maxwell's equations for the above geometry, with the superscript of E and H representing the time index. Each discrete equation is related to the continuous scalar equations given in eq. (2.51) respectively.

$$E_x^{n+1}(i+1/2,j,k) = \mathrm{K}_{i+1/2,j,k} E_x^n(i+1/2,j,k) + \Lambda_{i+1/2,j,k}\left[\begin{array}{l}\dfrac{H_z^{n+1/2}(i+1/2,j+1/2,k)-H_z^{n+1/2}(i+1/2,j-1/2,k)}{\Delta y} \\ +\dfrac{H_y^{n+1/2}(i+1/2,j,k-1/2)-H_y^{n+1/2}(i+1/2,j,k+1/2)}{\Delta z}\end{array}\right], \quad (2.54a)$$

$$E_y^{n+1}(i,j+1/2,k) = \mathrm{K}_{i,j+1/2,k} E_y^n(i,j+1/2,k) + \Lambda_{i,j+1/2,k}\left[\begin{array}{l}\dfrac{H_x^{n+1/2}(i,j+1/2,k+1/2)-H_x^{n+1/2}(i,j+1/2,k-1/2)}{\Delta z} \\ +\dfrac{H_z^{n+1/2}(i,j-1/2,k+1/2)-H_z^{n+1/2}(i+1/2,j+1/2,k)}{\Delta x}\end{array}\right], \quad (2.54b)$$

$$E_z^{n+1}(i,j,k+1/2) = \mathrm{K}_{i,j,k+1/2} E_y^n(i,j,k+1/2) + \Lambda_{i,j,k+1/2}\left[\begin{array}{l}\dfrac{H_y^{n+1/2}(i+1/2,j,k+1/2)-H_y^{n+1/2}(i-1/2,j,k+1/2)}{\Delta x} \\ +\dfrac{H_x^{n+1/2}(i,j-1/2,k+1/2)-H_x^{n+1/2}(i,j+1/2,k+1/2)}{\Delta y}\end{array}\right], \quad (2.54c)$$

$$H_x^{n+1/2}(i,j+1/2,k+1/2) = H_x^{n-1/2}(i,j+1/2,k+1/2) + \frac{\Delta t}{\mu(i,j+1/2,k+1/2)}\left[\begin{array}{l}\dfrac{E_y^n(i,j+1/2,k+1)-E_y^n(i,j+1/2,k)}{\Delta z} \\ +\dfrac{E_z^n(i,j,k+1/2)-E_z^n(i,j+1,k+1/2)}{\Delta y}\end{array}\right], \quad (2.54d)$$

$$H_y^{n+1/2}(i+1/2,j,k+1/2) = H_y^{n-1/2}(i+1/2,j,k+1/2) + \frac{\Delta t}{\mu(i+1/2,j,k+1/2)}\left[\begin{array}{l}\dfrac{E_z^n(i+1,j,k+1/2)-E_z^n(i,j,k+1/2)}{\Delta x} \\ +\dfrac{E_x^n(i+1/2,j,k)-E_x^n(i+1/2,j,k+1)}{\Delta z}\end{array}\right], \quad (2.54e)$$

$$H_z^{n+1/2}(i+1/2, j+1/2, k) = H_z^{n-1/2}(i+1/2, j+1/2, k) + \frac{\Delta t}{\mu(i+1/2, j+1/2, k)} \left[\frac{E_x^n(i+1/2, j+1, k) - E_z^n(i+1/2, j, k)}{\Delta y} + \frac{E_x^n(i, j+1/2, k) - E_x^n(i+1, j+1/2, k+1)}{\Delta x} \right], \quad (2.54f)$$

with $K_{i,j,k} = 1 - \Delta t \frac{\sigma(i,j,k)}{2\varepsilon(i,j,k)}$, and $\Lambda_{i,j,k} = \frac{2\Delta t}{2\varepsilon(i,j,k) + \Delta t\, \sigma(i,j,k)}$.

As signals are defined in the time domain in this technique, one convenient aspect of this algorithm is that it does not discriminate between continuous and pulsed waves and therefore there is no requirement for spectral analysis of the amplitude signal, which we will show in a later chapter to be a feature of the analysis of pulsed fields using conventional diffraction techniques.

The author of this thesis used Matlab™ to develop a two-dimensional (*x*-*z*) FDTD simulation. Initially, the code was written using FOR loops, addressing each data array element independently. However, total running time can be reduced greatly when the process of vectorisation is used. Vectorisation allows for a data array to be manipulated in a single operation without referring to array elements individually. The segments of Matlab™ code below compare the two programming methods for the computation of H_x in a two-dimensional TE_y simulation. Both sections of code are nested in FOR loops that advance the time value.

```
%for loop method
for m=1:Nx,
     for n=1:Nz,
          Hx(m,n)=Hx(m,n)+dt*(Ey(m,n+1)- Ey(m,n))/(mu0*dz);
     end
end
```

```
%Vectorisation method

Hx(1:Nx-1,1:Nz-1) = Hx(1:Nx-1,1:Nz-1) ...
                      + dt*(Ey(1:Nx-1,2:Nz)-Ey(1:Nx-1,1:Nz-))/(mu0*dz);
```

When using the vectorisation method the arithmetic expressions are initiated for all array positions at the same time rather than one element at a time. While such operations on arrays require a longer time than with a single variable, this form of code gave a three-fold decrease of the computation time when compared to the version of the

program that used FOR loops. The vectorisation method of array manipulation is also available in the Octave and Python open-source programming languages.

The simulation was tested briefly on an enhanced desktop PC (6 GB of RAM, and a 3.1GHz CPU), and resulted in a further threefold decrease in computation time. The memory allocation for each array is reduced by using a single precision representation of the values halving the memory required for the default double precision. This can affect the numerical precision but only minutely for the relatively low field values used here, with errors of the order of a hundredth of a percent between the two representations. Further minor improvements to the software could have been continuously achieved, but it must be stated that for simulations of realistic three-dimensional Cartesian systems the use of computing clusters may have to be incorporated into the development of simulations, depending on the required volumes of the calculation regions.

To illustrate the general capabilities of FDTD we can exhibit as a simple example the propagation of a one-dimensional infinitely wide pulsed plane wave, (a time limited signal will allow for clearer depiction of reflection effects). With such a field electrically polarised in the y-direction and propagating along the z axis, only two field components are required, E_y and H_x. The physics of this situation is relatively straightforward, but if we simulate the wave being transmitted from a vacuum through a material of a higher refractive index we can exhibit the possible applications of this powerful technique. In the simulated results presented in Figure 2.31 a 1 THz pulsed plane wave with a duration of 2.54 ps is transmitted from free-space through a section of homogenous material with refractive index $n = 1.732$, ($\varepsilon = 3\varepsilon_0$). The FDTD results show a much more realistic description of field propagation within a material than that achievable with diffraction integral techniques. The reflection of the field at the left-hand side of the dense medium, the first-order effects of dispersion within the material shown by the decrease in wavelength, and the internal reflection at its right hand boundary are all predicted with FDTD, whereas the scalar techniques discussed in this chapter neglect such important physical effects.

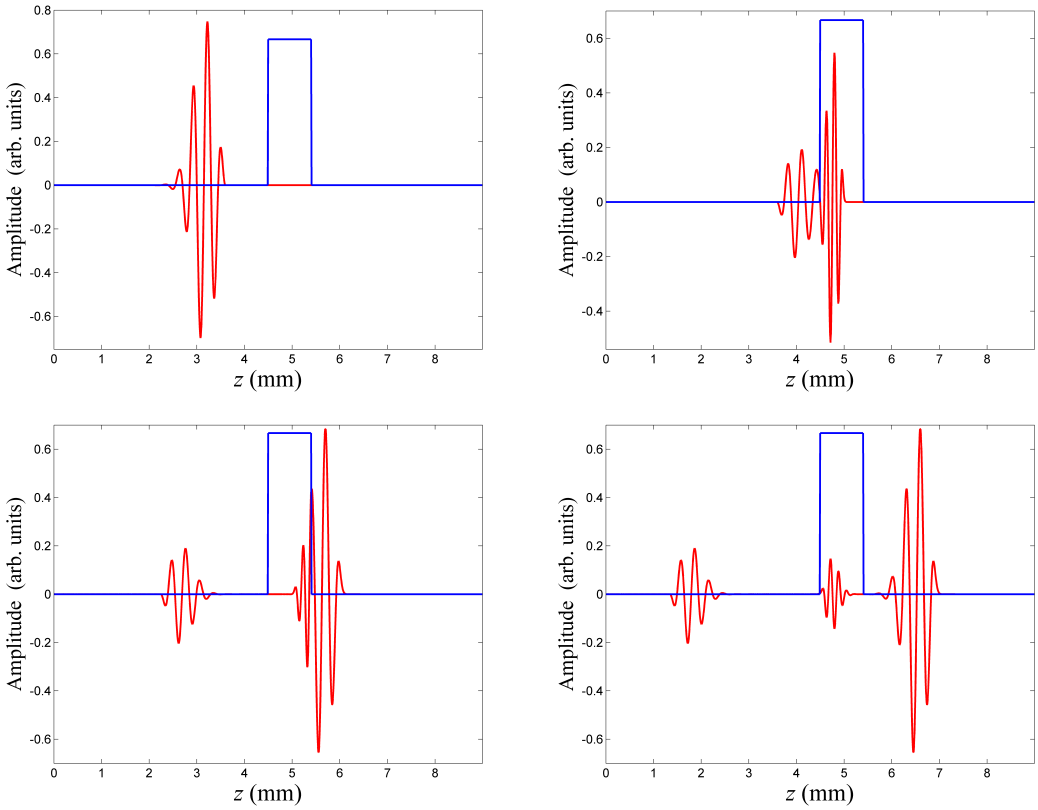

Figure 2.31 – Propagation of a 2.54 ps plane wave pulse, with ν_0 = 1 THz with a Gaussian temporal shape, calculated using the FDTD algorithm. A region of higher refractive index, n = 1.732, is marked by the blue lines.

The solution of differential wave equations by the finite-difference time-domain algorithm has been referred to as the "workhorse" of computational electrodynamics as it is, along with finite-element analysis, the most robust algorithm for the calculation of electromagnetic fields in complicated structures [KAN06]. It is, however, still a relatively modern technique, and has not gained widespread use. A fact which can be partially attributed to the rigorous computation involved using large arrays of memory, which is necessary because of the fine sampling of the fields required to accurately represent continuous derivatives by discrete differences. The FDTD results presented in this chapter were calculated on a conventional PC with 3GB of random access memory, and a processor speed of 2.17 GHz. Even with such a standard machine, and although the two-dimensional results to be shown may require up to thirty minutes, the computation times using the algorithm were found to be very acceptable given the thoroughness of the analysis.

When using scalar diffraction integrals or associated methods such as GBMA, the intensity of a field is proportional to the square of the complex electric field value. With FDTD the time-averaged intensity of the field can be calculated numerically by integration of the square of the electric field, $|E_x+E_y+E_z|^2$, and subsequent division by the duration of the simulation. This is a much more useful quantity for comparison of predicted fields with those measured by experiment.

The following plots, Figure 2.32 (a) and (b), show a comparison of calculations from the FDTD method and the two forms of Gaussian beam mode analysis, paraxial and non-paraxial, described in this chapter for diffraction of a plane wave by a one dimensional aperture, with semi-width $a = 3.33\ \lambda$, aperture dimensions which are typical of millimetre wave sources. The fields are predicted at $z = 2.27a^2 / \lambda$.

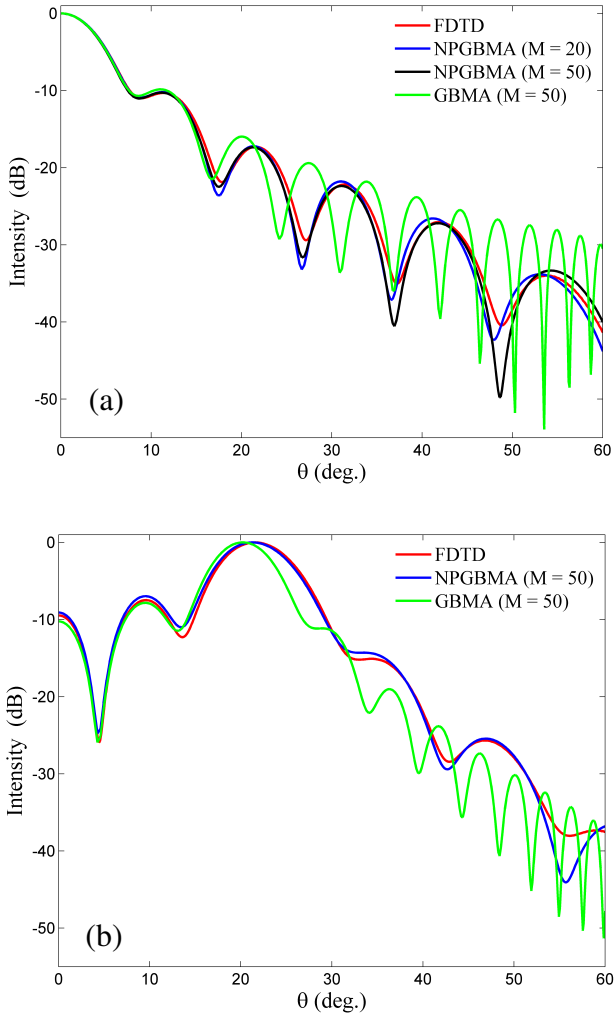

Figure 2.32 - Comparison of the FDTD and HG syntheses of diffraction of a plane wave by (a) a one-dimensional slit and (b) the aperture function $E_0(x_0)=\cos(2.5\pi\, x_0 / a)$, both apertures have a width of $2a = 6.66\ \lambda$. Predicted at $z = 2.27a^2/\lambda$, the data is shown with a logarithmic scale normalized to the maximum intensity value.

Comparing the calculated fields of Figure 2.32 visually through features such as the positions and relative intensity levels of the off-axis nulls and peaks, the non-paraxial GBMA and FDTD methods can be seen to show very good agreement with each other. The discrepancies that do occur between these schemes could, in the opinion of the author, be attributed to the numerical approximations used in the FDTD method. The FDTD process applied by this author follows the conventional description of the method given in the majority of literature describing electromagnetic applications of the technique. This is a first-order form of the algorithm in that the derivatives occurring in the Maxwell curl equations are represented by finite differences determined from a Taylor expansion with neglect of terms involving higher order derivatives, d^2/dx^2 etc. With the convergence of the non-paraxial GBMA synthesis to the values of the Rayleigh-Sommerfeld integrals in the far-field, which are quoted in the literature as exact solutions [DUAN05], [BORN97], the author predicts that by using a higher-order formulation of the FDTD technique greater agreement would be found between the two methods. Use of a higher order Taylor series in deriving the finite difference expressions would also allow for less frequent spatial sampling of the propagation space, but does require the storage of instances of the field at multiple times, requiring more memory.

The paraxial calculations shown in Figure 2.32 again exhibit significant deviations, but within angular regions of approximately 15° show strong convergence to the non-paraxial results.

The paraxial and non-paraxial methods of field calculation that have been described all have their positive and negative attributes. The following tables below summarise the strengths and weaknesses, in the opinion of this author, for the paraxial Gaussian beam mode and finite-difference time-domain methods of field calculation.

FDTD Advantages	FDTD Disdvantages
Provides solution with no constraints on the complete wave equation. A previous knowledge of diffraction or other optical effects is not required as they are inherent in the evolution of the field.	Computation time is almost certainly going to be extensive, due to the high sampling rate. Particularly true if the calculation involves propagation through both free-space and materials of higher refractive index, or indeed, negative refractive index
Numerical approximations, i.e. finite difference representation of derivatives, have very little influence on the accuracy of the calculation when used appropriately.	Without extreme computer power, calculations in the far-field of a source are difficult to process. However, transform techniques do exist to predict fields in that region.
Allows for a robust determination of propagation effects in optically dense and conductive media with arbitrary shapes.	Does not allow for variable sampling rates, which would enable more accurate calculations in regions of greater interest and less rigourous analysis in other areas. This feature is permitted in finite-element analysis.

GBMA Advantages	GBMA Disadvantages
In terms of computation time, this can be a rapid method. And gives reliable results within an off-axis angle of ~12°.	In its conventional form it provides solutions only for the paraxial wave equation. Aperture dimensions must be relatively large in comparison with the field wavelength.
Information required for field calculations can be determined from *M* integrals. The field at any plane can then be established directly using this data, without any further reference to the aperture that may be represented with high sampling.	Optical elements must be modelled as an infinitesimal planar surface. Calculated effects can be inaccurate for thick components. This is also a feature of non-paraxial scalar methods,

Table 2.2 – Advantages and disadvantages of the FDTD and paraxial GBMA techniques.

2.8.2.2 – Example: FDTD simulation of a dielectric lens antenna

Horn antennas, and in particular, cylindrical corrugated horns require intricate design and manufacture and the tolerance required in creating $\lambda / 4$ corrugations used to create linear polarisations incurs high costs from specialist tool makers. A potential simple and cost-effective alternative for transmitter and detector horn antennas lies in the use of dielectric lens antennas (DLA's), which have garnered some application at frequencies higher into the terahertz and infrared waveband as manufacturing of horn

antennas can be difficult to create for operation at such small wavelengths in those bands [BORK04],[SAU06]. Such lens antennas are, in comparison with horn antennas, extremely easy to manufacture and design. However, despite having such a simplistic shape, prediction of the electromagnetic structure of waves reflected, diffracted and refracted within a DLA has proven itself to be a very difficult task [LAV08].

The structure of the antenna surface is essentially a hemispherical lens supplanted on a cylinder of the same material and equal radius, see Figure 2.33. But with a small radius, and therefore increased thickness, simplifications such as the use of the binomial expansion as described earlier in relation to the thin spherical lens cannot be used, as the approximation of such a highly curved surface as being planar would be completely deviant from the real physical nature of this situation.

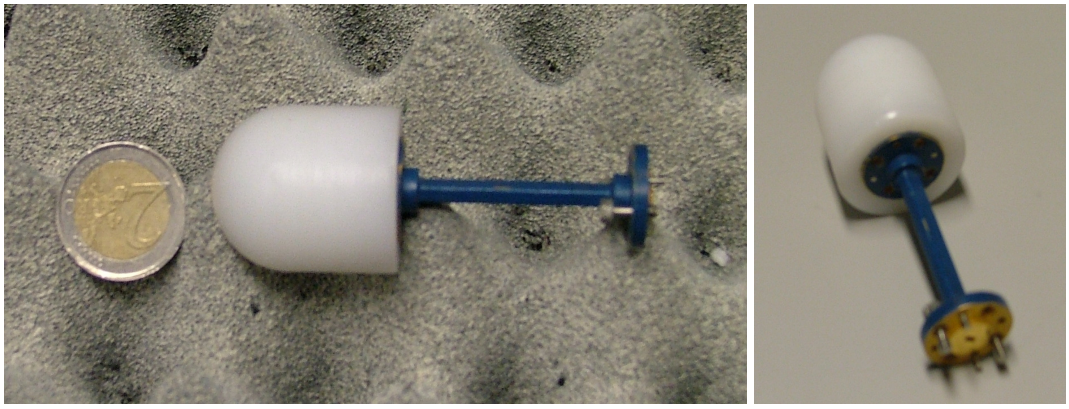

Figure 2.33 – A dielectric lens antenna for operation at 100GHz.

The focusing of a field to such a short focal length within the dielectric by the hemispherical structure will create large convergent angles, and conversely when used as a radiation source the diffraction of the field from the feed antenna can cause rapid evolution of the beam width over a short distance within the lens, rendering the paraxial techniques inapplicable in this scenario. This is a scenario in which a full-wave algorithm must be used and FDTD is an ideal candidate due to its completeness in describing both complete propagation effects and its ability to determine the electric and magnetic effects of unconventional dielectric and conductor structures.

The reader should note that the simulations presented here are two dimensional representations of the real 3D antenna system. A full three-dimensional simulation is presently beyond the capabilities of the author, with such a computational domain requiring large computer memory and possibly “parallelisation” of the software. Nevertheless, prediction of wave effects in a three-dimensional system through two-

dimensional numerical FDTD schemes, like those used here, has gained some acceptance in the optics community due to the computational difficulty involved with the method and there are several examples of work which simplify the prediction of optical effects in three-dimensional systems using two-dimensional models [DRE00,FENG04]. An algorithm described in [PRA99] presents a finite-difference formulation of the Maxwell equations in the cylindrical regime. But even with such a more relevant description of the coordinate system simulating the linear polarisation and rectangular structure of the waveguide source using this technique will also have a high level of complexity. The method involves the use of a Fourier series expansion of the field in angular coordinates which may not converge with great accuracy to the required rectangular symmetry of the feed waveguide.

To exhibit a practical application of FDTD we define a conventional high-density polyethylene (HDPE) DLA for operation at 100GHz with hemispherical surface with radius 15mm (5λ) and a cylindrical base with an equal radius and depth of 15mm, the dimensions of such an element as described in [LAV08], see Figure 2.33. For optimum performance of the lens antenna the focusing of the incoming field must concentrate a significant portion of the total incident power to the receiving antenna at the base of the lens. At terahertz frequencies lens antennas are conventionally applied in the focusing of fields generated by planar sources, for example, microstrip patch antennas [JHA09]. Figure 2.34 shows the simulated components of a vertically polarised 100 GHz field within such a lens antenna fed by a waveguide transmitting a fundamental mode.

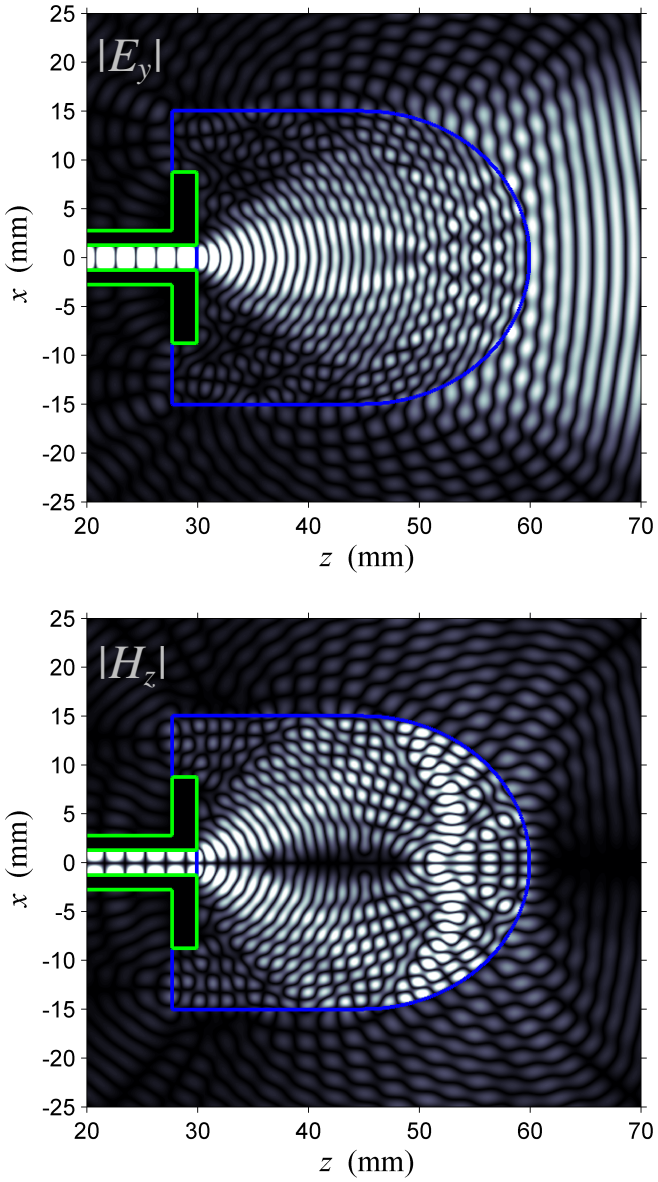

Figure 2.34 - The components of an electromagnetic field originating in a waveguide within a two-dimensional dielectric lens antenna, showing the lens itself marked with a blue line, and the flange of the feed waveguide at the left of the figures indicated in green. (Shown with a saturated linear scale).

The results in Figure 2.34 show the complexity of the field structure and why accurate analytical descriptions of such fields may be impossible to obtain. [LAV08] shows far-field measurements of the lens antenna described at 100 GHz and while the measured structures show smoothly varying intensity patterns at large distances from the source, one could easily assume that such behaviour is predictable, but as shown above the far-field is derived from a very complicated electromagnetic field structure. As mentioned, the computational power available to the author was limited so far-field

predictions were not possible, but Figure 2.35 demonstrates the field divergence just outside the lens.

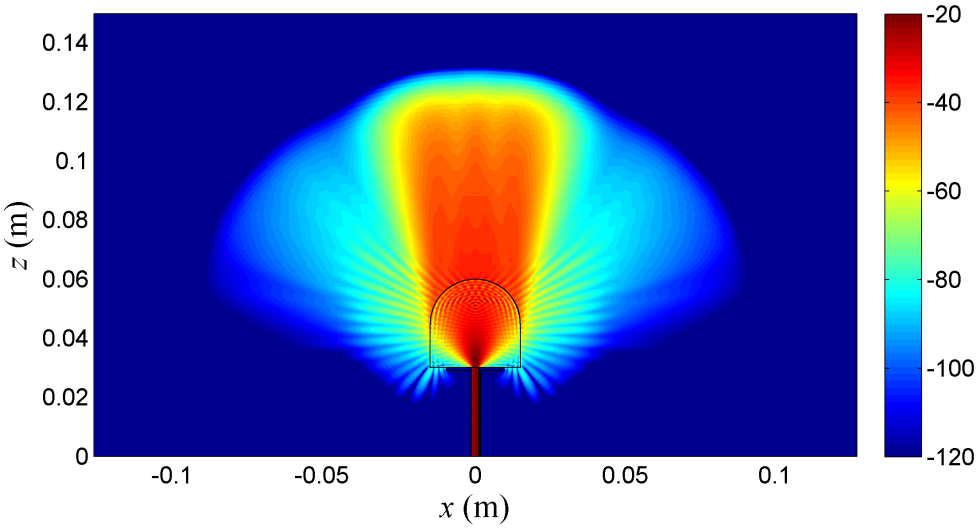

Figure 2.35 - The time averaged normalized electric and magnetic field intensities of dielectric lens antenna. Plots have been clipped at -20dB for clarity. (dB scale).

For simulation of the DLA as a receiver the detected field was modelled to represent a planar wavefront but with a Gaussian envelope a short distance from the central maximum of the antenna surface. The amplitude envelope would avoid any discrepancies caused by unwanted reflections at the boundaries of the simulation region. See Figure 2.36.

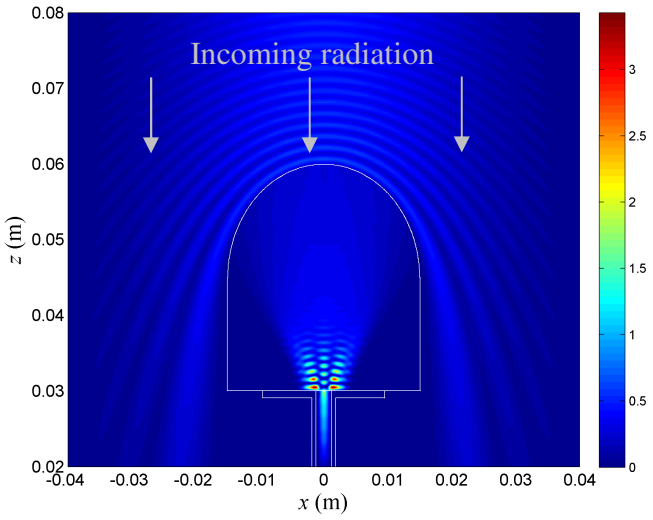

Figure 2.36 – False-colour plot of the time averaged intensity of E_y with the lens antenna operating as a receiver. Note the creation of fringe features near the surface of the lens due to reflection from its surface. Shown with a linear scale.

While the possibility of defining optical elements according to their true structure is a significant advantage over scalar methods, a feature of FDTD not apparent in the above depictions is that the discrete sampling of the surface of a component, such as a lens surface or horn antenna wall, results in a representation of the surface by continuous lines which will deviate from the ideal description of the surface. However, with the extremely fine sampling rate required in the algorithm this effect will only cause noticeable discrepancies in the calculation of fields at surfaces with extremely small radii of curvature.

As explained in all introductory literature relating to the finite-difference time-domain algorithm, it is always suggested that the technique is suitable only for "electrically small" regions, i.e. volumes or areas only two or three times the order of the wavelength. With such unavoidable computational restrictions on the distance from the source at which the field can be predicted directly, one must use a suitable technique in calculating the far-field scattering effects based on the near-field electric field structures calculated by FDTD. Numerical techniques to perform this are referred to as "far-field transforms" and there are a variety of approaches described in the literature, often applied to the study of scattering effects of various materials [GON00, KUNZ93]**.** Here, the accuracy of the non-paraxial Gaussian beam mode analysis, shown in the previous section, could suggest its use as a simple but very efficient approach of far-field calculation from the FDTD predictions of electromagnetic fields derived from horn antennas.

2.9 - Conclusion

The properties of diffractive effects in basic optical arrangements have been presented in terms of the Fourier/Fresnel theory of diffraction and its representaion through the method of Gaussian beam mode analysis (GBMA) using orthogonal Laguerre-Gaussian and Hermite-Gaussian functions. Comparison of the two methods shows complete agreement within a predictable finite transverse range, with the advantage of the GBMA theory shown by a smaller number of integrations required and the synthesis of a field as an efficient finite term series.

The application of the Fourier transform and Gaussian mode expansions in optical diffraction calculations has been exhibited. In the case of the Fourier transform, the optical information is contained in the transform data itself, i.e. far-field diffraction patterns are related to the Fourier coefficients of the aperture function. Whereas with

Hermite-Gaussian calculations the optical information is not obtained directly from the expansion coefficients, rather they are used to weight a convergent series from which diffraction effects are computed, akin to the Fourier series expansion of a function.

For the problem of diffraction at a circular aperture, simplified expressions for the calculation of the mode coefficients were derived and extended to the focusing of plane waves by a thin lens. Such expressions rely on only one numerical integration and common recurrence relations can be then used to derive coefficient values. This can be an even more accurate calculation when using Mathematica™, as that software package appears to have difficulty integrating high frequency functions such as the HG and LG modes of higher indices.

While this thesis is concerned mainly with optical diffraction techniques applied within the validity of the paraxial approximation, the author has described methods for the calculation of widely diverging electromagnetic fields that cannot be analysed by the Huygens/Fresnel theory of optical diffraction. With direct relevance to the modal method of diffraction calculation described in this thesis, the author has shown how recently derived expressions for the propagation of Gaussian beam modes beyond the paraxial limit can be used to accurately describe the far-field diffraction of arbitrary fields in a similar fashion to the convention paraxial technique. As far-field calculations have high importance in the analysis of millimetre and terahertz antennas, this method has the potential be a very efficient and accurate method for far-field calculations within such wavebands, but further work will be required to achieve its full potential as a complete technique, particularly in understanding the limitations of the expressions due to the approximation used in eq. (2.46).

The finite-difference time-domain algorithm has been described as a method for solving Maxwell's equations directly. While inevitably time-consuming in comparison with the modal synthesis of optical fields, the technique is directly suited to the determination of electromagnetic behaviour involving the interaction of fields with complicated structures and media. Several commercial software packages, for example HFSS™ [HUA08] and CST Microwave Studio™ [*http://www.cst.com*], have been used in the NUIM mm-wave group for the electromagnetic analysis of millimetre wave sources using methods similar to FDTD. HFSS is based on Finite Element models, while CST Microwave Studio™ employs a finite-*integration* technique, which uses a similar grid scheme to that of FDTD but instead employs the Yee's grids to evaluate an integral form of Maxwell's equations [CLE01]. Also, the well documented free FDTD

package “MEEP”, developed by researchers at MIT, is a flexible program and ideal candidate package for analysis of millimetre wave receivers and transmitters [OSK10]. However, the simplicity of the FDTD procedure allows for researchers to generate custom written code, with equally accurate results.

Finite-difference time-domain is far from being a standard technique in mm-wave research, but the calculations shown in this chapter exhibit how a rigorous analysis of electromagnetic structures is possible without the excessive financial costs of software packages, which may ultimately lack transparency to the user. FDTD is also becoming a widely applied numerical tool in Geophysics for the simulation of earthquakes, and the procedure has been suggested within that field as “the future of Seismology?” [SHE09]. With powerful computing capabilities becoming more affordable, and in particular the growing use of graphics processing units in scientific computing, the proposal that FDTD is the future of electrodynamics does not lack merit.

Chapter Three

Hermite - Gaussian Modal Expansion of Far-Infrared Digital Holograms

3.1 – Introduction to holography

In general, methods of far-infrared imaging require direct measurement of physical intensity distributions obtained using conventional optical techniques using lenses and mirrors. In this chapter we present work undertaken in the application of *digital holography* at 100 GHz. Rather than recording an image directly, the method involves the measurement of data from which the image data is then extracted using numerical representation of the diffraction process,[HAR02].

In the science surrounding electromagnetic radiation, given the enormity of the frequencies of light, an averaged value of the intensity $|E|^2$ of an oscillating field over a significant time is usually the only possible measured quantity, either by direct observation with the eye, photographic recording, or electronic detection. However, in optical imaging systems intensity measurements of diffracted fields are generally of little use in obtaining information about the source of the radiation (object), for we cannot comment on the course of a field based solely on the intensity measurement due to the diffraction which occurs between the object and the recording plane. Without knowledge of the phase properties of the beam no comment can be made about the direction of the field, its divergence, or convergence, or the amplitude structure at the source plane.

In an attempt towards solving the problem of phase retrieval from intensity measurements only, the Hungarian scientist Dennis Gabor invented the method of holography in 1948 [GAB48]. An alternative name for the technique originating in the 1960's, *wavefront reconstruction*, is perhaps a more descriptive label for the technique in which the recording and subsequent retrieval of the phase, and therefore the direction, of the diffracted radiation is possible. Gabor's method involved the superposition of a scattered field, the *object beam*, the imaging of which is desired, with another field defined as the *reference beam,* the properties of which are known or are easy to replicate in an experimental scene. Through his seminal 1948 paper Gabor proposed,

and proved experimentally that by recording such an interference structure (*hologram*) on a photographic plate, and illuminating the recorded hologram with the original reference beam, one could reconstruct exactly the behaviour of the object beam thus allowing for viewing of the original target. The figure below shows images obtained through the use of Gabors original inline method.

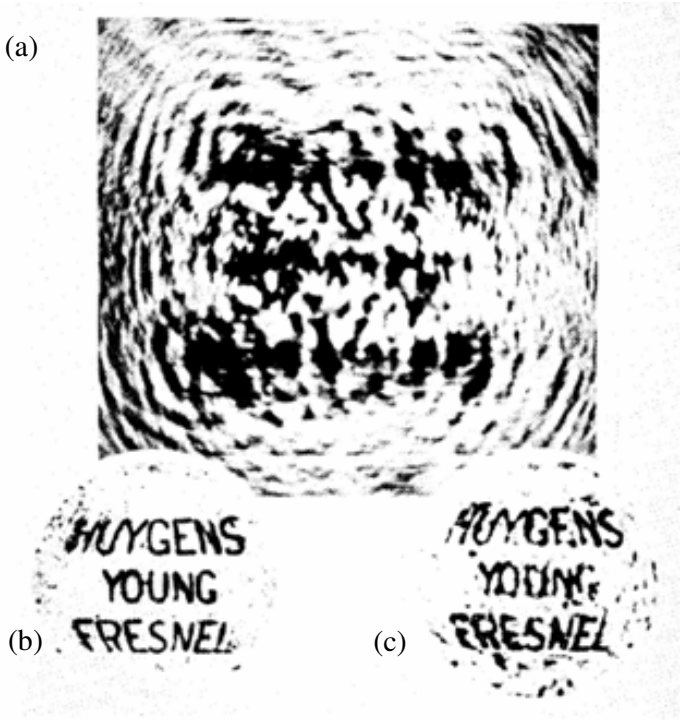

Figure 3.1 - One of the first published results of wavefront reconstruction by Gabor. (a) The recorded hologram, (b) the object, (c) reconstructed image.

However, Gabors original method went unnoticed for two reasons:

1) In order to form a clear interference pattern, the radiation used must have a high degree of temporal coherence, i.e. the interference pattern remains constant over time. Although the mercury arc lamp used by Gabor had a relatively narrow bandwidth compared to other light sources available at the time, his original imaging results, in Figure 3.1 (c), show that improvements to his technique were desired.
2) Gabors original design of a holography experiment involved a simple on-axis optical arrangement. Thus, the multiple diffraction orders caused by the hologram resulted in a superposition of the desired image field with the transmitted zeroth order reference beam, restricting the imaging capability.

It was almost fifteen years before Gabors technique would gain significant attention with the invention of the laser. Through the work of Emmet Leith and Jurith Upatneiks at the University of Michigan, a new field of optical research was founded by the publication of their paper "*Wavefront reconstruction with Diffused Illumination and Three-Dimensional Objects"* [LEI64]. That publication described an optical arrangement using the then newly invented Laser which enhanced Gabor's original design through the long coherence length of the source and the novel idea of an obliquely incident reference beam which could separate the transmitted reference beam from the reconstructed object wave to allow for clear viewing of the object image without obscuration by the reference beam. A typical modern arrangement of hologram formation in the visible band is shown in Figure 3.2.

The form of holography described by Leith and Upatneiks and throughout this chapter is known as *transmission holography*, referring to the fact that reconstruction of the three-dimensional images are formed by the direct transmission of a reference beam through the photographic plate (hologram). This is in contrast to *reflection holography* where the object beam and reference beam are incident upon the recording medium from opposite sides, and for the reconstruction process the image is viewed from the same side of the hologram as the source of the reference beam. This is the most popular and commercial form of that non-scientists would be familiar with, and is used as a media application more often than a scientific technique.

One of the advantages of holography is the fact that while lenses and mirrors are used in the generation of both the object and reference beams as shown in Figure 3.2, the imaging process is not reliant on any focusing elements (with the exception of the human eye), thus eliminating any aberrations or other imperfections in the reconstructed image. The term *lensless* is often used to describe such imaging techniques, and this feature is a main reason for research into the application of holography.

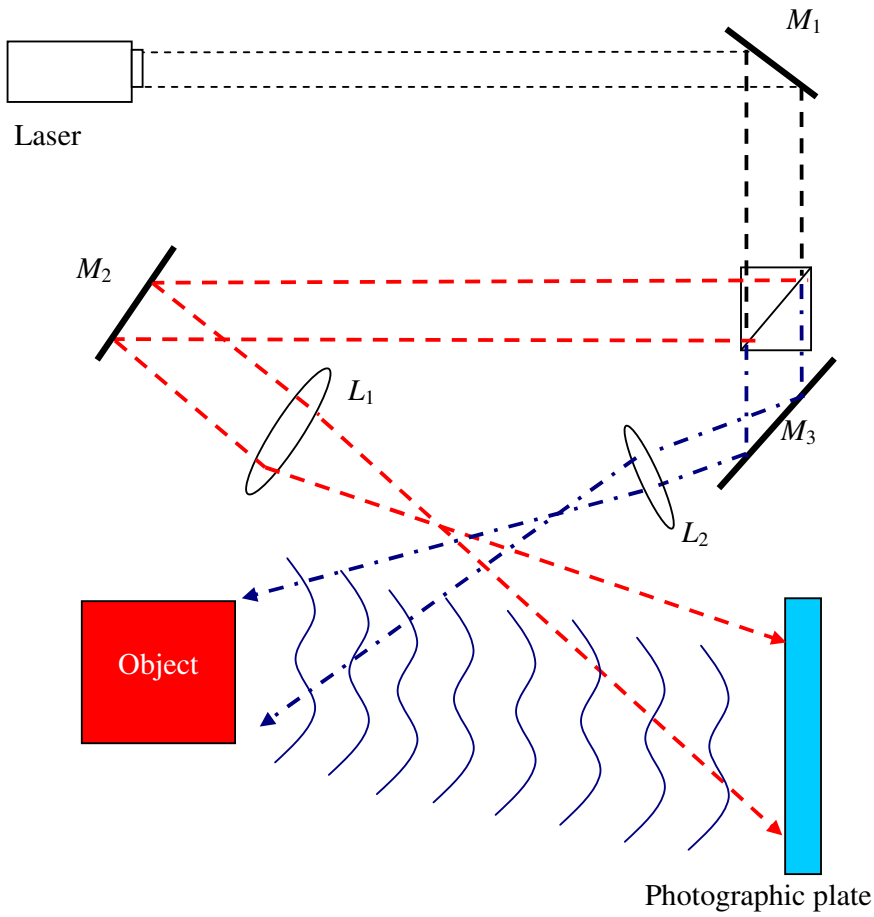

Figure 3.2 - A typical optical layout for the formation of a transmission hologram. L_1: Reference lens, L_2: Object lens, M_2: Reference mirror, M_3: Object mirror. The reference beam is shown in red and the object beam in blue.

The process of image reconstruction by holography is mathematically straightforward, and is described as follows. At the plane of the hologram, the object and reference beams, defined here as being linearly polarised, take the respective forms of

$$E_O(x_0, y_0) = O(x_0, y_0)\exp(i\phi_O) \tag{3.1}$$

$$E_R(x_0, y_0) = R(x_0, y_0)\exp(i\phi_R) \tag{3.2}$$

where ϕ_O and ϕ_R are the phase of the object and reference beams at the plane of the hologram recording respectively. When both waves interfere, their interaction is described by the resulting intensity calculated as

$$
\begin{aligned}
h(x,y) &= \left|E_O + E_R\right|^2 \\
&= \left|O(x_0,y_0)\exp\left(i\phi_O(x_0,y_0)\right) + R(x_0,y_0)\exp\left(i\phi_R(x_0,y_0)\right)\right|^2 \\
&= \left(O\exp\left(i\phi_O\right) + R\exp\left(i\phi_R\right)\right)\left(O\exp\left(-i\phi_O\right) + R\exp\left(-i\phi_R\right)\right) \\
&= \left|O\right|^2 + \left|R\right|^2 + OR\exp\left(i\phi_O - i\phi_R\right) + RO\exp\left(i\phi_R - i\phi_O\right) \qquad (3.3)
\end{aligned}
$$

and this quantity represents the actual measured hologram. When recorded at visible wavelengths the strength of the hologram is dependant on the duration over which the photographic plate is exposed to the radiation but with electronic detection by a diode detector this factor can be neglected.

The method by which a holographic image is viewed is termed *reconstruction* and is achieved through illumination of the recorded hologram with the original reference beam, which is represented mathematically as

$$E_I = E_R(x_0,y_0)\,h(x_0,y_0)\,.$$

Reconstruction of images is achieved by illumination of the recorded interference pattern with the original reference beam E_R.

$$E_I(x_0,y_0) = E_R\ h = E_R\left(\left|O\right|^2 + \left|R\right|^2\right) + \left|R\right|^2 O\exp\left(i\phi_O\right) + \left|R\right|^2 O\exp\left(2i\phi_R - i\phi_O\right).$$

When this multiplication is performed the result defines the presence of three optical fields at the plane of the hologram, each representing independent fields :

$$
\begin{aligned}
E_I(x,y) &= E_I^{(1)} + E_I^{(2)} + E_I^{(3)} \\
E_I^{(1)} &= E_R\left(\left|O\right|^2 + \left|R\right|^2\right) \\
E_I^{(2)} &= E_O\left|R\right|^2 \\
E_I^{(3)} &= E_O^*\left|R\right|^2\exp\left(i2\phi_R\right)
\end{aligned}
$$

Figure 3.3 illustrates the physical meaning of each term.

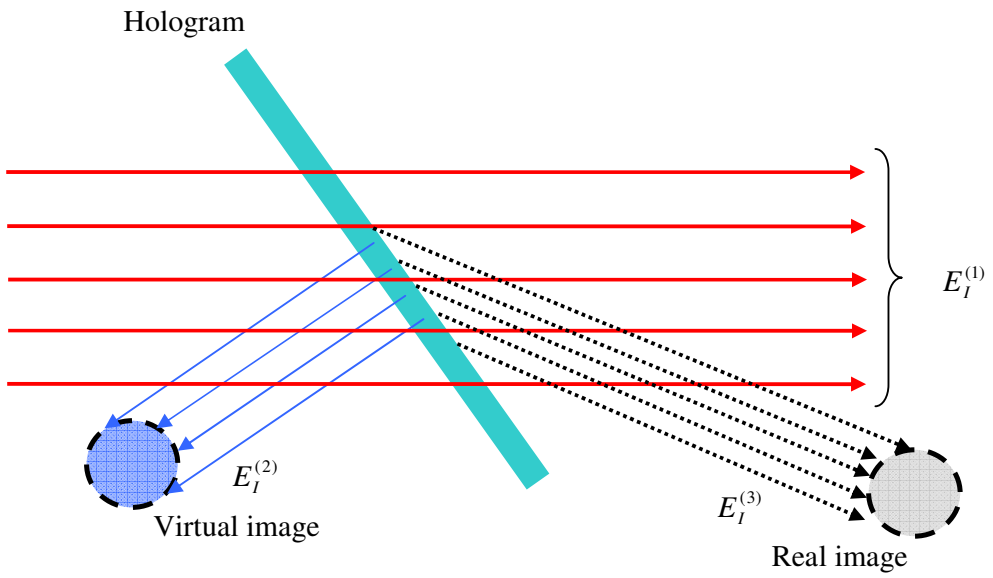

Figure 3.3 – Reconstruction of images from a transmission hologram with an off axis reference beam.

The first term $E_I^{(1)}$ defines the propagation of the reference beam through the hologram. The second term $E_I^{(2)}$ is the most important, and contains the desired information of the object field which is obtained by viewing the hologram from the side opposite the original object. $E_I^{(3)}$ signifies the formation of a conjugate real image which has an angular separation from the optical axis twice that of the reference beam.

The experimental process of holography to be presented in this chapter relates to the detection of radiation and subsequent image retrieval, using the numerical techniques of diffraction to simulate the image formation. However, in a reversal of the process the method can be used to generate a desired amplitude structure. This involves the numerical design of a *computer generated hologram* (CGH), a synthesised interference pattern which when realised and illuminated by a wave of the correct form will produce a desired image/field at a certain plane. At millimetre wavelength an example of this work is given in [MEL03] where the authors describe the measurement of a large scale CGH for operation at 310 GHz in a compact antenna test range. The results presented show that the formation of complex amplitude structures is possible, but perhaps the most practical application for antenna testing may be the use of CGHs in generating an approximate localised plane wave with uniform amplitude and phase in the far-field of the component, as shown in Figure 3.4.

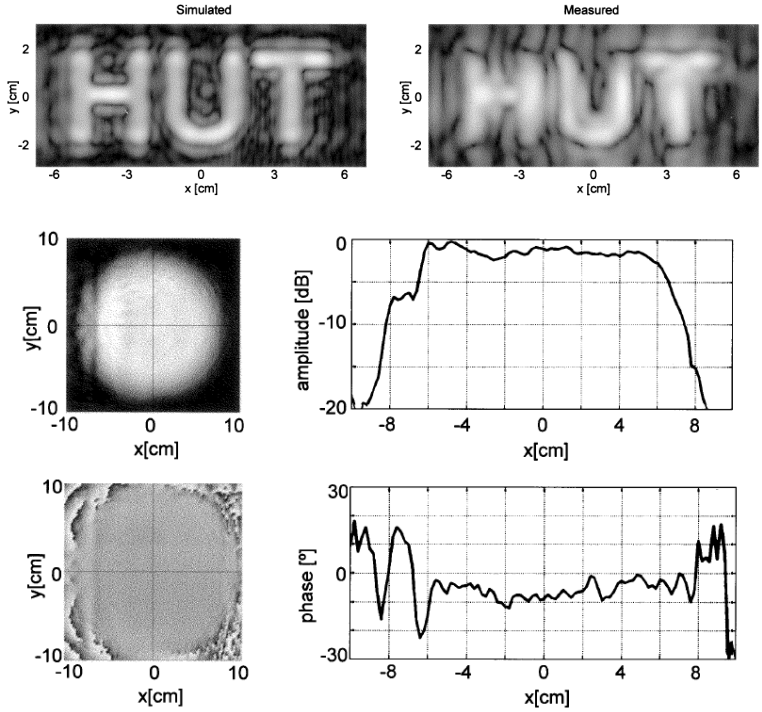

Figure 3.4 - Results of beam formation using computer generated holograms at 310GHz, in [MEL03] Comparison of simulated and measured data of structured field. Ampliude and phase of a beam approximating a plane wave generated with a CGH.

The results shown above are derived from the testing of computer generated holograms where the field incident on the hologram has its field modulated in terms of its amplitude only. A phase modulation can be included in such optical elements by adjusting the position of transparent cells so as to modify the relative phase at a point on the reconstruction plane, [LOH68]. The holographic element can also be purely phase modulating. By applying the Gertchberg-Saxton algorithm the desired intensity distribution at a plane can be related to the required phase distribution at the source of a field [GER72]. By repeated simulation of the propagation of the field between the two planes, optimisation techniques can be used to determine the most appropriate phase structure for generation of the desired field. This algorithm has been applied to the millimetre wave band by [GRAF01] and [MAY08] with the prospect of applications for radio telescope receivers.

3.2 - Digital holography

The two-step physical process of recording and viewing an optical hologram can be reduced through the measurement of a hologram by electronic means instead of the photographic recording methods that were conventionally used. While the layout of the optical system used to form the holograms can remain the same for both photographic and electronic recording methods, a digital measurement of the hologram structure can allow for reconstruction of the desired image with numerical simulation of the image formation through the methods outlined in chapter 2.

This process of *digital holography* has several advantages over the photographic form of the reconstruction technique in that the measurement of a digital hologram can allow for further analysis of the recorded data. For example, the technique of double exposure interferometry is often used in the analysis of materials to examine the effects of deformation by an applied force. By recording digital holograms before and after the application of a load on an object, the fringe pattern formed by the interference of the image fields obtained from both holograms can be analysed to gain information about the deformation. With photographic holography, the interference of both images has to be determined visually from the reconstructed images, whereas with the technique of digital holography such images can be manipulated digitally, allowing for analysis of the retrieved data.

The idea and experimental verification of the digital recording of a hologram and the reconstruction of images using numerical simulations of diffraction was first proposed in [LAW67]. However, it was a paper by *Schnars and Jueptner* in 1994 that launched the technique as a huge field of research [SCH94]. In that publication, the authors suggested that instead of using a photographic plate as a hologram and optical reconstruction methods, CCD detectors could be used to record the intensity pattern of a hologram while digital simulation of the diffraction effects could reconstruct the desire image. This allows for storage and manipulation of the hologram and a fast computational reconstruction of the image without the photographic development of photographic plates as used in traditional holography.

In Fourier holography, the reference beam may be generated by a point like source, in most cases a pinhole located the same distance from the hologram as the object. This allows for simplified reconstruction, where knowledge of the reference beam is not required as a direct Fourier transform of the measured data can separate the relevant spatial frequency components for image reconstruction. With photographic

transmission holograms, the reconstruction procedure recovers an image precisely with a viewer having great difficulty in identifying if indeed the image is holographic or physically real. With digital holography there is obviously a loss of the parallax effect and realism due to the 2D nature of the reconstruction, however, the image resolution promised by the theory has led to great interest in the application of the technique [COL02].

Dr. Thomas Naughton of the Department of Computer Science at NUI Maynooth is one of the leading researchers in the field of digital holography within the visible band. An experimental result from his work is exhibited below.

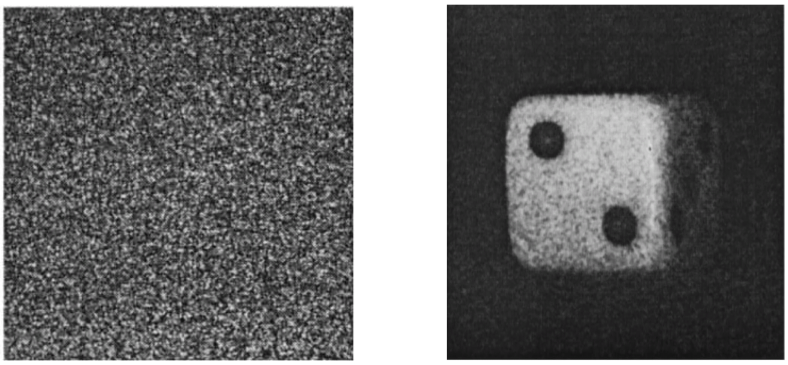

Figure 3.5 - (a) Visible wavelength digital hologram recorded on a CCD camera and (b) digital reconstruction. Reproduced from [NAU02].

Gabor's original interest in holography was based in the potential use of the techniques use in electron microscopy, and while the technique has evaded significant application in that area, optical microscopy using digital holography is a technique which has begun to be commercialized, and promises improvement over conventional techniques due to the lack of aberrations in construction of the image. Figure 3.6 shows an example of microscopy by holography, from [GAR08], where the technique was used to visualise fluid flow on the micron scale in real time.

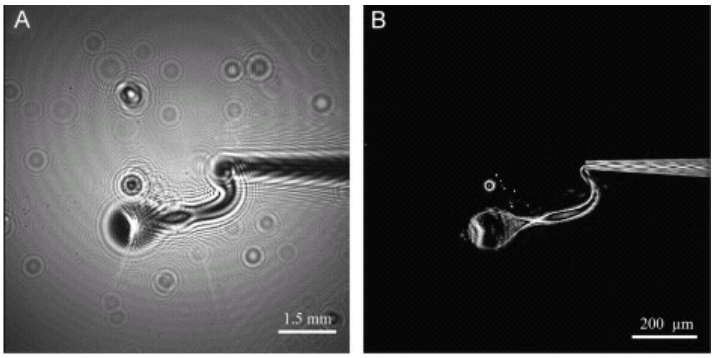

Figure 3.6 – (a) Hologram of fluid flow (b) Reconstruction of the microscopic image by holography, from [GAR08] .

Holography was initially developed for application at visible wavelengths, and the application of the technique has, for the most part, been in that band of the spectrum. But the theory of the optical processes involved in holography are not limited to visible optics but can be, in theory, applied to any wave phenomenon and there has therefore also been significant research into the use of holography with radiation outside of the visible part of the electromagnetic spectrum, and indeed with non-electromagnetic waves.

One recent application of wavefront reconstruction was highlighted on the front cover of the journal *Nature,* in the paper by *Eisebitt et. al.* [EIS04]. The authors described a digital holography arrangement for the imaging of objects on the nanometer scale using X-rays. As demonstration, an amplitude mask was used to generate both the object and reference beams, with the reference field created by an off-axis point source generating an off-axis spherical reference wave, which is the definition of a Fourier hologram. Images obtained using this system are illustrated in Figure 3.7.

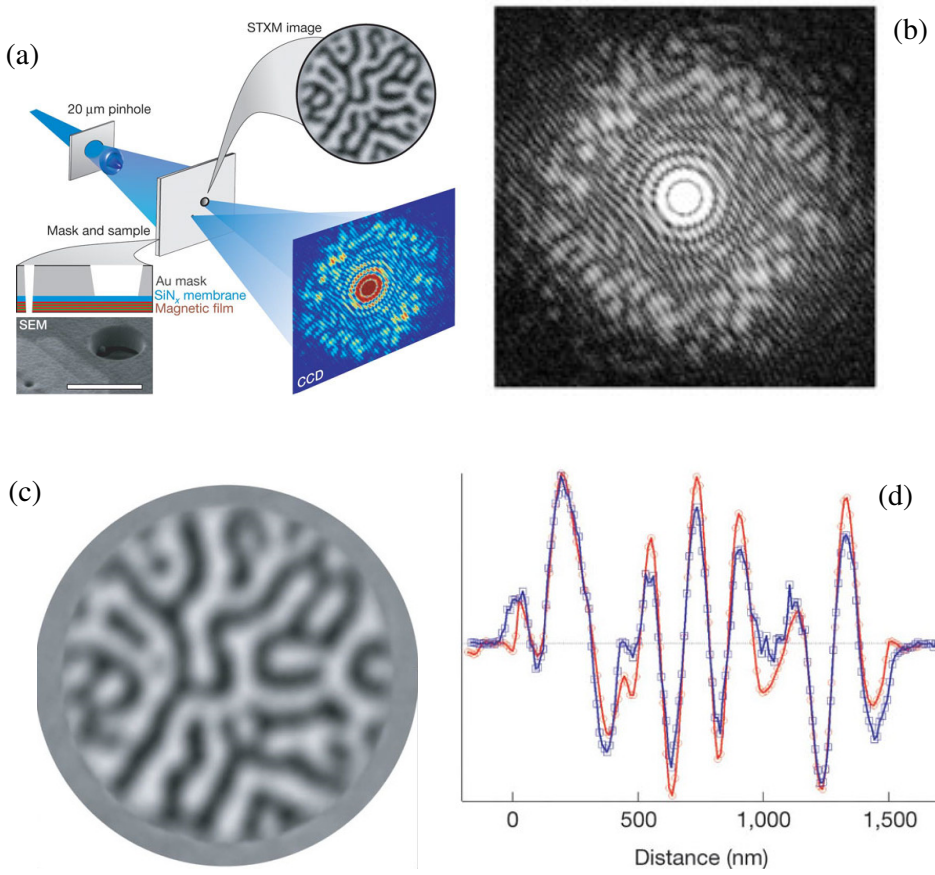

Figure 3.7 – Data from Eisebitt et. al. [EIS04]. (a) Illustration of experimental layout. (b) The recorded hologram, (c) the reconstructed image, and (d) A comparison of the reconstructed image with a direct measurement of the object, the blue line shows the reconstruction from the digital hologram.

The resources required by the group developing this technique were beyond the capabilities of standard laboratories, with the project involving the use of the Advanced Light Source at Berkeley, California, and complicated nano-fabrication techniques used in creating the object. At the opposite side of the visible band from X-rays, with longer wavelengths the application of holography is a much more approachable undertaking.

For near infra-red radiation with wavelengths only up to one order of magnitude greater than visible laser light, the process of infra-red digital holography could potentially be carried out with the same optical arrangement and components as a visible band setup, with the exception of altering the source of coherent radiation and detector. *Allaria et. al.* [All03] carried out research into the use of directly recorded digital holograms using a CCD camera responsive to near infra-red radiation at $\lambda = 10.6$ µm, with a camera having 124 × 124 pixels each covering an area of 85×85 μm^2. The

spatial resolution possible in this case is similar to the resolution at visible wavelengths with standard CCD technology, and such coarse sampling restricts the angle of the reference beam to large angles in relation to the detection plane to allow for measurement of the fringes formed by the interference. The recorded data and reconstructed images are shown in Figure 3.8.

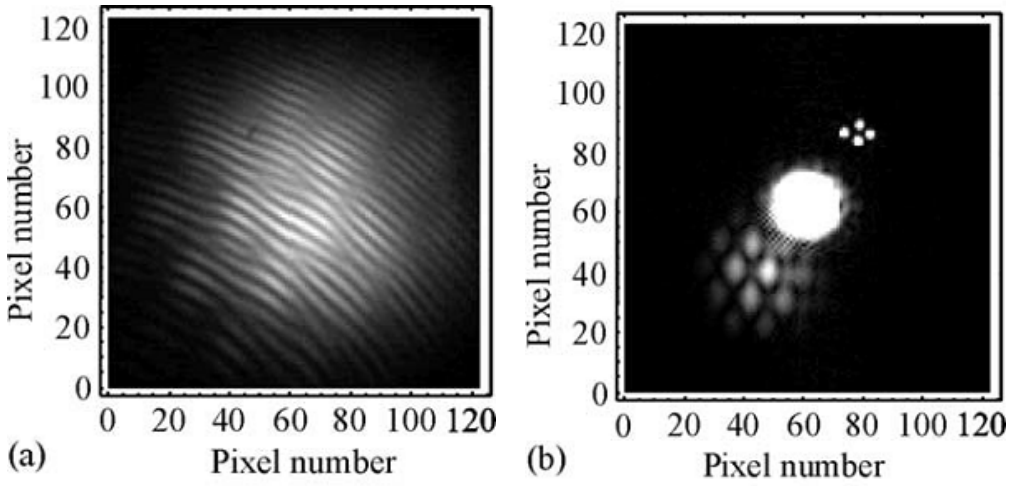

Figure 3.8 - (a) Hologram, and (b) reconstruction of recorded data showing image of object in the upper right hand side. Reproduced from [ALL03].

Using radiation within the same region of the EM spectrum as the work of [ALL03], [MIY07] reports a system that uses two bands of EM radiation, with electronic technology related to the visible region alongside physical processes particular to the infra-red band to measure diffraction effects. The group used a material called nitroanisole which displays a thermal lens effect in which the refractive index is proportional to the temperature change induced by the intensity and duration of infrared radiation incident upon it. By examining the phase distribution of visible light modulated by the nitroanisole, i.e. by recording a visible wavelength digital hologram of the material, the phase properties of the diffracted infra-red radiation can be recovered. See Figure 3.9.

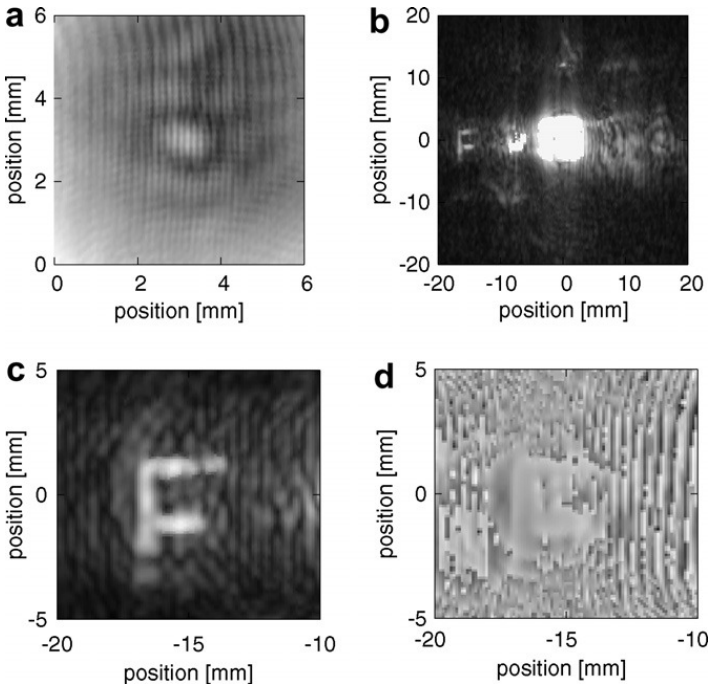

Figure 3.9 - Experimental results of Miyamoto et. al. (2007). The figure shows (a) The recorded hologram. (b) Reconstruction by FFT of the image plane. (c) Close up of object reconstruction in (b), and (c) the phase of the reconstructed object field.

The digital holography technique has also been applied in acoustic imaging where energy is propagated by pressure variations. Brenden described the recording of holograms of objects submerged in water by photographically capturing the interference pattern of the acoustic reference and object beams formed on the surface of the water, and then applying a numerical reconstruction to obtain the desired image [BRE75].

The work summarised in this section shows the trend of applying digital holography to radiation, and other wave variations, beyond the conventional visible band, and also presents the generality of the holographic procedure.

3.3 - Numerical reconstruction of digital holograms

In the previous chapter the author described several methods, with varying degrees of accuracy, which can be used to simulate the phenomenon of diffraction. Conventionally, the numerical image formation from the measured hologram data is performed by the Fresnel diffraction integral, which can be accelerated with application of the fast Fourier transform (FFT). Although we have shown the paraxial diffraction methods to be an approximate model for the physical propagation of EM waves, this

chapter serves as a further example of how the Fresnel formulism, and paraxial techniques in general, can give an excellent description of the behaviour of waves in practical applications. The figure below describes the coordinate system used in our description of the holographic process.

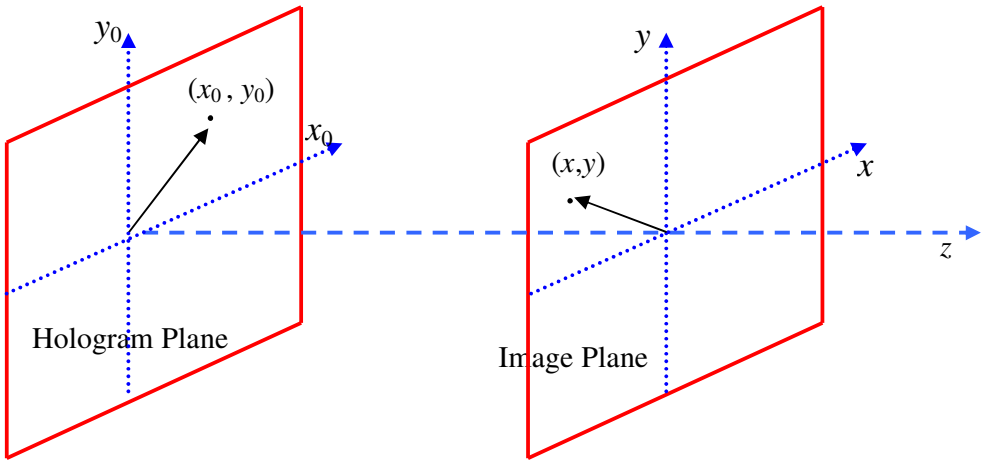

Figure 3.10 – Schematic of the coordinate system used in the numerical reconstruction of digital holograms.

In reconstruction of waves diffracted by rectangular apertures, such as digitally recorded holograms, the diffracted field can be determined from the Fresnel diffraction integral [GOO05].

$$E_I(x,y,z) = \frac{i}{\lambda z} e^{-i\frac{\pi}{\lambda z}(x^2+y^2)} \iint_{x_0,y_0} E_R(x_0,y_0) h(x_0,y_0) e^{-i\frac{k}{2z}\left(x_0^2+y_0^2\right)} e^{-i\frac{k}{z}(x\,x_0+y\,y_0)} dx_0\,dy_0$$

While direct numerical calculation of this integral is not a difficult task, its solution can be simplified and greatly accelerated by recognising that the double integral on the right-hand side of the equation can represent a Fourier transform of the function $E_R(x_0,y_0)h(x_0,y_0)\exp\left(-i\,k\,(x_0^2+y_0^2)/2z\right)$. Thus, the diffracted field can be calculated as

$$E_I(x,y) = \frac{i}{\lambda z}\exp\left(-i\frac{k\,(x^2+y^2)}{2z}\right) F\left\{E_R(x_0,y_0)h(x_0,y_0)\exp\left(-ik\frac{\left(x_0^2+y_0^2\right)}{2z}\right)\right\} \qquad (3.4)$$

where again F represents a Fourier transformation, which will be calculated numerically using the fast Fourier transform. Comparing the second exponential term of the diffraction integral with a complex Fourier component

$$\exp\left(i\frac{k}{z}(x_0 x + y_0 y)\right) = \exp\left(ik_x x_0 + ik_y y_0\right)$$

we can calculate the spatial Fourier frequencies in the image plane as

$$k_x = k\frac{x}{z}, \text{ and } k_y = k\frac{y}{z} \tag{3.5}$$

In practical terms, these relations are important as they allow for transformation of the array indices of the Fast Fourier transform data into more useful spatial co-ordinates. Digital holography is one field of research that has had huge benefit through the application of the fast Fourier transform, and throughout the literature on digital holography, the theories invariably involve the application of that algorithm. For example, an alternative formulation frequently presented in the literature describes the reconstruction as a convolution process. The Fresnel integral given above is a binomial (paraxial) approximation to the following equation

$$E_I(x,y) = \int_{-\infty}^{\infty}\int_{-\infty}^{\infty} h(x_0,y_0)E_R(x_0,y_0)g(x,y,x_0,y_0)dx_0dy_0$$

where

$$g(x,y,x_0,y_0) = \frac{i}{\lambda}\frac{\exp\left(-ik\sqrt{(x-x_0)^2+(y-y_0)^2+z^2}\right)}{\sqrt{(x-x_0)^2+(y-y_0)^2+z^2}}$$

This integral can described as a superposition integral, with *g* referred to as the impulse response. Using the well-known convolution theorem [WEI02], it can shown that the Fourier transform of the convolution of the two functions is equal to the product of the Fourier transforms of the individual functions i.e.

$$p(x,y) \otimes q(x,y) = F^{-1}\{P(k_x,k_y)Q(k_x,k_y)\}$$

where *P* and *Q* are Fourier transforms of the two functions *p* and *q* respectively.

For a numerical implementation with application to discretely sampled data, the impulse response $g(x,y)$ is expressed in terms of the indices of a square array (m,n) (with N^2 elements and pixel separation of Δx and Δy in the horizontal and vertical directions respectively) as

$$g(m,n) = \frac{i}{\lambda}\frac{\exp\left(-ik\sqrt{\left(m-\frac{N}{2}\right)^2\Delta x^2+\left(n-\frac{N}{2}\right)^2\Delta y^2+z^2}\right)}{\sqrt{\left(m-\frac{N}{2}\right)^2\Delta x^2+\left(n-\frac{N}{2}\right)^2\Delta y^2+z^2}}$$

The reconstruction at the image plane can then be calculated by

$$E_I(x,y) = F^{-1}\{F\{h(x_0,y_0)E_R(x_0,y_0)\}\times F\{g(x_0,y_0)\}\}$$

The Fourier transform of $g(m,n)$ can be expressed analytically as [SCH04]

$$G(m,n) = \exp\left\{ i k_0 z \sqrt{\frac{\lambda^2\left(m+\frac{N^2\Delta x^2}{2\lambda z}\right)}{N^2\Delta x^2} - \frac{\lambda^2\left(n+\frac{N^2\Delta y^2}{2\lambda z}\right)}{N^2\Delta x^2}} \right\}$$

which is useful, reducing the number of times that the FFT has to be applied. Therefore the amplitude in the image plane of the hologram can be determined from

$$E_I(m,n) = F^{-1}\{F\{h(m,n)E_R(m,n)\}G(m,n)\} \tag{3.6}$$

An advantageous and direct consequence of this convolution method is that the simulated reconstruction plane has the same spatial dimensions of the hologram plane, allowing here for viewing of the on-axis object, also the image field will have the same resolution as the measured interference pattern. This may have to be modified depending on the optical layout, but in the system we employ this was a convenient feature of the method. This is in contrast to the Fourier transform method where scaling techniques may have to be used to obtain an image with sufficient resolution.

In the following sections, we will describe the use of a proof-of-concept digital holography arrangement for operation at millimetre wavelengths, specifically 100GHz, and apply these numerical procedures discussed in this section to experimental data. While the primary intended application of the technique is through its imaging capability, the process of phase retrieval could also allow for an efficient and inexpensive method of phase measurement of antenna fields.

3.4 - Digital holography at millimetre wavelengths

Direct phase measurement at millimetre wavelengths is a more viable endeavour than at lower frequency bands of the electromagnetic spectrum. The vector network analyzer (VNA) is a system commonly used in antenna testing and provides the possibility of phase measurement, giving complete knowledge of a field. However, the financial expense of these complex devices does inhibit their widespread use.

Sheen et. al. at the Pacific Northwest National Laboratories (PNNL), have developed a fully operation personnel scanner with intended operation in airports and other areas where objects and people are prone to scrutiny. As is obvious from the

descriptions given above, the imaging process used in the NUIM system which is based entirely on photonic techniques, whereas the holographic, or phase-retrieval techniques used at PNNL are based on the direct measurement of phase using electronic techniques whereby phase can be measured directly without the need for a reference field [SHE01].

We will describe the use of a basic millimetre-wave digital holographic system developed by the author and co-workers, based on optical phase retrieval, and the theories of reconstruction that can be used in such a technique. In particular, the application of Hermite-Gaussian beam mode analysis to image formation by holography will be presented. Imaging results obtained using this system has previously been presented in [MAH06]. The layout for a millimetre-wave holographic system, with the intention of measurement of beams that could be regarded as being generally on-axis, is shown in Figure 3.11.

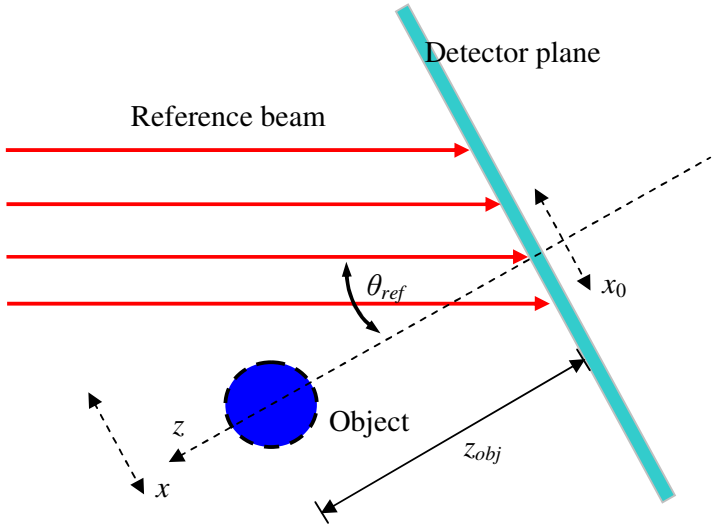

Figure 3.11 - General schematic of the holography arrangement used.

For our optical setup, a reference beam with a large angular separation, θ_{ref}, between itself and the object beam was used, which would separate the object and reference wave vectors allowing for greater distances over which the field and the reconstructed image of the object would not be obscured, a frequent problem with conventional DH. In addition, to reduce the range of Fourier coefficients in the reference field and allow for more accurate determination of the angle of incidence, a plane wave approximation generated using a collimating mirror was considered most appropriate, producing a beam at the hologram plane with a phase of the form $\phi_R(x)=kx\sin\theta_{ref}$, θ_{ref} being the horizontal angle of incidence of the reference beam in

relation to a normal of the hologram plane, assuming in this description that there is no angular incidence in the vertical plane, which is viable given the optical arrangement. There are advantages for the use of digital holography at millimetre wavelengths, because the intensity of a field can be recorded with high sub-wavelength resolution. This is in contrast to the same process with light in the visible band, where CCD cameras are only beginning to gain the necessary pixel sizes to record spatially small fringe separations which are inevitable with a large reference angle and short wavelengths. This is the major restriction to the further development of digital holography in the visible band, like most areas of physics where the theory surrounding an application predates the available technology.

3.4.1 - Hologram measurement system

The electronic system used for measurements in this thesis is that developed by William Lanigan [LAN98]. The mechanical element of the arrangement consists of two stepper motors each controlling two belts which translate a stage on which a Schottky diode detector is mounted. Each motor controls the movement of the stage in the horizontal (x_0) and vertical (y_0) directions. The area and resolution of the scan can be adjusted by the user. The detector then moves horizontally from the origin to the left-most edge of the defined region and then moves down vertically in a continuous motion, recording a sample at each desired sample position. At the bottom of the scanning stage an LED sensor detects the presence of the detector at the vertical extent and the motors bring the detector back to the maximum vertical limit, the detector moves horizontally to the position of the next sample and continues with the next vertical scan, and so on, see Figure 3.12.

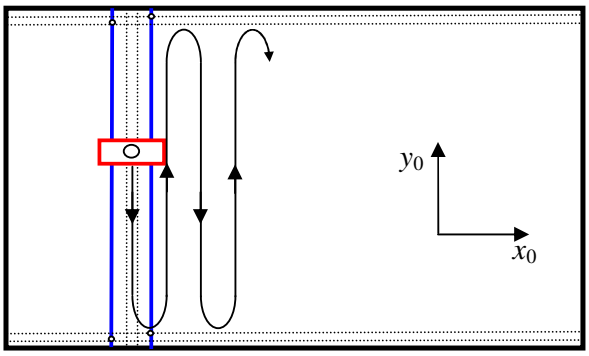

Figure 3.12 – The movement of the radiation detector used in the measurement of 100 GHz holograms.

A phase locking system allowing two different sources of mm-wave radiation is quite expensive and complicated, so in this work both the reference and object beams were derived from the same Gunn diode source. For generation of both object and reference beams, a 3 dB cross waveguide coupler was attached to the transmitting chain of a 100 GHz Gunn diode oscillator source thus eliminating the requirement for beam-splitter in the optical setup, as is usually done at visible wavelengths, and this allowed for a very compact source. A 3 dB cross-guide coupler is effectively an optical 2-channel multiplexing waveguide component, dividing the total Gunn output, with maximum power of approximately 35 mW, into two beams with equal powers. The reference beam was derived by placing the predicted phase centre of a conical corrugated horn at the focal plane of a parabolic mirror, which collimated the reflected beam with an angle of incidence of 45° to the hologram plane. See Figure 3.13.

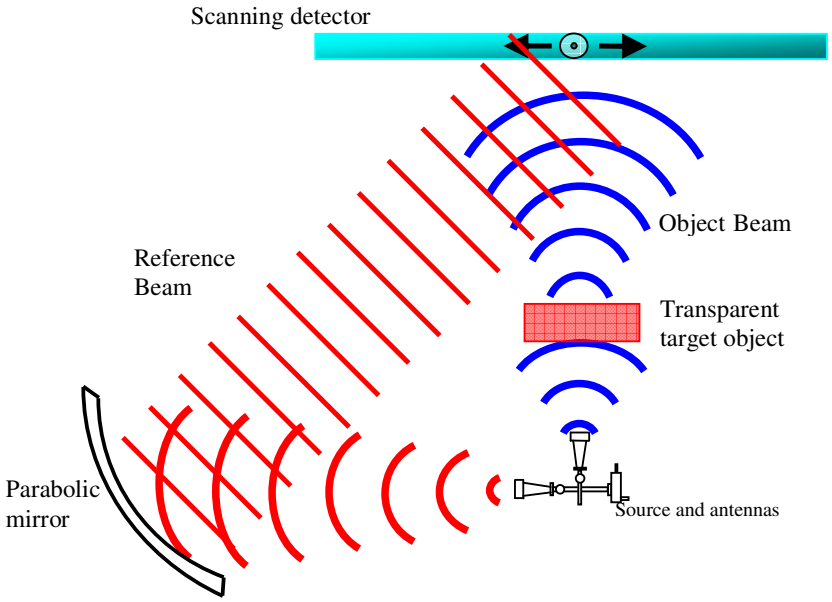

Figure 3.13 – Schematic of 100 GHz digital holography system.

The quantity

$$\frac{I_{\max} - I_{\min}}{I_{\max} + I_{\min}} \tag{3.7}$$

of an interference pattern defines its contrast (fringe visibility) where $I_{\max}$ and $I_{\min}$ are the maximum and minimum recorded intensities. The value of the contrast can greatly affect the quality of reconstructed images in a holography system. In the technique described here, a maximum contrast of unity was attainable through the adjusting of signal attenuators attached to the object and reference beam sources. Calculation of the

contrast value can only be calculated from regions of the hologram where obvious interference fringes are generated. Inclusion of areas with low or no recorded intensity is obviously invalid.

The movement of the detector along the vertical axis is continuous, thus changing the sample rate/resolution of a scan does not affect the duration of a single vertical line scan. The system allows for a measurement to be recorded every 100 ms which is suitable for the averaging of a steady signal. This time sample was typically used to minimise any effects of the continuous motion of the detector.

The photograph in Figure 3.14 shows the transmitting chain used in the holography arrangement. To eliminate any cross polarisation loss in the reference beam a cylindrical corrugated horn was used, and for the object beam, which would directly illuminate the object, or act as an object itself, a relatively small rectangular horn was used to ensure sufficient coverage of the object.

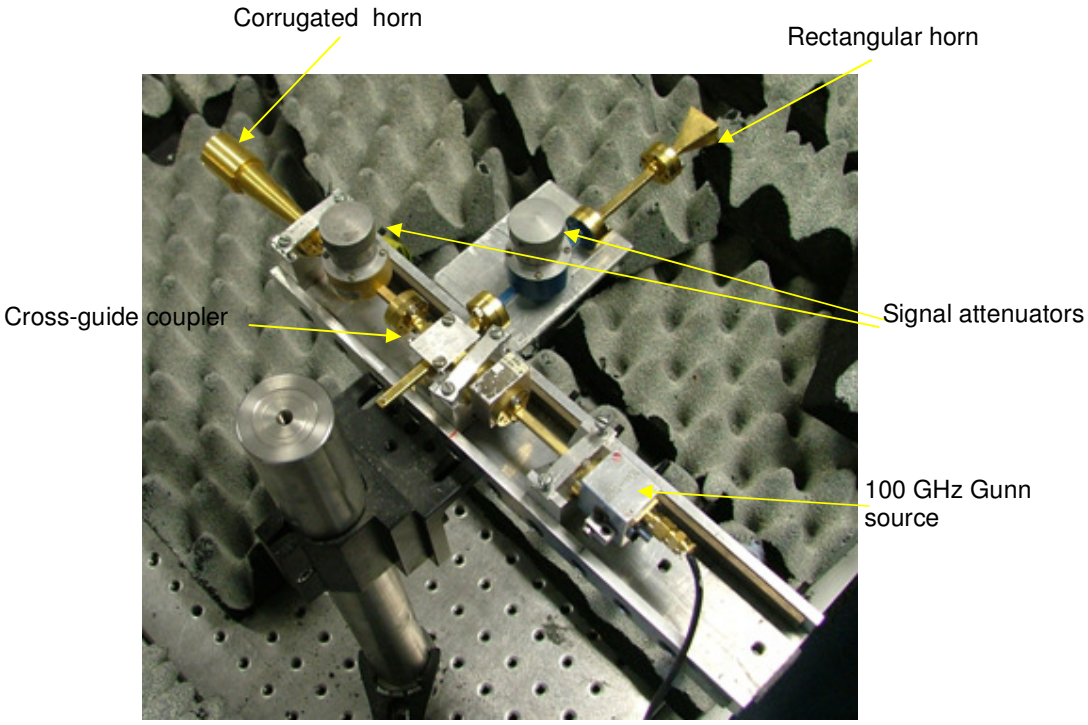

Figure 3.14 – Photograph of the 100GHz transmission chain used to generate the object and reference beams necessary for holography.

The software used to automate and synchronise the mechanical and electronic components is based in Labview™ allowing for a transparent setup of each measurement. The graphical user interface allows for arbitrary movement of the receiver with a digital readout of the signal strength which is useful in setting the position for the centre of the scan, particularly for recording Gaussian-like antenna beams where the position of the maximum intensity value should coincide with the centre of the scanned area. It must be said that the total time of a highly resolved scan is very long with most measurements recorded overnight. The detector itself is a Schottky barrier diode detector mounted with a beveled WR10 waveguide as the detector feed antenna.

3.4.2 - Frequency and sampling considerations

The reconstruction of holographic images using the Fourier transform immediately suggests that the range of spatial frequencies involved in the image formation is very important to the quality of the image obtained.

The spatial transverse wavenumbers k_x of a field at a recording plane are determined by the angle of incidence of the field at any given point. In the case of a parabolically diverging field with a wavefront $\exp(ikx^2/2z)$ the local angular frequency is $k_x = k\ x\ /\ z$. For an axially centred spherical wave at a distance z from the hologram plane the maximum range of frequencies, or bandwidth, Δk attainable over the measurement plane, is given by

$$\Delta k = \frac{2\,k\,a}{z} \tag{3.8}$$

Therefore an object that is located further from the hologram measurement plane will be more difficult to reconstruct as less Fourier frequencies will be detected at the hologram plane, and therefore less spectral components are involved in the image synthesis**.** Also, when illuminating an object that contains features that are small in relation to the wavelength diffraction into larger angles will occur requiring a larger recording area to sample the higher spatial frequencies in the scattered beam. Thus a Fourier representation of the scattered radiation will require larger spectral components to synthesise these finer details of the object. Clearly this limits resolution to approximately a wavelength as features smaller than this scatter the fields with large angles approaching 180°.

As an example a one dimensional interference pattern (hologram) of a spherical wave and a plane reference beam can be simulated with the equation

$$h(x) = \left| \exp\left(i\,k\,x \sin\theta_{ref}\right) + \exp\left(i\frac{k\,x^2}{2z}\right) \right|^2 . \tag{3.9}$$

The frequency content of a hologram, like any other measured signal, can be determined from the discrete Fourier transform. Performing an FFT of a section of a hologram with an obliquely incident plane reference field, as is done here, the wavevectors of the object field are shown with a shift in frequency space equal to the frequency of the approximately planar reference beam $k_0 \sin\theta_{ref}$. A synthesised hologram corresponding to eq. (3.9), with $k = 2\pi$ mm^{-1}, $\theta_{ref} = 45°$, and $z = 100$mm is shown below with its associated Fourier Spectrum.

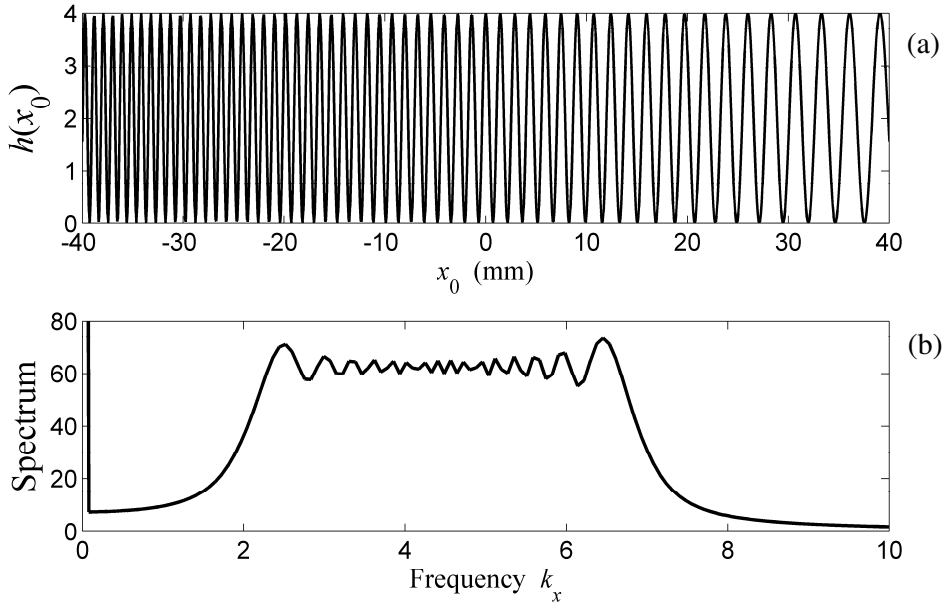

Figure 3.15 – Simulated hologram calculated using eq. (3.9) and its corresponding Fourier spectrum. Calculated with λ=1, $\theta_{ref} = 45°$.

In this case,with a plane reference beam with an angle of incidence of 45° the spectrum shows a shift of the spectrum in frequency space to $k \sin\theta_{\text{ref}} = 4.44$ mm^{-1}, and around this frequency the bandwidth of frequencies is approximately $2ka / z \approx 5$mm^{-1}.

In the system developed here with an object beam such as one derived from a horn antenna the divergence and spatial width of the beam are limited and complete information of the field divergence can be theoretically attained. However everyday objects will frequently contain features on the order of a wavelength that will cause large divergence of the field. This may be a problem for millimetre wave holography in terms of the dynamic range of the detector which may lack sensitivity to measure the reduced

power of such widely diffracted portions of a field. However, mm-wave imaging research is generally concerned with observation and detection of objects generally much larger than the wavelength, therefore these limitations in resolution may be negligible in practical applications. Using the holographic technique in the visible band, the wavelength is normally much smaller than any features of the inspected object reducing the divergence of the field, although truncation of the field may be an issue with small CCD arrays and may require measurement over a larger area using a scanning system.

The Nyquist sampling theorem states that for a complete disrete reconstruction of a signal with zero power spectrum for frequencies $v > v_{max}$, the signal must be sampled at a rate with a minimum value $v_N \geq 2v_{max}$. No information on the properties of signal is lost by sampling at this Nyquist frequency ν_N, and little information is gained by sampling at a greater rate. The theorem is stated more concisely in [PRE07] as

"*Critical sampling of a sine wave is two sample points per cycle*"

In this work, the highest frequency was in general found to correspond to the radiation wavelength, therefore $\nu_N = 2/3$ mm^{-1}. Holograms were generally sampled discretely in steps of 1mm.

3.4.3 - Results

To demonstrate the application of the digital holography technique, a hologram was formed by the measurement of the interference between the reference beam and two rectangular horn antennas arranged vertically. The hologram measured with this arrangement, shown in Figure 3.16, shows horizontal and vertical fringing representing the horizontal incidence of the reference beam and the interference of antenna fields with each other.

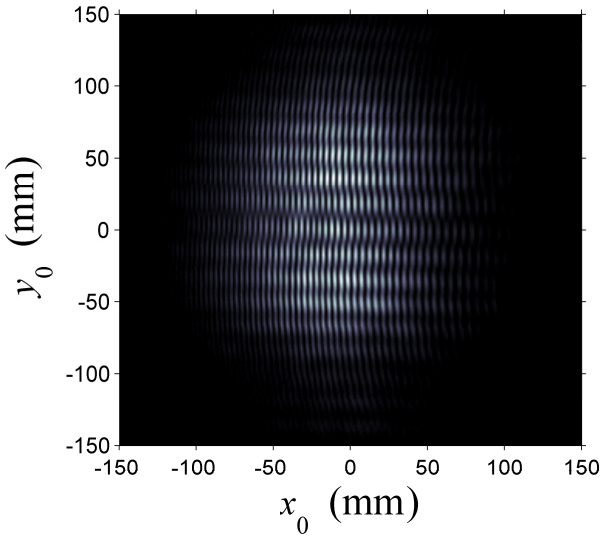

Figure 3.16 – Recorded hologram of two vertically arranged rectangular horns.

The horns were placed 90mm apart, and at 500mm from the hologram measurement plane, with the source fields polarised horizontal to the optical bench. The aperture dimensions of each horn was ~20mm×28mm (6.6λ×9.3λ). The following figures show the numerical reconstruction of the object field at various distances from the hologram plane, calculated using the convolution approach.

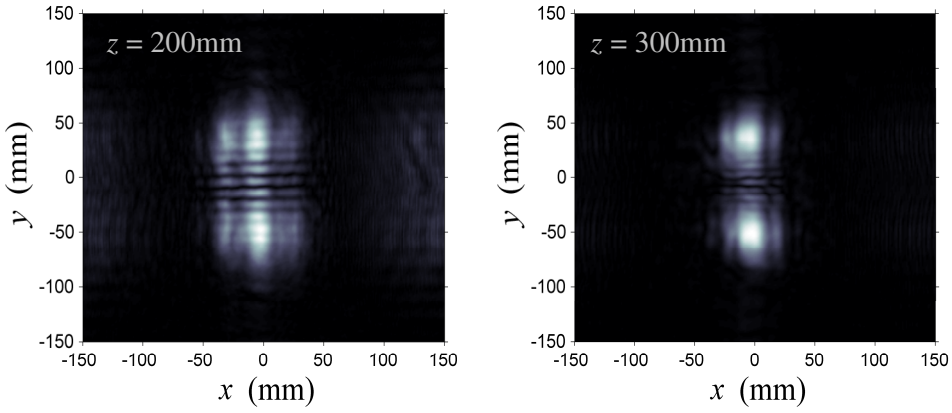

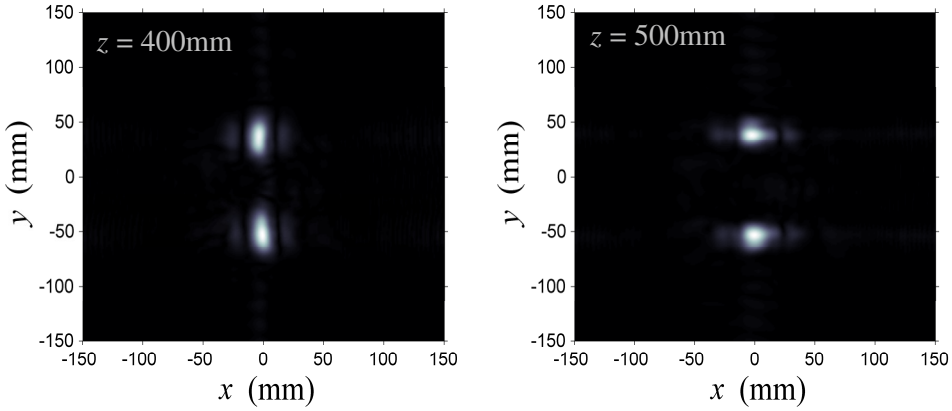

Figure 3.17 –Reconstruction of the object field with increasing distance from the hologram plane, using the convolution approach given by eq. (3.6).

The total reconstructed field is shown in Figure 3.18, as a function of distance from the hologram z. This type of reconstruction could be very useful in the testing of optical elements as a method of visualising phase and amplitude structures without the requirement of making multiple experimental measurements which can be very time consuming.

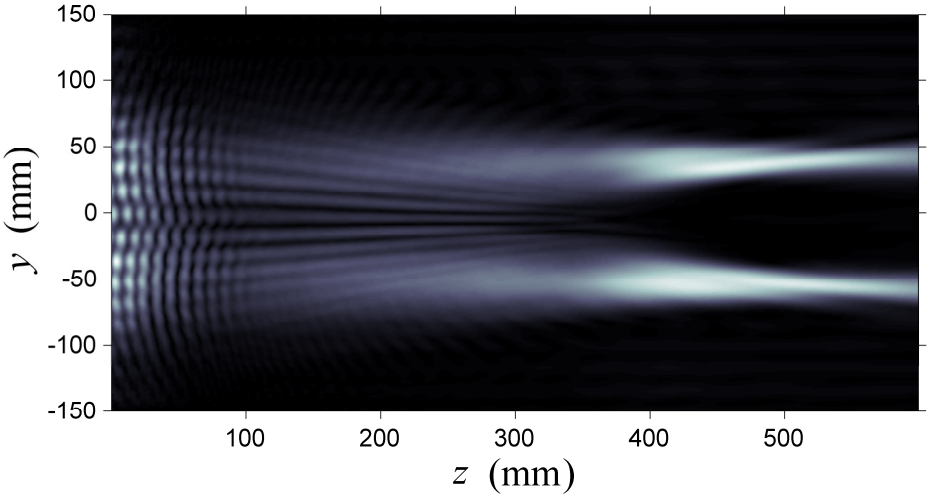

Figure 3.18 – Two dimensional reconstruction of the object field from the hologram Figure 3.16.

Figure 3.19 shows the hologram of an 'M' shaped section cut from the absorbing material Eccosorb^{TM} and Figure 3.20 depicts its reconstruction using the two methods defined, the FFT, and the convolution method.

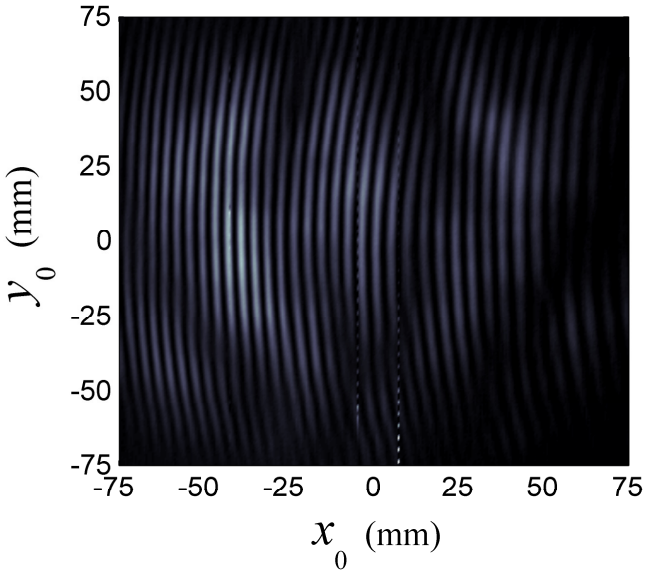

Figure 3.19 – The 100 GHz hologram of an 'M' shaped amplitude mask cut from Eccosorb, with a reference beam angle of incidence of ~45°.

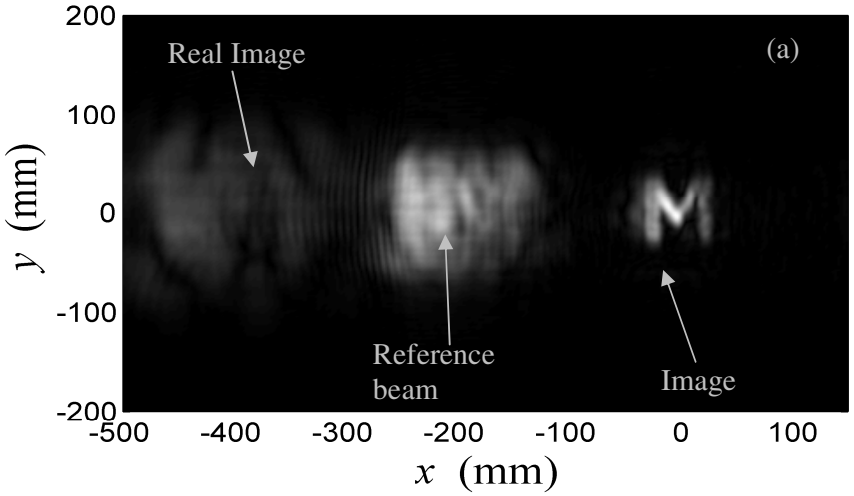

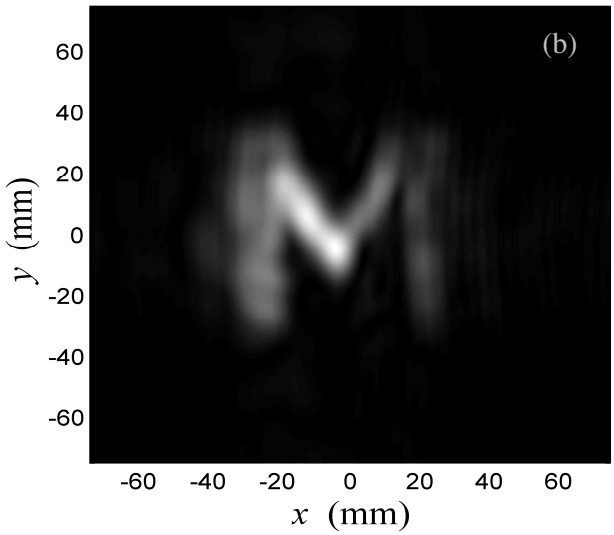

Figure 3.20 – Reconstruction of a '*M*' shaped section cut from Eccosorb. (a) Image obtained using the FFT implementation of the Fresnel diffraction integral (eq. 3.4), and (b) Reconstruction with the convolution approach (eq. 3.6).

The indentation on the right hand diagonal of the reconstructed image was an actual feature of the amplitude mask, and shows the potential accuracy possible with this method of imaging.

3.5 - Reconstruction of digital holograms using Hermite-Gaussian modes

The conventional approach to digital holographic image formation is through the use of fast Fourier transforms, but with the system developed for this thesis, we are in a position to investigate hologram reconstruction with the alternative technique of Gaussian beam mode analysis, which is a novel application of the method. This is possible due to the high sampling rate, as a fraction of the wavelength, and also the size of the complete recorded hologram is only 50-100 times the dimensions of the wavelength. From the data presented in the previous sections here it can be easily seen that holograms may contain as few as 20-30 interference fringes. Thus it may be possible to simulate image formation from a recorded hologram with fewer modes than would be required with a Fourier synthesis. The work shown here for reconstruction of millimetre wave holograms may also be applied to similar work in the near-infrared band, as digitally recorded infrared holograms, for example in Figure 3.8 (a), show similar structures in terms of the number of fringes in the recorded field patterns.

For a modal synthesis of two-dimensional holograms, the HG modes structures are evaluated in Matlab™ from the zeroth and first indexed modes using recurrence relations. This becomes a relatively swift calculation using the vectorisation process available in the software but becomes less efficient with a very large number of modes (>200×200), and finely sampled measured holograms (>300×300 pixels). Due to the discrete nature of the holograms, integration of the overlap integral must now be based on numerical techniques. As a basic approximation the discrete integration over the hologram was generally implemented as a basic sum. The accuracy could be increased with various numerical techniques like the trapezoidal rule, but for examples in this chapter the enhancement is negligible.

Before any link with optical arrangements is made, the adequacy of a two-dimensional Hermite-Gaussian synthesis in representing digital images would be a good indication of their use in holography. Digital images can be represented using the portable gray map (.pgm) scheme, with which a simple text file defines the number of pixels within the image and then defines intensity values for each picture element on a scale of 0 to 255, 0 representing black, and 255 representing white. To illustrate the capability of the discrete Hermite-Gaussian expansion, we can briefly show such a synthesis of the high contrast image shown below which is commonly referred to in literature relating to image processing.

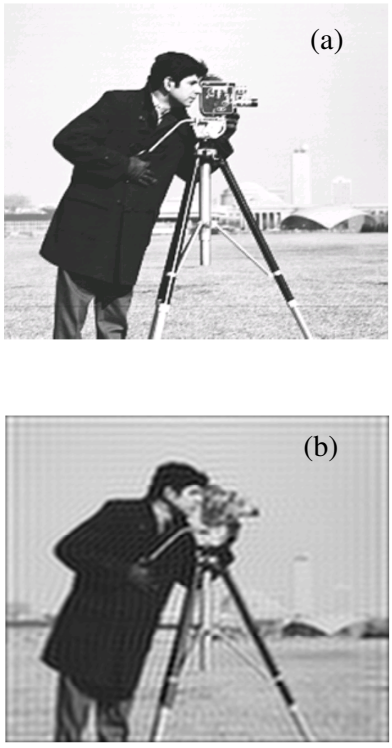

Figure 3.21 – Reconstruction of the "*Cameraman*" image using 101 Hermite-Gaussian modes. (a) Original image. (b) HG synthesis.

It must be noted that like in the GBM synthesis of ideal aperture functions with hard truncation in other chapters, the waist parameter used in the image synthesis above is given by the value described in [LIU06]. However, in the example given above it is almost certain that this waist value does not determine the most efficient mode set, as the highest pixel values occur toward the centre of the image, whereas the waist value used is optimal for a variation with abrupt truncation at the edge of the sampled field. For the synthesis of the above images, a large number of modes is required for strong convergence to the desired signal, due to the minute features which require modes with very high frequency. However, it will be shown that for synthesis of the holograms measured in the system discussed, complete reconstruction of the measured intensity structure is not necessary.

As we saw in chapter 2, the roots of the Hermite polynomials are irregular and thus no simple expression can be defined to precisely represent the spatial frequency of a Hermite-Gaussian mode due to this irregularity. An estimation of the average frequency of a HG mode with index l and width parameter w is given in [SIE86] as

$$\nu_l = \frac{\sqrt{l}}{4w} \tag{3.10}$$

and its angular analogue

$$\kappa_l = 2\pi \frac{\sqrt{l}}{4w}. \tag{3.11}$$

Figure 3.22 compares two modes with their corresponding sinusoids with equal frequency obtained from eq. (3.11).

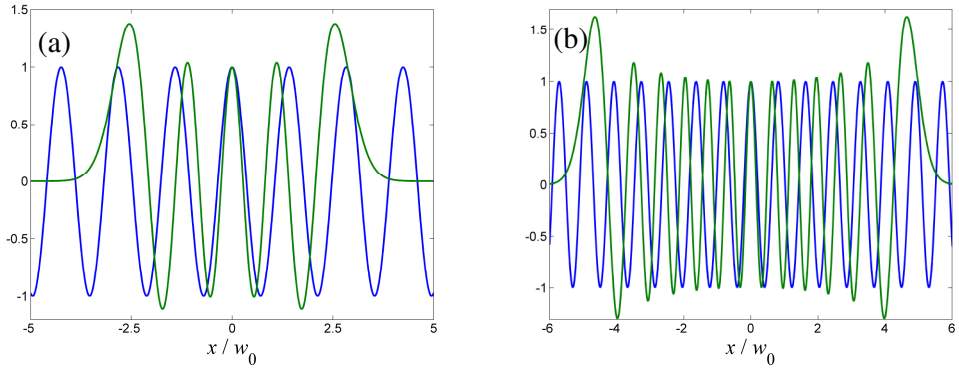

Figure 3.22 – Comparison of the Hermite-Gaussian modes (red) with sinusoids of "equal" frequency (blue). (a) $m = 4$, (b) $m = 12$.

For a modal synthesis of field data consisting of features that are small in comparison with the dimensions of the total field attention must be given to the relationship of the waist parameter and the effective frequency of the HG modes. The expression given by eq.(2.22) for the effective extent of a HG function can be approximated for large values of l or m as $\sigma_m = w_0\sqrt{m}$. If we assume that the smallest feature of the field data, with dimension dx, is to correspond to the minimum frequency contained in the mode set for which the value is $\sqrt{m}/4w$ then the maximum mode index can be shown to be [SIE86]

$$M > \frac{4a}{dx} \tag{3.12}$$

with

$$w_0 \leq \frac{dx\sqrt{M}}{4} \tag{3.13}$$

These values however are only necessary when a complete reconstruction of the aperture structure is required. We shall retain the discussion here in relation to one hologram of an '*M*' shaped aperture cut from an Eccosorb^{TM} mask shown in Figure 3.20 (a).

In the system described here, the object lies directly in front of the hologram plane, while the reference beam has a significant angle of incidence, here ~45°. The appreciable separation of the reference beam from the object, the spatial dimensions of which are generally relatively larger than the wavelength, ensures that the divergent wavefront of the diffracted object field will diverge at angles much less than those of the reference beam at the hologram plane. So in a spectral analysis the wavevectors of the object beam and those relating to the reference beam are separated in spatial and frequency space. Therefore, as we are interested only in reconstructing the object field, we can attempt to reconstruct a holographic image with a relatively small number of modes, in comparison with the mode set size used to reconstruct the complete recorded hologram.

This simplifies the application of the Hermite-Gaussian expansion for the holograms depicted here, in that a complete reconstruction of the measured hologram structure is not required thus higher order modes are not necessarily needed for reconstruction of the high frequency interference fringes associated with the reference beam. This will naturally affect the form of the actual field reconstructed at the hologram plane which will contain information only on the object beam with elimination of the high-frequency features generated by its interference with the reference beam. Therefore the reference beam can be eliminated from any reconstruction, without significant effect on the reconstructed image in this arrangement.

The mode coefficients of the hologram in Figure 3.19 are shown as a function of mode indices and the approximate vertical and horizontal frequencies given by eq. (3.11).

With larger mode sets such as in Figure 3.23 (e)-(f), the mode coefficients of the higher order modes, in l, become more significant, which corresponds to a reconstruction of the high-frequency fringes associated with the reference beam. Although in this section we have depicted the HG mode coefficients in a similar manner as Fourier coefficients, i.e. as a function of frequency, this is only to illustrate an approximate correspondence of frequency and mode index.

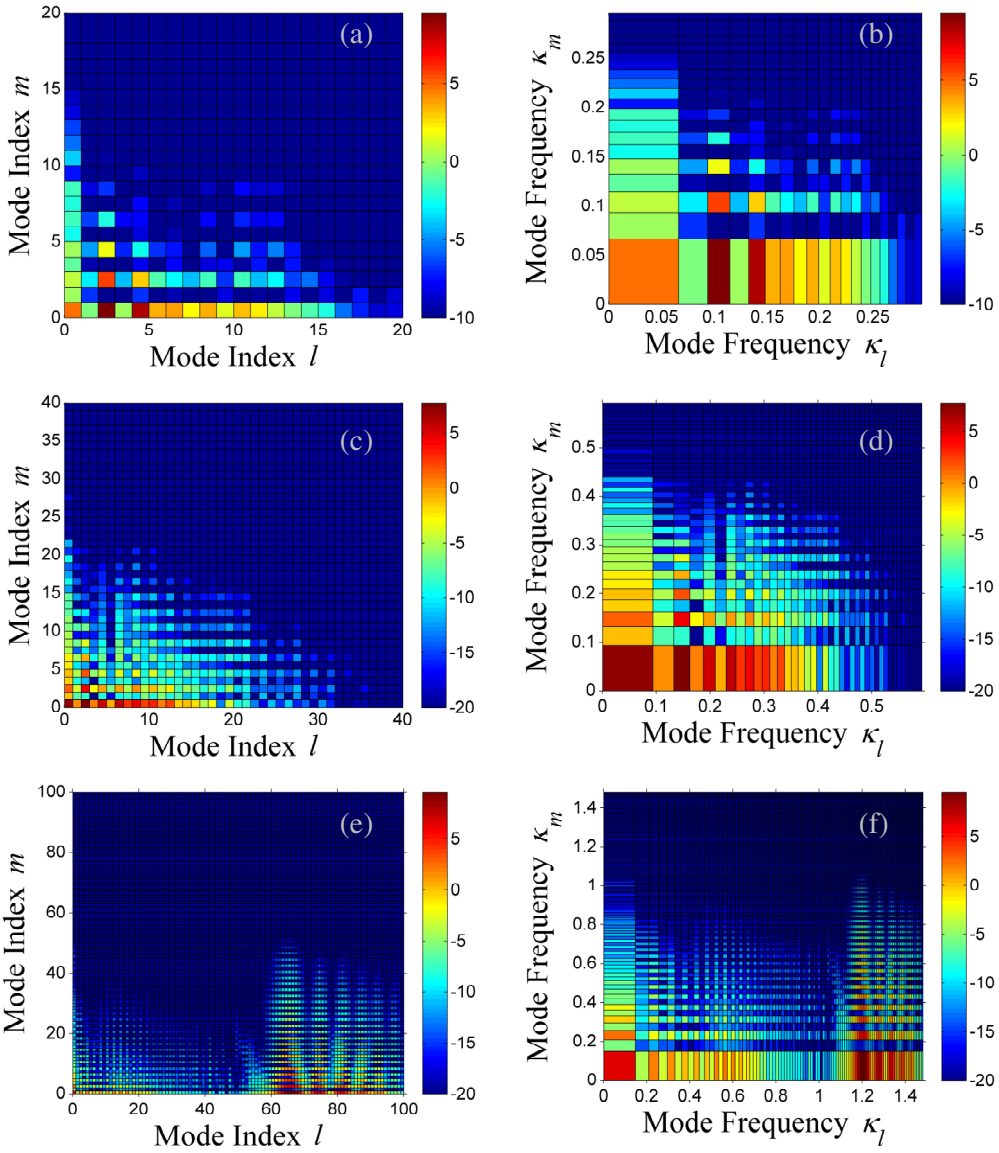

Figure 3.23 - The Hermite-Gaussian mode coefficients A_{lm}, of the recorded hologram shown in Figure 3.19. The coefficients are described according to the mode indices in the left column, and in the right column the coefficients are depicted with their related approximate frequencies, given by eq. (3.12). M = (a)-(b) 20, (c)-(d) 40, (e)-(f) 100. Shown with a logarithmic scale.

Figure 3.24 shows the reconstruction of the phase and amplitude at the hologram plane with differing number of modes, showing an elimination of the high frequency fringes associated with the reference beam.

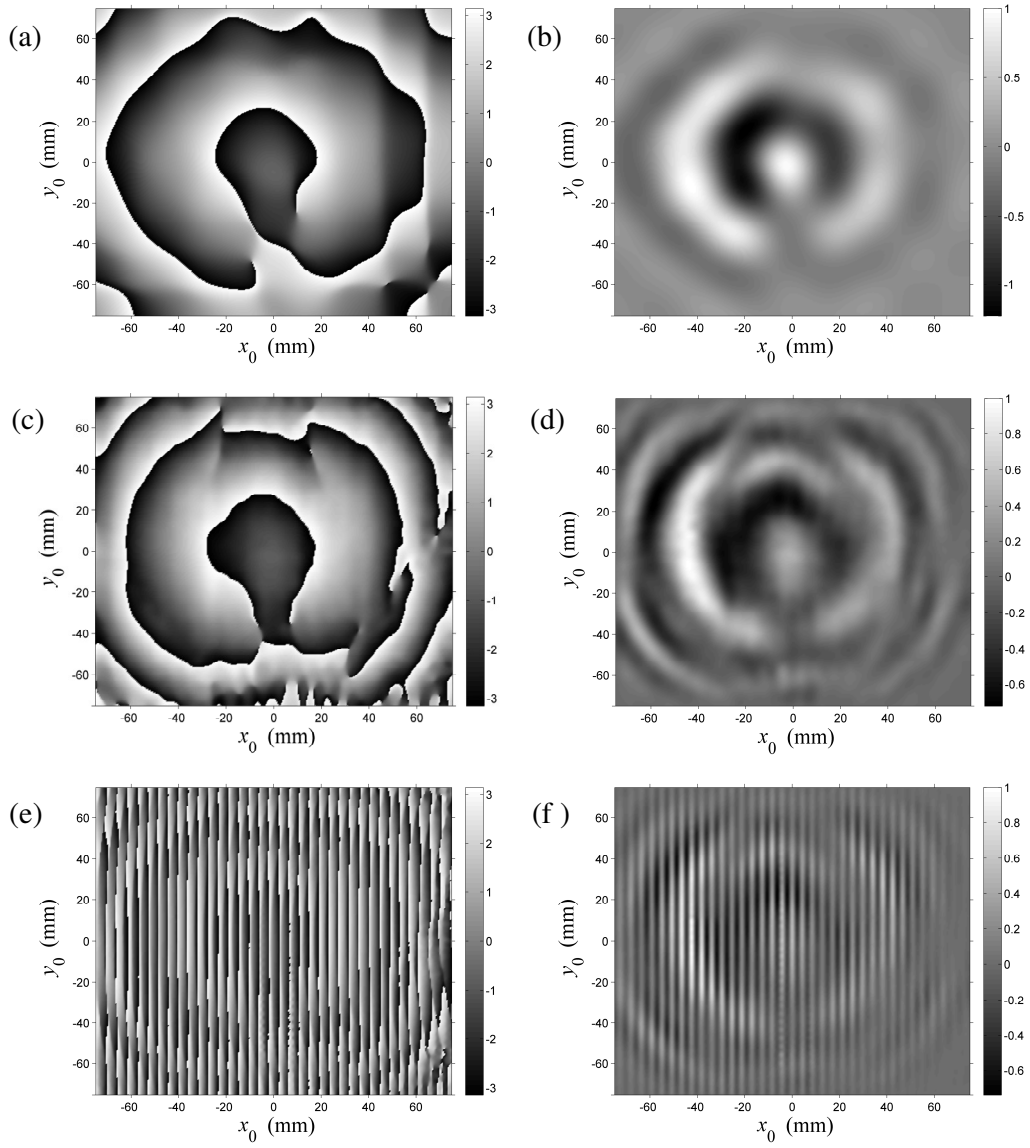

Figure 3.24 - The phase and amplitude of the hologram in Figure 3.19 as formed using a truncated HG synthesis. The left column shows the reconstructed phase, and the right depicts the amplitude $Re\{E_0(x_0,y_0)\}$, with (a)–(b) $M = 10$, (c)–(d) $M = 40$, (e)–(f) $M = 100$.

The image can be reconstructed with an arbitrary number of modes although the quality is greatly reduced for very small mode sets. See Figure 3.25.

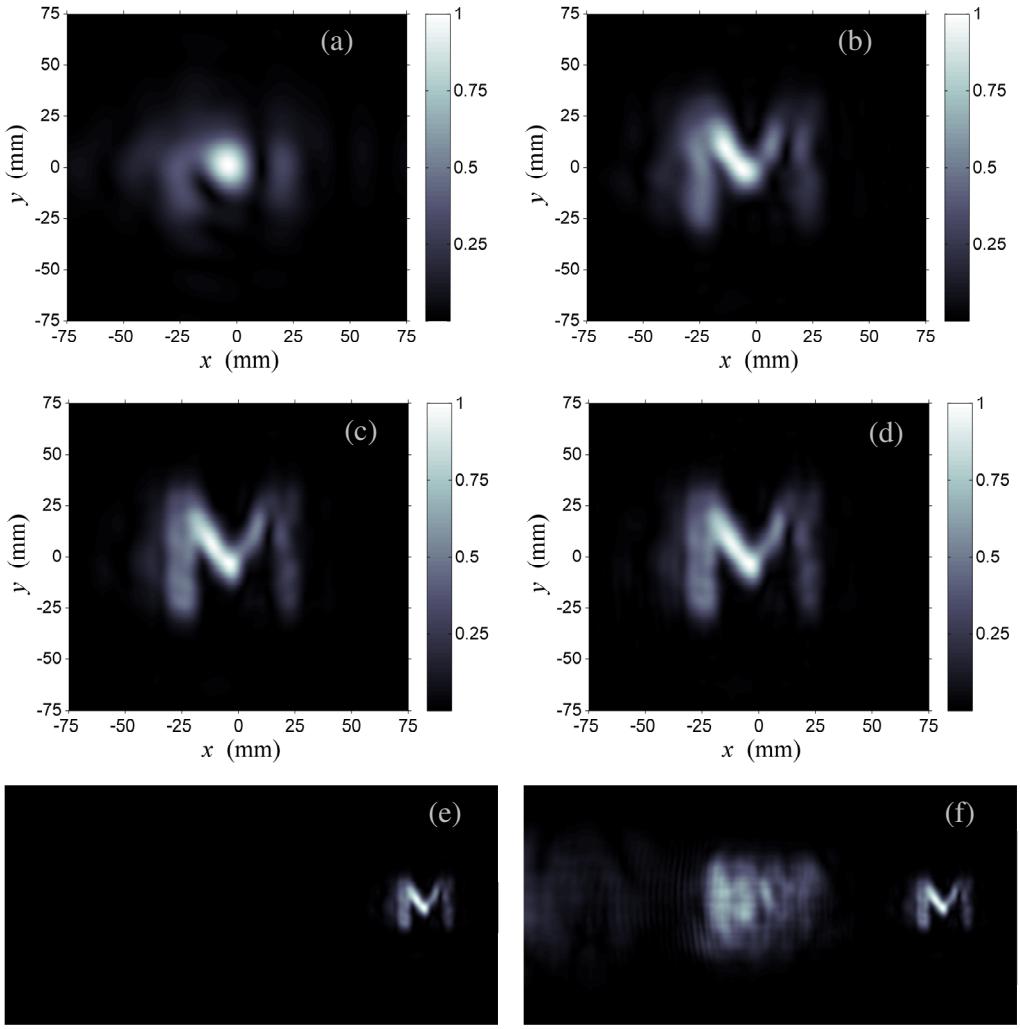

Figure 3.25 – Reconstruction of a hologram using Hermite-Gaussian modes with various sizes of the mode set M = (a) 10, (b) 20, (c) 40, (d) 100. (e) shows the elimination of the reference beam using M = 40 compared to the M = 100 reconstruction in (f).

The elimination of the reference beam from the reconstruction is a desired result in digital holography in the visible band where there is usually only small angular separation between the object and reference beams thus the reconstructed image will likely be obscured in some way. Using the conventional FFT technique, [KRE97] suggested that the influence of reference beam could be eliminated from the image reconstruction through subtraction of the mean of the recorded intensity values, i.e.

$$h(x_0, y_0) = h_0(x_0, y_0) - \langle h_0 \rangle$$

where $\langle h_0 \rangle$ is the mean intensity value of the original recorded hologram h_0.

In Figure 3.25, it is clearly shown that the increase in modes, with comparison of (c) and (d) show no significant improvement of the image with an increase of $M = 40$ to $M = 100$, thus allowing for image reconstruction without the complete frequency content of the hologram and elimination of the reference beam.

The author must emphasise that this method may only have useful application in long-wavelength holography systems such as the one developed by the author and co-workers involving a large angular separation between the reference and object beams.

3.6 - Conclusion

The details of a millimetre wave digital holographic system have been presented. With reference to the literature and other descriptions of digital holography at visible wavelengths, a measurement system operating at 100 GHz has been modified to record holograms from which the field structure of diffracted fields have been determined using numerical techniques.

The Hermite-Gaussian mode expansion as an alternative technique for holographic image reconstruction has been demonstrated. The technique allows for the formation of images with an incomplete description of the hologram structure using a fewer number of modes, and thus less spectral information than is used in the fast Fourier transform. While not inefficient, the technique does not "compete" with the speed of the FFT which is the benchmark for methods of image reconstruction in digital holography. The Hermite-Gaussian expansion, in its standard form, does not allow for the near real-time reconstruction of images like the more established method, thus development of a similar speedy algorithm for generation of Hermite-Gaussian modes is required. The technique of singular value decomposition (SVD) has been investigated by other researchers within this department, [WHI06], [GRD04], and although it returns approximate values of mode coefficients, its employment in software could go some way towards increasing the efficiency of modal calculations. One elementary time saving method would be the generation of "look-up" tables for each of the HG modes for commonly used mode quantities and sampling rates. This would be suitable when measuring holograms of consistent dimensions. With no specific scaling these modes could be used for synthesis of holograms without the need to generate large two-dimensional arrays every occasion a mode is required, which can be inefficient. Nevertheless, the method has the potential of being a useful application particularly in the retrieval of phase information from long-wavelength holograms and may have use in

the application of the system for determination of, for example, the phase centres of horn antennas, and work is ongoing within the NUIM Physics department on such a function.

Since the publication of [MAH06] the technique has also been applied at millimetre wavelengths (310GHz) in a reflection imaging mode by [TAM08].

In future work, the phase properties of the reference beam may have to be obtained more accurately to improve the quality of the image reconstruction. This may involve the use of a simple plane mirror instead of the parabolic reflector that was employed here. Although a plane mirror will create a wider beam at the plane of the hologram, its phase will be easier to predict allowing for even greater accuracy in the image reconstruction.

Chapter Four

Gaussian Beam Mode Expansion of Optical Pulses

4.1 – Introduction

In this chapter we discuss the novel application of GBMA to short electromagnetic fields and illustrate the power of the technique over the conventional use of the Fresnel diffraction integral, which requires a description of the behaviour of pulsed Gaussian beam modes (PGBM).

The nature of light that the human eye detects everyday is vastly different from the coherent and almost ideally monochromatic radiation generated by lasers and millimetre wave sources. The white light that we see is a superposition of all wavelengths of light in the visible band of the EM spectrum, resulting in an incoherent field due to the unrelated phase between waves of different colours scattered by objects. But when the phases of each spectral component in a polychromatic field have a definable relationship, the behaviour is much different to that of white light.

Up to this we have discussed the propagation of continuous wave (*cw*) monochromatic beams, with uniform amplitude and durations large enough to allow for neglect of the time dependence of a field in an intensity calculation. However, advances in laser technology have allowed for the generation and, perhaps more importantly, the detection of pulses caused by signals with durations on the order of femtoseconds (10^{-15}s) at visible wavelengths, with the low number of substantial oscillations in the signals earning these fields the description *ultrashort*. These types of pulses are particularly useful for experiments where fields with energies and durations associated with atomic transitions are required, [HARR90, MCK07]. The study of short pulses is also applied in telecommunications with transmission of such fields along fibre optical cables [KAM97].

At terahertz frequencies, the techniques of time domain imaging and spectroscopy using pulsed radiation has become a powerful research tool in the process of material classification using ultrashort pulses, [PRA07, KIN96,WAT04)]. Figure 4.1 shows an example of a typical experimental layout for terahertz imaging in the time-domain.

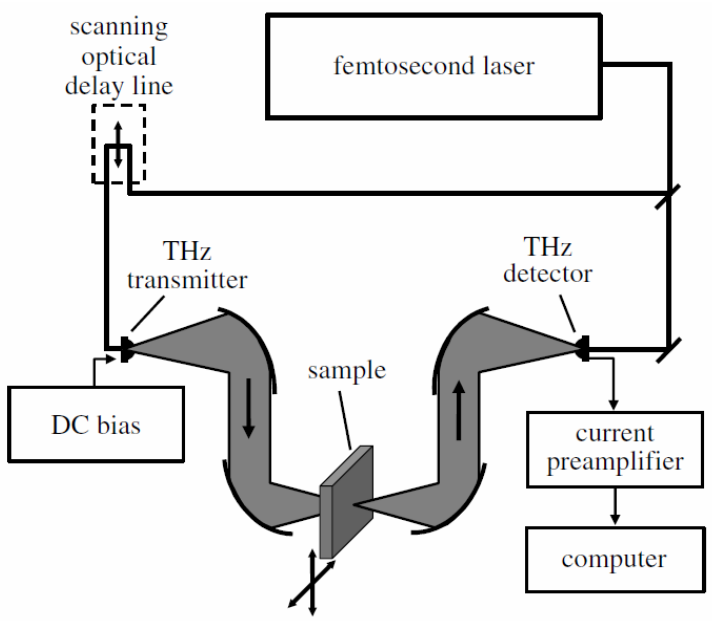

Figure 4.1 - Schematic of a THz time domain optical system. Reproduced from [CHA07].

The system described in Figure 4.1 consists of a femtosecond source generating a train of pulses assumed to have identical temporal shapes, usually with a repetition rate in the kHz range. Using a beam-splitter the pulse train is divided into two further signals with one used to generate the terahertz pulse for illumination of an object, while the other is employed to define the time and duration of each detection. The terahertz radiation is generated by targeting a photoconductive antenna with an ultrashort femtosecond pulse in the visible or near-IR bands generated by a mode-locked laser. A bias voltage is applied across electrodes attached to a sample of, for example, Gallium-Arsenide (GaAs), but with no illumination by the laser pulse the resistivity of the material is very large and no significant movement of charge occurs. When the sample is illuminated by the laser field charge carriers are created in the semiconductor allowing a current to flow within the material which generates a short terahertz pulse, the strength of which is related to the rate of change of the current density *J,* i.e. $E \propto dJ / dt$. The detector relies on similar physical processes but in this case photocurrents in the GaAs substrate are generated by the detection of a laser pulse and the illuminating terahertz pulse induces currents which are then measured using an ammeter attached to the terminal electrodes. The temporal structure of the pulse then determined, not from a single pulse, but by sampling pulses in the wave train at different times which is made possible with a mechanical variation of the optical path length of the pulse responsible for the generation of the THz field.

Generally, millimetre-wave imaging systems rely strongly on the prediction or measurement of the diffractive behaviour of the fields and obtaining information from the field intensity. Image formation using THz time-domain systems relies more on analysis of temporal properties such as the delay caused by the interaction of the pulse with media of differing refractive indices, with lesser attention paid to diffraction effects of the pulse. Time-of-flight measurements have been demonstrated using pulsed fields which with post processing can determine, for instance, the interior make-up of a test object based on the arrival times and phases of the pulse peaks reflected by interior surfaces, which can then be used to calculate the position of material interfaces within the target. Figure 4.2 shows an example of results obtained using this technique.

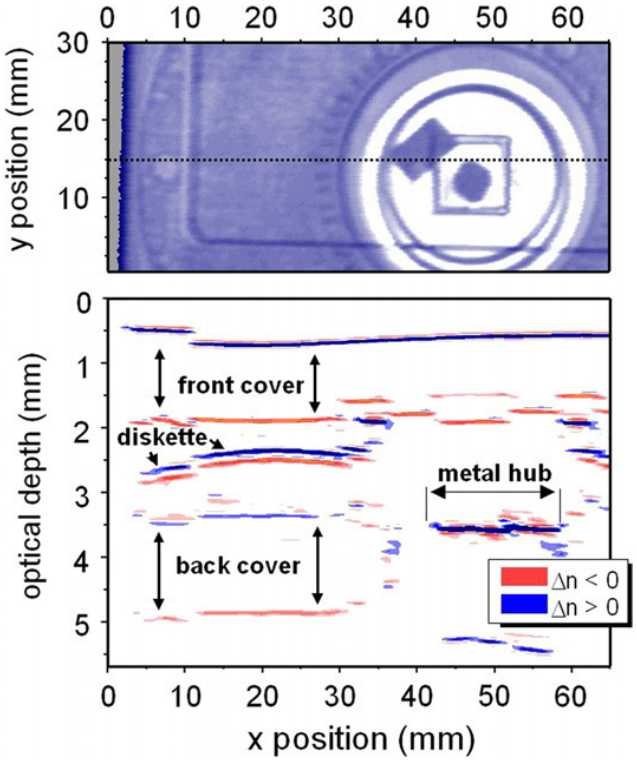

Figure 4.2 - Terahertz image recorded by time-of-flight measurements of a pulse. The lower image represents the depth of the object discs' features at the dashed line in the upper figure, calculated from the measured delay of the reflected pulse. Reproduced from [MIT97].

While the study of ultrashort pulse behaviour is a relatively recent endeavour, there is nevertheless a wide variation of techniques used to model the behaviour of time dependent fields, from the intensive finite-difference time-domain approach [GOO92,LUE90] to integral techniques such as the Smythe-Kirkhoff and Rayleigh-Sommerfeld formulations of diffraction, [GUR00, BUD98]. Nevertheless, the use of the paraxial approximation has gained widespread acceptance in valid situations such as, for

example, the case of a pulse with narrow “bandwidth” and truncation of such a field by an aperture relatively larger than the carrier wavelength, [KEL08, SHE97, VEE06], and we shall continue to apply that approximation in this chapter. Firstly, to illustrate the dynamics of pulse diffraction the author used a two-dimensional FDTD model to simulate the general effects involved in the truncation of an ultrashort pulse at an aperture. Results of this simulation are illustrated in Figure 4.3.

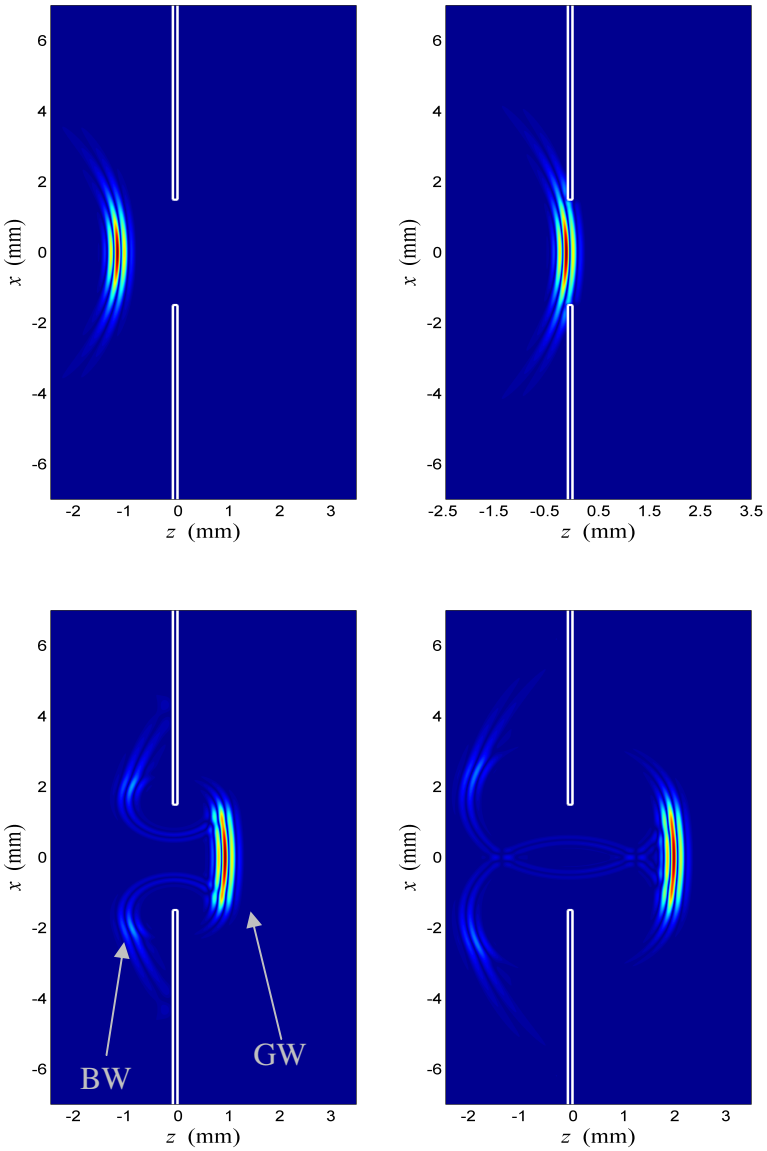

Figure 4.3 - The diffraction of an ultrashort pulsed Gaussian mode by an aperture shown by the absolute value of its amplitude $|E|$. The duration of the field is 1.27 ps with a central frequency of ν_0 = 1 THz. The arrows depict the boundary wave (BW) and the geometric wave (GW).

In Figure 4.3, if the aperture shown is defined by the presence of two opaque screens which are assumed to be infinitely thin, the features generated at the aperture

edge can then, in two dimensions, be considered as completely circular secondary pulses, or *boundary waves* (BW), which will have significant influence on pulse measurements in the near-field of the aperture. The portion of the field directed approximately perpendicular to the aperture plane is often referred to as the *geometric wave* (GW) [MEN07]. However, as described in chapter two, the FDTD method in its elementary form is not suitable for efficient calculation of fields at distances further from the source, and in general, unless material effects are a concern, such rigourous simulation can be very excessive.

In the case of a continuous wave field, the generating signal amplitude is constant over time, oscillating at a single frequency. If the strength of that signal was modulated to have significant amplitude only within a finite time period, a spectral analysis would show energy content at frequencies surrounding the carrier frequency. Here, the diffraction of a field generated by a time-limited excitation is determined by the Fourier decomposition of the time signal into its constituent frequencies. The diffractive propagation of the individual monochromatic waves at each frequency is determined, and then the integration of the calculated fields for all spectral components, weighted by the corresponding spectral coefficients, is performed to determine the characteristics of the total structure of the diffracted pulse.

In theoretical studies, the time signal of a pulse most commonly referred to within the literature involves a Gaussian envelope which we describe as

$$s(t) = \exp\left(-\frac{t^2}{\tau^2}\right)\exp\left(-i\omega_0 t\right) \tag{4.1}$$

where t is the time, ω_0 is the central or *carrier* angular frequency, and we shall refer to 2τ as the pulse duration, which in the case of a true continuous wave is infinite. This form of excitation is commonly used due to the mathematical simplicity of the Gaussian function. Also, this function allows for numerical truncation of the spectrum in an analysis without any appreciable loss of energy contained within the pulse. This is in contrast to, say, the sinc function which defines the spectrum used for the modelling of a constant signal over a finite time ("top hat"). That requires a much larger spectral extent for accurate representation of the time signal due to the relatively large local maxima of the sinc function far from the carrier frequency. The form of signal given by eq. (4.1) will be used throughout this discussion.

Although the scalar diffraction methods described in chapter 2 show greater computational efficiency than the finite-difference time-domain method, the simulation of pulsed fields using FDTD actually has an advantage over this Fourier method in that the time signal can be explicitly set in a numerical simulation without having to address each component of a Fourier spectrum separately. Therefore the duration of simulations is not greatly increased from continuous wave models, which is a significant feature of the Fourier method discussed in this chapter.

For the Gaussian signal defined in eq. (4.1), the analytical Fourier-transform is well known, and is given by

$$S(\omega) = \frac{1}{\sqrt{2\pi}} \int_{-\infty}^{\infty} s(t) \exp(-i\omega t) d\omega$$

$$S(\omega) = \frac{\tau}{\sqrt{2}} \exp\left(-\tau^2 \frac{(\omega - \omega_0)^2}{4} \right) \tag{4.2}$$

The definition for the bandwidth of a spectrum, $\Delta\omega$, differs within the literature, with some researchers quoting it as the full width at half maximum of the spectra. Here, for consistency with the conventional characterisation of the Gaussian function used throughout, we define the bandwidth of a Gaussian spectrum as the frequency range between a spectral width of $4 / \tau$ surrounding the central frequency, i.e. the standard Gaussian $1/e$ width. The spectrum can be generalised by the dimensionless *fractional bandwidth* $\gamma = \Delta\omega / \omega_0$, with $\gamma = 0$ representing a continuous wave. For a comparison, the FWHM of any Gaussian function can be easily calculated from its width parameter w by

$$FWHM = 2w\sqrt{\ln 2} \,. \tag{4.3}$$

For the Gaussian bandwidths of 0.2 and 0.5, used here by the author, the FWHM fractional bandwidths correspond to 0.166 and 0.42 respectively. The number of oscillations over the duration of a signal, 2τ, is also a useful quantity for reference and, for a Gaussian definition of the signal, is given by $4 / (\gamma \pi)$, ($\gamma = 0.2 \rightarrow$~6.36 cycles, $\gamma =$ 0.5→~2.5 cycles). While these bandwidths are comparatively large, the effects of pulse propagation are more easily visualised with shorter durations. The reader should note the use of both the temporal frequency v and the angular frequency ω will be used interchangeably. Figure 4.4 depicts an example of such a time signal and its corresponding Fourier spectra.

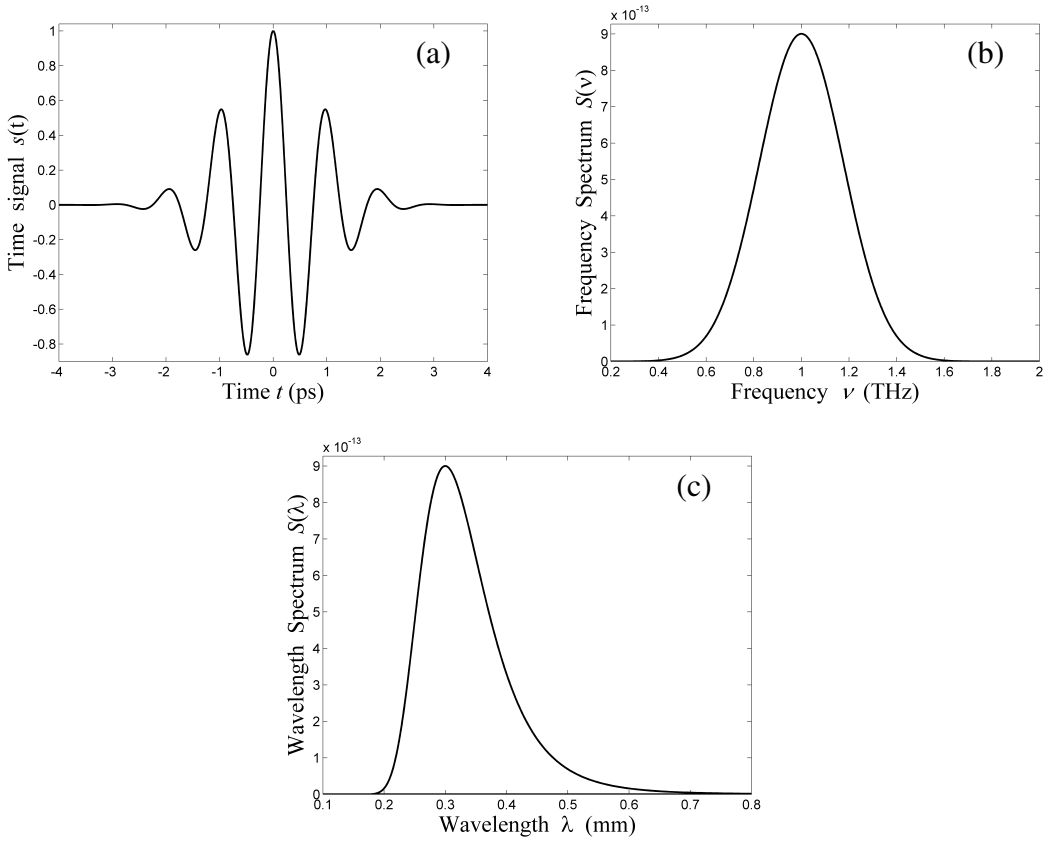

Figure 4.4 – (a) An example of a time signal and its Fourier spectra expressed in terms of (b) frequency and (c) wavelength. $\lambda_0 = 0.3$mm, $\gamma = 0.5$, $2\tau = 2.54$ ps. Note the asymmetry of the spectrum in (c).

In the literature, the general method of calculation of the paraxial diffraction of pulsed fields is again through the use of the Fresnel diffraction integral, eq. (2.2 and 2.5). The following equation (4.4) describes this computation in the cylindrical regime as the integration of each monochromatic field within the spectral range of the defined spectrum with relative amplitudes defined by $S(\omega)$.

$$E(r,z,t) = \frac{1}{\sqrt{2\pi}} \int_{-\infty}^{\infty} S(\omega) \left\{ -\frac{i\omega}{c\,z} \exp\left(-i\omega \left(t + \frac{z}{c} + \frac{r^2}{2c\,z} \right) \right) \right.$$
$$\left. \times \int_0^a E_0(r_0) J_0\left(\omega \frac{r\,r_0}{c\,z} \right) \exp\left(-i \frac{\omega r_0^2}{2c\,z} \right) r_0 dr_0 \right\} d\omega \qquad (4.4)$$

with ω the angular frequency, related to the temporal frequency v as $\omega = 2\pi v$. The term within the braces defines the diffracted field of an individual component for an individual value of ω first defined in chapter 2 by eq. (2.5). The outer integral, over ω, defines that the diffracted monochromatic field is calculated for all values of ω and superimposed to determine the nature of the resulting pulse.

As the spectral technique described requires integration over the frequency range the resulting analysis is obviously a double integral, further increasing the complexity of the calculation and therefore greatly increasing its computation time. The most significant cause of excessive computation times in the Fourier method of pulse calculation, regardless of the method by which diffraction effects are predicted, is the number of samples, N_ω, used to discretise the continuous frequency spectrum. With a discrete representation aliasing of the field will always occur and unwanted features are replicated in the time domain at delayed times of

$$\delta t = 2\pi \frac{N_\omega}{\delta\omega},$$

where $\delta\omega$ is the range over which the spectrum is defined, which, in the simulations here involving Gaussian spectra, is six times the bandwidth, $6\Delta\omega$, so as to ensure an accurate representation of the spectrum. Therefore, a sufficient number of samples should be used to eliminate the aliasing effects from the region of interest, which can add significant computation time to the models.

Some publications attempt to reduce the complexity of eq. (4.4) by development of algorithms simplifying the spectral integration through signal processing techniques, [VEE06, KEL08]. However, with our knowledge of modal diffraction techniques we can reduce the complexity of that calculation by introducing the Gaussian beam mode approach for field propagation in the time domain.

Here we will describe the propagation of pulsed orthogonal beam modes and how the summation of such modes can be used to calculate the structure of pulsed fields diffracted by practical apertures. As with continuous wave calculations in the preceding chapters, the GBMA method serves to reduce the computation time of the Fresnel formulation of pulses, by reducing the complexity of the diffraction integral to an $M+1$ term sum with negligible loss of accuracy in regions of interest. This theory of diffraction also provides an alternative physical insight into the propagation of ultrashort pulses, in that rather than an integration of monochromatic beams in frequency space, as is the conventional method, the complete field of the diffracted pulse can be thought of as a superposition of individual and independent pulsed beam modes which, when superimposed with correct weightings, combine to form the total pulsed field diffracted by the aperture. In particular, we highlight the similarities in the propagation of higher order pulse modes and the boundary waves generated by a discontinuous aperture edge.

Here, and throughout this thesis, Matlab™ was used in numerical simulations. The amount of code required is much more extensive than, say, Mathematica™ or Maple™, but the increase in calculation speed is adequate cause. In particular, the use of vectorisation, described briefly in chapter 2, is a very useful programming tool for numerical work.

4.2 - Pulsed Laguerre-Gaussian beam modes

The structure of an unobstructed infinitely wide pulsed plane wave can be determined by the inverse Fourier transform

$$\xi_{pw}(r,z,t) = \frac{1}{\sqrt{2\pi}} \int_{-\infty}^{\infty} S(\omega) \exp\left(-i\omega \left(t - \frac{z}{c} \right) \right) d\omega \tag{4.5}$$

With a Gaussian spectrum in the form of eq. (4.2), eq. (4.5) can be solved analytically to give

$$\xi_{pw}(r,z,t) = \exp\left(-\frac{(z-ct)^2}{c^2\tau^2} \right) \exp\left(-i\omega_0 \left(t - \frac{z}{c} \right) \right) \tag{4.6}$$

The amplitude part of the field, as a function of the longitudinal position, is defined as a Gaussian due to the properties of the Fourier transform of the Gaussian time signal, and this form of plane wave can be used as the benchmark for comparison with pulses that undergo diffraction and transformation. The longitudinal length of the plane wave pulse is easily extracted from the Gaussian amplitude term of equation (4.6) and is given as $2c\tau$. In a similar manner to eq. (4.5), the diffracted field of a *pulsed* Laguerre-Gaussian beam mode of index m in free-space can be determined from

$$\xi_m(r,z,t) = \frac{1}{\sqrt{2\pi}} \int_{-\infty}^{\infty} S(\omega) \left\{ \sqrt{\frac{2}{\pi w^2(\omega,z)}} L_m\left(2\frac{r^2}{w^2(\omega,z)} \right) \exp\left(-\frac{r^2}{w^2(\omega,z)} \right) \right.$$
$$\left. \times \exp\left(-i\omega \left(t - \frac{z}{c} - \frac{r^2}{2c\,R(\omega,z)} \right) \right) \exp\left(-i(2m+1)\tan^{-1}\left(\frac{z}{Z_c(\omega)} \right) \right) \right\} d\omega \tag{4.7}$$

We can rewrite the Gaussian beam parameters in terms of the angular frequency, for convenience, as

$$w(\omega,z) = w_0^2 \left(1 + \left(\frac{2cz}{\omega w_0^2} \right)^2 \right), R(\omega,z) = z\left(1 + \left(\frac{\omega w_0^2}{2cz} \right)^2 \right), \text{ and } Z_c(\omega) = \frac{\omega w_0^2}{2c}.$$

We shall refer to the confocal distance at the central frequency as $Z_0 = Z_c(\omega_0)$. Figure 4.5 shows the evolution of LG pulses over time at various distances calculated from eq.

(4.7). At $z = 0$, the pulse structure resembles the *cw* mode with a temporal modulating envelope. But as the distance z increases one can see the influence of the deviating diffractive behaviour of each spectral component on the overall structure of the pulse. For depiction of pulsed fields in the time domain, the results are shown with relative values on the temporal axis using a retarded time of z / c, which is the arrival time at each z plane of an undisturbed planar pulse, and scaled in relation to the temporal half-duration τ of the Gaussian time signal.

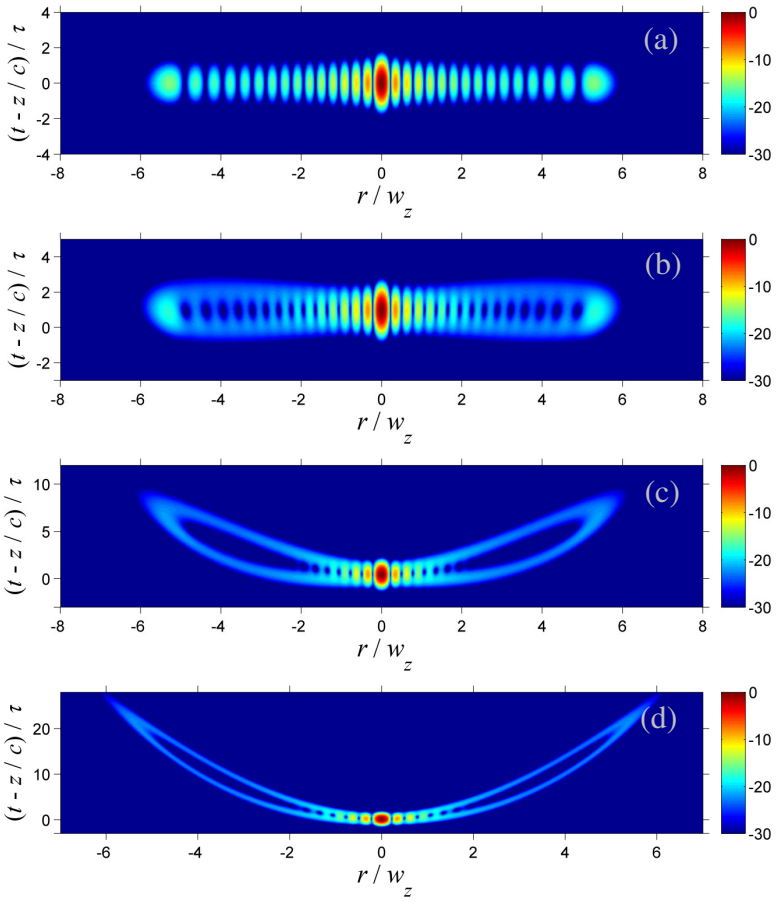

Figure 4.5 – Propagation of the $m = 15$ pulsed paraxial Laguerre-Gaussian beam mode shown. $\gamma = 0.2$, $w_0 = 100\ \lambda_0$. The fields are calculated with (a) $z = 0$, (b) Z_0, (c) 4 Z_0, (d) 12 Z_0, and are shown on a logarithmic scale normalised to the maximum intensity value $|E|^2$. The radial coordinate is shown in relation to the waist parameter at the central frequency $w_z = w(\omega_0, z)$, at each plane.

Due to their more complicated transverse amplitude profile, pulsed Laguerre-Gaussian beams obviously exhibit strong deviation from the propagation of pulsed plane waves, and their analysis shows some peculiarities due to the Gouy phase shift of each spectral component. While the above plots show the changing structure of the PGBMs, such fields are subject to phenomena that may not be apparent in the illustrations given.

These effects are more distinct in the propagation of much higher ordered pulsed modes as described in Figure 4.6 with an on-axis comparison of pulsed modes with an unobstructed pulsed plane wave given by eq. (4.6).

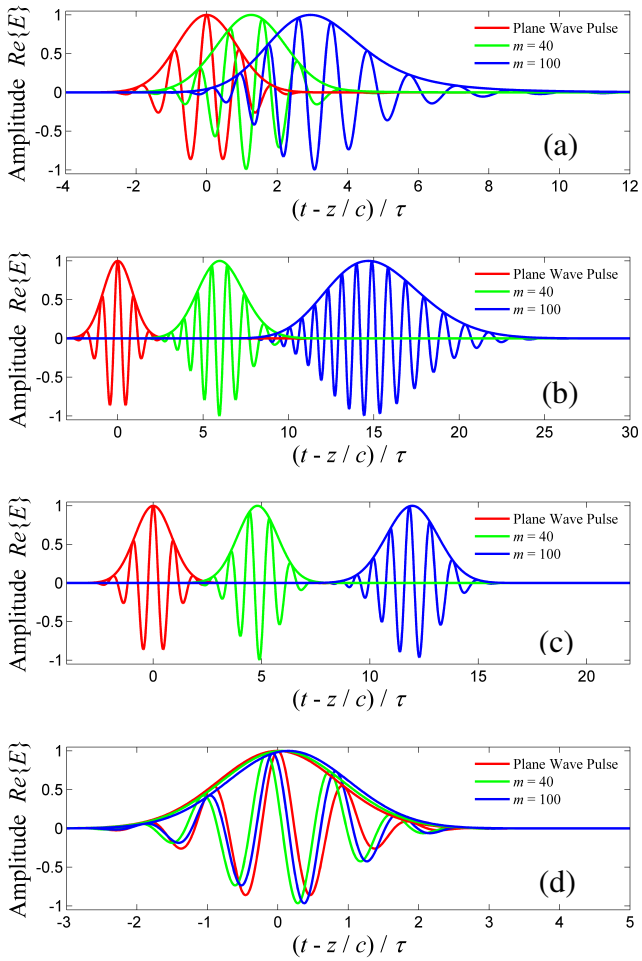

Figure 4.6 - A comparison of the m = 40 and m = 100 pulsed Laguerre-Gaussian modes with a pulsed plane wave (red) with $\gamma = 0.5$, $\lambda_0 = 0.3$ mm, $w_0 = 100\ \lambda_0$. Calculated at z = (a) 0.1 Z_0 (b) Z_0 (c) 2 Z_0 (d) 200 Z_0. The amplitude of the LG modes has been normalised to unity for comparison.

Note that the peaks of the amplitude envelopes do not necessarily coincide with the peak of the oscillatory real part of the fields. A discussion of this delay in the amplitude envelope relative to the phase of lower index ultrashort Laguerre-Gaussian beams is presented in [YANG08].

The fields described in Figure 4.6 show behaviour very similar to that exhibited by pulsed fields affected by dispersion within an optically dense medium, which is caused by a variation of the phase velocity of the frequency component. A temporal and spatial delay in the propagation of the GBM pulses along with a broadening of their temporal and spatial width causes a reduction in the peak amplitude alongside a delay in

the pulse peak, all of which are representative of the effects of normal dispersion. While after a certain distance it can be seen that the pulse duration begins to decrease towards its original duration, and linked with this phenomena the delay of the pulse in arriving at z is reduced, indicating a greater speed, which is behaviour akin to anomalous dispersion. Following the suggestion in [POR02], and from the investigative numerical results shown above, a suitable description of the on-axis propagation of a pulsed Laguerre-Gaussian beam can be achieved through the analogy of a plane wave propagating through a dispersive medium, with the inhomogenous dispersion relation $n(\omega)$ of the hypothetical effective medium causing behaviour equal to that generated by the Gouy phase term.

Although not particularly noticeable with narrow bandwidths and lower order pulsed modes, similar associated effects have previously been described in relation to pulsed Bessel-Gauss beams in [HU02]. In that report the effects are suggested to represent a "spatially induced dispersion" (SID) which is a very suitable description of the behaviour.

4.2.1 – Elements of optical dispersion

In a famous experiment, Isaac Newton demonstrated the dependence of the refractive index on the colour of the light, thus proving the notion of dispersion, a variation in the velocities of light of different colours in transparent material. This thesis, and indeed a large proportion of literature relating to diffraction, has been primarily concerned with the free-space propagation of electromagnetic fields, where the permeability and permittivity result in a refractive index n that is normally approximated to be unity, equating the wavelength to that in a vacuum. The modern theory of dispersion is described through the bulk polarisation of the electrons in a medium acted upon by an oscillating electric field, see [BORN97]. When one is dealing with the interaction of broadband pulsed fields with optically dense materials such as those used in lenses, the variation in refractive index across the frequency spectrum of the pulse must be incorporated into any mathematical description.

The refractive index n of a material can be calculated by use of the Cauchy or, as given here, the Sellmeir formula:

$$n^2(\lambda) = 1 + \sum_j \frac{B_j \lambda^2}{\lambda^2 - C_j}, \tag{4.8}$$

where B_j and C_j are the "Sellmeir coefficients", determined from experiments. Note that in the above equation, λ is the radiation wavelength in a vacuum, assumed to be in μm, while the wavelength in the medium is given by $\lambda/n(\lambda)$. Table 4.1 below gives the Sellmeir coefficients, for λ in μm, for three frequently used forms of glass, with each coefficient corresponding to a resonance frequency of the material at which radiation of the corresponding wavelength is absorbed.

	Borosilicate (BK7)	Quartz (SiO_2)	Fluorite (CaF_2)
B_1	1.03961212	6.9616630×10^{-1}	5.675888×10^{-1}
B_2	2.31792344×10^{-1}	4.0794260×10^{-1}	4.710914×10^{-1}
B_3	1.01046945	8.974794×10^{-1}	3.8484723
C_1	6.00069867×10^{-1}	6.8404300×10^{-2}	2.5264299×10^{-3}
C_2	2.00179144×10^{-2}	1.1624140×10^{-1}	1.00783328×10^{-2}
C_3	1.03560653×10^{2}	9.8961610	1.20055597×10^{3}

Table 4.1 – Sellmeir coefficients of BK7, SiO_2, CaF_2. Reproduced from the Schott optical catalogue.

Figure 4.7 displays the variation of refractive index for BK7 using the data of table 4.1 in the Sellmeir relation of eq. (4.8).

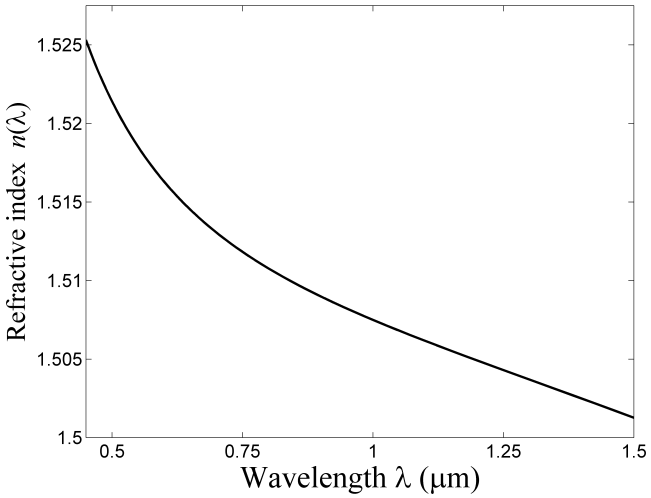

Figure 4.7 - The refractive index in BK7 for a Gaussian frequency spectrum with the central wavelength λ_0=800nm.

In an elementary sense, a variation of refractive index, $n(\omega)$, within a medium reduces the speed of a monochromatic wave with angular frequency ω from c to $c/n(\omega)$, therefore the wavenumber within the material is $n\,k$. The on-axis propagation of the m^{th} pulsed Laguerre-Gaussian beam mode can be calculated from

$$\xi_m(r=0,z,t)=\frac{1}{\sqrt{2\pi}}\int_{-\infty}^{\infty}\left\{\sqrt{2\Big/\pi\left(\frac{n(\omega)\omega w_0^2}{2cz}\right)^2}\exp\left(\tau^2\left(n(\omega)\omega-n(\omega_0)\frac{\omega_0}{c}\right)^2\Big/4\right)\right.$$

$$\left.\times\exp\left(i\,n(\omega)\frac{\omega}{c}\left(z-\frac{ct}{n(\omega)}\right)-i(2m+1)\tan^{-1}\left(\frac{2cz}{n(\omega)\omega w_0^2}\right)\right)\right\} \tag{4.9}$$

The primary phenomenon of concern in dispersive materials is the alteration of the pulse velocity that depends on the variation of refractive index across the frequency spectrum, which will also create a broadening in space and time due to a variation in velocity of each spectral component. Shown in Figure 4.8 is the structure of a plane wave pulse after propagation in borosilicate (BK7).

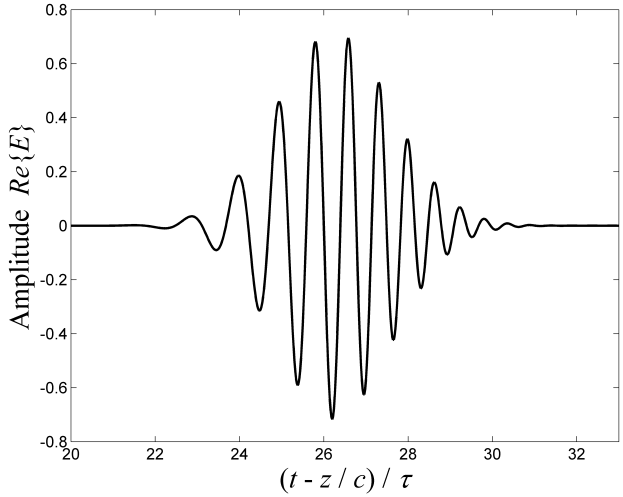

Figure 4.8 – Example of dispersion of a plane wave pulse in quartz (SiO_2). $\gamma = 0.5$, λ_0=800nm. Note the temporal delay, asymmetric broadening, and variation in wavelength along the pulse.

The effects of dispersion on the pulse are very evident in Figure 4.8. In that case, the group velocity of the pulse is reduced to ~0.6*c*, illustrated by the significant delay in comparison to a wave with group velocity of *c*. The variation of the individual phase velocities at each frequency creates an irregularity in the amplitude structure, commonly known as a chirp, along with a broadening of the pulse length. With the emergence of such a pulse from a dispersive material of length *L* into free space the increased pulse duration acquired by the wave train in the medium is maintained in free space, with the dispersed pulse trailing an ideal free space pulse by a distance of cL / v_g. This has significant consequences in the focusing of ultrashort femtosecond pulses by lenses, and will be applied in a later chapter. See also [BOR89,DENG05].

4.2.2 – Free-space dispersion effects in pulsed Gaussian fields

While the propagation of pulses is determined by a superposition of frequency components over continuous spectra, the addition of two individual monochromatic waves is a very simple demonstration for the calculation of the general properties of polychromatic wave-trains. Suppose two right-travelling waves of differing wavelengths, but equal velocities and wavelengths, are given by

$$E_1 = E_0 \sin(k_1 z - \omega_1 t) \text{ and } E_2 = E_0 \sin(k_2 z - \omega_2 t)$$

The sum of these two waves is given by use of the identity,

$$\sin(A) + \sin(B) = 2\sin\left(\frac{A+B}{2}\right)\cos\left(\frac{A-B}{2}\right)$$

which gives the total amplitude as

$$E_{total} = E_1 + E_2 = 2E_0 \sin\left(\frac{(k_1 + k_2)}{2} z - \frac{(\omega_1 + \omega_2)}{2} t\right) \cos\left(\frac{(k_1 - k_2)}{2} z - \frac{(\omega_1 - \omega_2)}{2} t\right)$$

and this results in a wave whose frequency is the average of ω_1 and ω_2 and the amplitude of which is modulated by the cosine term in the above expression. The velocity at which the phase of a sinusoidal travelling wave propagates is given by ω / k. However, in the expression of E_{total} as given above the total resultant wave is given by the superposition of a sine and cosine term, each representing waves with propagation velocities that may vary. For the disturbance defined by the sine term, the speed at which this wave energy propagates defines the *phase velocity* given by

$$v_p = \frac{\omega_p}{k_p}$$

where $\omega_p = (\omega_1 + \omega_2)/2$ and $k_p = (k_1 + k_2)/2$ are the average values of the angular frequency and wavenumber respectively of each individual wave. The multiplication of the sine term by the cosine term produces an amplitude modulated field evident in the total wave field by the appearance of clusters of nodes along the wave train, see Figure 4.9. The propagation rate of this modulating envelope, the *group velocity*, is calculated in the same manner as above, but results in a velocity given by

$$v_g = \frac{\omega_1 - \omega_2}{k_1 - k_2} = \frac{\Delta\omega}{\Delta k}$$

As the difference between wavelengths become infinitesimal, as is the case with continuous spectra, the general expression for the group velocity v_g is given by

$$v_g = \frac{d\omega}{dk}$$

which can, but not necessarily, equal the phase velocity v_p.

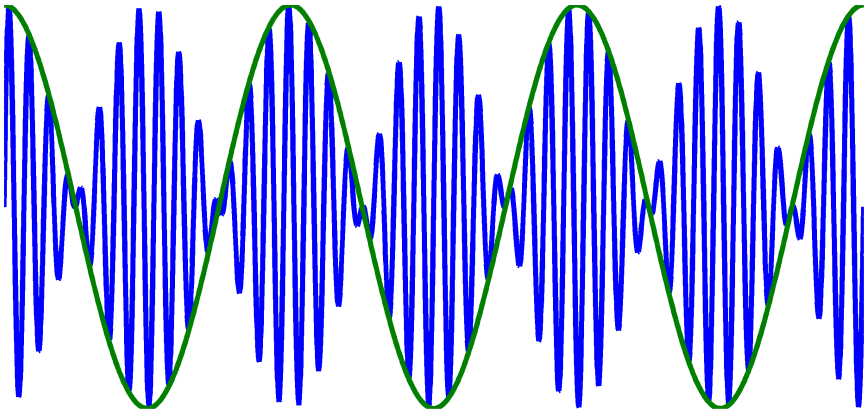

Figure 4.9 – Superposition of two sinusoidal waves of differing wavelengths. The red line indicates the amplitude modulation for which the group velocity is defined.

This expression for group velocity in general holds for multi-spectral fields. However, a more broad definition is given in [BORN97], with $\Delta\omega/\omega_0 << 1$, and expresses the group velocity as

$$v_g = \frac{1}{\left| grad\left(\frac{\partial \phi(x,y,z)}{\partial \omega} \right)_{\omega=\omega_0} \right|} \tag{4.10}$$

where ϕ represents the phase of each spectral component at each point (x,y,z). For pulsed plane waves $\phi(\omega) = \omega\ z\ /\ c$ giving $v_g = c$. A more practical expression for the group velocity of a pulse propagating in a dispersive medium with refractive index $n(\omega)$ can be derived from $d(n(\omega)\omega/c)\ /\ d\omega$ and is given in [PED93] as

$$v_g = \frac{c}{n(\omega_0) + \omega_0 \left. \frac{dn}{d\omega} \right|_{\omega=\omega_0}} \tag{4.11}$$

and essentially defines the velocity of the amplitude modulating waveform, [DENG05]. From the definition of a Gaussian beam given in chapter 2, it can be seen that the Gouy phase shift creates a variation of the *local* wavenumber proportional to the propagation distance z. For waves described by complex exponential or sinusoidal variations the local wavenumber of the field is calculated from the derivative of the phase term with respect to z [GOO05]. So, for a radially symmetrical Laguerre-Gaussian beam mode, the on-axis phase is

$$\phi(z) = k\,z - (2m+1)\tan^{-1}\left(\frac{2z}{k\,w_0^2}\right)$$

and using $\frac{\partial}{\partial x}\tan^{-1}(x) = \frac{1}{1+x^2}$, we can write the local wavenumber $\kappa(z)$ as

$$\kappa(z) = \frac{\partial\phi(z)}{\partial z} = k - \frac{2(2m+1)}{k\,w_0^2\left(1+\frac{4z^2}{k^2 w_0^4}\right)} \tag{4.12}$$

Now, to proceed with a formulation of the group velocity of the pulsed Gaussian beam, we can make an analogy with the propagation of a plane wave through an optically dense material. If the refractive index of a material such as glass or high density polyethylene is given by *n,* then an on-axis description of the monochromatic wave is given by

$$E(z,t) = \exp(i\,\kappa\,z - \omega t), \text{ with } \kappa = n\,k$$

Thus, the on-axis field of a Gaussian beam can be equated, after division of $\kappa(z)$ by, and substitution of, $k = \omega / c$, to a plane wave propagating through a hypothetical material with a refractive index that varies on the optical axis according to the propagation distance as

$$n_G(z,\omega) = 1 - \frac{2(2m+1)c^2}{\omega^2 w_0^2\left(1+\frac{4c^2z^2}{\omega^2 w_0^4}\right)} \tag{4.13}$$

$$\left.\frac{\partial n_G(z)}{\partial\omega}\right|_{\omega=\omega_0} = \frac{4(2m+1)\omega_0 c^2 w_0^6}{\left(4c^2z^2+\omega_0^2 w_0^4\right)^2}$$

Then we can write, using (4.11), for a short pulsed LG mode with index *m*

$$v_g^m(z) = \frac{c}{n_G(z,\omega_0) + \omega_0\,\frac{4(2m+1)\omega_0 c^2 w_0^6}{\left(4c^2z^2+\omega_0^2 w_0^4\right)^2}}$$

$$v_m^g(z) = c\left(1 - \frac{(2m+1)w_0^2(z^2 - Z_0^2)}{2(z^2+Z_0^2)^2}\right)^{-1} \tag{4.14}$$

where Z_0 is the confocal/Rayleigh distance for the central frequency component ω_0. Note that this expression is also valid for a one-dimensional Hermite-Gaussian pulse with a replacement of the mode indices $2m + 1 \Longrightarrow m + 1/2$, without interfering with the preceding derivation. This analytical result, equation (4.14), is verified by the numerical results depicted in the following plots for a "very" paraxial pulse, i.e. $w_0 / \lambda >> 1$, but

does naturally have restrictions beyond the paraxial regime that causes this prediction (4.14) to deviate from the true physical behaviour with $w_0 \leq \lambda$, based on the effects described in section 2.8.1. Porras et. al. describe such non-paraxial behaviour for the pulsed fundamental Gaussian beams in [POR02].

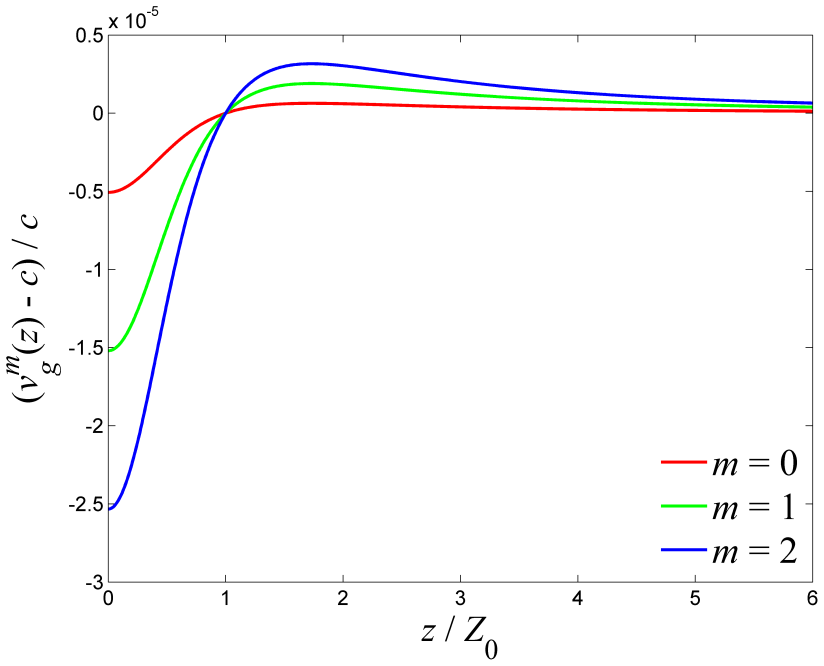

Figure 4.10 – The group velocity of an ultrashort pulsed Laguerre-Gaussian beam. λ_0=0.3mm, $w_0 = 100\ \lambda_0$, and $\gamma = 0.2$.

The group velocity of the pulse has a value $v_g < c$ at distances less than the confocal distance, but at $z = Z_0$ its speed has increased to c and acquires a greater *group* velocity, which reaches a maximum superluminal value at $z = \sqrt{3}\,Z_c$ beyond which the group velocity decreasingly converges upon the vacuum speed of light. The temporal delay of the m^{th} pulsed LG mode at a plane z can be determined by accounting for the delay incurred within each previous infinitesimal distance dz'.

$$\Delta t_m(z) = \int_0^z \frac{dz'}{v_g^m(z')} = \frac{2c\,(2m+1)\,w_0^2\,z}{4c^2 z^2 + w_0^4\,\omega_0^2}$$

Figure 4.11 shows the variation of the temporal delay, Δt_m, of Laguerre-Gaussian beam modes due to the Gouy phase shift, quantified by the difference in their arrival time at a plane to that of a plane wave pulse with equal duration and bandwidth.

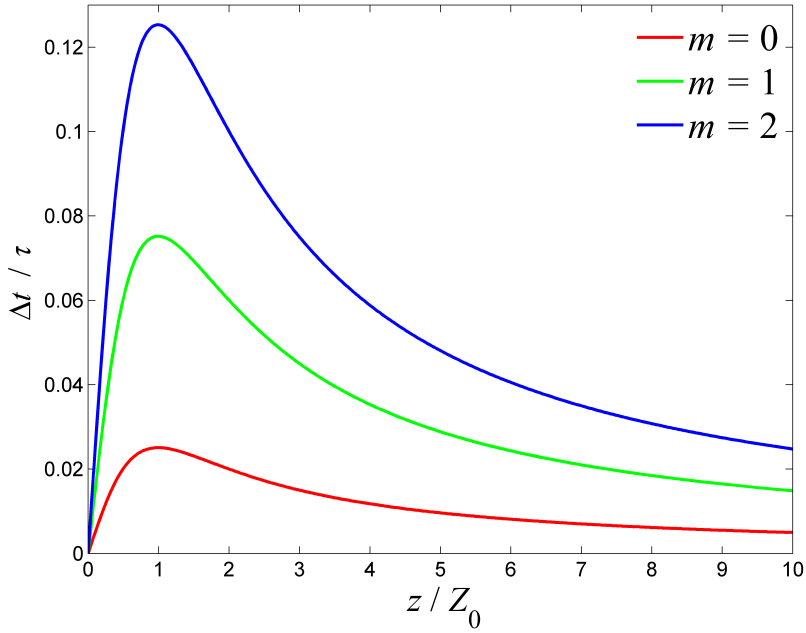

Figure 4.11 – The temporal on-axis delay, Δt, of the amplitude envelope peak of a pulsed Laguerre-Gaussian mode at a plane z. The delay is shown relative to the value of τ. $\lambda_0 = 0.3$ mm, $w_0 = 100\ \lambda_0$, $\gamma = 0.2$.

For Laguerre-Gaussian pulses with $m > 0$, the variation in delay follows the same trend as those of the fundamental fields but with increased magnitude, with each mode showing a maximum delay from z / c at the confocal distance Z_0 which has a magnitude of

$$(\Delta t_m)_{\max} = \frac{m + 1/2}{\omega_0}$$

The increased delay in detection of the modes of higher indices is determined by the Gouy phase shift and is found to be $(2m+1)$ times the shift of the $m = 0$ mode, [VAS09].

With numerical simulation of the propagation of pulsed LG modes using eq.(4.7) further phenomena involving the pulse structure are identified. One such effect observed in this work is that of free-space temporal and spatial broadening of the pulsed LG modes, particularly in the near field of their propagation. At the source ($z = 0$), the duration of the LG pulses is consistent with that of a pulsed plane wave with the same signal modulation. But as z increases, the duration of the detected pulse, $2\tau(z)$, reaches a maximum value before the confocal distance, and converges to a value that slightly exceeds the original duration 2τ. See Figure 4.12.

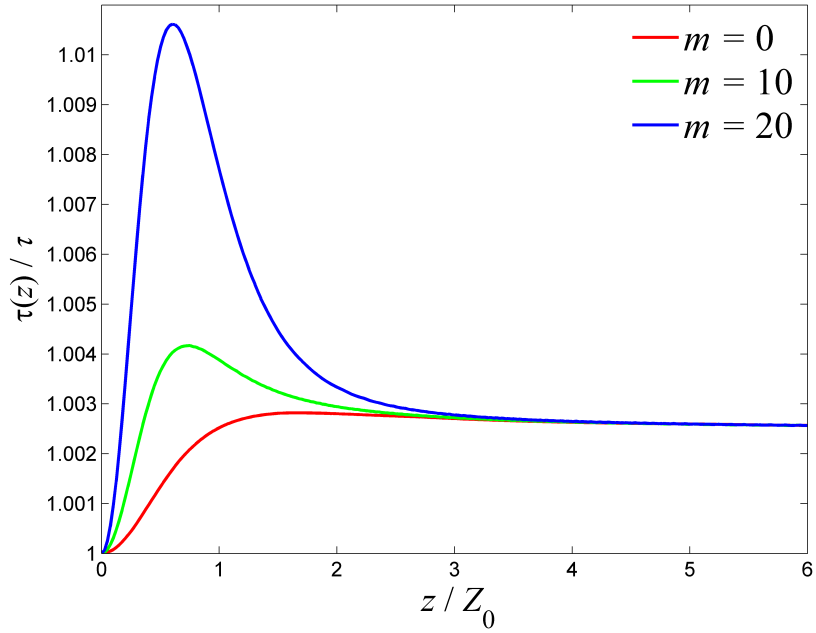

Figure 4.12 – Free-space pulse broadening of a pulsed Laguerre-Gaussian beam. The variation is described in relation to the original duration of the pulse τ at the source. γ = 0.2, λ_0 = 0.3mm. w_0 = 100 λ_0.

The comparison of pulsed plane waves with ultrashort LG modes in Figure 4.6 does not exhibit the variation in amplitude, which has been normalised to that at its source for easier assessment. However, the dispersion-like effects observed in the near field create a deviation in the amplitude fall-off of the LG modes compared to the monochromatic amplitude variation given by $\sqrt{2/\pi\, w(z)^2}$ (or $w_0/w(z)$ when normalised to the amplitude value at z = 0). This divergence from the continuous-wave field strength is brought about by the pulse broadening depicted in Figure 4.12, and in conserving energy the peak axial amplitude of the pulse envelope is reduced in regions where pulse expansion occurs. Shown below are examples of the longitudinal envelope peak amplitude at increasing distances for LG pulses with various mode indices.

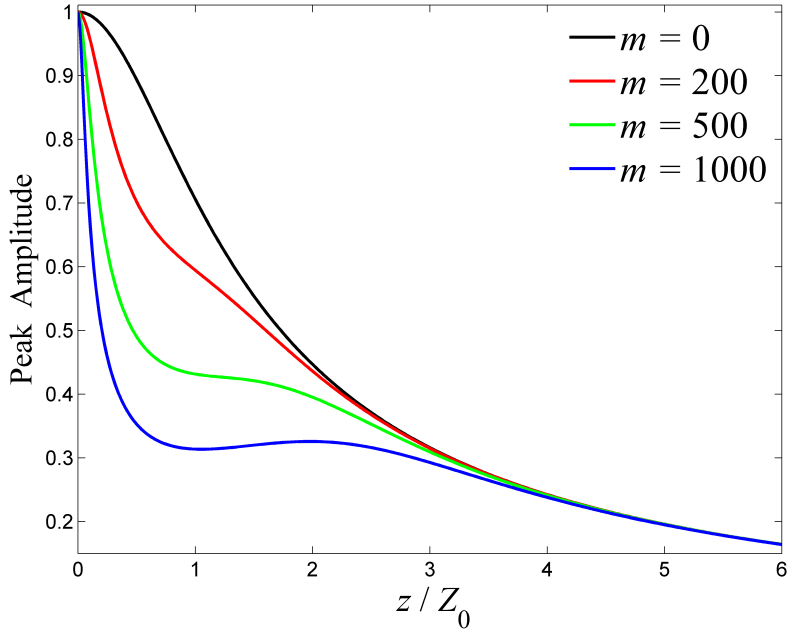

Figure 4.13 – The normalised variation of the maximum on-axis amplitude of Laguerre-Gaussian pulses at distance z. Calculated with $\gamma = 0.2$, $\lambda_0 = 0.3$ mm, $w_0 = 100\ \lambda_0$.

For consistency with the preceding plots a value of $w_0 = 100\ \lambda_0$ was used in calculating the data of Figure 4.13, and modes of extremely high indices were required to illustrate the behaviour of the on-axis amplitude. With smaller values of w_0 / λ, these effects are much more obvious in the propagation of lower index modes. As a point reference, the variation of the peak axial amplitude in the case of $m = 0$ deviates only negligibly with these parameters from that of the corresponding continuous wave mode, $w_0 / w(z)$.

The pulses described in the preceding text have the common feature of more than one oscillation over the pulse duration 2τ and generally exhibit similar spatial and temporal features in relation to this time. In the case of signals with less than one significant cycle within the pulses defined duration, the behaviour of Gaussian beam modes driven by such a short impulse show significant deviation from those described previously, with a large increase in the relative temporal delay and broadening. See Figure 4.14.

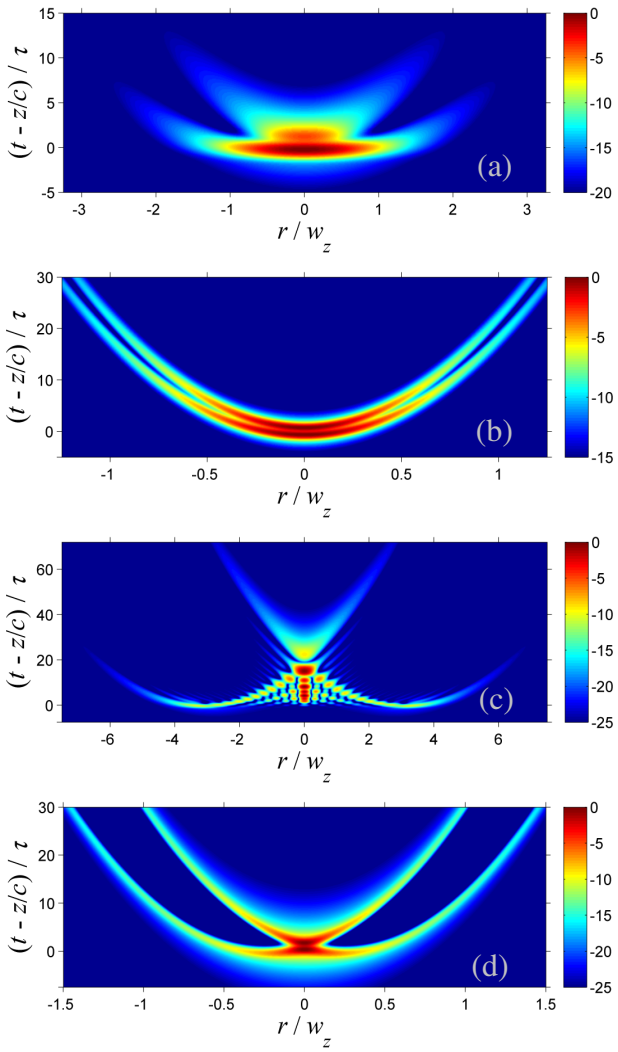

Figure 4.14 – The structure of the (a) - (b) $m = 0$ and (c) - (d) $m = 10$ Laguerre-Gaussian pulses with an extremely wide bandwidth, $\gamma = 4$, $\nu_0 = 1$ THz, $w_0 = 100\ \lambda_0$. The fields are calculated at $z = Z_0$ in (a) and (c), and at $z = 20\ Z_0$ in (b) and (d).

The validity of the fields plotted in Figure 4.14, with $\gamma = 4$, is questionable. With such a large bandwidth, similar calculations involving significant wavelength components in the spectrum that are much larger relative to the beam dimensions will cause divergence beyond that accounted for in the paraxial regime. However, the propagation of fundamental paraxial Gaussian pulses with similar "ultrawide" bandwidths has been explored in [ZIO92], with the fields exhibiting the same structure of Figure 4.14 (a) and (b), and with a large value of w_0 / λ the predictions should maintain some accuracy along the optical axis.

4.3 – Diffraction of an ultrashort pulse at a circular aperture using Laguerre-Gaussian pulse modes

The knowledge obtained of pulsed Laguerre-Gaussian beams in the previous sections can now contribute to a more practical numerical application, the prediction of pulse dynamics diffracted by general aperture functions. Instead of using the Fresnel integral, the calculation can be simplified using the Gaussian beam mode expansion for each monochromatic spectral component. We can apply the calculation of mode sets for each individual frequency in the pulse spectrum, but in the modelling of an aperture transmission function that is independent of wavelength, i.e. those that affect only the amplitude of the illuminating wavefront, the mode sets are equivalent for all wavelengths which allows for very efficient execution of numerical simulations. In the case of optical elements such as lenses, with the aperture function $\exp(i\omega r^2/2cf)$, the structure of the field at the source varies according to frequency, therefore an overlap integral is required for each individual monochromatic component.

For a phase independent aperture, replacing the monochromatic diffraction integral in (4.4) with the Gaussian mode expansion, eq. (2.37), the field of a pulse diffracted by an aperture can now be written as

$$E(r,z,t) \cong \frac{1}{\sqrt{2\pi}} \int_{-\infty}^{\infty} S(\omega) \left(\sum_{m=0}^{M} A_m \psi_m^L(\omega, r, z, t) \right) \exp(-i\omega t) \tag{4.15}$$

This form of calculation will be applied in the description of modulation of pulses by diffractive optical elements in chapter five. However, in this chapter we present the calculation of general pulses as a sum of ultrashort Laguerre-Gaussian modes described in section 4.2.

If we assume the aperture $E_0(r_0)$ to be an amplitude modulation only with no variation of the transmission properties across the frequency spectrum, then the mode set A_m is constant for all frequency components, and we can then interchange the summation and integral in (4.15) to give

$$E(r,z,t) \cong \sum_{m=0}^{M} A_m \xi_m(r,z,t) \ , \tag{4.16}$$

where the modal constituents of the field now have the form of pulsed LG modes ξ_m

$$\xi_m(r,z,t) = \frac{1}{\sqrt{2\pi}} \int_{-\infty}^{\infty} S(\omega)\, \psi_m^L(\omega, r, z, t)\, d\omega \tag{4.17}$$

a simplified form of eq. (4.7). Therefore, instead of a superposition of monochromatic waves, eq. (4.16) represents the diffracted field of a pulse through summation of individual and independently propagating pulses which the author believes to be a novel interpretation of the physical situation. We will show in the following pages how features of pulse diffraction by an aperture can be described intuitively through the behaviour of the individual modes as described in the previous section.

In practical terms, we can solve for the diffraction of pulses by an aperture using eq. (4.15) or eq. (4.16). But when using Matlab^{TM}, in which Laguerre polynomials have to be defined through customised recursive methods, eq. (4.15) is the most efficient description, as it reduces the number of times that such functions have to be calculated. The advantage of the GBM expansion of pulses over the conventional diffraction integral techniques, as with cw calculations, is that once the mode coefficients have been determined, which can be speedy, the calculation of diffraction effects no longer relies on the sampling rate of the aperture function, which, particularly for oscillatory transmission functions, can be necessarily large. At further distances from the aperture the complexity of the diffraction calculation can be reduced by truncating the sum at lower values of M without any detrimental effects on the accuracy of the pulse field calculation, in regions within the limited transverse extent of the modes. As a novel approach, in this chapter we will discuss pulse simulation using (4.16), paying attention to the properties of PGBMs as described in the previous section.

It *may* be possible to obtain an analytical solution for $\xi_m(r,z,t)$ in the far-field, particularly if an idealised pulse spectrum is based on the exponential function which could be combined with the Gaussian amplitude and exponential phase terms of the LG modes. This was shown in [ZIO92] with the authors deriving approximate expressions for the propagation of an ultrashort pulsed fundamental ($m = 0$) Gaussian mode, but for the specific Gaussian temporal pulse shape. A similar derivation for higher order LG and HG pulses would allow for a very efficient method, eliminating the time expense in equation (4.17), but here, for generality, we employ numerical calculation of each pulsed LG mode without restricting the technique to one particular form of temporal signal.

In the following example of pulse propagation we show the near-field on-axis diffraction effects of a pulse with $\gamma = 0.2$, diffracted by a circular aperture with radius $a = 25\lambda_0$, calculated using (4.16) with $M = 500$. We define the carrier angular frequency as $\omega_0 = 6.28\times10^{12}$ rad / s corresponding to a frequency of $\nu_0 = 1$ THz (λ_0~0.3mm), and

the radius of the aperture is 7.5mm. However, we will present the results with a generic description of the diffraction parameters based on the Fresnel number of the optical system at the carrier wavelength, $N_F = a^2/(\lambda_0 z)$. See Figure 4.15.

As seen in the following Figure 4.15, the diffraction of a pulse at a hard aperture is apparent in the form of a boundary wave that trails the geometric wave on the optical axis. This is an artefact of the generation of spherical pulsed waves by Huygens' sources at the edge of the aperture and is a more evident feature in the near-field of the propagation, see also Figure 4.3. At a time t, the boundary waves are centred at the edges of the aperture and manifest themselves on the axis at a position of

$$z = \sqrt{c^2 t^2 - a^2},$$

and in the time domain the boundary waves are detected at a given plane at the time

$$t = \frac{\sqrt{z^2 + a^2}}{c}.$$

Under the paraxial approximation there are deviations from this value at distances very close to the aperture, with the boundary waves predicted to arrive at a plane z at a time of

$$t = \frac{z}{c} + \frac{a^2}{2cz}. \tag{4.18}$$

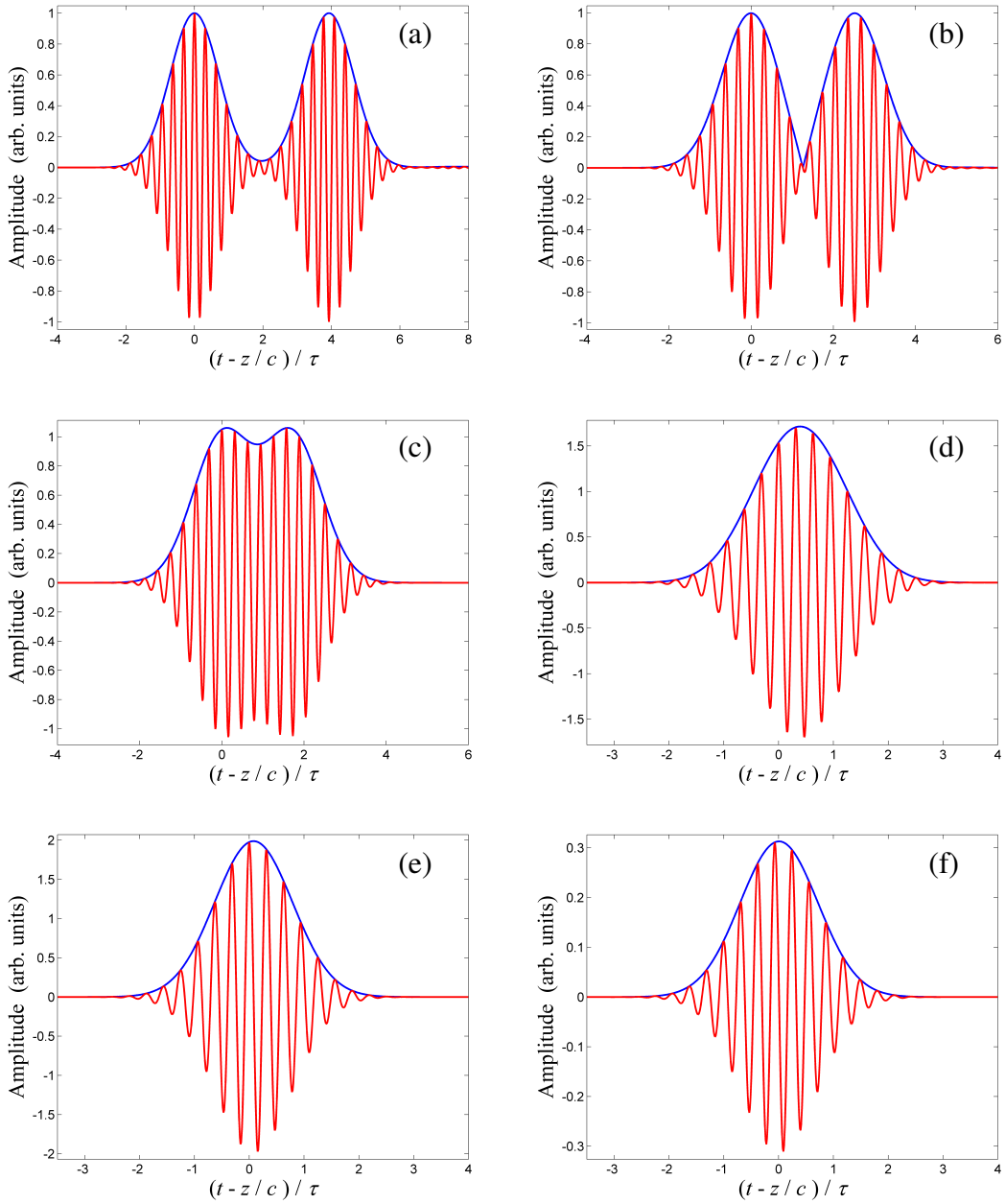

Figure 4.15 – The on-axis field $Re\{E(r = 0,z,t)\}$, in red, and the envelope $|E(r = 0,z,t)|$, shown in blue, of a paraxial pulse truncated by a circular aperture, with increasing distance, $N_F = a^2/\lambda_0 z$ = (a) 25, (b) 16, (c) 11, (d) 5, (e) 1, (f) 0.1, using $M = 500$, $\gamma = 0.2$.

As the propagation distance increases, the position of the secondary peak increases towards the primary pulse, with superluminal velocity, until both pulses converge upon each other. When this occurs both peak features interfere to cause a further delay of the pulse maximum from the plane wave arrival time $(t - z / c) = 0$ as well as an increase in amplitude, see Figure 4.15 (c) and (d). This feature is discussed in detail in [MEN07], where the authors discuss the application of the Rayleigh-Sommerfeld integral to the analysis of this axial phenomenon.

The occurrence of the secondary on-axis pulse is not so apparent with longer pulses (i.e. narrow spectral bandwidths) in which case there is an overlap of the main geometric pulse with the boundary waves. In the case of extremely short pulses the effect becomes more pronounced when the narrow pulse length creates an evident on-axis trailing feature over a much greater distance into the far-field.

As well as affecting the valid transverse range of the mode, see Figure 2.17, truncation of an LG series to a finite number also restricts the longitudinal representation of a pulsed field more obviously at planes close to the aperture with very large Fresnel numbers, see Figure 4.16. Even when accurate convergence to the Fresnel result is obtained using a truncated LG expansion, one mode (with index $m = M$) becomes more evident in the near-field reconstruction, as there are no higher order modes with which this mode interferes and this causes divergence from the desired signal at that modes position. Yet, in the case of a $M = 500$ calculation used in the previous example the peak of the highest order mode, including the mode coefficient factor, occurs in the normalised axial near-field at approximately -50dB near the aperture, which is a negligible variation from the diffraction integral method.

The process of calculating the on-axis amplitude for a pulse using the GBM method is swift and we can describe the longitudinal on-axis field calculation with various values of M using the complete mode set and compare the result with that of the Fresnel diffraction integral. Calculated at $r = 0$, and $z = a^2 / 20\lambda_0$, the temporal amplitude patterns in Figure 4.16 and Figure 4.17 show the presence of the predicted boundary wave on the optical axis at a later time (~8τ).

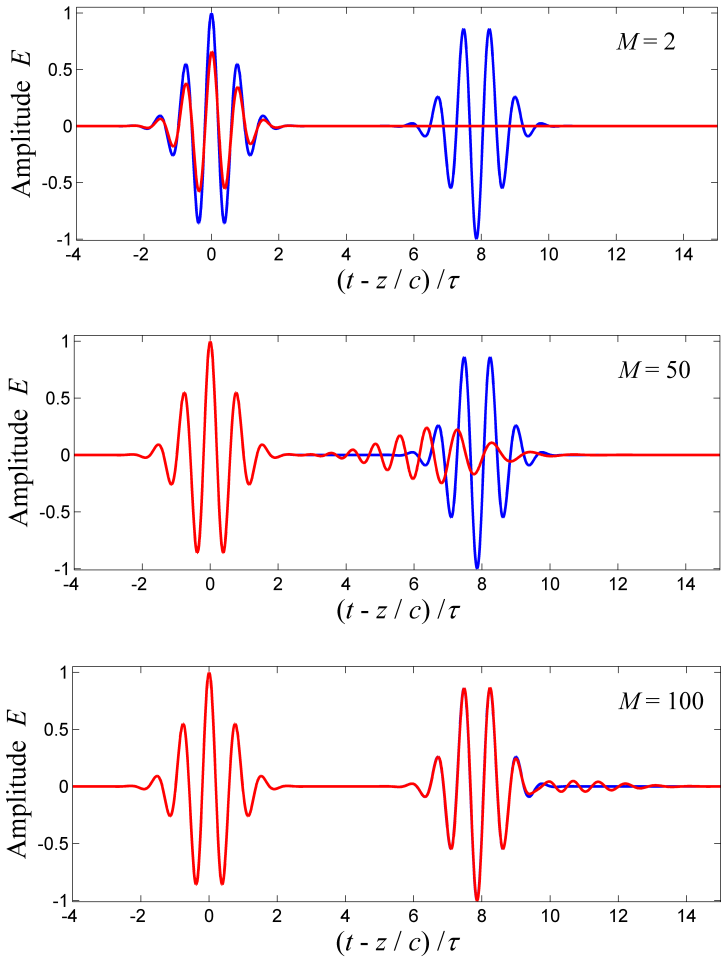

Figure 4.16 - The convergence of the on-axis pulsed Gaussian beam synthesis given by (4.16) (in red) to the Fresnel diffraction integral solution (blue) at $z = a^2/(20\lambda_0)$, with varying sizes of the mode sets. The aperture radius $a = 25\ \lambda_0$, λ_0=0.3mm, $\gamma = 0.5$.

In Figure 4.17, it is seen that in the very near-field of the aperture, $N_F = 20$, a relatively large number of modes is required for the result to converge to a sufficiently accurate result just as in continuous wave simulations. However, at further distances from the aperture, the field can be calculated using a significantly smaller mode set with negligible loss of accuracy, significantly reducing the computation time. Figure 4.18 shows the variation of the normalised mean squared error between the on-axis LG synthesis, from eq. (4.16) compared with the prediction of the Fresnel diffraction integral eq. (4.4) for various values of the Fresnel number $N_F = a^2/(\lambda_0 z)$.

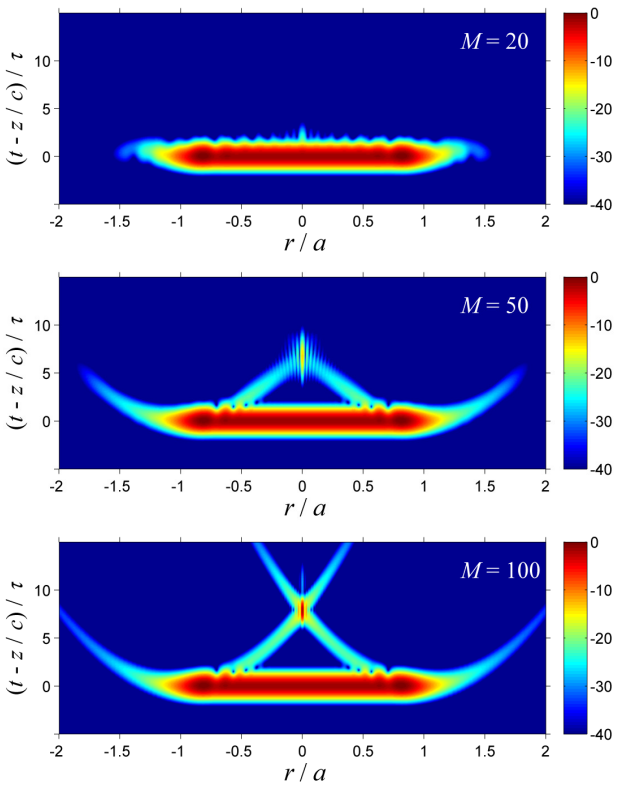

Figure 4.17 – Two-dimensional reconstruction of $|E(r,z,t)|$ with the same parameters as used in Figure 4.16, at $z = a^2/20\lambda_0$. Shown with a dB scale with the field normalised to the maximum value of $|E|$.

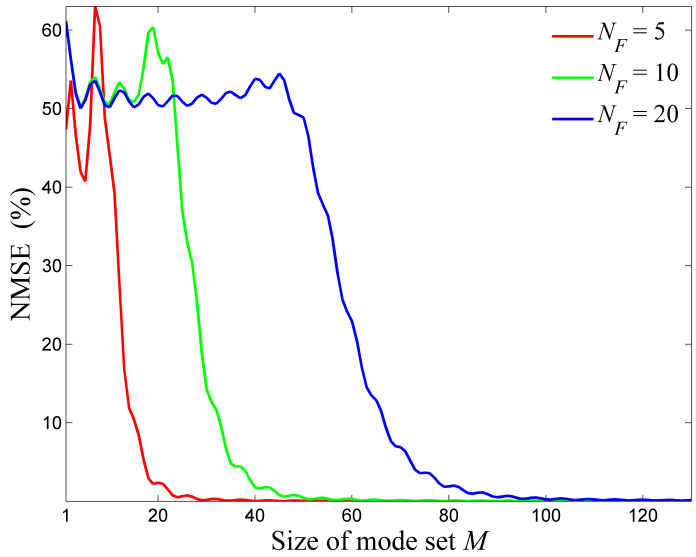

Figure 4.18 – The normalised mean squared error (NMSE) of the LG expansion of a $\gamma = 0.5$ Gaussian temporal pulse diffracted by an aperture of radius $a = 25\ \lambda_0$.

Figure 4.19 shows results of a two-dimensional beam mode calculation at various distances in the diffraction scenario described above using a superposition of

501 pulsed modes, allowing for transverse calculation of the field well beyond the angular region of paraxial applicability.

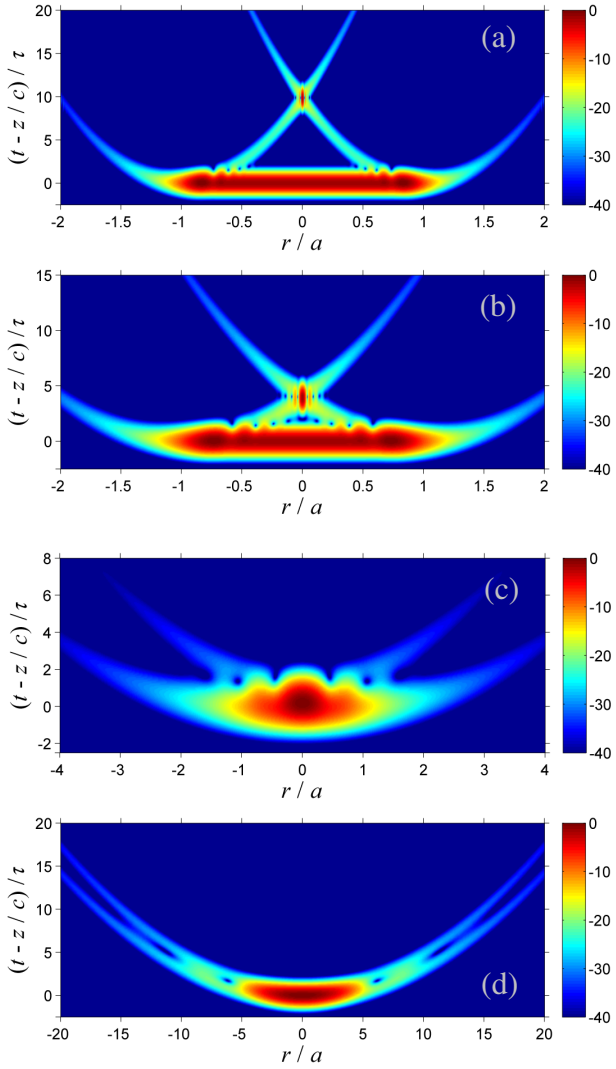

Figure 4.19 – The temporal form of a pulsed plane wave intensity $|E|^2$ diffracted by a circular aperture at $a^2 / \lambda_0 z$ = (a) 25, (b) 10, (c) 1, (d) 0.1, using the pulsed GBM expansion eq.(4.16). $\gamma = 0.5$, $\nu_0 = 1$ THz. The fields are shown with a logarithmic dB scale normalised to the maximum amplitude value.

Now, a comment on the reconstruction of such fields with a Gaussian beam mode expansion is necessary. In our formulation of pulse diffraction as a superposition of ultrashort LG modes given by eq. (4.17), the reconstruction of the trailing boundary wave in the near-field, as depicted in the preceding figures, is made possible by the "dispersive" properties of the higher order modes described in section 4.2. Boundary waves are reconstructed only with a synthesis that includes a large number of pulse modes, and this is because of the similarity in propagation between these features and the higher order pulse modes. Like the pulsed Gaussian beam modes, the on-axis

manifestation of the boundary waves also has a superluminal velocity. The on-axis feature is generated by the interference of the spherical boundary waves and first appears on the axis at $z = 0$ at a time of $t = a / c$. See Figure 4.20.

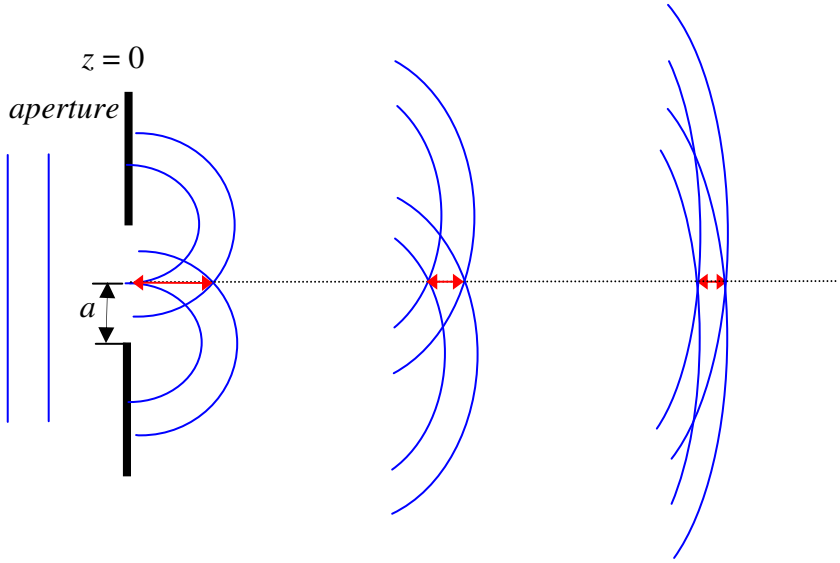

Figure 4.20 – Schematic of boundary wave propagation from a hard aperture.

The length of the on-axis feature caused by the boundary waves, symbolised by the red arrows in Figure 4.20, decreases with increasing z which is similar to the spatially induced dispersive behaviour of the gaussian beam mode pulses, which show significant expansion in their near-field propagation, as shown in Figure 4.12.

With an increasing mode number m the group velocity of a pulsed GBM at $z = 0$ decreases, see Figure 4.10, thus it is only with high order gaussian pulses that the delay in the formation of the on-axis boundary wave feature begins to be mimicked. This is also in accordance with the GBM synthesis of the circ function described in chapter 2, where the discontinuity at the aperture boundary is simulated more accurately with larger values of M, thus the formation of boundary waves in a pulsed GBM diffraction calculation is an obvious exhibition of an accurate aperture synthesis.

With increasing z the high frequency axial boundary waves converge upon the main geometric wave, and likewise the delay between the fundamental and the higher order pulsed mode components becomes less significant. Then, in the far-field the GBM solution can converge with a much smaller number of modes (within the transverse distances allowable by the finite extents of the modes). As an example, for the predicted field shown in Figure 4.19 (c) a similar calculation using $M = 80$ gave negligable deviation within the region shown from the field values obtained with the $M = 500$ series, and for the data in Figure 4.19 (d) a superposition of 11 modes was sufficient to

reconstruct the same field. This adaptable approach of the modal technique is one of the primary advantages of the GBM calculation of pulses over the use of diffraction integrals.

The similarity in structure of the pulsed modes and the boundary wave are highlighted in a further example, which also shows the applicabilty of the method with a somewhat more arbitrary source. We can easily illustrate the diffraction of a pulse by the aperture function given by

$$E_0(r_0) = \left(1 + \mathrm{sgn}\left(\cos\left(\frac{5\pi\, r_0}{2a}\right)\right)\right)/2 \tag{4.19}$$

using the Laguerre-Gaussian expansion, with coefficients as shown in Figure 4.21.

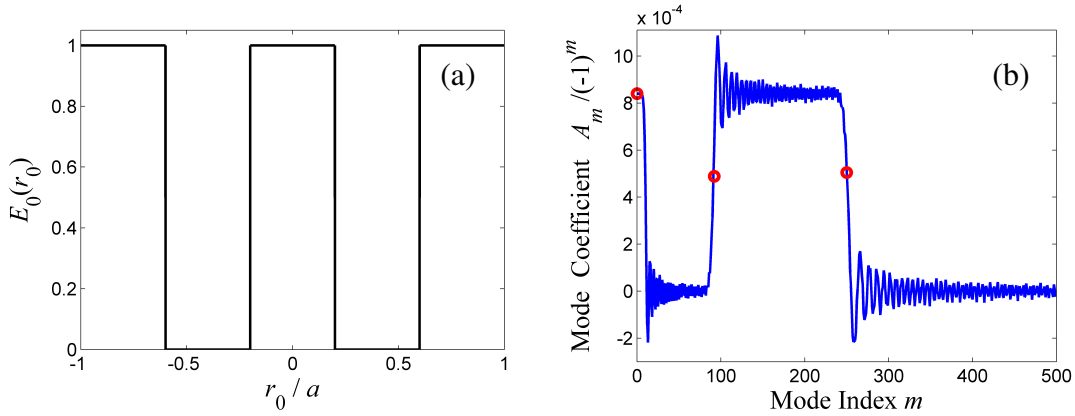

Figure 4.21 – (a) The aperture function defined by eq. (4.19), and (b) the Laguerre-Gaussian mode coefficients of the same function.

The red symbols in Figure 4.21 indicate the positions in the mode set of the fundamental m = 0 LG mode, and the m = 91 and m = 250 modes, with the effective extents of the latter two modes coinciding with the two outer discontinuities of the aperture in Figure 4.21 (a). In Figure 4.22 the pulsed modes with the indices, ξ_0, ξ_{91}, and ξ_{250}, are overlaid with the total pulse field emerging from the aperture calculated with the complete mode set shown in Figure 4.21 (b). The association of the behaviour of these individual modes with the formation of the geometric and boundary waves can be clearly seen.

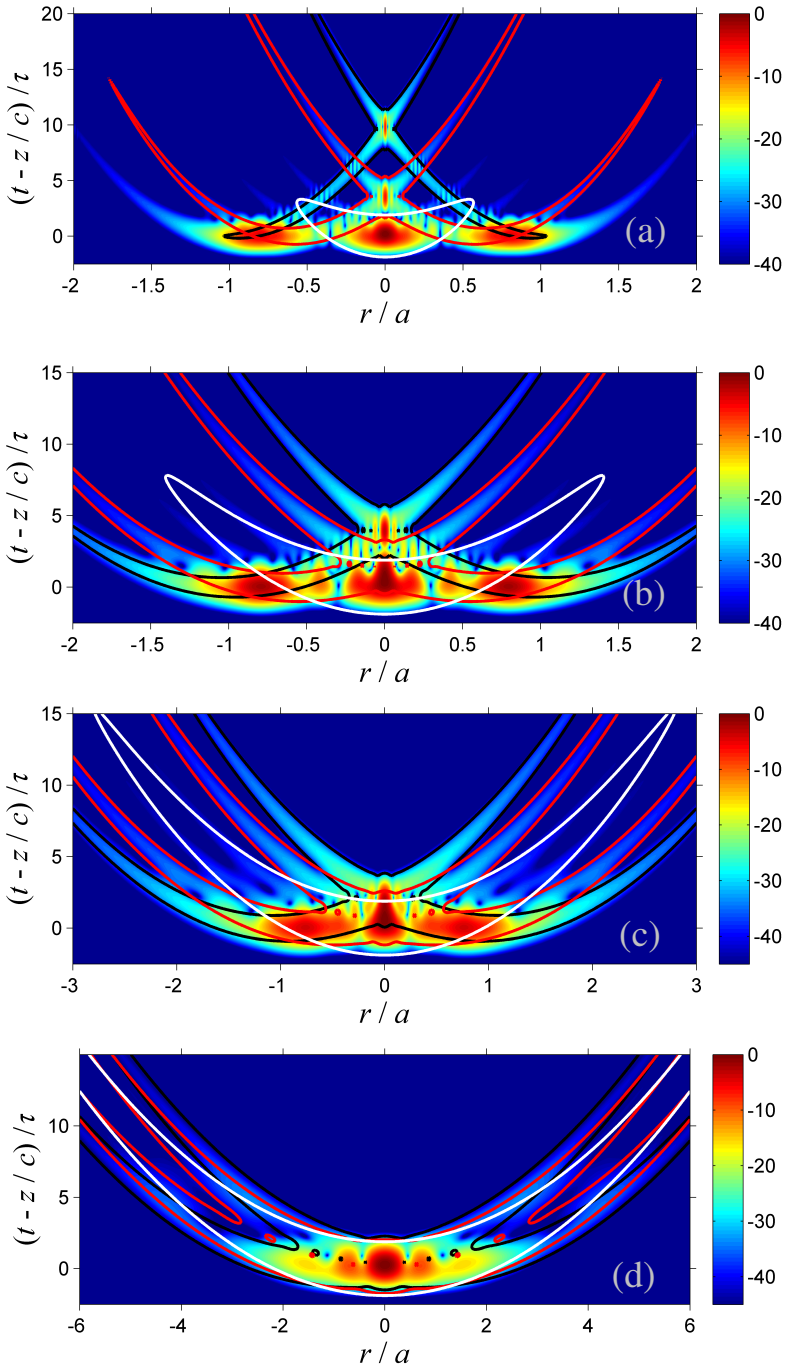

Figure 4.22 - False-Colour map of the diffraction of a pulse with $\gamma = 0.5$ by the amplitude grating defined by eq. (4.19) as calculated using eq. (4.16), with $a = 25\ \lambda_0$, and $M = 500$. Calculated at z = (a) $a^2 / 25\lambda_0$, (b) $a^2/10\lambda_0$, (c) $a^2/5\lambda_0$. The -30dB contours of the normalised pulsed LG modes with $m = 0$ (white), $m = 91$ (red), and $m = 250$ ($M/2$) (black), are shown to exhibit the roles of these modes in the pulse synthesis.

For propagation within dispersive media, the diffraction effects of an aperture can also be determined with a GBM analysis. But it must be noted that within a dispersive medium the duration of the field is increased significantly thus higher sampling of the frequency spectrum is required to eliminate temporal aliasing effects in

the calculation that may overlap with the desired field. However, even in this more time-consuming calculation the GBM method again showed its efficiency over the diffraction integral approach. Figure 4.23 shows the propagation of a $\gamma = 0.4$ pulse in a dispersive media after diffraction by a circular aperture with radius $a = 25\ \lambda_0$.

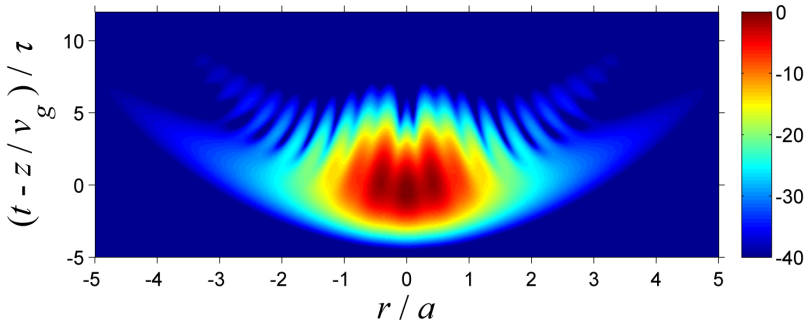

Figure 4.23 - Propagation of a $\gamma = 0.4$ field in BK7 after diffraction by a circular aperture. Predicted at $z = a^2 / (\lambda_0 z) = 1$. $\lambda_0 = 800$nm is the central wavelength of the spectrum in free-space . Dispersion has broadened the pulse to approximately 2.3 times its original duration.

The effects shown in Figure 4.23 have great significance in determining the dynamics of pulses modulated by transparent optical lenses. Dispersion will be discussed further in a later chapter, where we will apply the techniques presented here in the prediction of pulse behaviour after modulation by disperive lenses.

4.4 - Amplitude smoothing of time dependent pulsed fields

With narrow bandwidths the near-field diffraction pattern of an ultrashort pulse, recorded at the main pulses arrival time $t = z / c$, is similar to that of the cw beam ($\gamma = 0$) in terms of its overall structure and dimensions, but the increase in the spectral bandwidth (reduction in pulse duration) does cause a smoothing of the diffraction pattern, with an elimination of the narrow high frequency features observed within continuous fields. Each spectral component produces a different diffraction pattern which interfere causing a smoothing of the transverse amplitude structure, as described in Figure 4.24. Note that in this section the plots represent the transverse instantaneous diffraction patterns at the plane z at a time $t = z / c$.

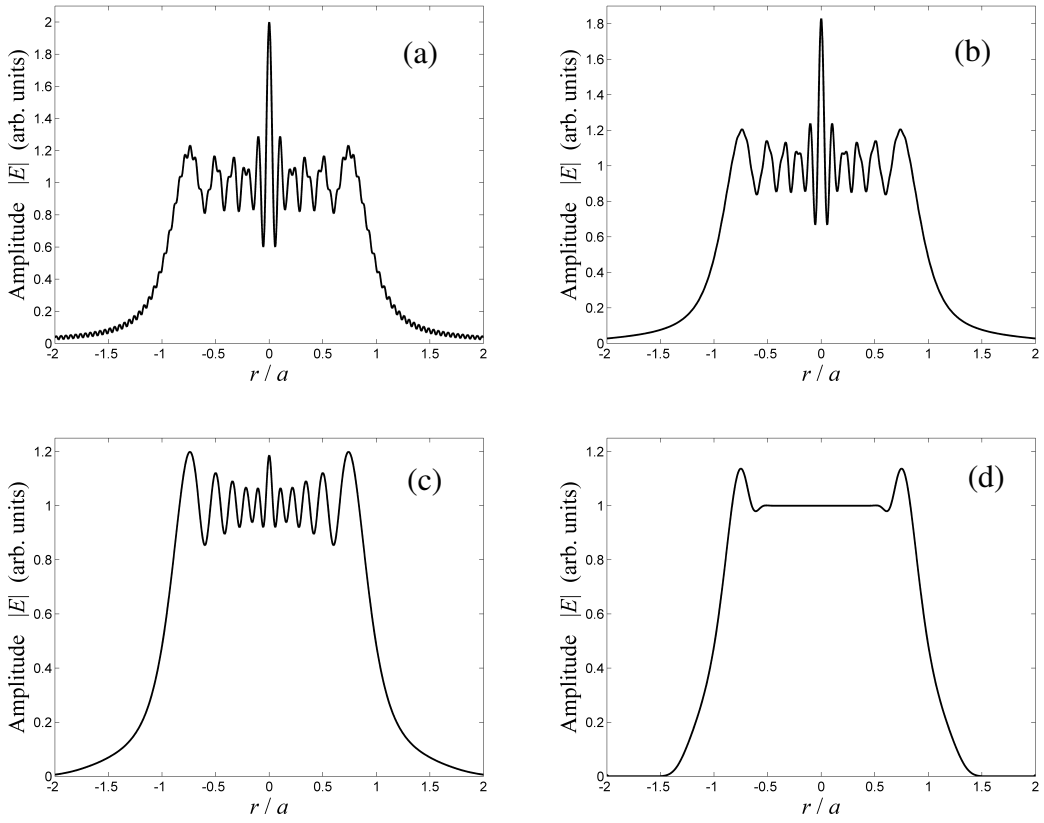

Figure 4.24 - The effect of the pulse bandwidth on the near-field diffraction pattern of a circular aperture at $z = a^2/(11\ \lambda_0)$, with $\lambda_0 = 0.3$ mm and $a = 25\ \lambda_0$. γ = (a) 0, (b) 0.05, (c) 0.15, (d) 1.

We know that for an infinitely long continuous wave field Huygens principle states that the field at any point is formed by the superposition of spherical waves derived from every point of a diffracting aperture, thus the field at any point consists of all possible frequency components defined by the location of the point in the diffraction plane and the dimensions and structure of the aperture. However, in the near field of a diffracted pulsed wave the high frequency wave-vectors, such as those involved in the formation of the boundary waves at the edges of the aperture, are separated in space and time from the geometric part of the field which has wave-vectors which are close to being parallel to the optical axis. Thus, the field at a constant transverse plane near the aperture does not, for the most part, contain the full range of spatial wave vectors created by diffraction at the aperture at any one instant, resulting in the effects shown in Figure 4.24.

Figure 4.25 shows this effect in two dimensions with a field diffracted by an one-dimensional aperture and scattered by an arbitrarily shaped dielectric structure, as calculated using the finite-difference time-domain method.

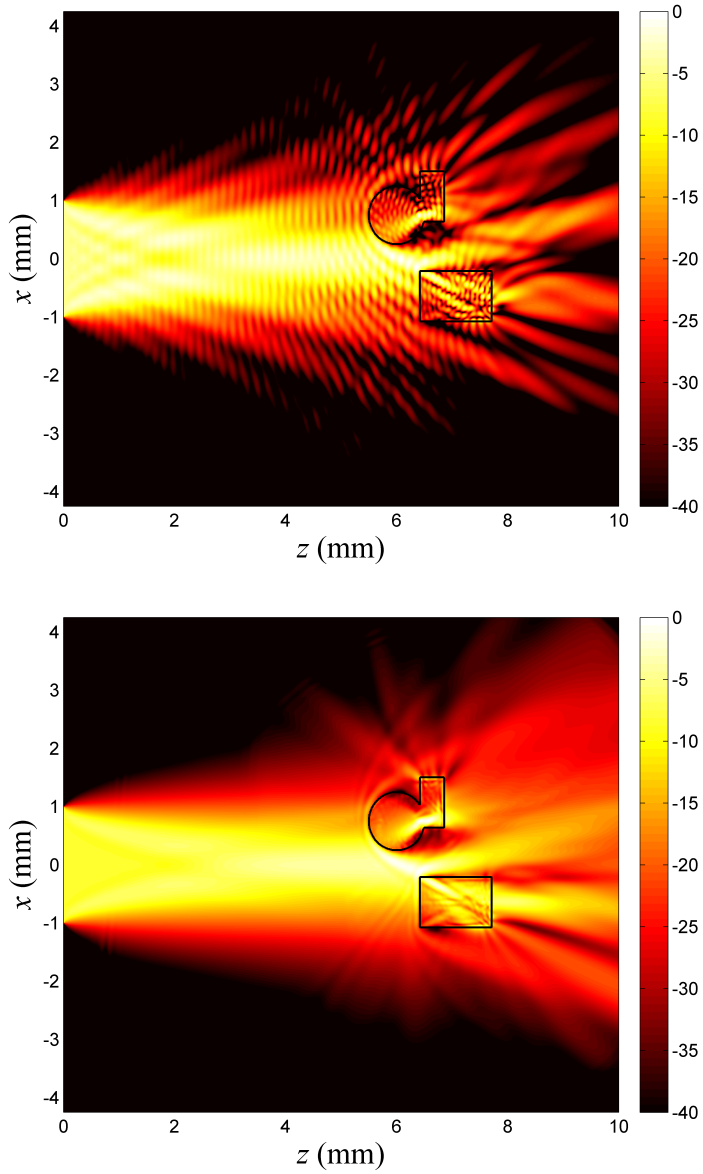

Figure 4.25 – The time-averaged intensity in the diffraction plane of a one-dimensional aperture illuminated by (a) a continuous plane wave, and (b) a broadband $\gamma = 1$ Gaussian pulse. $\lambda_0 = 0.3$ mm. (dB scale).

The duration of the pulse signal affects the transverse amplitude variation at all planes for $z > 0$, but in the far-field the effects are somewhat different from those shown in Figure 4.24; the narrower longitudinal beam length combined with a smaller radius of curvature of the pulsed wavefront at greater distances means that a transverse measurement of the field at a constant plane z shows a beam with a greatly reduced width with larger bandwidths. While the near-field diffraction patterns of Figure 4.24 generally maintain their original spatial width with increasing bandwidth, Figure 4.26 shows that the duration of a pulse significantly affects the beam width of the

instantaneuous intensity distribution at the far-field plane $z = c\ t$, with elimination of the side lobe structure and significant narrowing of the measured field.

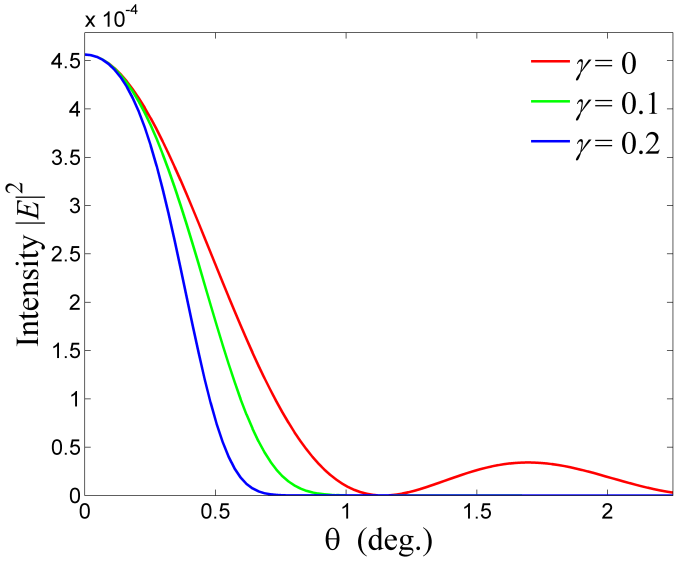

Figure 4.26 – Far-field pattern of a plane wave field diffracted by circular aperture with varying bandwidth of a Gaussian modulating signal, calculated at a time $t = z / c$, with $z = 100\ a^2/\lambda_0$.

These aspects of pulsed diffraction could be important in the design of pulsed imaging systems where the illumination of a sample with complete coverage at any given time is required. The effects shown are also somewhat related to the smoothing of irradiance distributions formed by incoherent polychromatic white light, which explains why the high frequency ringing seen in continuous wave diffraction patterns described throughout this thesis are rarely seen visually outside of laser laboratories.

4.5 - Diffraction induced variation of pulse spectra

While the prediction of a pulsed field amplitude at a certain point is an important issue in this research, the spectra of pulses are also affected by diffractive propagation, particulary in the near field of the propagation region, and effects relating to this must be accounted for in any analysis.

Throughout the literature, the spectrum $S(\omega)$ used in theoretical computer simulations of pulse propagation is generally given within numerical software as an easily definable function, such as the Gaussian temporal variation used in this work. Another example of a commonly used spectrum is the Lorentzian distribution given by

$$S(\omega) = \frac{1}{2\pi} \frac{\Gamma}{(\omega - \omega_0)^2 + \left(\frac{1}{2}\Gamma\right)^2}$$

with spectral full-width at half maximum Γ. However, such functions are used to define the behaviour of the pulse at the source of the field only. Upon propagation away from the source, the diffraction characteristics of the individual Fourier component fields at a point create a deviation of the measured spectral composition at each location from the original definition of the spectrum at the source. Consider a wave train defined as the sum of two Gaussian beams, one "blue" and one "red", both with equal amplitude values at $z = 0$, and therefore equal coefficients in a Fourier analysis. Beyond the source plane the amplitude fall-off, say on-axis, will be greater for the beam with the longer red wavelength so the Fourier spectrum of the total field will show a less significant content of longer wavelengths, and maximum spectral amplitude will be seen at a frequency higher than ω_0.

For a pulsed Gaussian beam mode the variation of diffractive behaviour of the individual spectral components must be accounted for in the spectral description, and doing so results in an altered on-axis spectrum given by

$$S'(\omega, z) = \frac{w_0}{w(\omega, z)} S(\omega)$$

which is independent of mode index. Therefore, in the case of the Gaussian spectrum assumed throughout this chapter, eq. (4.2), the altered frequency spectrum of the diffracted LG pulse modes can be described along the $r = 0$ axis as

$$S'(\omega, z) = \frac{\tau}{\sqrt{2 + 8\frac{c^2 z^2}{\omega^2 w_0^4}}} \exp\left(-\tau^2 \frac{(\omega - \omega_0)^2}{4} \right) \tag{4.20}$$

This on-axis spectrum maintains a Gaussian-like spectral structure, but shows a shift of the maximum spectral amplitude to $\omega > \omega_0$. Figure 4.27 shows, through numerical calculation, the on-axis influence of diffraction at a circular aperture on a pulse's Gaussian spectrum in the near and far fields.

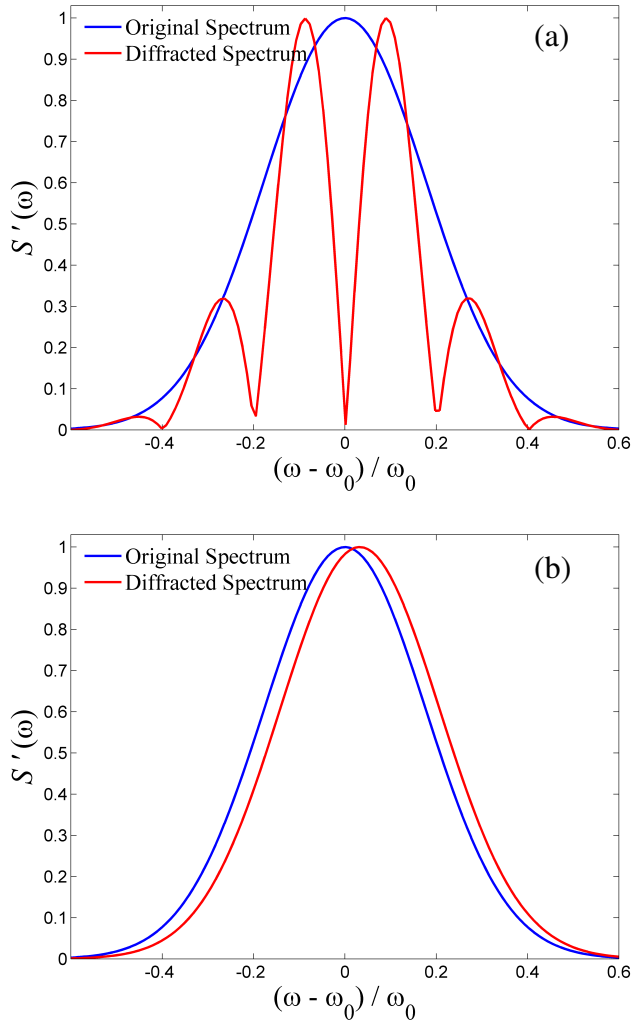

Figure 4.27 - The axial variation of the normalized Gaussian source spectrum of a pulse after diffraction by a circular aperture. Calculated with $\gamma = 0.5$, (a) $z = 0.1\ a^2 / \lambda_0$, and (b) $z = 1000\ a^2 / \lambda_0$.

In section 2.6.1 it was shown that a null occurs in the on-axis amplitude of a field diffracted by circular apertures at a distance with an even integral Fresnel number. With the field data shown in Figure 4.27 (a), with $N_F = 10$, this effect is shown with an elimination of the spectral strength at the carrier frequency ω_0, as well as at other frequencies which also have an even Fresnel number at that plane.

Figure 4.27 (b) shows how the field is subjected to a blue-shift in the far-field. Due to the greater diffraction effects that occur with longer wavelengths, their on-axis amplitude far from the source has relatively decreased more significantly, thus their content in the spectrum at that position is reduced. Also, while not obvious in Figure 4.27 (b), the far-field spectrum shows a small reduction in the width of the spectrum. In the case of fields diffracted by basic aperture functions, the spectral behaviour can be

written explicitly and [HAN07] has derived paraxial expressions from the Fresnel diffraction integral for such spectral shift and compression in pulses diffracted by annular apertures in the far-field. [YAN07] presents a description of the spectral shift observed in pulsed Bessel beams.

Like the phenomenon shown in the preceding section, these effects could have important implications in time-domain spectroscopy or imaging experiments where a spectrum at each point on a sample varies and a diffractive shift or compression of the spectrum must be accounted for in any analysis of a measured spectra.

Conclusion

Prediction of the characteristics of pulse diffraction is a relatively recent endeavour in the field of Optics, becoming a significant field of research only in the last fifteen years, primarily due to the complexity of the numerical calculations required. The methods we have employed in analysis of ultrashort fields could be a very useful supplement to the existing techniques within the literature, which, in the paraxial regime rely almost entirely on the integral formulation of diffraction. Through its numerical efficiency in depicting the evolution of diffraction effects quickly, the use of the Gaussian beam expansion in the calculation of pulsed fields was extremely beneficial to the author in his understanding of the dynamics of few-cycle pulses. The application of the Gaussian beam mode analysis in simulation of pulse propagation has allowed for a description of the behaviour of higher order pulsed Gaussian beam modes which has received little attention in optical research. Effects of the deviant behaviour in pulsed Gaussian modes from the ideal planar pulse due to the Gouy phase shift have been described. These cause a variation of the phase velocity in each spectral component and thus induce a group velocity deviating from c, which causes a spatial shift and temporal delay of the pulse peak. Related to this behaviour, a broadening of the pulse, in space and time, is created which is a phenomenon usually associated with the dispersion of beams within optically dense media, thus we have used this analogy, referred to as spatially induced dispersion to determine the group velocity of pulsed LG modes, and illustrated the occurrence of these free-space phenomena in the near field of Laguerre-Gaussian beam modes according the mode indices.

We have presented the use of Gaussian beam mode analysis in the calculation of few-cycle pulses both as a numerical technique and as an alternative physical model

of the diffraction of such short fields. In particular we have exhibited a qualitative relationship between the propagation of the pulsed higher-order modes and the formation of boundary waves created by diffraction aperture and the similarity in superluminal features exhibited by both.

Gaussian beam mode analysis has been used in the numerical prediction of time-dependent fields within a refractive medium, with the effects of pulse dispersion in a linear dielectric being briefly described. The phenomena shown will have implications in the calculation of optical and terahertz pulsed fields diffracted/refracted by optically dense components such as lenses or optical fibres. Applying the GBM method to the calculation of diffractive effects by a dispersive optical component requires an overlap integral for each spectral component which can be time-consuming, but the GBMA procedure is again suggested to be efficient and will be employed in a later chapter.

As a recommendation for future work, the modal description of pulses may perhaps also be applied to non-paraxial fields. The description of higher order Gaussian beam modes reported in [DUAN05] and applied by this author in section 2.8.1, could be easily adapted to the analysis of pulsed fields. Although those descriptions would lose validity near the aperture plane, the method would be a simple approach to solving the complicated Rayleigh-Sommerfeld diffraction integrals for pulses over a broad frequency range with less restriction on the validity of a calculated field at large angles off-axis in the far-field.

Chapter Five

Focusing of Continuous and Pulsed Optical Waves by Diffractive Lenses

5.1 – Introduction

At millimetre wavelengths, optical systems are often confined to small volumes, particularly in telescope systems where numerous frequency channels may have to exist in the same confined space. Mirrors and lenses are necessarily large due to the wavelength and beam widths, and in particular lenses can be excessively bulky both in the transverse and longitudinal planes. With short focal lengths the resulting small radius of curvature of a lens means that absorptive losses, especially towards the centre of a thin spherical lens, may become very significant. Diffractive effects that can occur within a thick section of dielectric, but which are not accounted for in a planar model, could also reduce the validity of a predicted field when using paraxial techniques.

For these reasons, planar lenses are desirable optical components for the concentration of radiation, and can be as thin as $\lambda/(2(n\text{-}1))$, making them easier to manufacture. The Fresnel lens, [ALDA06, ZHA07], is a typical example of such a lens, whereby the surface of a spherical lens is reduced in thickness by a modulo 2π operation on its phase modulation, resulting in a phase variation across the surface corresponding to its spherical analogue. These lenses are traditionally used, for example, in lighthouses where spatial and material restrictions demand the use thinner elements. This form of lens, however, remains difficult to manufacture due to small spherical variations in the surface height over minute regions. Thus for easier milling or lithographic etching, as is used for operation at visible wavelengths, such lenses are approximated by "staircase" profiles of the spherically varying surfaces with a number of surface levels P. While this formulation can reduce the suitability of the lens in an imaging scenario, particularly with a small number of surface steps, it allows for a much simpler method for the focusing of radiation to a detector while maintaining an acceptable degree of efficiency. Diffractive lenses, and in particular Fresnel zone plates have for example also become popular in X-ray systems where accurate manufacture of lenses with features on the

scale of nanometres becomes very difficult reducing the ability to create ideally spherical features, [MIC86].

The applicability of scalar and more rigourous numerical techniques in accurately predicting the performance of diffractive lenses has been offered by [PRA01] where the authors highlighted the deviations between models that account for shadowing by the lens surface and non-paraxial propagation, i.e. finite-difference time-domain, and those that do not, such as the scalar diffraction integrals. However, that paper did show, see Figure 5.1, that scalar diffraction techniques were suitable for the modelling of two-level (binary) lenses with *F*-numbers (ratio of the focal length to the lens diameter) as low as ~ 0.3. This value is an exceptionally low value for the *F*-number of a millimetre wavelength system, and the scalar theory is therefore suitable for most practical diffractive lenses for operation in the far-infrared. Figure 5.1 shows the regions of validity for the scalar techniques as proposed by *Prather*.

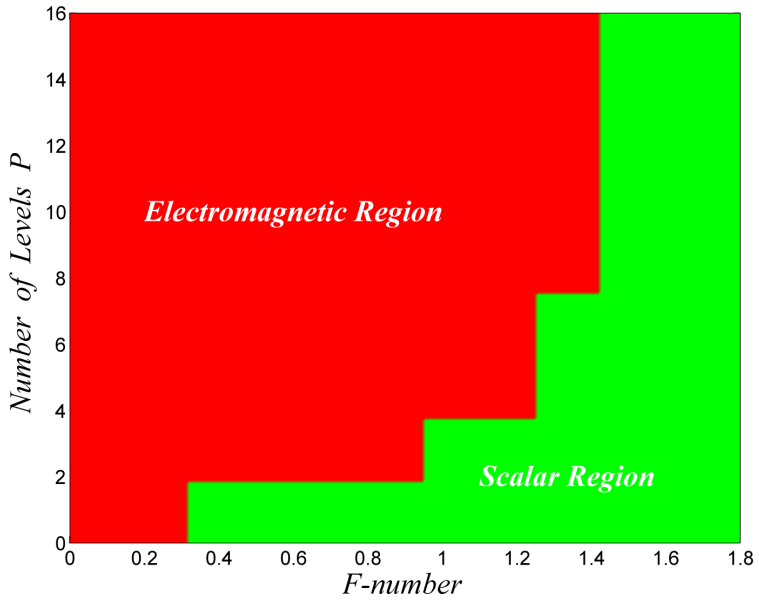

Figure 5.1 – The validity of the scalar diffraction theory in the study of diffractive lenses. Reproduced from [PRA01].

In this chapter we shall discuss the scalar diffraction of incident plane waves upon propagation through diffractive lenses and zone plates using the method of Gaussian beam mode analysis, and shall apply the same techniques as outlined in chapter 4 in the simulation of the effects of pulsed illumination of such elements.

The object for comparison of the field structure of diffractive lenses is, of course, the field of an ideal thin spherical lens at its focal plane which can be calculated

analytically by substitution of the phase transformation term of a thin lens, $\exp(ikr^2/2f)$, into the Fresnel diffraction integral, eq.(2.5), which, with $z = f$, eliminates the complex exponential terms from the integrand resulting in

$$I(r,f) = \left|E(r,f)\right|^2 \propto \left| -i\frac{k}{z}\exp\left(i\frac{kr^2}{2z}\right)\int_0^a J_0\left(\frac{k\,r\,r_0}{f}\right) r_0 dr_0 \right|^2$$

where a is the outer radius of the lens, r_0 is the radial position on the aperture plane and r the coordinate in the image plane. Using the identity

$$\int_0^a J_0(x)\,x\,dx = a\,J_1(a)$$

gives the intensity variation at the focal plane as

$$I(r,f) = \left| a\frac{J_1\left(k\,r\,a \big/ f\right)}{r} \right|^2 \qquad (5.1)$$

where we have again assumed plane wave illumination of the lens. The field in the focal plane of a thin spherical lens is thus related to the first order Bessel function of the first kind $J_1(r)$, which has its first root at 3.832, thus $kra/f = 3.832$ gives the radius of the inner lobe as $0.61\ \lambda\ f\ /\ a$, a common result stated in undergraduate texts on the resolution of imaging systems. The field structure given by eq. 5.1 is very convenient as it has very low-level sidelobes, with the first off-axis maximum of the function $J_1(r)/r$ occurring at $r = 5.136$, with an intensity of -17.57 dB for a normalised on-axis intensity of 0 dB.

5.2 - The Fresnel Zone Plate

The simplest form of diffractive focusing element is the Fresnel zone plate (FZP), which modulates an illuminating beam through amplitude modulation of its wavefront only. Its surface consists of alternating opaque and transparent zones whose radii decrease with increasing distance from the centre of the lens, and due to the presence of the opaque rings the energy throughput of the component is significantly reduced. However, in active systems employing radiation sources that allow for adjustment of power levels, in contrast with passive systems, this may not be such an important feature, with the emphasis being primarily on the focusing of the field to the correct focal plane for illumination in an imaging system for example. Zone plates are

popular due to their basic structure and the comparative ease at which they are manufactured, compared to the high precision required for creation of a spherical surface. At visible wavelengths, FZPs can be created by photoreduction in which a large scaled representation of the transmittance is photographed and reduced to its design size on photographic film. At millimetre wavelengths zone plates can be created through the use of ultraviolet lithography where a printed circuit board is created by an appropriate masked illumination, and the resulting board acts a zone plate or hologram, [MEL03].

The purpose of the amplitude zone plate is to mimic the effects of refraction within a lens by the focusing of light to a point using diffraction and the related interference effects. When the optical path length difference between the emanate rays is an integral number of wavelengths, constructive interference occurs and an interference maximum is observed at the desired focal plane. This is done by setting the radii of alternating transparent and opaque zones such that the optical path lens of rays emanating from each zone differs by a suitable phase value, thus, in the geometrical limit, constructive interference will occur at the defined position of the focal length.

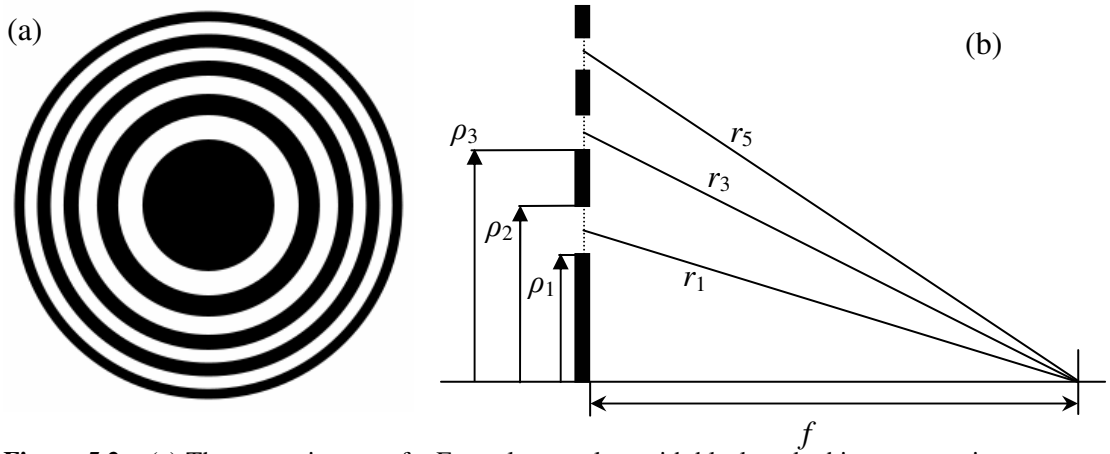

Figure 5.2 – (a) The transmittance of a Fresnel zone plate with black and white representing opaque and transparent regions respectively. (b) The geometry of the focusing effect produced by a zone plate.

The structure of a zone plate can also be in the form of a negative of that illustrated in Figure 5.2, as the total throughput of energy and phase properties will remain the same for both forms when there is complete beam coverage of the element. In fact, it can be assumed in this work that the central zone is transparent, and that the element contains an odd number of zones so that fields are transmitted by the outermost zone.

For a Fresnel zone plate the outer radus of the j^{th} zone is given by

$$\rho_j^2 = \left(f^2 + \frac{j\lambda}{2} \right)^2 - f^2 = f^2 \left(j\left(\frac{\lambda}{f}\right) + \frac{j^2}{4}\left(\frac{\lambda}{f}\right)^2 \right).$$

A common approximation to this expression can be given when the value λ/f is much less than unity and the second term in the brackets may be ignored as it is negligible compared to the first term, thus we can estimate the zone radii as

$$\rho_j = \sqrt{j\, f\, \lambda}\,. \tag{5.2}$$

In general, the zone plates and similar lenses discussed in this chapter will have conventional ratios of wavelength to lens diameter for the terahertz and millimetre-wave regime. But the size of the elements relative to the wavelength will also allow for a direct comparison with so-called "microlenses" frequently discussed in literature relating to visible wave and X-ray manipulation, and we will simulate coherent radiation in the near-infrared band in some examples.

The structure of an amplitude zone plate may also be expressed analytically as

$$E_0(r_0) = \frac{1}{2}\left(1 + \operatorname{sgn}\left(\sin\left(\frac{k\, r_0^2}{2f} \right) \right) \right), \tag{5.3}$$

which highlights the elements structure as a modified representation of the traditional form of spherical lens based on the parabolic phase term $kr_0^2/2f$. Figure 5.3 shows the diffraction half-space of a zone plate when illuminated by a plane wave as calculated using a Laguerre-Gaussian beam mode expansion of eq. (5.3).

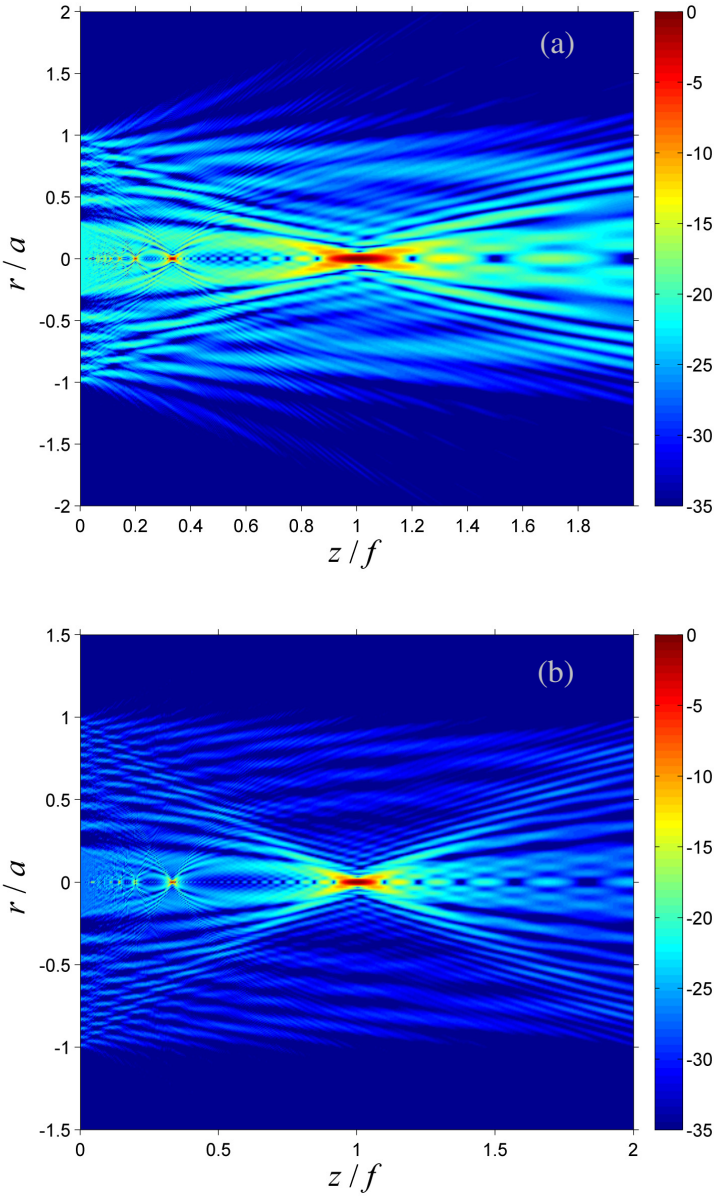

Figure 5.3 - The focusing of a plane wave by a Fresnel Zone plate with (a) $N_F = 11$, (b) $N_F = 21$. (dB scale).

While there is an obvious and desired focal point at the designated distance f, the structure of the zone plates in Figure 5.3 also generates multiple foci at distances between the element and the focal plane where constructive interference also occurs, these foci occur at longitudinal distances of

$$f_j = \frac{f}{2j+1} \tag{5.4}$$

where j is an integer, and are clearly visible in Figure 5.4.

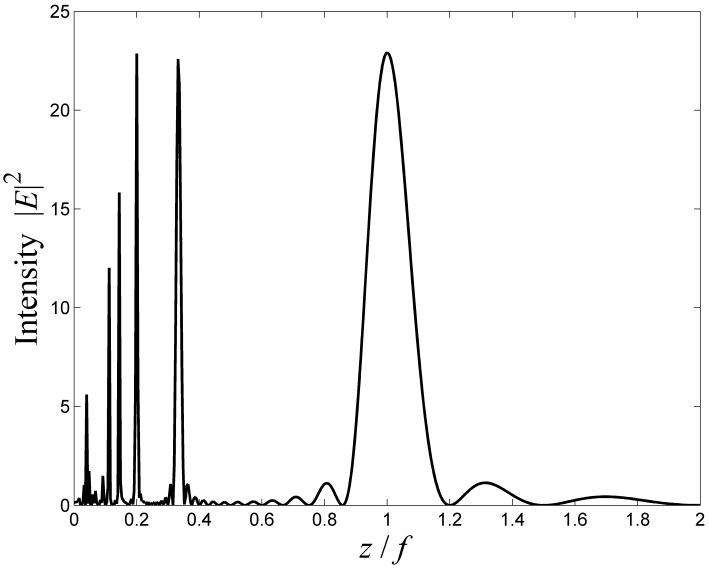

Figure 5.4 - The on-axis intensity variation of a plane wave focused by a FZP with N_F = 11. The plot shows secondary focal points at $z = f/3, f/5, f/7$ etc.

5.3 – Diffractive Fresnel Lenses

While zone plates are very useful and cost effective elements, the opaque regions of the lens can significantly reduce the throughput of energy within an optical system. The diffractive Fresnel lens is an improvement to the zone plate in that while the structure of the field modulation it creates can be similar to that of amplitude zone plates in some cases, all regions of the lens surface transmit energy thus maintaining a greater proportion of the optical energy in a system. The phase profile of a Fresnel lens can be defined by

$$\phi(r_0) = \frac{k\, r_0^2}{2f} \bmod 2\pi \,.$$

This function creates a phase variation that contains spherical features which can be difficult to manufacture, but can be reduced further to create a form of quantised or "staircase" approximation by a phase function of the form

$$\phi_P(r_0) = \frac{2\pi}{P} \left\lfloor \frac{P\left(\frac{kr_0^2}{2f} \bmod 2\pi \right)}{2\pi} \right\rfloor \tag{5.5}$$

where $\lfloor x \rfloor$ represents the floor function, giving the largest integer lower than x, and P is the integer number of levels to which the surface is quantised. The phase structures

arising from this operation of eq.(5.5) for various values of the quantisation level P are shown in Figure 5.5.

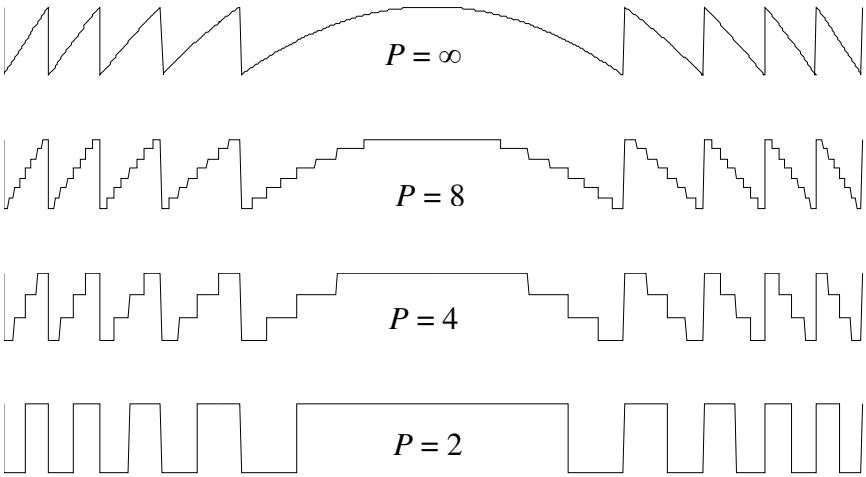

Figure 5.5 – The profile of P level diffractive lenses.

Figure 5.6 illustrates the determination of phase effects of a diffractive Fresnel lens.

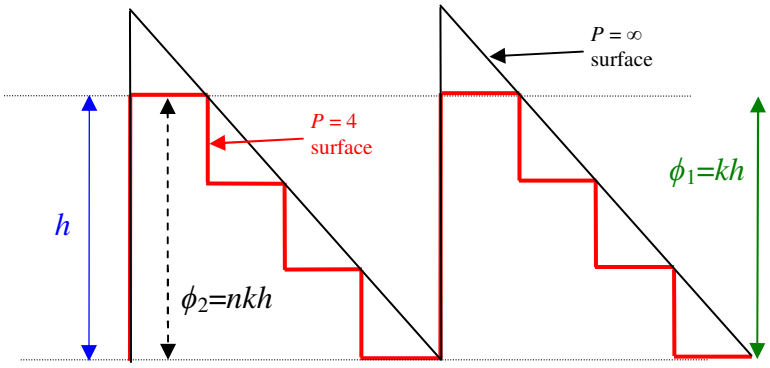

Figure 5.6 – Calculation of phase function of a diffractive lens.

The desired phase profile of the lens is generated by modifying the height h of the lens such that the phase difference along the two optical path lengths in free-space and within the dielectric, ϕ_2-ϕ_1, creates the desired phase $\phi_P(r_0)$. For a lens with P surface levels, the maximum phase difference introduced by the lens is

$$\phi_2 - \phi_1 = nkh - kh = \frac{(P-1)}{P} 2\pi \,. \tag{5.6}$$

The maximum thickness of the lens is then determined by

$$h_0 = \frac{\lambda}{(n-1)} \frac{(P-1)}{P}. \tag{5.7}$$

One of the main restriction of the scalar diffraction techniques, discussed in [PRA01], is that for low *F*-numbers, see Figure 5.1, the focal plane is close to the element and the lens will be simulated as a planar phase variation. As well as the typical restrictions of the paraxial techniques in this situations, the geometrical angles between the more distant transverse points on the lens and the optical axis introduces errors associated with shadowing that may occur through reflection and refraction of the field by neighbouring zones, see Figure 5.7 and Figure 5.8.

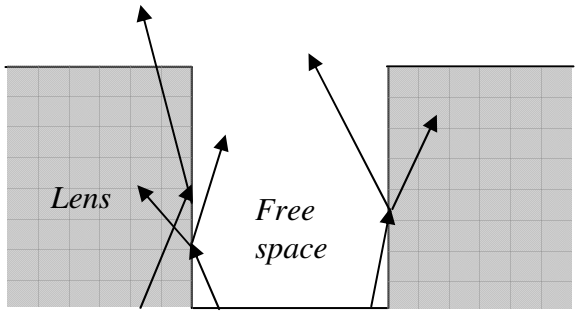

Figure 5.7 – Shadowing effects by refraction and reflection are not accounted for in the general scalar theory.

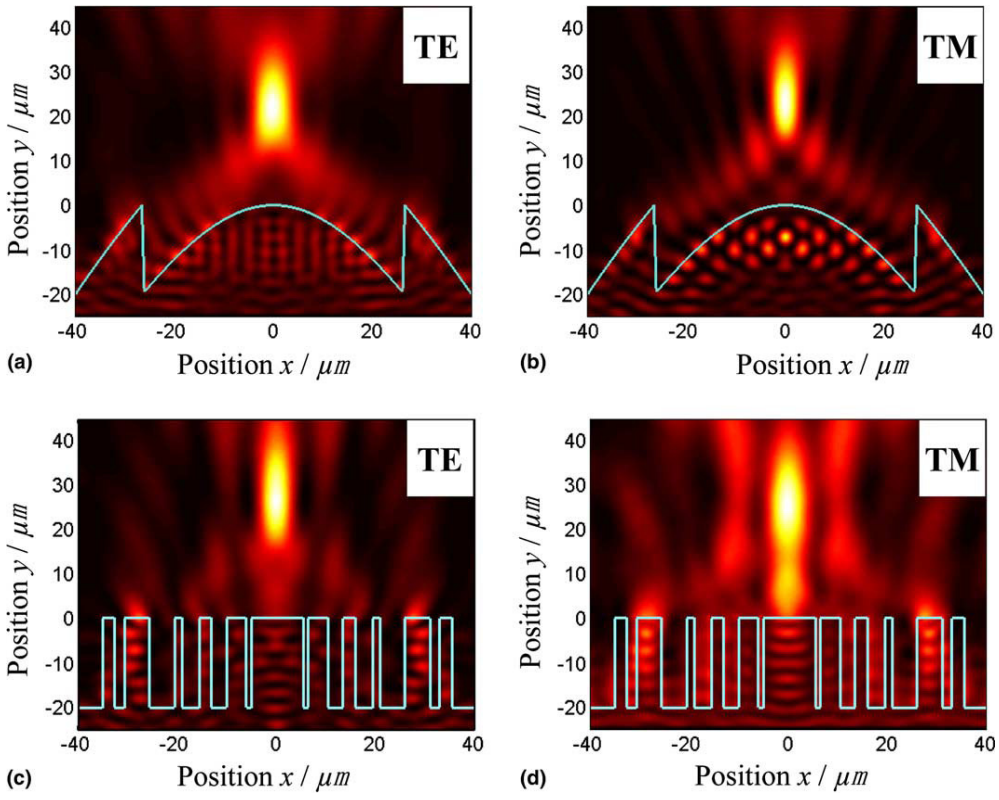

Figure 5.8 – Two-dimensional FDTD calculations by [FENG04] of a modified binary diffractive lens compared with its un-quantised analogue.

Figure 5.8 (a)-(d) show the effects within the diffractive lens which prevents the scalar techniques from modelling the true physical behaviour of the lens within the lens material. However, we will maintain this discussion to elements with paraxial and scalar validity as expressed in Figure 5.1.

To expand the phase effect of a diffractive lens in terms of Laguerre-Gaussian modes, assuming uniform illumination with a plane wave, the mode coefficients are determined by the integral

$$A_m = \sqrt{\frac{2}{\pi w_0^2}} \int_0^a L_n\left(2\frac{r_0^2}{w_0^2}\right) \exp\left(-\frac{r_0^2}{w_0^2}\right) \exp\left(i\frac{2\pi}{P}\left\lfloor \frac{P\left(\frac{kr_0^2}{2f} \bmod 2\pi\right)}{2\pi} \right\rfloor\right) 2\pi r_0 dr_0 \ . \quad (5.8)$$

The modes calculated by this equation are shown in Figure 5.9, with $M = 100$, and $w_0 = (a / M)^{1/2}$.

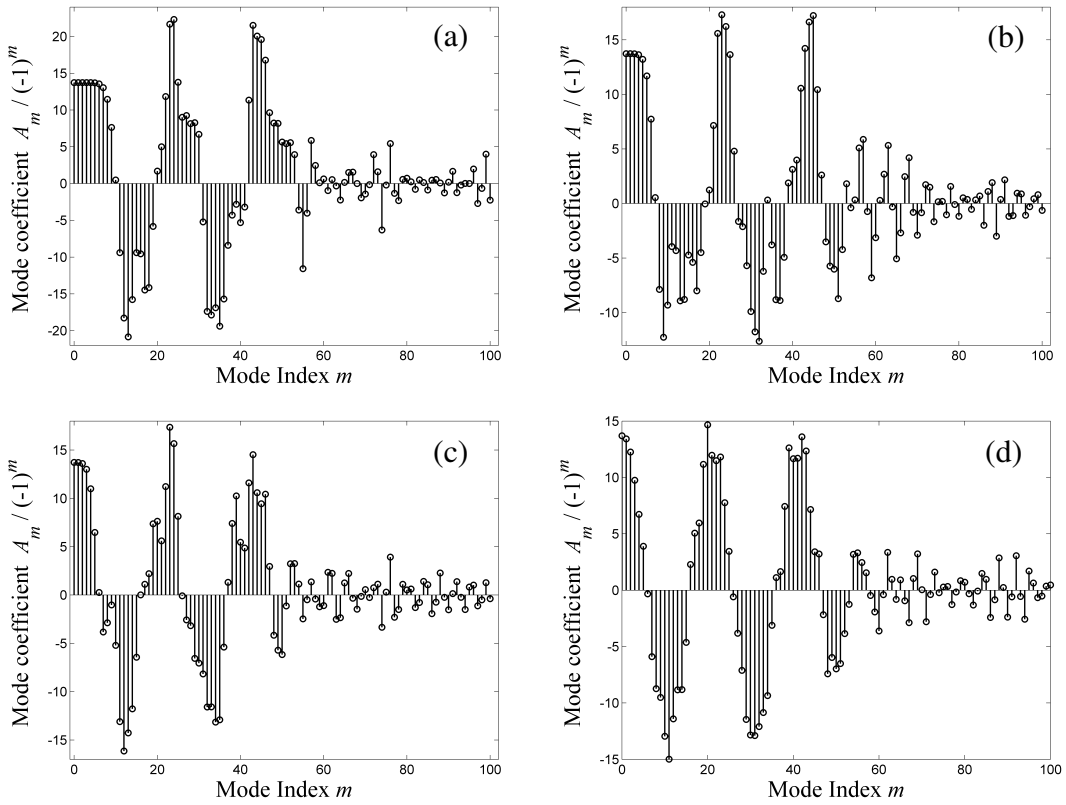

Figure 5.9 - The Laguerre-Gaussian mode coefficients of a binary diffractive lens with $N_F = 5$, with the number of surface levels P = (a) 2 (b) 4 (c) 8 (d) 16.

The effect of the lens surface is apparent in the variation of the mode coefficients, particularly the step-like trend replicated in Figure 5.9 (a). For a larger number of surface levels, the values of the coefficients, and thus the diffracted field,

converge to that of the corresponding thin spherical lens, which with a finite number of modes limits the application of GBMA with large values of P. From these figures, the value of $P = 2$ can be assumed to cause the most significant deviation from the ideal lens field which is exhibited in Figure 5.10 with the focusing of an incident plane wave by diffractive Fresnel lenses with varying number of surface levels.

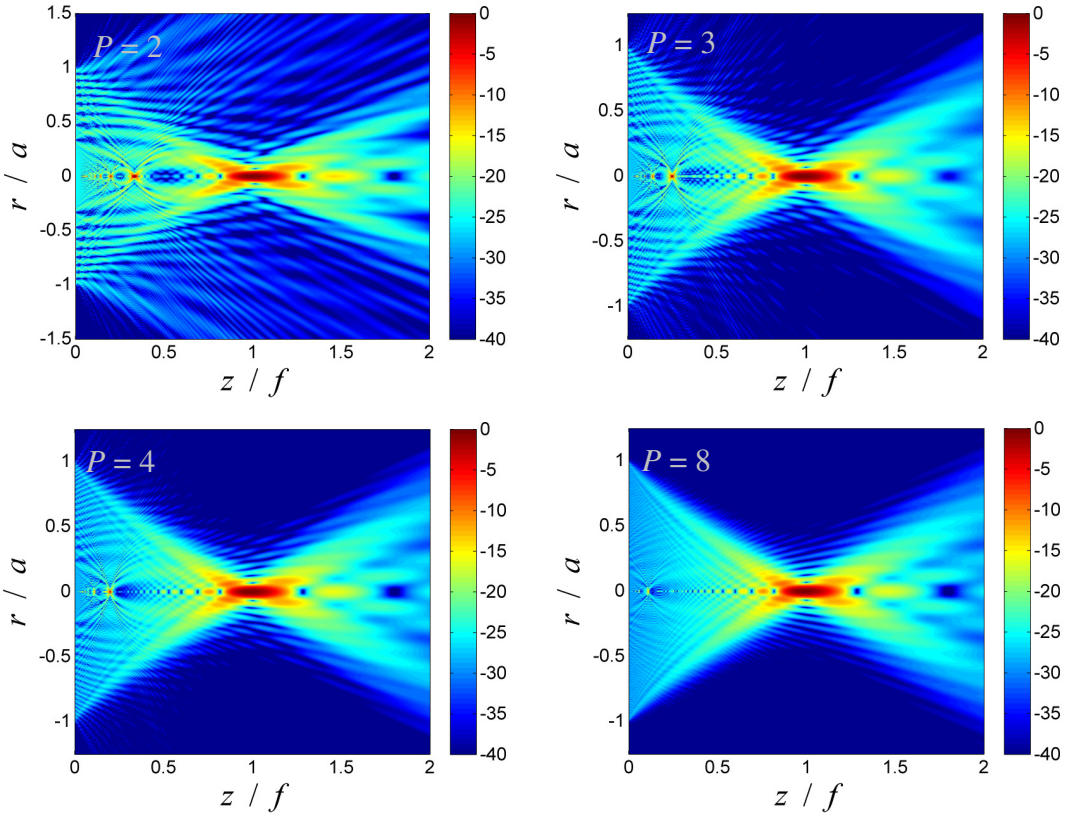

Figure 5.10 - The focused intensity of a plane wave by a diffractive lens with a varying number of surface levels P, with $N_F = 9$. Each plot is shown with a logarithmic dB scale normalised to the maximum field intensity.

The increase in diffraction effects generated by the quantised surface of the lens now induces a decrease of the amplitude at the focal plane due to diffraction away from the optical axis caused by the smaller features of the lens surface, see Figure 5.11.

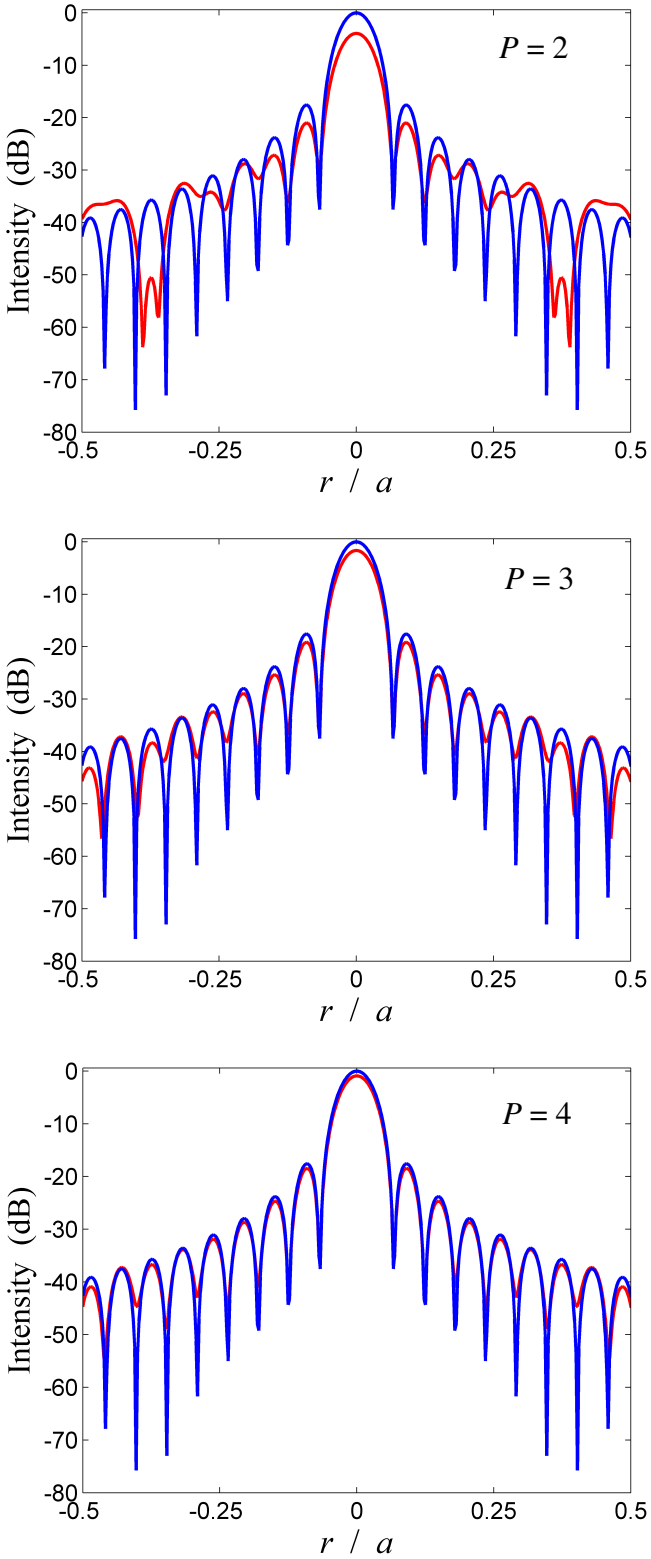

Figure 5.11 - The intensity at the focal plane of a diffractive lens under plane wave illumination with a varying number of levels P, with $N_F = 9$ (in red). Each plot is normalised to the intensity at the focus of an ideal Fresnel lens with $P = \infty$ (shown in blue).

As was seen with the focusing effects of the Fresnel zone plate, the quantisation of the surface of a Fresnel lens also creates minor secondary foci, the structure and position of which changes according to the level of quantisation, as shown below.

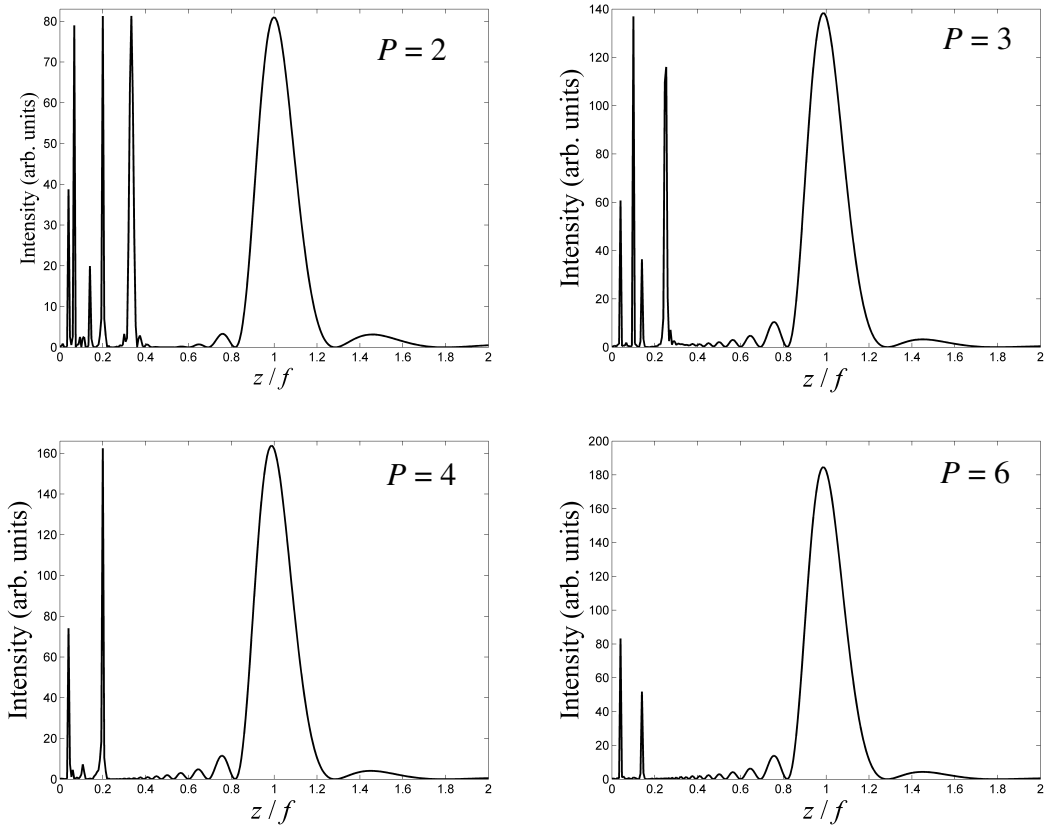

Figure 5.12 - The on-axis longitudinal intensity of a $N_F = 9$ diffractive Fresnel lens at the focal plane f with various values of the number of surface steps P.

The profile described by eq. (5.1) occurs at the geometrical focal plane, and not necessarily the plane of the maximum intensity value. The data in Figure 5.13 describes the effect of the quantisation of a Fresnel lens surface on the intensity at the focal plane of a diffractive Fresnel lens.

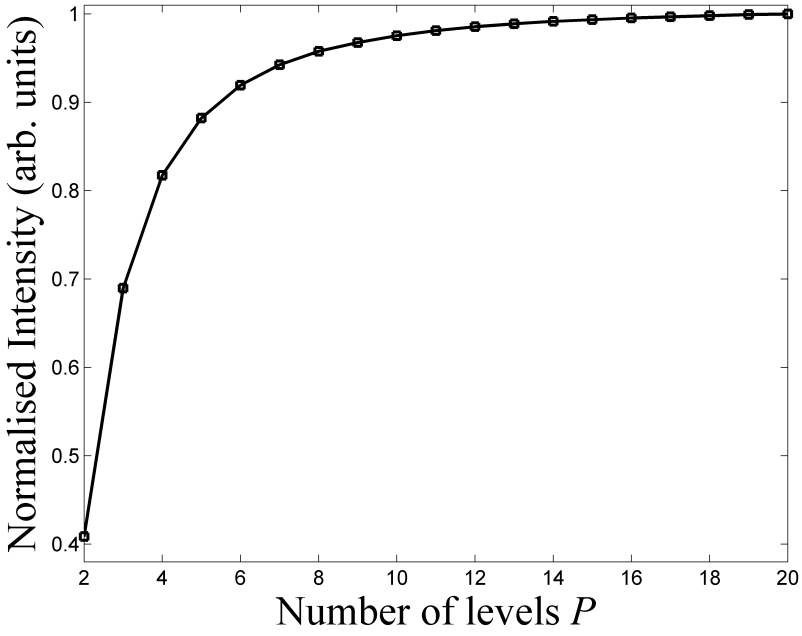

Figure 5.13 - The variation of the focal intensity of diffractive lenses as a ratio of the maximum (on-axis) intensity at the focal plane $z = f$ of a thin spherical lens illuminated by a plane wave.

In Figure 5.13, there is a quite large variation in the maximum focal intensity between lenses having $P = 2$ and those with $P = 8$. For values of $P \geq 8$ there is less variation in focusing ability, with the intensity converging to that of the ideal thin lens. The greatest deviation in intensity occurs in the transition from $P = 3$ to $P = 2$ with a decrease of almost 30 %. The efficiency of such lenses can be quantified by the ratio of the intensity within the central lobe of the focused field to the total intensity of the field illuminating the lens. With unit amplitude plane wave illumination of a lens of radius a the total input intensity is simply πa^2, thus the efficiency of a diffractive lens with P surface levels can be numerically determined from

$$\eta_P = \frac{2\int_0^{R_1} \left|E_P(r)\right|^2 r\,dr}{a^2} \tag{5.9}$$

where R_1 is the radius of the first off-axis intensity null at the focal plane of the field E_P of a P-level diffractive lens. The values of the diffraction efficiencies were calculated for four lenses with various values of P, for variation of the Fresnel number from 1 to 30, which for $f = 100\ \lambda$ corresponds to respective F-numbers of 27.4 and 0.91. It was found that using the theoretical value of $R_1 = 0.61\ \lambda f / a$ in the numerical evaluation of η_P gave almost identical results to those found by calculating the location of the first

off-axis local minimum directly, which itself is a further sign of the diffractive lens's ability to mimic the focal profile of the ideal lens.

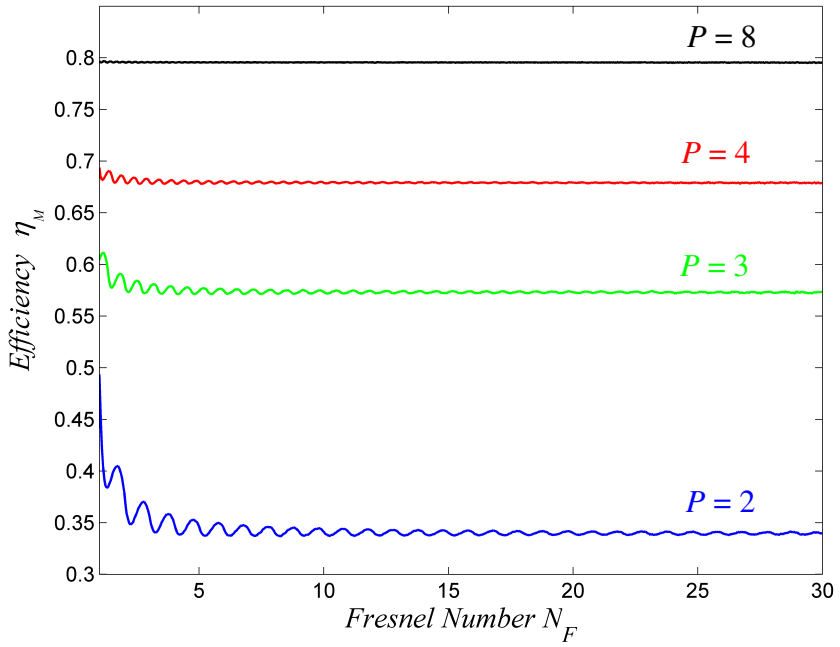

Figure 5.14 – Diffraction efficiencies for diffractive lenses with $P = 2$ (blue), $P = 3$ (green), $P = 4$ (red), $P = 8$ (black).

The efficiency of the $P = 2$ lens as shown in Figure 5.14 represents a great loss of focusing ability with the quantisation of the lens surface. This may possibly inhibit the application of such lenses in passive systems where mirrors may be the optimum choice of focusing optics. However, in active imaging systems with radiation sources allowing for the adjustment of output power this loss of efficiency may be insignificant.

5.4 - Bandwidth effects of diffractive lenses

The design of binary and diffractive lenses is generally carried out with the motive of use at a single wavelength. In the case of conventional spherical lenses found in the optics laboratory, effective focusing can be obtained for a wide range of wavelengths with a variation in the focal length for different wavelengths based on the dispersion relation of the glass or dielectric used. However, the Fresnel lens does show some level of focusing ability with wavelengths deviating from the design wavelength, albeit with a reduction of efficiency.

The focal length of a Fresnel zone plate or diffractive lens varies according to the wavelength of the monochromatic radiation illuminating the component, which is also a feature of refractive spherical lenses known as chromatic aberration, but should not to be thought of as being due by the same physical processes. The focal length, $f(\lambda)$, of a Fresnel zone plate illuminated with wavelength λ, deviating from the design wavelength, can be determined from the radius of the innermost zone region, i.e.

$$f(\lambda) = \frac{\rho_1^2}{\lambda} = \frac{\lambda_0}{\lambda} f(\lambda_0) = \frac{\nu}{\nu_0} f_0(\nu_0) \tag{5.10}$$

with f_0 the focal distance for the design wavelength λ_0 or frequency ν_0. The profile of a diffractive Fresnel lens is related to the structure of a FZP, therefore the same movement of the focal length according to the field wavelength will also occur with these phase elements.

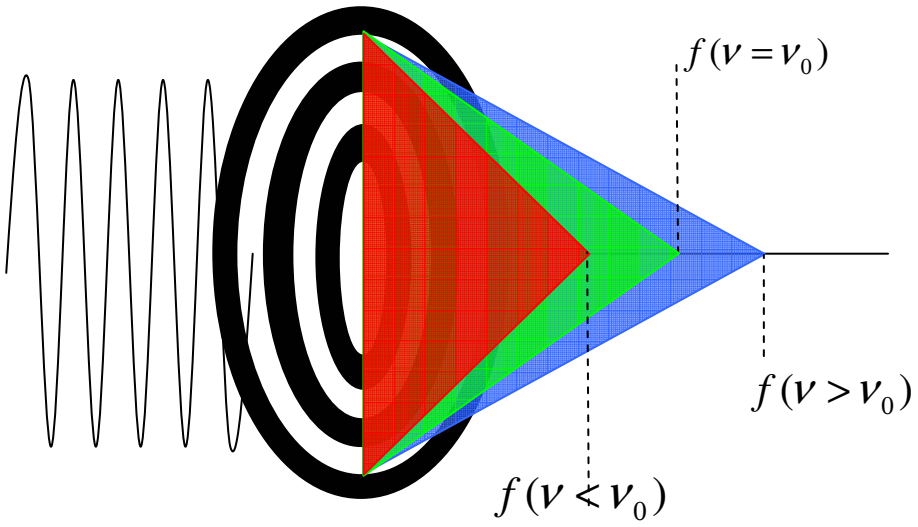

Figure 5.15 – Illustration of chromatic effects in a Fresnel lens/zone plate.

However, the phase modulation imposed by the diffractive lens will be altered due to the change in the ratio of the incident wavelength to the lens depth, which is responsible for the variation of the phase values across the lens.

With a P level diffractive lens of depth h, the phase variation ϕ_P' imposed when illuminated by a field with wavelength λ is

$$\phi_P^{'} = k\, n(\lambda)h - kh = \frac{(n(\lambda)-1)}{(n(\lambda_0)-1)} \frac{\lambda_0}{\lambda} 2\pi \frac{(P-1)}{P}. \tag{5.11}$$

Now, while the Fresnel zone radii of the lens correspond to an altered focal length $f(\lambda)$, the average phase difference of rays from adjacent zones no longer

corresponds to the correct phase to support complete constructive interference at the focal plane. With the variation in the phase profile of the element created by the wavelength mismatch the desired constructive interference at the focal plane is reduced. In fact, in some cases the focusing ability is completely eliminated. Consider eq. (5.11) in the case of a dispersionless ($n(\lambda)=n(\lambda_0)$), $P = 2$ lens, with illumination by a field of wavelength $\lambda = \lambda_0/2$. The phase profile then corresponds to a binary variation with values 0 and 2π, which both create identical values in a complex exponential function. Thus the lens has no focusing influence on the incident field, producing a field profile equal to that of a completely transparent circular aperture. With such exceptions, the Fresnel lenses do show an ability to generate efficient focusing for a practical range of wavelengths surrounding the design wavelength. This is shown in the examples given in Figure 5.16, data is presented for the case of a binary lens with $\lambda_0 = 3$mm ($\nu_0 = 100$ GHz), with the refractive index $n_0 = n(\lambda_0) = 1.52$.

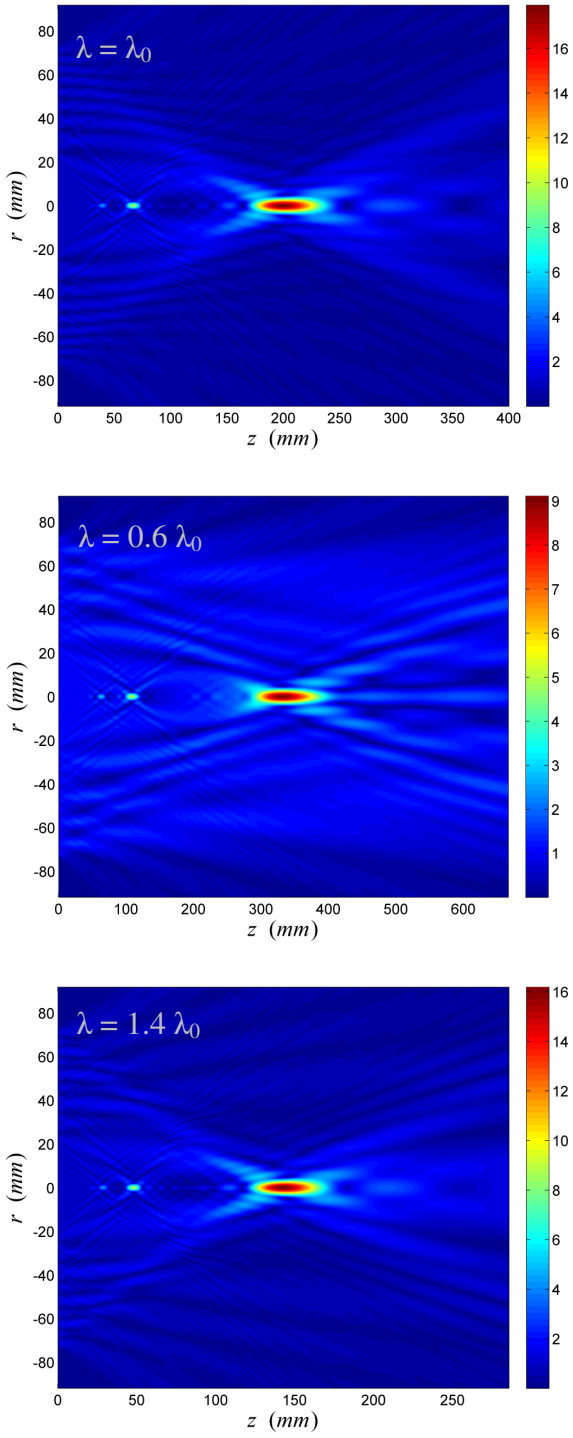

Figure 5.16 – The effects of wavelength mismatch on a planar field with a $P = 2$ diffractive lens. $\lambda_0 =$ 3mm (100GHz), $f_0 = 200$mm, $N_F = 9$.

The main effect of the mismatch is the movement of the point of maximum intensity to the plane $z = f_0 \lambda_0/\lambda$. But at this plane the effect of the alteration in the lens phase structure causes a deviation from the ideal focal plane structure. However, the

figure shows that the fields maintain the beam width of the focal spot at that plane predicted using eq. (5.1).

The application of the diffractive lens in terahertz imaging has been discussed by *Wang et. al.* [WANG04]. There, the authors of that paper used the frequency dependent variation of the focal length of a diffractive lens, as discussed, to form the images of objects located at different planes, see Figure 5.17.

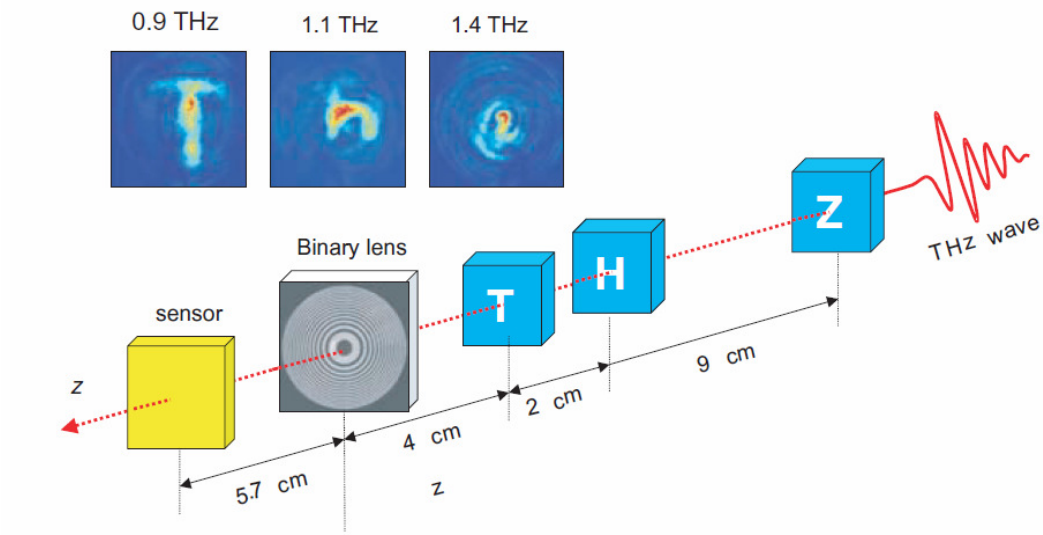

Figure 5.17 – Schematic of imaging system utilising a binary diffractive lens. Reproduced from [WANG04]. The chromatic properties of the binary lens allows for the measurement of images of objects at different distances without having to move the detector longitudinally.

The fundamental equation of image formation by a thin lens is given by [GOO05]

$$\frac{1}{z_o}+\frac{1}{z_i}=\frac{1}{f(\nu)} \tag{5.12}$$

with z_o the distance of an object from the lens of focal length f, and z_i is the plane at which an image of the object is formed, and $f(\nu)$ represents the variation of the focal plane with frequency. Referring to Figure 5.17, the broadband nature of the input field causes the focusing effect of the lens to become dependent on the frequency/wavelength of the illuminating field. With the radiation measured at a constant distance z_i from the lens, the field of a specific wavelength with optimal focus at z_i is related to an object at a distance z_o which varies for each frequency, thus the binary/Fresnel lens can be used to image several objects that are positioned at different planes. However, as can be see in Figure 5.17 the images of fields with frequencies deviating from the design frequency of 1 THz are somewhat degraded, particularly in the case of the 1.4 THz measurement.

5.4.1 - Experimental Results

A two-level high-density polyethylene (HDPE) Fresnel lens was manufactured by Mr. David Watson in the engineering workshop at the NUIM Experimental Physics department. Following the lens simulated in the preceding section, the lens was designed by the author for operation at $\nu_0 = 100$ GHz, so that with a refractive index of 1.52 for HDPE at that frequency [BIR92], the difference in depth between adjacent zones is 2.88mm. The lens has a radius of 73.5 mm, and incorporates nine Fresnel zones, with $\rho_1 = 24.5$mm, $\rho_2 = 34.6$mm, $\rho_3 = 42.4$mm, etc, defined by the lens focal length of 200mm. The F-number of the component is therefore 1.36.

Figure 5.18 – A F#1.36 binary lens manufactured at the NUIM physics department.

The element was tested experimentally by measurement of a field derived from a cylindrical corrugated horn object with a radius of $a = 7.14$mm at its mouth, and a slant length of 65mm. Figure 5.20 shows the measured fields compared with predictions calculated using Gaussian beam mode theory for different frequencies. It was assumed that there is no variation in the refractive index of HDPE ($n = 1.52$) at the frequencies measured.

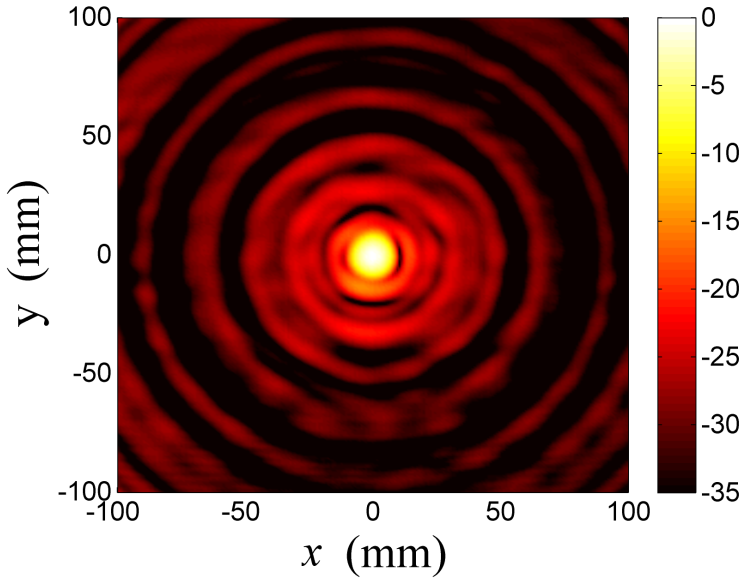

Figure 5.19 – Two dimensional measurement at the image plane of binary Fresnel lens with $N_F = 9$ and $F\#1.36$ at 100 GHz.

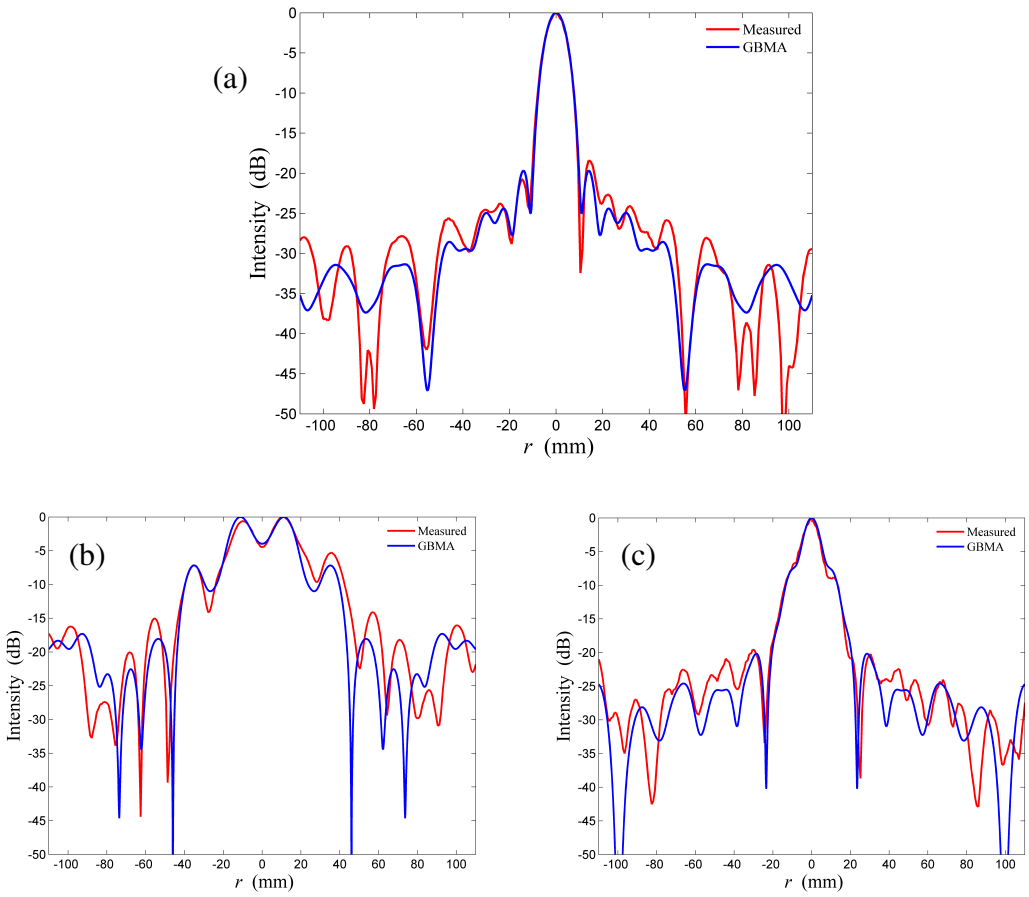

Figure 5.20 – The recorded and Gaussian beam mode prediction intensity at the design image plane $2f_0$ = 400mm of a binary HDPE Fresnel lens with different frequencies (a) 100 GHz, (b) 80 GHz, (c) 110 GHz.

At 80 GHz, no concentration of energy occurs at the plane of the 100GHz focus, and while there is some central localisation of energy shown in the 110GHz field at the same plane, the effect could not be considered an efficient focus. For a frequency of 80 GHz with an object/source at $-2f_0$ the frequency specific image plane is located at $z_i \approx$ 267mm. The measurement of the intensity at this plane is shown below with a comparison with a GBMA model.

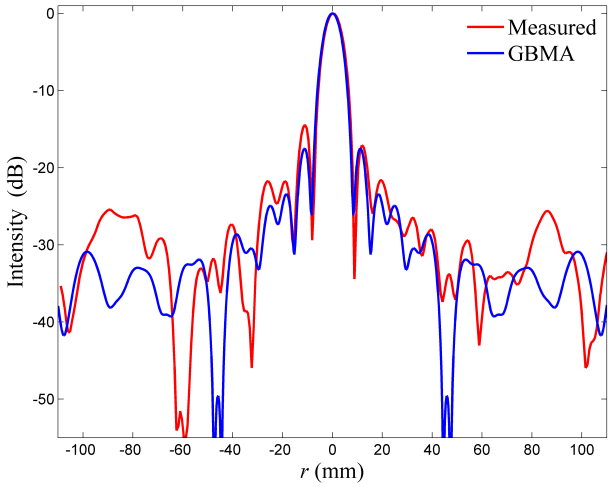

Figure 5.21 – Measurement at the image plane (z = 267mm) of an 80 GHz field focused by a diffractive lens designed for operation at 100GHz.

The first off-axis local maximum in Figure 5.21 of the focused field has increased in amplitude from a level of approximately -19.5 dB in the predicted distribution (for Gaussian illumination) to -17.14 dB (calculated from the model) which is insignificant. For 80 GHz illumination, the phase step between adjacent zones is 0.8π which does create some constructive interference between fields from each zone, although it is reduced from the measurement at 100GHz. The predicted focal radius of 8.31mm at the image plane shows excellent agreement with the measured data.

5.5 - Diffraction of optical pulses by Fresnel zone plates

While the properties of the conventional optical tools such as mirrors and lenses have been well known for centuries, the knowledge of their effects has in general been derived from observation of their manipulation of continuous wave fields either coherent or incoherent. As the field of pulsed terahertz spectroscopy and imaging grows, suitable methods for the determination of diffractive propagation of pulses

through focusing components must be analysed. In the previous section we have seen through numerical and experimental data that the deviation of a monochromatic wave's frequency v from the design frequency v_0 of a diffractive lens has a great effect on the nature of the diffracted wave. Now we can look at how that behaviour affects the performance of Fresnel lenses and zone plates when illuminated by a coherent superposition of a spectrum of optical fields spread around the design frequency of the lens representing a time-dependent signal, using the Gaussian beam mode expansion.

Assuming that the amplitude variation of a Fresnel zone plate is consistent for all wavelengths, i.e. the material is either fully transparent or opaque only, the calculation of mode coefficients for this structure is a single task, independent of frequency and so only one overlap integral is required, allowing for efficient prediction of paraxial optical effects. However, as we have seen, the diffracted field of each spectral component will have a focus at a different distance from the zone plate, and this will affect greatly the structure and quality (in terms of intensity and localization) of the focused field, if, as it remains to be seen, the term "focused" may be applied to the complete diffracted pulse field at the focal plane.

Using the GBM expansion, as a test example we will look at pulse diffraction by zone plate with a focal length of 100 λ_0 and define the radius of the plate according to the desired focusing power represented by the Fresnel number N_F, defined using the most powerful spectral component ν_0, $N_F = \nu_0 a^2/(cf)$. For the following example, N_F = 11, $F\#$ = 1.5076, λ_0 = 0.3 mm, f_0 = 30 mm). In calculation of pulse structures in the spatial domain the term focal "point" or "plane" may be ambiguous when describing the spatial variation of a pulsed field as each spectral component will have a different focal position as we have seen, thus we will shall first refer to the spatial structure of a pulse at the "focal time", the time taken for a pulsed plane wave originating at the plane of the zone plate to reach the focal plane $z = f_0$ for the central frequency ω_0.

The simulated pulsed fields shown in Figure 5.22 are calculated from the inverse Fourier transform of each diffracted monochromatic spectral field, again defined using the Laguerre-Gaussian beam expansion of the zone plate aperture function

$$E(r,z,t = f_0/c) \cong \frac{1}{\sqrt{2\pi}} \int_{-\infty}^{\infty} S(\omega) \left[\sum_{m=0}^{M} A_m \psi_m^L(\omega, r, z, t) \right] \exp(-i\omega t) d\omega . \quad (5.13)$$

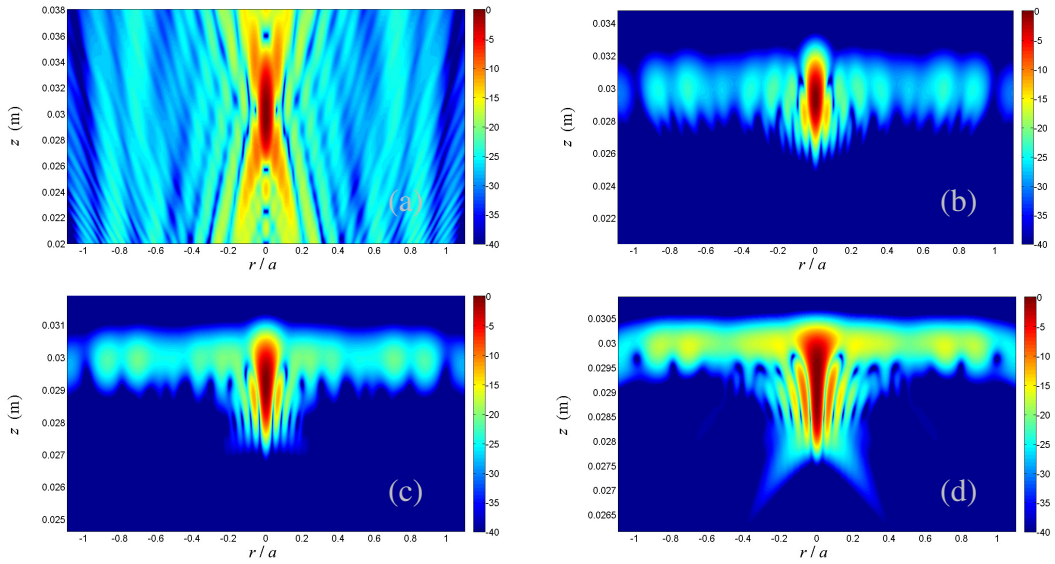

Figure 5.22 -The spatial intensity on a logarithmic dB scale at a time of $t = f_0 / c$, for a $N_F = 5$ Fresnel zone plate. γ = (a) 0 (b) 0.1, (c), 0.5, (d) 1. $\lambda_0 = 0.3$ mm, $f = 30$ mm.

As is evident in the above figures, an increase in the bandwidth of a time dependant signal has a great influence in the focusing of the pulse by a zone plate, see also [ASH03]. Of utmost importance is the generation of spherical boundary waves by the diffraction at off-axis zone boundaries, which are then manifested on the optical axis at a distance significantly less than ct causing a broadening of the on-axis field as illustrated in Figure 5.23.

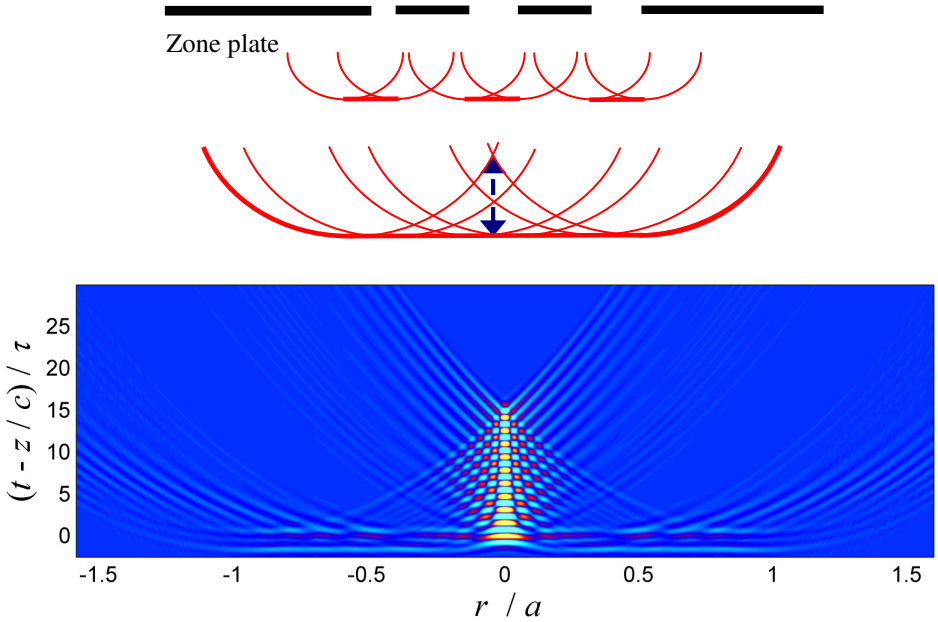

Figure 5.23 – Schematic and saturated plot, in the time-domain, of the amplitude $Re\{E(r, z = f_0,t)\}$ at the focal plane of a zone plate ($N_F = 21$) showing the axial lengthening of the pulse on the optical axis due to edge diffraction at each individual zone of the component.

The amplitude variation $Re\{E\}$ in Figure 5.23 shows, more so than plots of intensity, how lengthened on-axis focal regions occur due to the formation of pulsed spherical features by the edge diffraction at the boundary of each zone. The effect of this in the spatial variation of $|E(r = 0,z,t = f / c)|^2$ along the optical axis at the focal time is shown below for various bandwidths. Note the change in limits along both axes.

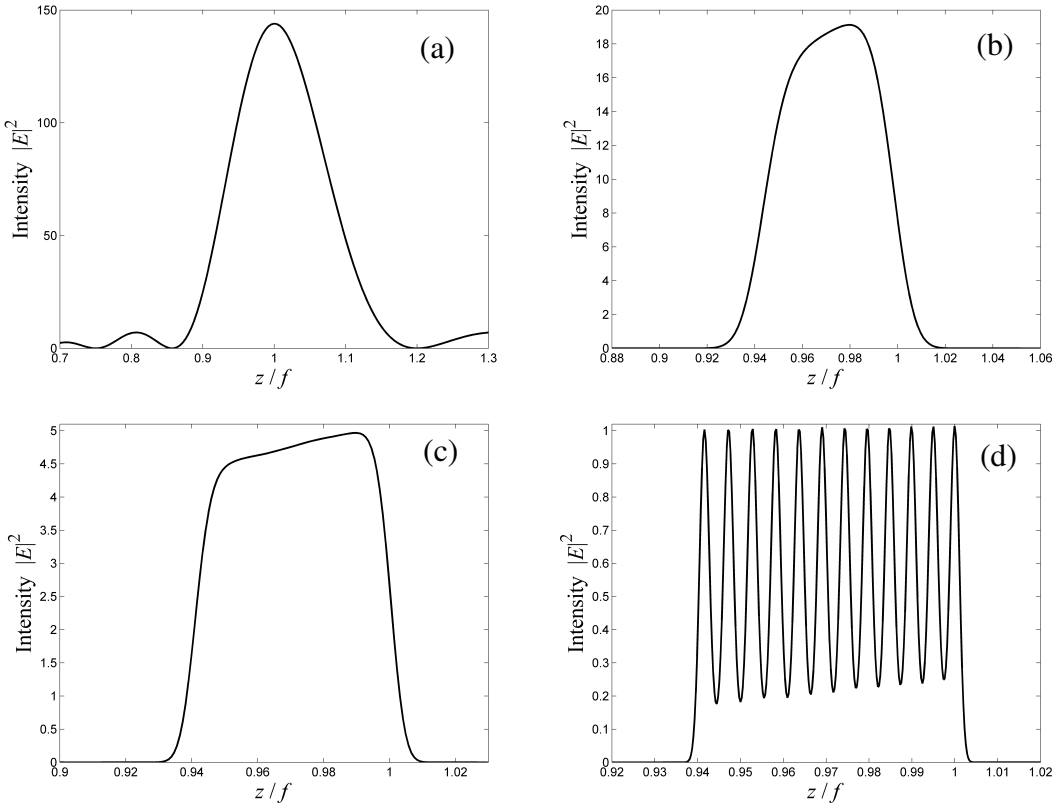

Figure 5.24 - The variation in the longitudinal spatial intensity at the time $t = f_0 / c$ of a Fresnel zone plate according to the fields bandwidth, with $\nu_0 = 1$ THz, $f_0 = 100$, $\lambda_0 = 0.3$mm, $N_F = 11$, $F\# = 1.51$. Illumination is by a plane wave pulse with unit amplitude. The fractional bandwidth for each plot is γ = (a) 0, (b) 0.5, (c) 1, (d) 3.

In previous examples of pulse propagation, in chapter 3, with increasing bandwidth (reducing duration) the duration of a pulse at its source and in the far-field remains very similar. Here we see that at the focal plane of a lens, even with a relatively high $F\#$, with decreasing duration of the pulse the on-axis length of the pulse diffracted by the zone plate increases significantly in comparison with the plane wave pulse length

$c\tau$. This is due to the edge diffraction at each individual zone of the diffractive element. As shown above, for a large bandwidth the spatial length of the complete signal converges, in the geometrical limit, to $ct - \sqrt{c^2t^2 - a^2}$ which deviates greatly from the spatial length of an unobstructed pulsed plane wave of equal duration. In the case of pulses with lower values of the fractional bandwidth γ, when calculated in the spatial domain the trailing on-axis boundary waves have greater lengths on the axis, are superimposed on each other, and will thus interfere to cause a smoother variation of the longitudinal intensity. But with pulses having extremely short durations, as in the case of Figure 5.24(d) , the narrow lengths of each boundary wave on the axis causes a much more obvious "spiking" effect at the focal plane with the creation of N_F+1 peaks along the axis.

As the bandwidth of a signal increases there continues to be a focusing effect of zone plate fields at the focal time, evident from an increase in intensity from that of a unit amplitude plane wave pulse diffracted by a circular aperture only. However, the diffractive broadening of shorter pulses by the element reduces the maximum focal intensity achieved. In the time domain, see Figure 5.25, calculation of the amplitude of the pulse at the focal plane describes a more smoothly varying field than that in the spatial calculations shown previously.

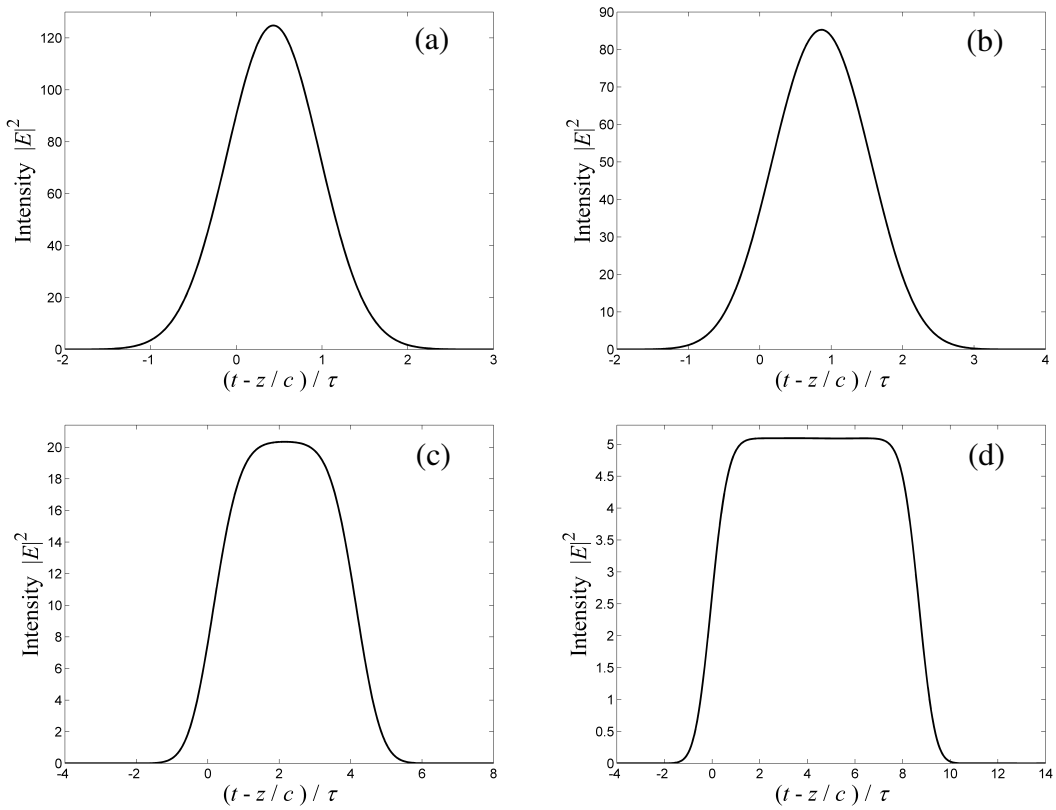

Figure 5.25 - The temporal behaviour of the axial field intensity $|E(r = 0, z = f_0, t)|^2$ of a Fresnel zone plate, for various bandwidths. $N_F = 11$, $F\# = 1.51$, $\nu_0 = 1$ THz.

The focusing ability of a lens element with pulsed illumination can be quantified by the maximum amplitude of the pulsed field at the focal plane relative to the focal strength produced with continuous wave illumination. As shown in the preceding results, an increase in the longitudinal on-axis length and temporal durations of a pulse at the focal plane is associated with a decrease in the maximum value of the field. With an increase in the bandwidth of the pulsed field there is a smooth but rapid decrease in the value of the maximum intensity, relative to the continuous wave illumination with $\gamma = 0$, at the focal plane particularly with large Fresnel numbers, see Figure 5.26.

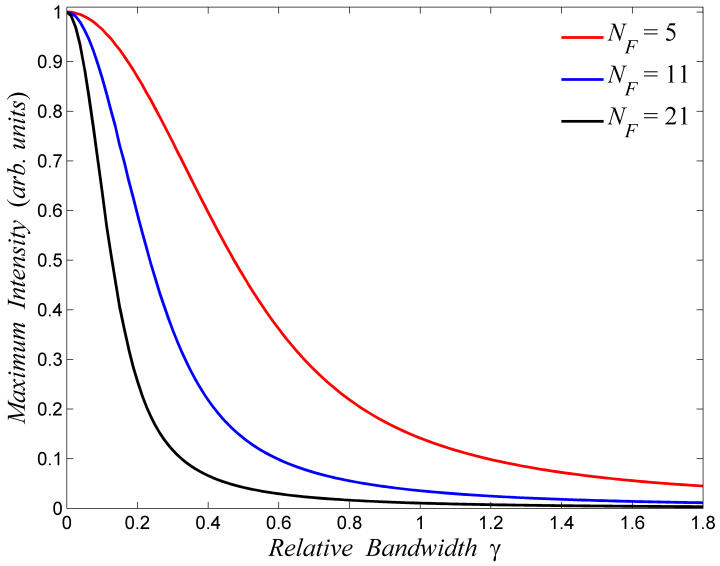

Figure 5.26 - The variation in maximum intensity $|E(r{=}0,z{=}f_0,t|^2$ at the focal distance f_0 of a uniformly illuminated Fresnel zone plate according to the bandwidth of a source driven by a Gaussian amplitude signal. The data is normalised to the maximum focal plane intensity of a cw ($\gamma = 0$) field focused by each zone plate. $\nu_0 = 1$ THz, $f_0 = 100\ \lambda_0$.

With low Fresnel numbers and relatively small bandwidths the FZP does show some level of a practical focusing ability in terms of generating increased amplitude at the focal plane, but with increasing bandwidth the amplitude of the focus plane becomes significantly reduced. Another effect of the zone plate transmittance is, as described in chapter 4, the deviation in the diffractive behaviour of each frequency component of the pulse also causes a variation in the spectral structure of the pulse at various points in space. Thus the axial pulse lengthening observed in the previous examples points to a significant variation in the spectral bandwidth along the optical axis at the focal plane, which could have significant effect on any experiment involving pulsed illumination of diffractive focusing elements. Simulation of a polychromatic field at planes within a broad region around $z = f_0$ shows increased spectral content at frequencies deviating from ω_0 (or ν_0) due to the frequency dependence of the focal length as given by (5.10), and predictions of this effect are shown in Figure 5.27.

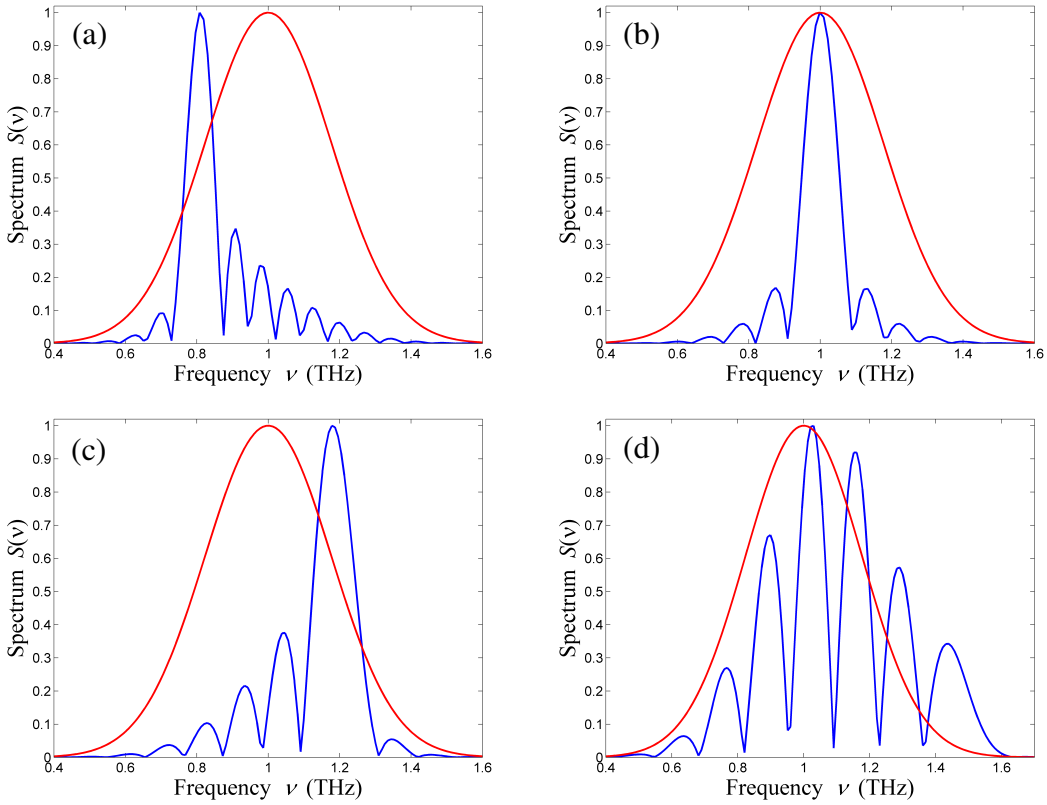

Figure 5.27 - The on-axis spectrum of a $\gamma = 0.5$ temporal field focused by a zone plate (blue line) compared to the original spectrum at the source (red line). $f_0 = 30$mm, $\nu_0 = 1$ THz, ($\lambda_0 = 0.3$mm), and $N_F = 21$. The relative spectral amplitudes have been normalised to unity. z = (a) $0.8\,f_0$, (b) $0.8\,f_0$, (c) $1.2\,f_0$, (d) $1.5\,f_0$.

Figure 5.27 (b) shows the spectrum of the on-axis field at the focal plane f_0 being altered to a "sinc-like" variation around ω_0, caused by an increase of the on-axis pulse duration due to boundary diffraction which also signifies a reduction in spectral amplitude of frequencies deviating from ω_0 that are focused to different planes.

A "focal range" can be attributed to a zone plate for a pulse of given bandwidth $\Delta\nu$ determined by the longitudinal distance over which one significantly powerful spectral component, i.e. with a frequency within $\nu_0 \pm \Delta\nu/2$, is focused, which is given as

$$\Delta f_\lambda = \frac{\Delta\nu}{\nu_0} f_0 , \tag{5.14}$$

which in the case of the element described in Figure 5.27 gives a focal range of the significant spectral components between distances of 24mm and 36mm. Beyond 36mm, as in figure 5.25 (d), no focusing of any single spectral component occurs.

To quantify the variation of the spectral distributions at the focal plane f_0 numerically, the FWHM of the spectral variations were calculated for comparison with

the original spectrum, rather than the spectral width at the 1/*e* level so as to avoid any possible discrepancies involving the secondary lobes of the spectra that may, or not, occur during the automated calculation. Figure 5.28 depicts the reduction in the FWHM of the spectral bandwidth at the focal plane of a zone plate.

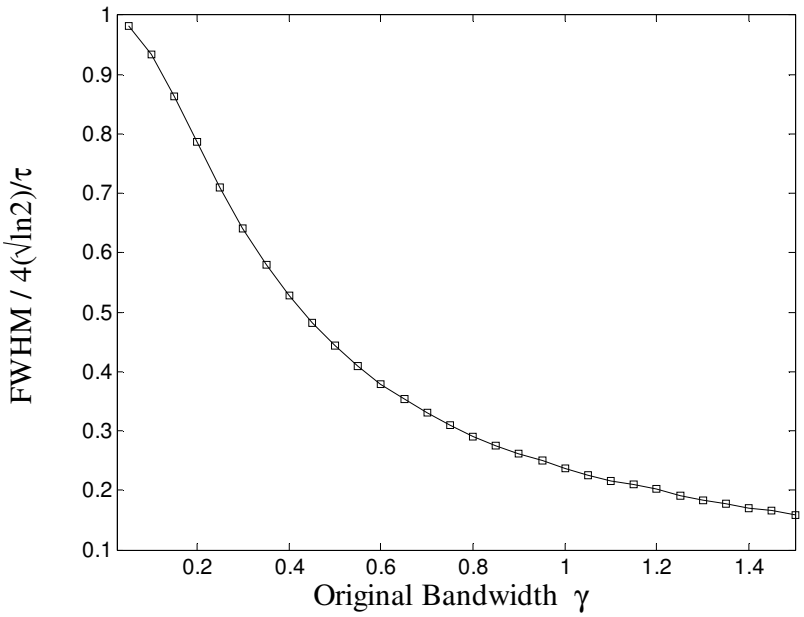

Figure 5.28 -The ratio of the on-axis spectral width calculated at the focal plane of a FZP to the original fractional bandwidth of the signal ($\gamma = \Delta\omega/\omega_0$) at the source. $N_F = 11$ and $f = 100\ \lambda_0$.

5.6 - Modulation of optical pulses by diffractive Fresnel lenses

Under illumination by ultrashort pulses, conventional thin spherical lenses also induce a vast change in the structure of the pulse at the focal plane. This deviation is caused by material dispersion resulting from the variation of the refractive index across the frequency spectrum which, for each spectral component, alters the focal length $f(\omega)$, causing a change in the dynamics and structure of the focused pulse. The effects described above relating to FZPs are somewhat similar to those caused by dispersion in thin spherical dielectric lenses, but are induced by diffraction in a Fresnel zone plate rather than dispersion.

In the preceding chapter we showed the propagation of a temporally modulated field through a transparent dispersive material and through numerical simulations showed the effects of group velocity and broadening due to the varying phase velocity of each frequency component within the medium. Now, we examine how dispersion in

a diffractive dielectric lens effects the focusing of a pulse, which requires simulating the emergence of the field from a dispersive dielectric with a suitable description of the materials influence on the wavefront. In this section, we refer to pulses in the near-infrared band. Although the free-space propagation can be related to fields in the terahertz band, the validity of dispersion relations of materials used in that EM region, such as HDPE or Teflon PTFE, was not known to the author.

To determine the dispersive effects suffered by a pulse after propagation through an optically dense material using a scalar theory, the dispersive influence of the glass/dielectric can be analysed analytically. As an example, the propagation of an ideal plane wave pulse through a homogenous dispersive medium of length z can be represented as

$$E(z,t) = \frac{1}{\sqrt{2\pi}} \int_0^\infty S(\omega) \exp\left(i\kappa(\omega)z - i\omega t\right) d\omega$$

where the wavenumber $\kappa(\omega) = n(\omega)\omega/c$. To avoid having to numerically simulate the dispersion effects caused within the lens as a separate computation to the freespace propagation, we use a Taylor series representation of the frequency dependent wavenumber within the lens, [DENG05]. A function $g(x)$ can be represented through the Taylor expansion

$$g(x) = \sum_{m=0}^{\infty} \frac{(x - x_0)^m \, g^{(m)}(x_0)}{m!}$$

where $g^{(m)}(x_0)$ is the m^{th} derivative of $g(x)$ at x_0. Applying this representation to the wavenumber $\omega n(\omega)/c$ and truncating the series to the first three terms gives

$$\begin{aligned}\kappa(\omega) = \frac{\omega n(\omega)}{c} &= \underbrace{\frac{\omega_0 n_0}{c}}_{\kappa_1(\omega)} + \underbrace{\frac{n_0 + \omega_0 \left.\frac{dn}{d\omega}\right|_{\omega_0}}{c}(\omega - \omega_0)}_{\kappa_2(\omega)} \\ &\quad + \underbrace{\frac{1}{2}\left(\frac{2}{c}\left.\frac{dn}{d\omega}\right|_{\omega_0} + \frac{\omega_0}{c}\left.\frac{d^2 n}{d\omega^2}\right|_{\omega_0}\right)(\omega - \omega_0)^2 + \ldots}_{\kappa_3(\omega)} \\ &= \kappa_1(\omega) + \kappa_2(\omega) + \kappa_3(\omega) + \ldots. \end{aligned} \tag{5.15}$$

The first term, $\kappa_1(\omega)$, on the right of eq. (5.15) defines the deviation of phase caused by the medium on the central wavenumber which creates an equal phase shift for every spectral component but does not affect the structure of the pulse. The second term $\kappa_2(\omega)$

of eq. (5.11) defines the phase difference caused by the delay of the pulse generated by the reduction in group velocity of the field within the medium, and is identical to an expression we used previously in chapter 4. The third phrase $\kappa_3(\omega)$ defines the effect on the phase due to the group velocity dispersion which accounts for the broadening of the pulse due to the deviating velocities of each spectral component. Generally, even for significant propagation distances z, it can be acceptable for higher-order Taylor dispersion terms (m>3) to be neglected. However, this assumption also requires that the variation of the refractive index across the frequency range in the simulated spectrum is relatively gradual, and for fields with carrier frequencies closer to resonance frequencies, much higher order Taylor terms may have to be included for an accurate description of the dispersion relation. Inclusion of these κ terms in the inverse Fourier transformation of the spectral components used in calculating the field will then allow for prediction of the dispersive effects. Figure 5.29 below shows the effect of truncation of the Taylor series on calculations of a ν_0 = 1 THz, γ = 1 pulse after propagation through a SiO_2 dielectric of depth 10 λ_0.

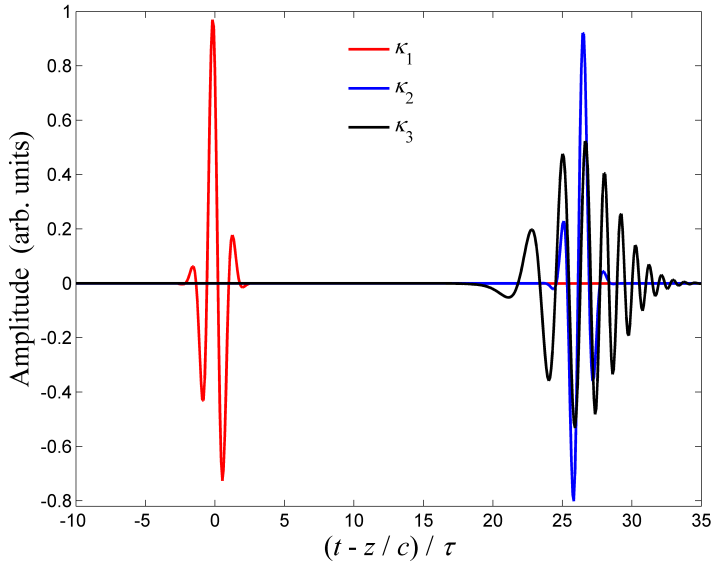

Figure 5.29 – Effect of inclusion of higher order Taylor terms κ_m in the dispersion of a planar γ = 1, λ_0 = 800 nm pulse within a SiO_2 dielectric.

While the approximation of (5.15) is not essential for numerically calculating the pulse, it does allow for analytical prediction of dispersion effects, such as the temporal pulse broadening introduced. The duration of the pulse after propagating a distance z, $\tau(z)$, in a dispersive media can be approximated from [KHE08]

$$\tau(z) = \tau \sqrt{1 + 4 \frac{\left(\frac{2}{c} \frac{dn}{d\omega}\Big|_{\omega_0} + \frac{\omega_0}{c} \frac{d^2 n}{d\omega^2}\Big|_{\omega_0} \right)^2 z^2}{\tau^4}}$$

The simulation of pulses modulated by dispersive lenses using the Gaussian beam mode expansion is a more extensive computation than that discussed in the case of amplitude modulating zone plates, although showing somewhat similar effects. Each frequency component of the pulse spectrum will now have a different amplitude profile at the plane of the optical element due to the frequency dependence of the radial phase variation. The mode coefficients must then be computed for each individual spectral component to determine the propagation dynamics of the pulse. As an example, we simulated the propagation of a field diffracted/refracted by quartz (Silicon Dioxide SiO_2) lenses with λ = 800 nm. This is the operating wavelength of the Titanium-Sapphire laser systems referred to in the literature as a common source of ultrashort femtosecond pulses. Also, the absorption frequencies required for evaluation of the refractive index using the Sellmeir equation are well known to be valid within this region of the EM spectrum. In simulating the propagation of a polychromatic field with a carrier wavelength of 800nm in SiO_2, a fractional bandwidth of γ = 0.5 was found to be acceptable in defining valid values of $n(\omega)$ without encountering resonance/absorption frequencies in the dispersion relation defined by the Sellmeir relations.

Using the Gaussian beam mode formulation, we can now describe the free-space propagation of a few-cycle pulse upon emergence from a dispersive plano-convex thin spherical lens defined by the structure outlined in Figure 5.30.

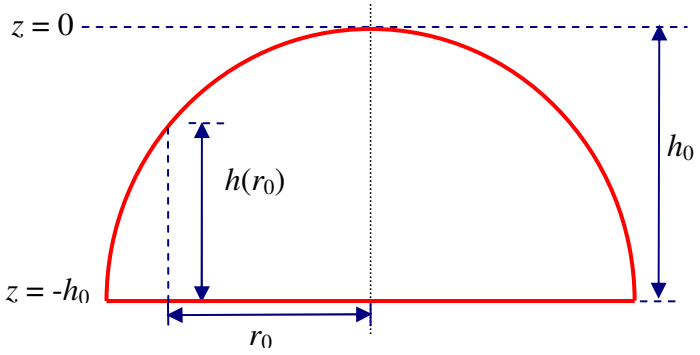

Figure 5.30 – Schematic of lens structure to be modelled using the GBM approach of pulse simulation.

For a focal length f_0 the radius of curvature of a lens of transverse radius a is given by $R_{lens} = f_0 (n_0 - 1)$ so the height of the lens as a function of the radial offset r_0 is then

$$h(r_0) = \sqrt{R_{lens}^2 - r_0^2} - \sqrt{R_{lens}^2 - a^2} \ .$$

The central and thickest point of the lens is defined at $z = 0$, with off axis points located at $z = -h(r_0)$. In an example case to be discussed, the maximum thickness of the lens is 16.64 μm (≈ 20.8 λ_0). The reader should note that in this section we have used the exact description of a sphere in defining the lens instead of the paraxial approximation derived in chapter 2. The main application of the parabolic portrayal is for mathematical simplicity, in that the variation of $\exp(ikr^2/2f)$ allows for easier manipulation compared to the square root term in the true spherical description, therefore allowing analytical solutions of the Fresnel-Kirchoff diffraction integrals to be obtained, such as eq. (5.1).

The Laguerre-Gaussian mode coefficients used to simulate this diffraction scenario are now a function of frequency and are determined from the following overlap integral

$$A_m(\omega) = \sqrt{\frac{8\pi}{w_0^2}} \int_0^a \left\{ L_m\left(2\frac{r_0^2}{w_0^2} \right) \exp\left(-\frac{r_0^2}{w_0^2} \right) \right.$$
$$\left. \times \exp\left(i\left(\kappa_1 + \kappa_2 + \kappa_3\right) h(r) + i\frac{\omega}{c}\left(h_0 - h(r)\right) \right) r_0 \right\} dr_0 . \qquad (5.16)$$

The argument of the complex exponential in equation (5.16) describes the change in phase imposed on the field upon transmission through the optically dense lens and subsequent propagation through free-space from the surface of the lens medium, at $z = -h(r_0)$, to the plane of the lens zenith which is defined to be at $z = 0$. Note that while a more realistic description of the spherical lens surface has been used, the calculations continue to neglect diffractive effects within the lens as with the paraxial approximation of the lens phase function. Predicting the combined effects of diffraction and dispersion within a curved lens is complicated, even assuming paraxial propagation, but would be a suitable and very practical application of the FDTD method♣.

♣ As it is obviously a time domain method, the frequency dependence of permittivity is not an inherent feature of the fundamental form of FDTD as described in chapter 2. The permittivity of a medium, $\varepsilon(\omega)$, with $n(\omega) = (\varepsilon(\omega)/\varepsilon_0)^{1/2}$, can be deduced from the Lorentzian model of an oscillating electron as

$$\varepsilon(\omega) = \frac{D(\omega)}{E(\omega)} = \varepsilon_\infty - \frac{\omega_R^2(\varepsilon_{DC} - \varepsilon_\infty)}{\omega^2 + 2i\omega\delta - \omega_R^2}$$

The GBM description of a pulsed field diffracted by a dispersive phase modulating element is now calculated from

$$E(r,z,t) \cong \frac{1}{\sqrt{2\pi}} \int_0^{\infty} S(\omega) \left(\sum_{m=0}^{M} A_m(\omega) \psi_m^L(\omega, r, z, t) \right) \exp(-i\omega t) d\omega \qquad (5.17)$$

which now incorporates the dispersive effects defined by κ_1, κ_2, and κ_3, as incorporated in eq. (5.16).

Despite the requirement of calculating Laguerre-Gaussian mode sets for all spectral components, the GBMA code does again maintain very practical efficiency compared to the use of the Fresnel diffraction integral in predicting the diffracted structure of pulses undergoing dispersive transformation. This is particularly true when studying a field at varying distances z for which the same mode sets can be used for calculations at multiple planes without involving numerical integrations of the aperture function. Figure 5.31 shows the paraxial calculations for the propagation of a $\gamma = 0.5$ pulse focused by a $N_F = 20$ spherical lens, with λ_0=800nm $a = 35.7\mu$m, and $f_0 = 80$ μm, F#1.18.

---

with ε_{DC} and ε_∞ the low and high frequency limits of $\varepsilon(\omega)$ respectively, while ω_R is some resonance frequency of the medium (perhaps one of many), and δ is a frictional damping constant of the electron motion. An inverse Fourier transform of $\varepsilon(\omega)$ gives the second order differential equation

$$\omega_R^2 D + 2\delta \frac{dD}{dt} + \frac{d^2 D}{dt^2} = \omega_R^2 \varepsilon_{DC} E + 2\delta \varepsilon_\infty \frac{dE}{dt} + \varepsilon_\infty \frac{d^2 E}{dt^2}$$

which when discretised, can be implemented in a model to determine the temporal response of a dispersive medium to a pulsed field. See [JOS91] for further details.

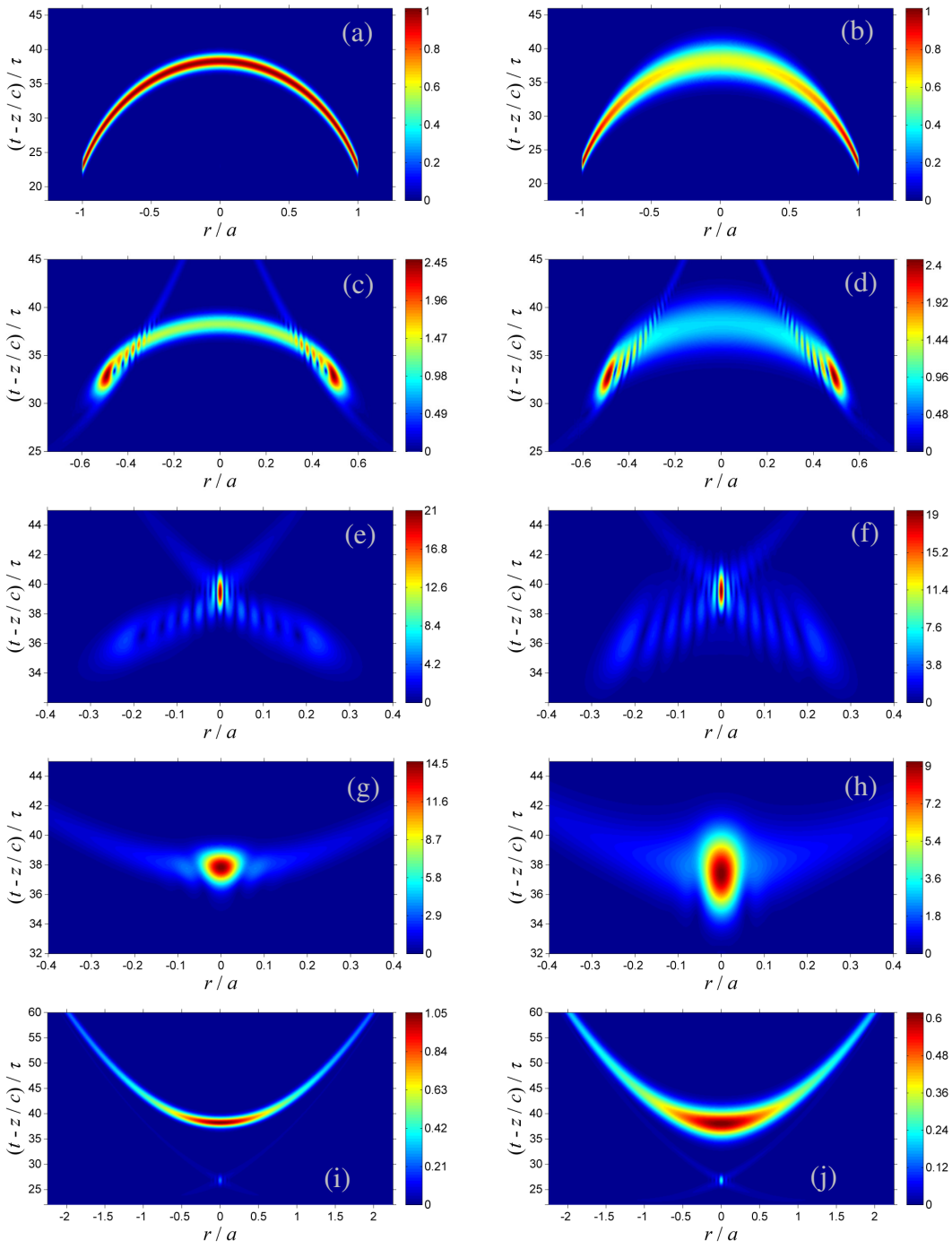

Figure 5.31 - The focusing of a planar pulse ($\gamma = 0.5$, $2\tau = 6.8$ fs, $\lambda_0 = 800$ nm) by a SiO_2 hemispherical lens with focal length $f_0 = 80\mu m$. The left column shows a first order dispersive calculation while the right column shows a second order dispersive calculation, noticeable through the temporal broadening of the pulse. z = (a)-(b) 0, (c)-(d) $f_0/4$, (e)-(f) $f_0/2$, (g)-(h) f_0, (i)-(j) 2 f_0. The fields are shown by their amplitude $|E(r,z,t)|$ on a linear scale.

In Figure 5.31 (a) the delay of the pulse wavefront caused by dispersion can be seen. At $r = a$, where the depth of the lens is zero, the relative delay is given by $h(a)/c \sim$ 77fs (22.9τ), while at $r = 0$ the relative delay is $h_0/v_g \sim$ 130 fs (38.27τ), where v_g is the

group velocity of the wavefront within the lens, in this case v_g = 1.795×10^8 m/s. The group velocity dispersion of the refractive index in the lens causes a temporal broadening in the pulse approximately twice the original pulse duration 2τ = 6.8 fs at r_0 = 0 as seen in Figure 5.31 (b). Due to the broadening there is also an increasing reduction in the maximum longitudinal amplitude of the pulse at each offset, which is proportional to the varying lens thickness. Because of the lesser pulse delay in the lens at $r = a$ the on-axis manifestation of the boundary waves from the edge of the lens actually arrives at a plane before the primary geometric wave, as can be seen in Figure 5.31 (i)-(j).

Now, for thin optical components such as the diffractive Fresnel lenses described in this chapter, with a maximum thickness of $h_0 = (P\text{-}1)\lambda_0/P(n_0\text{-}1)$ the effects of the lens profile on an incident pulsed field are so small that they can be determined without necessarily accounting for dispersion effects. As the pulse broadening is dependent on the optical path length of the pulse in the dispersive medium, the field will, to a good approximation, hold its temporal form in propagating through very thin diffractive lenses. Therefore, the complete pulse wavefront at the surface of the lens may be computed by accounting only for the phase modulation on each spectral component. With a dielectric diffractive lens, neglecting dispersion in the relatively small optical depth of the lens, the mode coefficients can be given as

$$A_m(\omega) = \sqrt{\frac{2}{\pi\, w_0^2}} \int_0^a L_m\left(2\frac{r_0^2}{w_0^2}\right) \exp\left(-\frac{r_0^2}{w_0^2}\right) \exp\left(i\left(\frac{n(\omega)-1}{n(\omega_0)-1}\right)\frac{\omega}{\omega_0}\phi_P(r_0)\right) 2\pi\, r_0\, dr_0, \qquad (5.18)$$

where $\phi_P(r_0)$ is the transverse phase variation imposed by the diffractive lens on a field at the design frequency ω_0, defined by eq. (5.5). Despite only minor differences between the results of this equation and eq. (5.16), with future work in mind, the dispersive description of propagation given by eq. (5.16) was used so as to gain an understanding of the type of field dynamics involved in a dispersive scenario.

The mode coefficients for a polychromatic field with γ = 0.5 were calculated for a two level SiO_2 diffractive lens with λ_0 = 800nm, and N_F = 10. The values of $A_m(\omega)$ are shown in Figure 5.32.

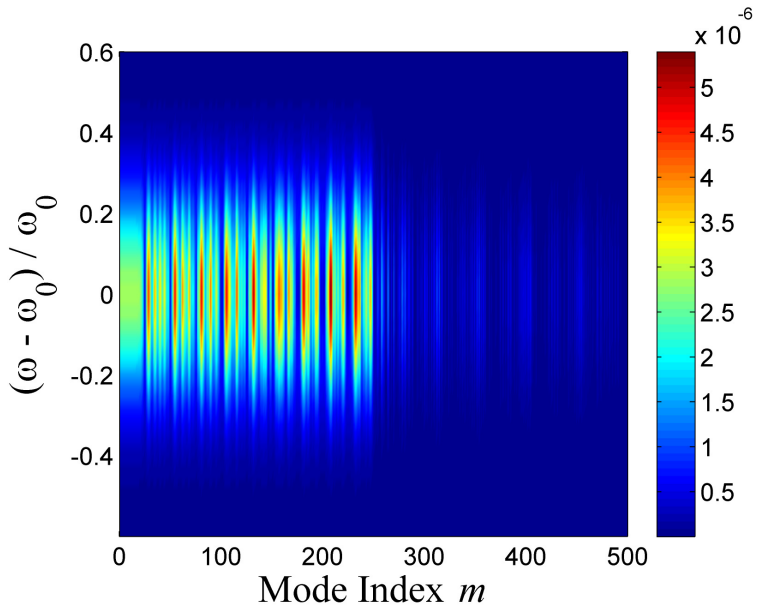

Figure 5.32 – The LG mode coefficients $|A_m(\omega)|$ of a $\gamma = 0.5$ pulsed plane field refracted by a SiO_2 diffractive lens with $N_F = 10$, $P = 2$. The normalised Gaussian spectral variation $S(\omega)$has been superimposed on the variation.

Using the mode set in Figure 5.32 the field can then be predicted at any point in the diffraction half-plane for $z > 0$. Figure 5.33 illustrates the predicted evolution of a $\gamma = 0.5$ pulsed plane waves modulated by diffractive lenses with $P = 2$, and $P = 6$. Calculations based on equations (5.16) and (5.18) predict almost identical pulse structures, with the exception that the computation used, which accounts for dispersive delay and broadening, i.e. eq. (5.16), predicts a small but realistic time delay of h_0/v_g compared to the field determined with the non-dispersive technique. A time delay between the $P = 2$ and $P = 6$ fields should also be noted due to the greater depth and the associated increased delay within the $P = 6$ lens.

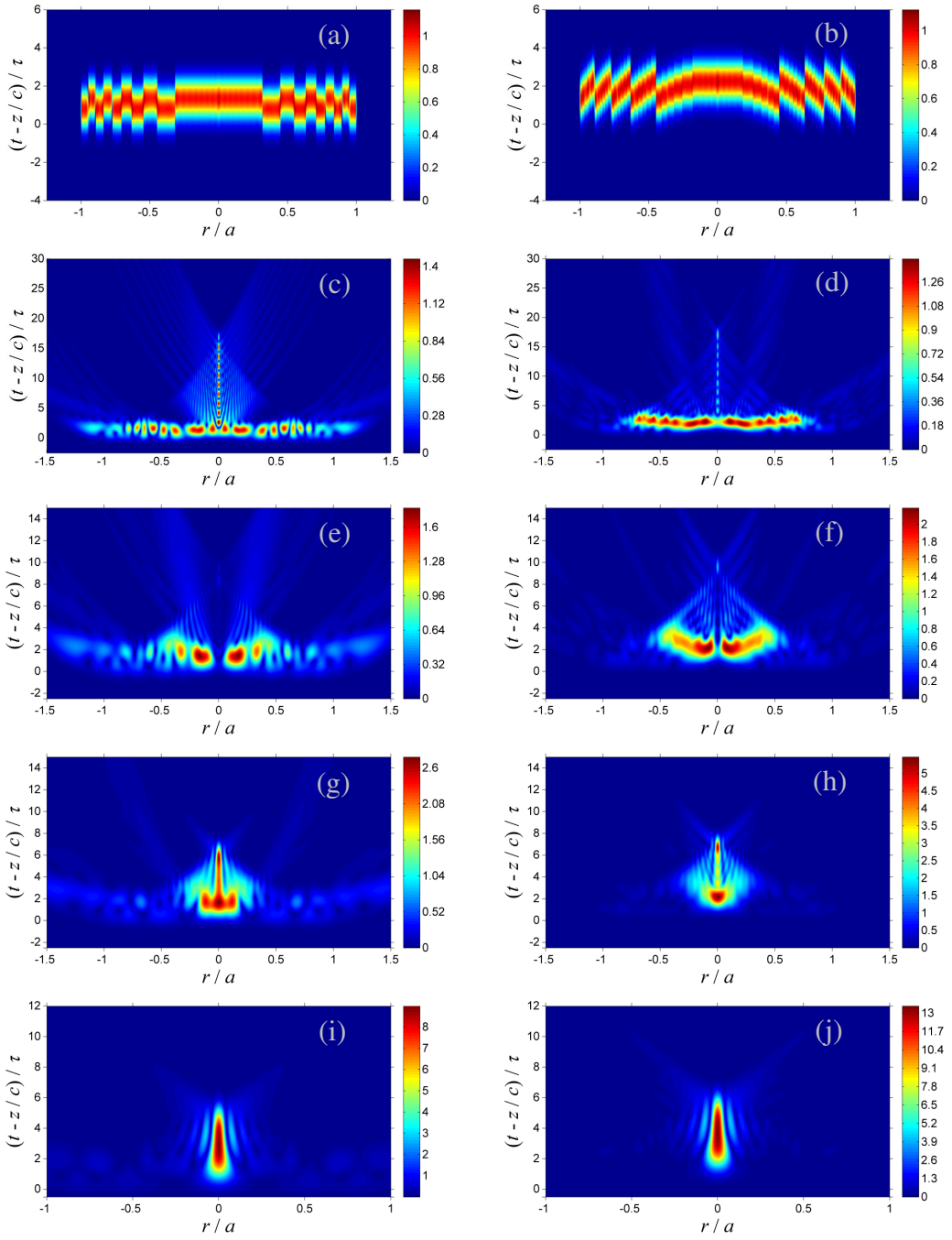

Figure 5.33 – The amplitude $|E(r,z,t)|$ of a $\gamma = 0.5$ pulse at various planes diffracted by a quartz (SiO_2) diffractive Fresnel lens. $\lambda_0 = 800$ nm, $f_0 = 100\ \lambda_0$, $N_F = 10$. The left column shows the effects of a lens with $P = 2$, and in the right column $P = 6$. The fields are predicted at $z =$ (a)-(b) 0 , (c)-(d) $f_0 / 4$, (e)-(f) $f_0 / 2$, (g)-(h) $0.75\ f_0$, (i)-(j) f_0.

With the exception of an approximately twofold increase in maximum amplitude values and a time delay due to dispersion, the effects of a diffractive lens modulation on the dynamics of pulsed fields, such as the influence of boundary waves, are generally similar for Fresnel lenses with $P = 2$ and Fresnel zone plates of equal dimensions and

Fresnel numbers. However, with a higher number of surface levels of a diffractive lens there is greater concentration of energy close to the optical axis with noticeable increase of the maximum intensity, which is described in Figure 5.34.

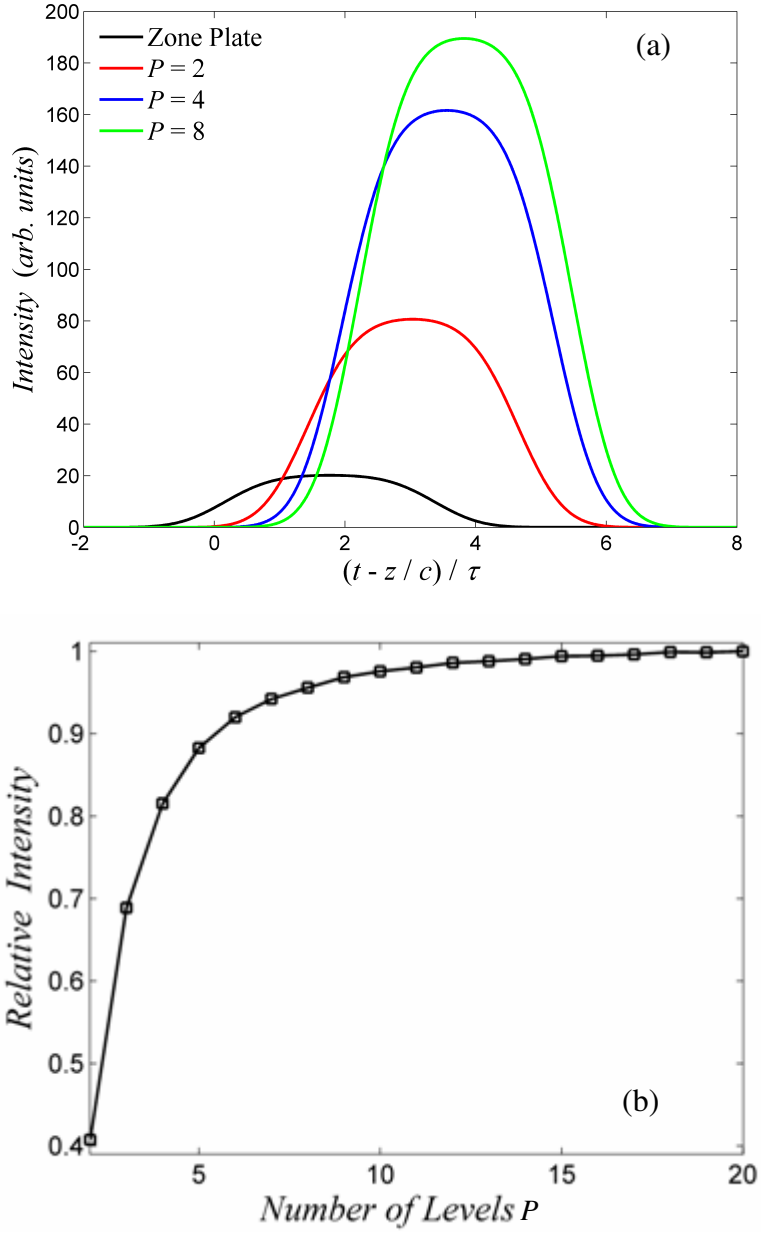

Figure 5.34 – (a) The axial intensity of a pulsed $\gamma = 0.5$ Gaussian shaped pulse at the focal plane of a $N_F = 10$, $f_0 = 100\lambda_0$ diffractive lens illuminated by a $\gamma = 0.5$ Gaussian shaped pulse. (b) The variation of the maximum intensity in relation of diffractive lenses to the ideal Fresnel lens ($P = \infty$)**.**

Figure 5.34 shows, upon comparison with the data in Figure 5.13, that the variation of the relative intensities at the focal plane of a diffractive lens with increasing P illuminated by a pulsed field differs only negligibly from the same characterisation of

a zone plate under continuous wave illumination. Figure 5.35 below compares the temporal field at the focal plane and shows the significant deviation in the duration and transverse structure of a pulse at the focal plane of one of these diffractive lenses.

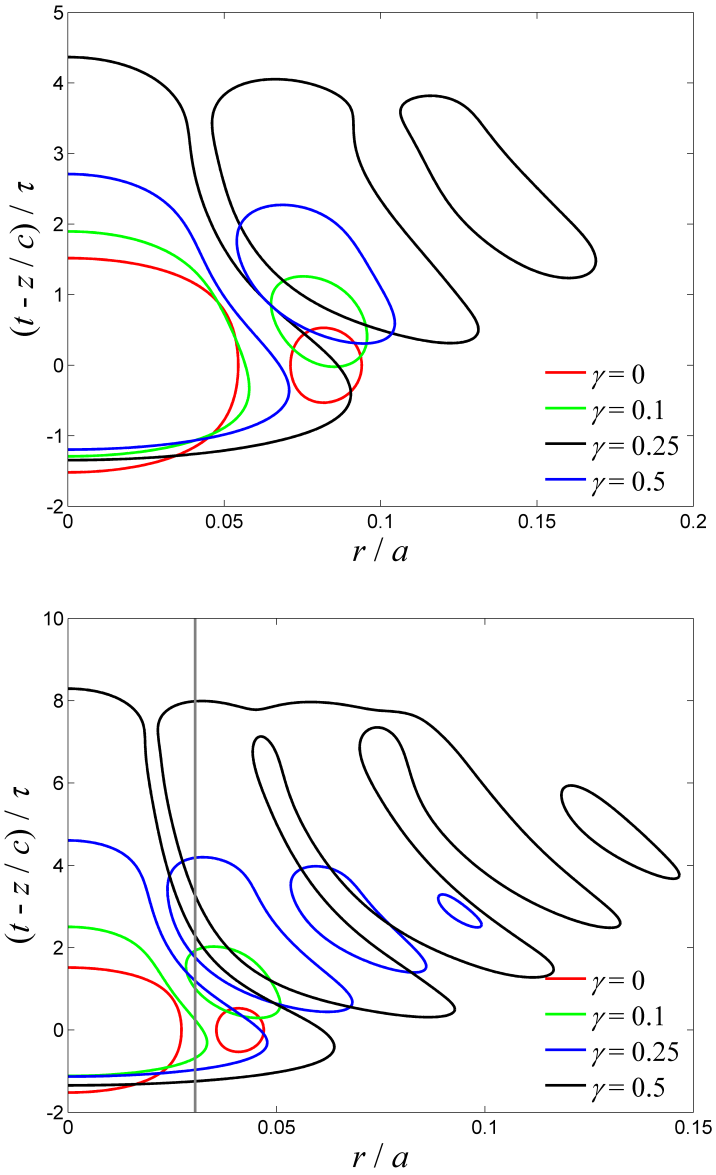

Figure 5.35 – Contours showing the -20dB levels of the normalised intensity structure at the focal plane of a binary (P = 2) Fresnel lens with (a) N_F = 10 and (b) N_F = 20 illuminated by a Gaussian temporal pulse. The vertical gray lines indicate the continuous-wave focal radius calculated from eq. (5.1).

The chromatic influence of Fresnel zone plates, eq. (5.10), which also has relevance in this section, shows an opposite effect to that of the material dispersion imposed in spherical lenses in that the individual focal planes of the fields with longer wavelengths focused by a complete ideal thin lens are located further from the element than those with shorter wavelengths, effectively a chromatic aberration. The fields

depicted in Figure 5.35 show that the pulsed fields arrive at the focal plane with a broad transverse width and reduce in breadth as the pulse passes through the focal plane. This is in contrast to the fields shown in Figure 5.31 (g) and (h). Assuming first-order dispersion, the focal length of a spherical lens with a radius of surface curvature R is determined by

$$f(\lambda) = \frac{R}{n(\lambda) - 1}.$$

Generally, far from absorption wavelengths, the refractive index $n(\lambda)$ of commonly used lens materials decreases with increasing wavelength, therefore focal lengths for longer wavelengths will be further from the ideal focal plane lens, which is an opposite effect to the variation of focal lengths for zone plates and diffractive lenses described by eq. 5.10.

An increase of a pulsed field's bandwidth results in a smoothing of the transverse amplitude variation, as shown in section 4.4, and in the fields discussed here, this effect will be important in determining the suitability of a diffractive lens for pulsed imaging. As shown in the following figures, the temporal modulation of the field causes significant deviation from the distribution described by equation 5.1.

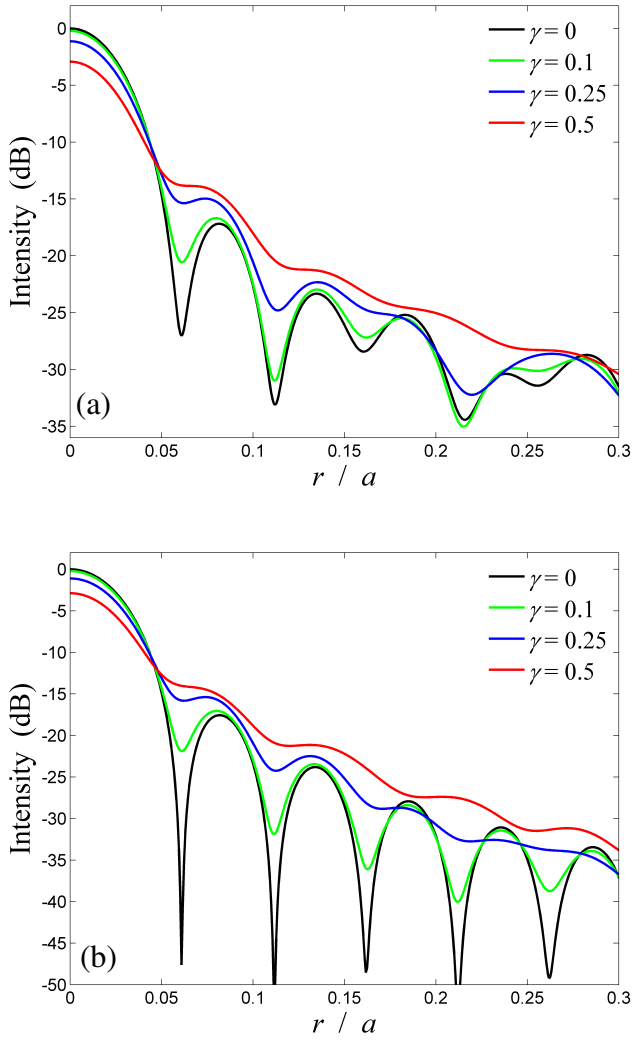

Figure 5.36 – The normalised variation, with bandwidth, of the transverse time-averaged intensity at the focal plane $z = f_0$ of a $N_F = 10$ diffractive lens with (*a*) $P = 2$, (*b*) $P = 6$, SiO_2, illuminated by a pulsed plane wave with central wavelength $\lambda_0 = 800$nm.

The calculated intensities show a definite focus of fields. As can be seen in the case of $\gamma = 0.1$ the relative intensity levels of the off-axis beam lobes do not vary significantly from the structure of the continuous wave field. But with a reduction of the signal duration the increase in the relative intensity levels of the first off-axis maxima show that useful localisation of the ultrashort pulsed fields becomes limited with these optical components.

Conclusion

The properties of diffractive lenses and Fresnel zone plates under illumination by continuous and pulsed fields have been discussed using the Laguerre-Gaussian beam approximation of the Fresnel diffraction theory.

A binary Fresnel lens with $N_F = 9$ and $F\#1.33$ was designed by the author and manufactured in the department workshop. Experimental measurement of the imaging of a corrugated horn was performed and the results showed excellent agreement with a 51 term Gaussian beam mode calculation.

We have exhibited the spatial and temporal characteristics of the electric field at the focal plane of a diffractive lens. In the case of time-dependent signals, we have shown that the generation of secondary pulses by the edges of each individual zone causes a significant broadening of the pulse when compared with the length $w_L\ (= c\tau)$ of an unobstructed pulsed plane wave. The effect is particularly noticeable at large bandwidths, but for signals with narrower frequency spectra the position of the peak of the trailing on-axis pulse from a zone boundary will occur within the extent of the main primary pulse and therefore broadening, relative to the pulse duration 2τ, is less significant. With such lengthening of the extent of a pulse there is an obvious decrease in maximum intensity of the pulse at the focal time. Again, it is with an increase in bandwidth that we see reduction in this property.

The results show that for pulsed wave illumination, the ability of a Fresnel zone plate in generating a significant concentration of energy at its focal plane is diminished due to the variation of the focal plane for each spectral component. However, diffractive lenses and FZPs do show maintain an ability to concentrate some energy towards this point which may be appropriate in spectroscopic and imaging experiments. However, the broadening of pulses by diffraction through a FZP shows similar effects to the dispersive effects of a thin lens on a pulse, and affects greatly the spectra of pulses at the focal plane of the elements, which must be accounted for in any application. We have exhibited the decrease in field bandwidth on-axis at the focal plane in comparison with the original spectra at the source for a zone plate of $N_F = 11$.

The propagation of few-cycle pulses in dispersive media has again been exhibited, but with a more practical application than in chapter four. Here we have applied the Gaussian beam mode method for simulating the free space propagation of ultrashort fields modulated by dispersive lenses. With the same method a discussion of the effects of diffractive and dispersive Fresnel lenses has been presented, and we have

exhibited the effects of dispersion on the focusing ability of these optical elements. However, it has been described that with the thin diffractive lenses, the field can be predicted, excepting a time delay at the focal plane, by neglecting the effects of group velocity dispersion within the element and considering only the effect of lens thickness on the modulation of the phase of the field.

The effect of non ideal focusing of pulses is also an issue in the conventional spherical lenses exhibiting chromatic aberration. With an ideal non-dispersive material, spherical lenses could generate highly focused pulses with a coincidence in the focal plane of each spectral component. However, the effects of dispersion that occur naturally in optical glasses disallow such propagation and the author has shown the behaviour of optical pulses subject to such phase modulation.

Attention must be brought to the fact that analysis of the modulation of pulses by diffractive lenses was carried out in this thesis with a spectrum with its most significant frequency component corresponding to the design frequency of each lens. The effects of diffractive lenses on EM fields will vary significantly for pulses with irregular spectra.

Chapter Six

Laguerre-Gaussian Expansion of Non-diffracting Beams

6.1 - Introduction

The linear lossless wave equation has several solutions, and the occurrence and usage of these solutions depend most often on the coordinate frame in which the equation is studied. For example, the vibrating membrane of a circular drum would be analysed using the cylindrical system where the z parameter is rendered insignificant and is reduced to an angular and radial problem only. On the other hand the Schrödinger equation in a square potential well is solved using the Cartesian description of space. As discussed in the previous chapters the paraxial wave equation yields different solutions, yet each of these paraxial fields is analogous to corresponding fields derived from the full wave equation using the same mathematical methods. Cylindrical systems give rise to, for example, the Bessel and Laguerre-Gaussian wave functions, in the Cartesian system the plane wave solutions $\exp(i(k_x x + k_y y + k_z z)$ are the paraxial analogues of the Hermite-Gaussian functions. For elliptical systems, which have limited application in optical systems, the Mathieu functions are solutions of the corresponding wave equation while the Ince-Gaussian beam modes are derived from the paraxial wave equation in the same system [BAN04].

In 1987 J. Durnin at the University of Rochester published a paper that described the generation of a form of electromagnetic field showing limited diffraction effects in comparison with any other known field, with the exception of the fundamental plane wave [DUR87]. These field structures, now known as Bessel beams (BB's), were obtained from a straightforward solution of the wave equation, and it was shown that approximations to such fields could be produced in a straightforward optical arrangement. The experimental results showed the propagation of a field containing a narrow, intense, spot that propagated much further without significant diffraction effects compared to a Gaussian beam of a similar full width at half maximum (FWHM). However, the term “non-diffracting beam”, which has been used widely, is a misnomer as those fields are subject to the same laws of wave propagation as any other field thus

diffraction must be a feature of their behaviour. In the same manner a Gaussian beam will maintain an approximately constant width for an appreciable distance, ideal BB's will propagate in the same way, but because of the structure of the Bessel functions, such beams will propagate with a very narrow intense central spot over an infinite distance.

The mathematical solution to the wave equation that represents these Bessel beams is valid over the spatial range of {-∞,∞}, and thus a truly non-diffracting beam cannot be realized in a laboratory, analogous of course to a uniform plane wave in the Cartesian coordinate system. However, several methods now exist for the generation of approximate BB's, including the focusing of an annular beam [DUR87], conical lens or axicon [MONK99], and computer generated holograms [MEL03]. In fact, the capability to produce Bessel Beams was described in the 1970's in [BRYN76], where a CGH was used in the creation of a conical wavefront, the phase variation necessary for the formation of Bessel beams, but the (non-)diffractive properties of the reconstructed object field was not recognised by the authors. Since the first experimental description in [DUR87], these fields have been formed at several regions of the spectrum, from the mm-wave band, [TRA04,MONK99], to ultraviolet wavelengths [DAO09]. Ultrasound has also been used to generate such a diffraction limited field and measurement of these fields has been visualized in water [LU90]. The prospect of generating an intense focal line is a very useful application in several areas of research that involves wave phenomena.

The main application of Bessel beams has been found in manipulation of micron-scale objects and optical trapping using intense visible laser light. [ZWI10] has recently shown the manipulation of microscopic particles using Bessel beams generated by a conical lens. Also in this area, the research carried out by a team at the University of St. Andrews has been the prime example of such work, see [ARLT01], [DHO06].

The field of nonlinear optics is an area which has applied the increased localized intensity possible with Bessel beams. With very intense fields the relationship between the applied electric field and induced dipole moments within a dielectric are no longer related through a linear relationship, and non-diffracting beams have been applied for generation of second harmonic radiation [WUL93)].

Various numerical techniques have been used in the analysis of BB's, including the stationary phase approximation [BUR04,FRI96], the Fresnel formulations [ZAP06]

and the Laguerre-Gaussian beam mode analysis [TRA04]. In this chapter we numerically analyze various methods for the production of Bessel beams/focal lines using the Gaussian beam mode approach, concentrating on the situation where the wavelength of the electromagnetic radiation is a similar order of magnitude to the scale size of the optical element being used, a signature of millimeter wave quasi-optics. We also present results of measurements of a conical lens with low Fresnel number measured at 100GHz.

6.2 - Derivation of non-diffracting Bessel beams

If the transverse amplitude profile of a circularly symmetric non-diffracting beam is to be described independently of z by $f(r)$, then the general solution for such a radially symmetric wave is given by

$$\psi^B(r,z,t) = f(r)\exp(ik_z z - \omega t) \tag{6.1}$$

where ω is the angular frequency of the radiation, $\omega = ck$, and k_z is a constant yet to be determined. As f is defined only in terms of the radial coordinate, it is obvious that the beam profile is invariant throughout its propagation along the z-axis. We are thus seeking a solution for $f(r)$ such that it obeys the wave equation in the regime of cylindrical coordinate systems where the wave equation has the following form

$$\nabla^2\psi = \frac{1}{r}\frac{\partial}{\partial r}\left(r\frac{\partial\psi}{\partial r}\right) + \frac{1}{r^2}\frac{\partial^2\psi}{\partial\theta^2} + \frac{\partial^2\psi}{\partial z^2} = \frac{1}{c^2}\frac{\partial^2\psi}{\partial t^2}. \tag{6.2}$$

Assuming no angular variation of the function, upon substitution of the desired profile (6.1) into (6.2), we obtain

$$f''(r) + \frac{1}{r}f'(r) - k_z^2 f(r) = -k^2 f(r)$$

$$r^2 f''(r) + r f'(r) + r^2\left(k^2 - k_z^2\right)f(r) - f(r) = 0.$$

Defining $k_r^2 = k^2 - k_z^2$ we can write

$$r^2 f''(r) + rf'(r) + (k_r r)^2 f(r) = 0.$$

This form of second order differential equation is very common in Physics and Engineering and is known as Bessel's equation. Applying the Frobenius method to solve this function [STE73], we assume that f can be defined by an infinite sum of polynomials and their coefficients, c_n, in a similar manner as Fourier series

$$f(r) = \sum_{n=0}^{\infty} c_n r^{n+m}$$

with constant c_n and integer m. Using this method it can be shown that f has the form $J_m(x)$, where J_m is a zeroth order Bessel function of the first kind described by

$$J_m(r) = \sum_{n=0}^{\infty} \frac{(-1)^n}{2^{2n+m} n!(m+n)!} r^{2n+m}$$

and from the equation above it can be shown that a fundamental solution of a non diffracting beam is given by

$$\psi^B = J_0(k_r r)\exp(ik_z z - \omega t) \tag{6.3}$$

with the condition

$$k_r^2 + k_z^2 = k^2 . \tag{6.4}$$

This expression, eq. (6.3), derived for a Bessel beam is the zeroth order form of the field, but higher order beams do exist, just like Laguerre-Gaussian fields, in the form [SALO97]

$$\psi_m^B = J_m(k_r r)\exp(im\theta)\exp(i(k_z z - \omega t)) . \tag{6.5}$$

The generation of these higher order fields is more complex than the fundamental Bessel beams of equation 6.2, and involve the propagation of what is known as an *optical vortex* describing an angular variation of the phase according to $m\theta$ which causes a singularity at $r = 0$. This feature of the higher order Bessel beams has been described in relation to the use of such fields in the manipulation of microscopic particles, for example, in atomic optical traps [LEE04] through transferral of angular momentum.

The structure of the Bessel functions of the first kind are shown in Figure 6.1.

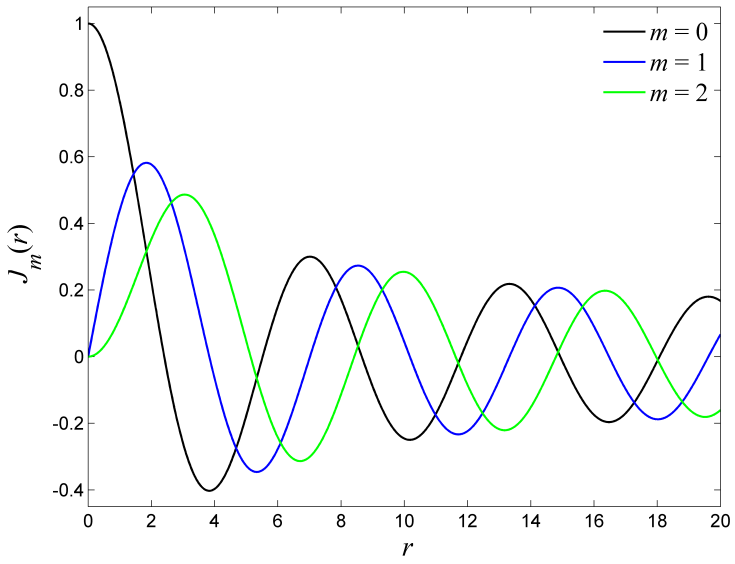

Figure 6.1 - Examples of m^{th} order Bessel functions $J_m(r)$ of the first kind.

Bessel functions are one of the most important polynomials in the study of wave phenomena. We have already seen their application in chapter 2 where the approximate intensity structure of a beam diffracted by a circular aperture can be represented in terms of the first order Bessel function. The Bessel functions were known to be solutions of the wave equation long before Durnins descriptions of their free space propagation, and they are commonly found in microwave and mm-wave methods in the theoretical description of circular waveguides where the field can be represented as an integration of Bessel modes in a similar manner to GBMA. In a cylindrically symmetric coordinate system, a function $E(r)$ can be represented as a series expansion given by

$$E(r) = \sum_{m=0}^{\infty} A_m J_0\left(\alpha_m \frac{r}{a}\right)$$

with A_m the analogue of the mode coefficients in LG synthesis, α_m is the m^{th} root of the zeroth order Bessel function of the first kind $J_0(r)$, and a is the extent of the function to be expanded, equivalent to the radius of an aperture in a optical system. This technique, known as the Fourier-Bessel expansion, will be applied to calculation of free-space diffraction of fields later in this chapter.

In this chapter we will retain the discussion of diffraction limited Bessel beams in relation to a cylindrically symmetric coordinate system. The Bessel functions will often be described in terms of the position of their roots with α_m representing the m^{th}

root of the J_0 function such that $J_0(\alpha_m r) = 0$ with the first five values of α_m given as 2.4048, 5.52, 8.654, 11.79,14.93.

6.3 - Proof of diffraction-free propagation in Bessel beams

By use of the Fresnel diffraction equation the diffraction free behaviour of the ideal Bessel beam can be easily shown using the typical form of the diffraction equation in a cylindrical system

$$E(r,z) = \left(-i\frac{k}{z}\right)\exp\left(kz + i\frac{k\,r^2}{2z}\right)\int_0^\infty E(r_0)e^{i\frac{kr_0^2}{2z}}J_0(k_r r_0)J_0\left(\frac{krr_0}{z}\right)r_0 dr_0 .$$

From [GRA07],

$$\int_0^\infty e^{-au}J_0\left(2b\sqrt{u}\right)J_0\left(2c\sqrt{u}\right)du = \left(\frac{1}{a}\right)J_0\left(2i\frac{bc}{a}\right)e^{-\frac{\left(b^2+c^2\right)}{a}}$$

or, through substitution of $u=r^2$, and $du=2rdr$,

$$\int_0^\infty e^{-ar^2}J_0(2br)J_0(2cr)rdr = \left(\frac{1}{2a}\right)J_0\left(2i\frac{bc}{a}\right)e^{-\frac{\left(b^2+c^2\right)}{a}}$$

which is a more suitable form for comparison with the diffraction integral. Substituting $a = ik/2z$, $b = k_r/2$ and $c = kr_0/2z$ into the diffraction integral gives the intensity variation (which allows for the neglect of the complex exponential terms) of an infinitely wide diffraction free Bessel beam as

$$\left|E(r,z)\right|^2 = \left|J_0(k_r r)\right|^2$$

showing the intensity profile to be independent of distance z.

6.4 - Propagation of truncated Bessel beams

The field amplitude of an ideal, untruncated zeroth order Bessel beam to be discussed in this chapter is given by eq. (6.3). The radial wave number k_r is an important parameter in a discussion of these Bessel beams. From this value the central spot size of the field is determined, and further characteristics of the field structure can be predicted, albeit within the limitations of geometrical optics. For example, the limitation of diffraction effects in a BB can be assessed through the magnitude of the *diffraction-free range,* which is defined as the longitudinal on-axis distance over which self-interference of the field occurs, thus, with a geometric approximation, maintaining a constant amplitude profile. For ideal BB's this distance is infinite due to the unlimited

transverse extent of the Bessel function, but in the case of practical Bessel beams, truncated at $r = a$, this distance is given as

$$Z_{\max} = a\frac{k_z}{k_r} \tag{6.6}$$

Using the Laguerre-Gaussian modal method, the amplitude patterns of Bessel beams with various radial wavenumbers were calculated and are shown in Figure 6.2.

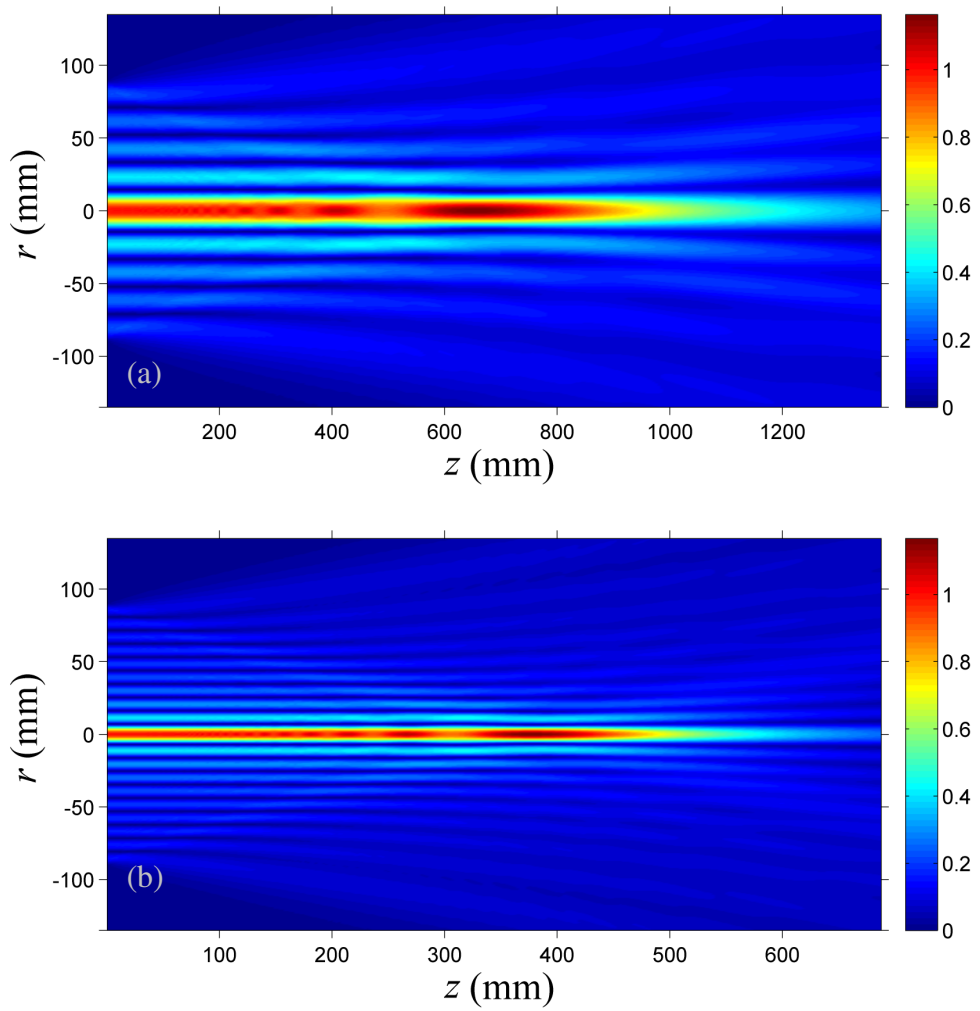

Figure 6.2 - The propagation of Bessel beams with k_r =(a) α_5 / a, (b) α_{10} / a. Shown in terms of the linear amplitude $|E(r,z)|$. The radius of the truncated Bessel field at $z = 0$ is 90mm, and the wavelength is λ=3mm.

The limitation of diffraction effects of the of the Bessel beam are obvious through observation of the central lobe of the beams in Figure 6.2 . This lobe has a full-width at half-maximum of $3.04/k_r$, with an off-axis secondary maximum at $r = 3.832/k_r$. The ideal normalised field at the focal plane of a thin lens which has a first off-axis lobe at -17.57dB, while the first sidelobe of Bessel has have an intensity level of -7.9dB,

which is a significant increase. For a Bessel beam, Z_{max} can be used as a reference distance in a similar manner to the focal point of a spherical lens. It does, however, give a value for the diffraction free range based only on geometrical considerations and with the approximations involved one would expect an abrupt amplitude fall off at this point in the case of $\lambda \longrightarrow 0$. However, as can be seen from the above false-colour graphs, diffraction effects related to the longer wavelengths deny this and instead an on-axis amplitude fall-off begins at a plane $z < Z_{max}$ after reaching a maximum value, see Figure 6.3.

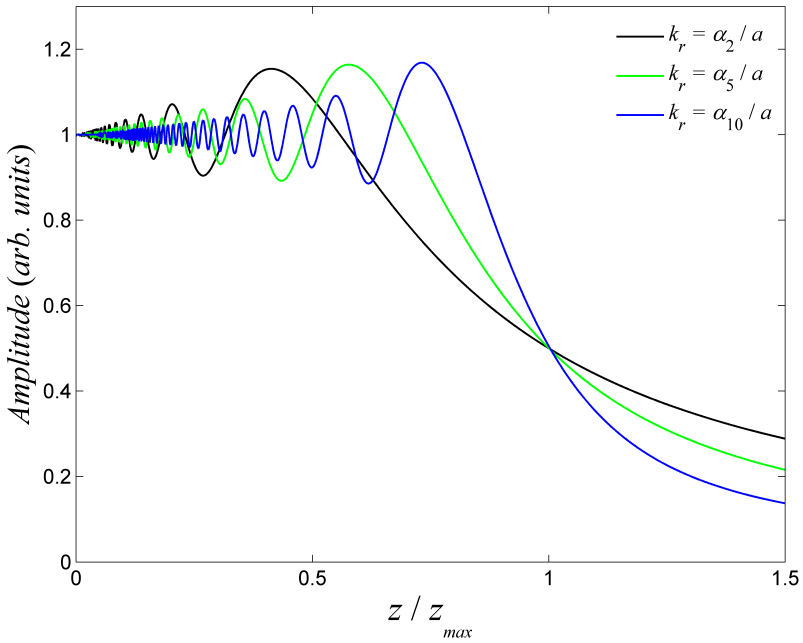

Figure 6.3 - The on-axis Amplitude $|E|$ of Bessel beams of various radial wavenumbers $k_r = \alpha_m / a$, where α_m is the position of the m^{th} root of the zeroth order Bessel function $J_0(\bullet)$.

With uniform plane wave illumination with amplitude E_0, the axial amplitude at Z_{max} is found to be approximately 0.5 $|E_0|$, and the gradient of the intensity variation at this point further highlights the limited application of the value of Z_{max} given by eq. (6.6), particularly for lower values of k_r, as can be seen in Figure 6.3

The authors of [ZAM04] discuss an interesting possible application of Bessel beams for generating axial intensity variations with specific structure. In that paper it was suggested that by superimposing Bessel beams of the same optical frequency but differing values of k_z, each individual beams on-axis variation could act as a Fourier sinusoid and by weighting each Bessel beam according to a the Fourier coefficients of the intensity function, a desired axial variation could be achieved. Thus far, this author

is unaware of any experimental verification of this method which would rely on holographic techniques for physical generation of polychromatic Bessel beams. Figure 6.4 shows a numerical demonstration of the formation of a predefined axial intensity structure [ZAM04]

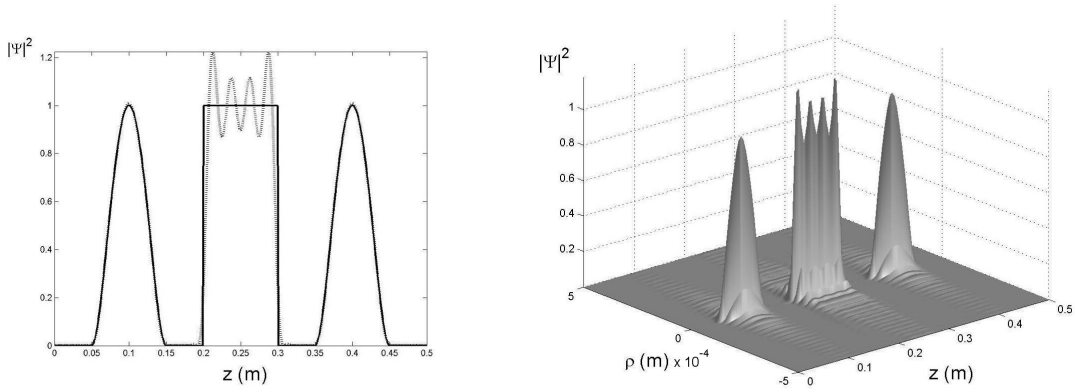

(a) (b)

Figure 6.4 – Synthesis of a specific axial variation by use of a superposition of Bessel beams, reproduced from [ZAM04].

[LAV10] describes an algorithm for the synthesis of desired transverse fields using Laguerre-Gaussian beam modes in a similar fashion to the above method.

6.5 - Laguerre-Gaussian synthesis of zeroth order Bessel functions

There is an obvious similarity in the amplitude structure of the Laguerre-Gaussian modes and the Bessel functions of the first kind, with both functions showing a large intense circular spot with a radial amplitude fall-off resulting in increasingly less intense outer lobes. An exception in such a comparison is the infinite extent of the Bessel functions, where as the LG modes show oscillatory behaviour only over a finite transverse range. To show the similarity between Laguerre-Gaussian structures and truncated Bessel functions, an overlap integral can be performed of the function

$$E_0(r_0) = \begin{cases} J_0(\alpha_j r / a), |r| \le a \\ 0, |r| > a \end{cases}.$$

With the radial wave number given as $k_r = \alpha_j / a$, for some integer value of j, the Lagurre-Gaussian expansion coefficients of this function is

$$A_m(w_0) = \sqrt{\frac{2}{\pi w_0^2}} \int_0^a L_m\left(2\frac{r_0^2}{w_0^2}\right) \exp\left(-\frac{r_0^2}{w_0^2}\right) J_0(k_r r_0) 2\pi r_0 dr_0 . \qquad (6.7)$$

In this example A_m is now a function of the waist parameter to allow for comparison of the LG mode make-up of the Bessel structures. Figure 6.5 describes how with increasing value of w_0 / a the number of modes with significant values becomes less.

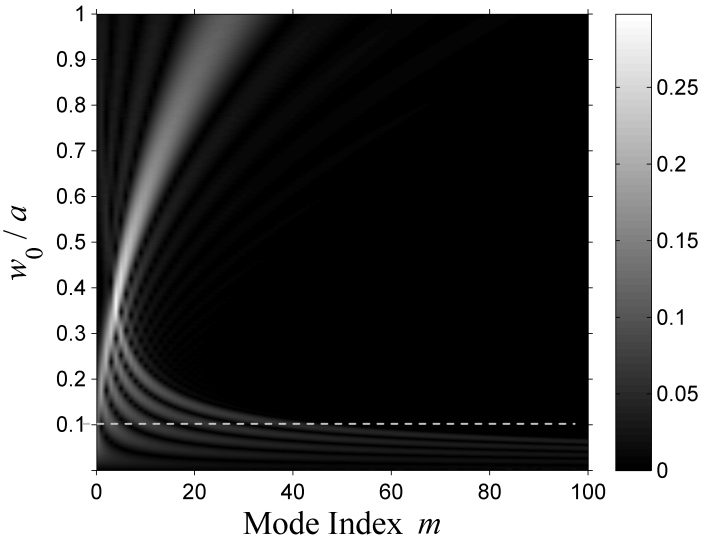

Figure 6.5 – The variation of the mode coefficients, from equation 6.7, with different values of w for a truncated zeroth order Bessel function (a) $k_r = \alpha_5$, (b) $k_r = \alpha_{10}$. The dashed line in the figure marks the value of w_0 which results in the best possible LG synthesis of the circ function of equal radius a, as defined in [BOR06].

As the value of w_0 / a increases the number of modes with substantial coefficient magnitudes is reduced, and a strong correlation between the truncated Bessel function and a just a few LG modes of higher indices appears, see Figure 6.6.

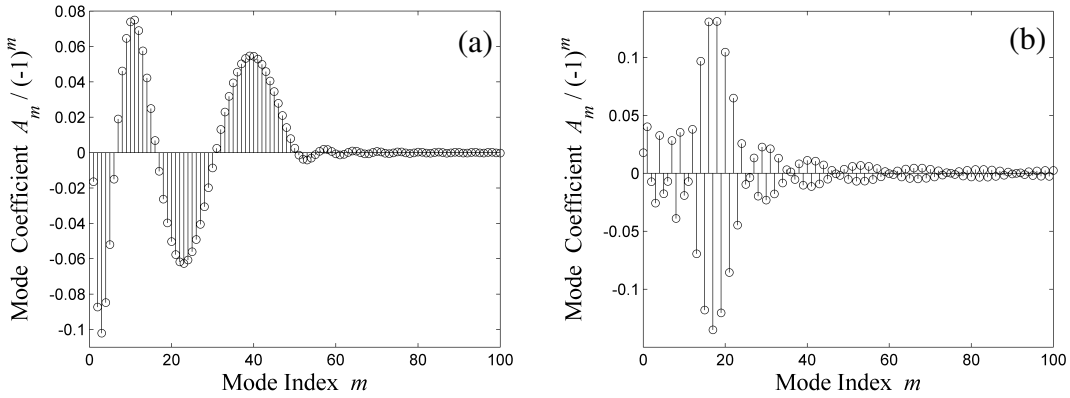

Figure 6.6 – The dependence of a one-dimensional Bessel function using synthesize LG functions on w and n. Mode coefficients for $J_0(\alpha_5 r)$, for w_0 = (a) $0.1a$ (b) $0.8a$.

The above results show how, with variation of w_0, an adequate description of a truncated beam with amplitude proportional to a Bessel function can be represented

with a few LG modes, as shown in Figure 6.6 (b) where the number of mode coefficients with significant value is reduced from that in (a). An analysis showing the rms error of the synthesis of a Bessel function with parameter $k_r = 30.63/a = (\alpha_{10} / a)$, is shown below.

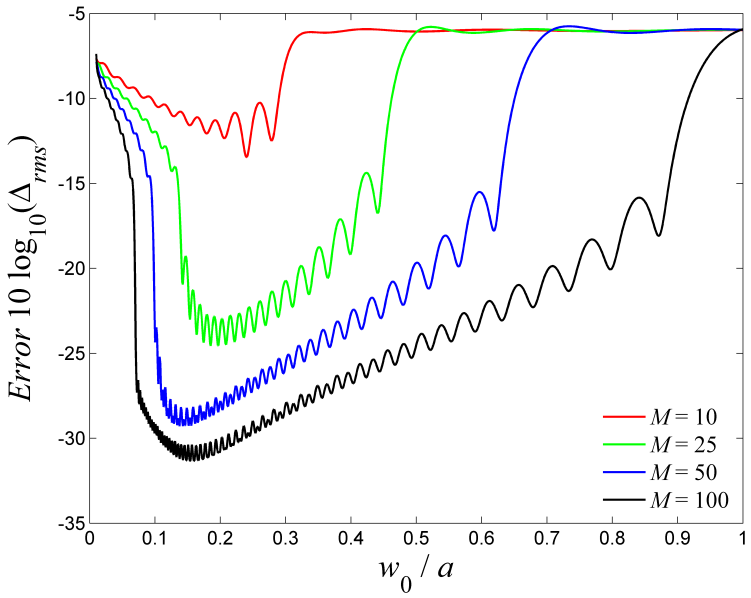

Figure 6.7 – The rms error of the Laguerre-Gaussian formulation of a Bessel amplitude profile $J_0(30.63\ r_0 / a)$.

In comparison with the quantified errors of the LG reconstruction of the circ function, shown in figure 2.14, the errors in the synthesis of a Bessel function in Figure 6.7 shows that there is only a finite window for the range of values of the width parameter w_0 with which significant reduction of the error in the synthesized function is achieved. Previously, the value of the optimum width parameter for the synthesis of the top-hat function was shown to be relatively consistent for increasing values of the mode set size $M+1$. However, as can be seen from Figure 6.7, the optimum value of w_0 calculated for $M = 100$ actually increases from its value for $M = 50$, which shows that the optimum value of $w_0 = (a / M)^{1/2}$ as defined by [BOR96] no longer holds for the Bessel functions, and the author predicts that this is true for other oscillatory functions also, e.g. sinusoidal functions. Nevertheless, although Borghi's value may not give an optimal figure, the discrepancies in diffraction calculations associated with a large mode set using that value of w_0 are so completely negligible even in the case of lenses with relatively large Fresnel numbers that its use will not cause significant effects on diffraction calculations in this work.

An appropriate integral for the decomposition of zeroth order Bessel beams is found in [GRA07]

$$\int_0^\infty r\, e^{-\frac{1}{2}\alpha r^2} L_n\left(\frac{1}{2}\beta r^2\right) J_0\left(k_r r\right) dr = \frac{(\alpha-\beta)^n}{\alpha^{n+1}} e^{-\frac{1}{2\alpha}k_r^2} L_n\left(\frac{\beta k_r^2}{2\alpha(\beta-\alpha)}\right).$$

Neglecting the absence of some constant normalization factors, and the Gaussian waist parameter w, this equation has the correct form for the calculation of the LG mode coefficients of an ideal Bessel beam of infinite extent. Letting $\alpha = 2/w^2$, and $\beta = 4 / w^2$ gives

$$A_m = 2\pi\sqrt{\frac{2}{\pi w_0^2}}\int_0^\infty r e^{-\frac{r^2}{w_0^2}} L_m\left(2\frac{r^2}{w_0^2}\right) J_0\left(k_r r\right) dr$$

$$= \sqrt{\frac{8\pi}{w_0^2}}\left(-\frac{2}{w_0^2}\right)^m \left(\frac{2}{w_0^2}\right)^{-m-1} e^{-\frac{w_0^2 k_r^2}{4}} L_m\left(\frac{w_0^2 k_r^2}{2}\right). \qquad (6.8)$$

While this expression is valid only for Bessel beams of infinite extent, it can be altered to include a localized (real) non-diffracting beam by including only modes whose extents lie within a certain finite distance. However, the drawback in this analytical formulation is the finite extent of such a truncated series, which would be inadequate for the representation of a sharp amplitude fall-off caused by a truncation at hard aperture, but is suitable for Bessel beams where the amplitude at the point of truncation is small, i.e. if the field is truncated at a zero-crossing of the Bessel function.

Not surprisingly and by analogy with the structure of the Bessel beams, the profile of Laguerre-Gaussian beam modes are themselves subject to some degree of resistance to diffractive effects relative to their associated confocal length in that their diffracted profiles are not altered. In fact, the observation of a LG mode in the near field could easily be mistakenly identified as a pseudo Bessel beam in the near field, but in the far-field the two fields are significantly different.

To show the contrasting behaviour in the propagation of these two similar field structures, we can compare a Bessel beam with a Laguerre-Gaussian mode with an equal central spot size and for which the value m-1 equals the number of lobes in the truncated BB. From eq.2.32, for a LG mode with a spot size of equal radius to that of a Bessel beam truncated at it's m^{th} root, the width parameter w_0 is approximately

$$w_0 = \frac{2.0413\sqrt{2(m-1)}}{\alpha_m 3\pi} a\,. \qquad (6.9)$$

Figure 6.8 compares the propagation of the LG and BB fields.

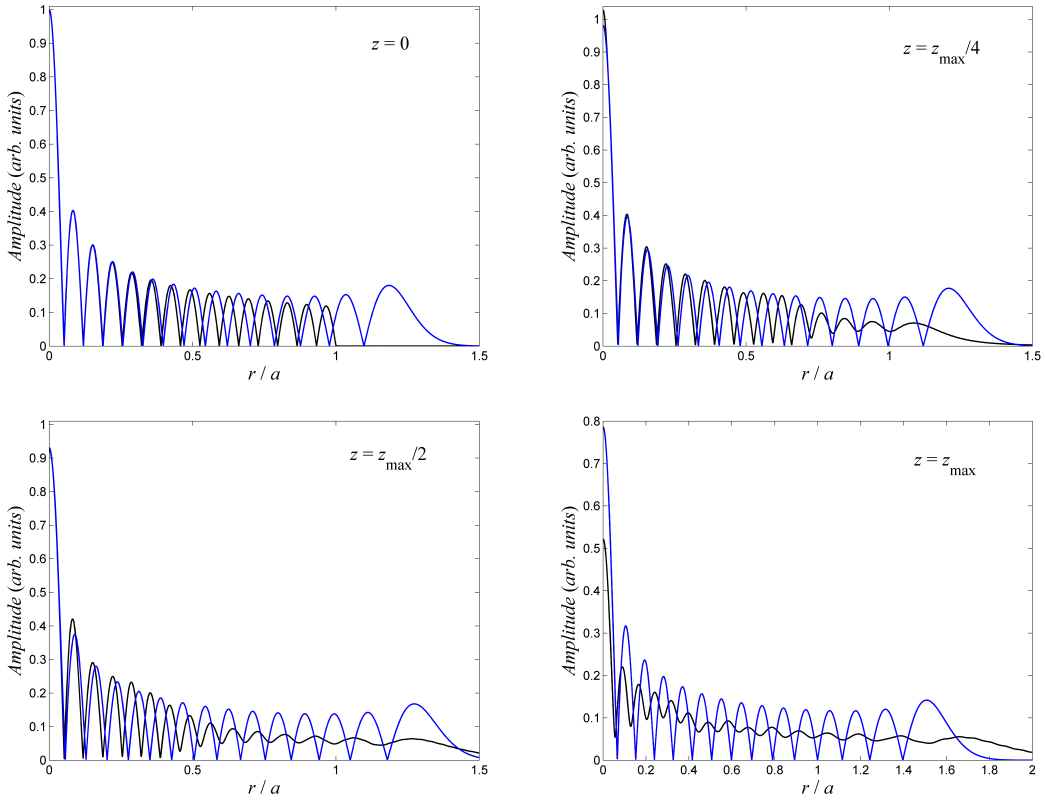

Figure 6.8 – Comparison of the propagation of a truncated Bessel beam (black) and an m = 14 Laguerre-Gaussian mode (blue) with an equal number of lobes and equal radius of the central spot in both fields.

The width of the Laguerre-Gaussian modes is defined by the parameter $w(z)$ given in chapter 2 and accordingly its FWHM behaves in a similar manner to w(z) increasing gradually in the near field. A truncated Bessel beam, although similar in structure, will exhibit oscillation of the FWHM value of the central lobe even within the so-called diffraction free range, as shown in Figure 6.9.

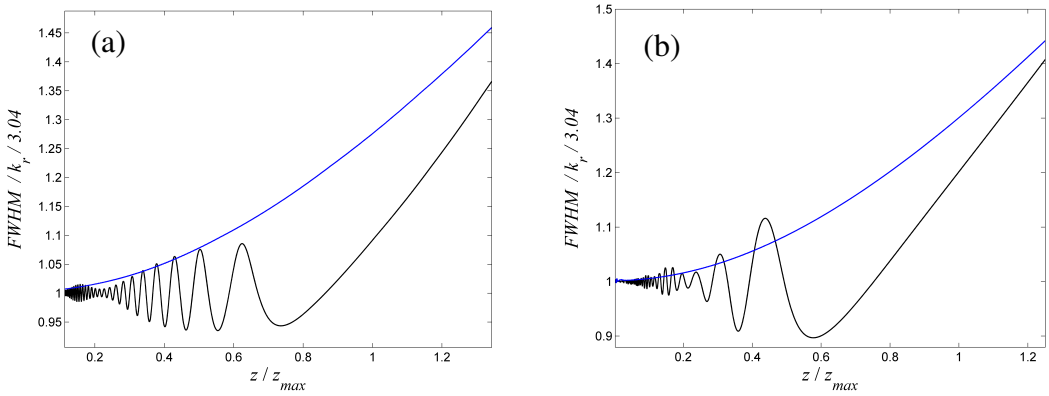

Figure 6.9 – Behaviour of the FWHM of the central lobe of the Bessel beam (black) truncated at the m^{th} root, and a Laguerre-Gaussian of order m - 1. (a) m = 5, (b) m = 15.

6.6 - The annular aperture method

There are various methods that are used to generate non-diffracting Bessel beams. The first experimental procedure used to specifically generate non-diffracting fields was that described in the seminal paper by Durnin, [DUR87]. This method involved the focusing of the diffracted field from a annular aperture (a circular aperture with a central circular obscuration), placed at the focal length *f* of a thin lens, see Figure 6.10.

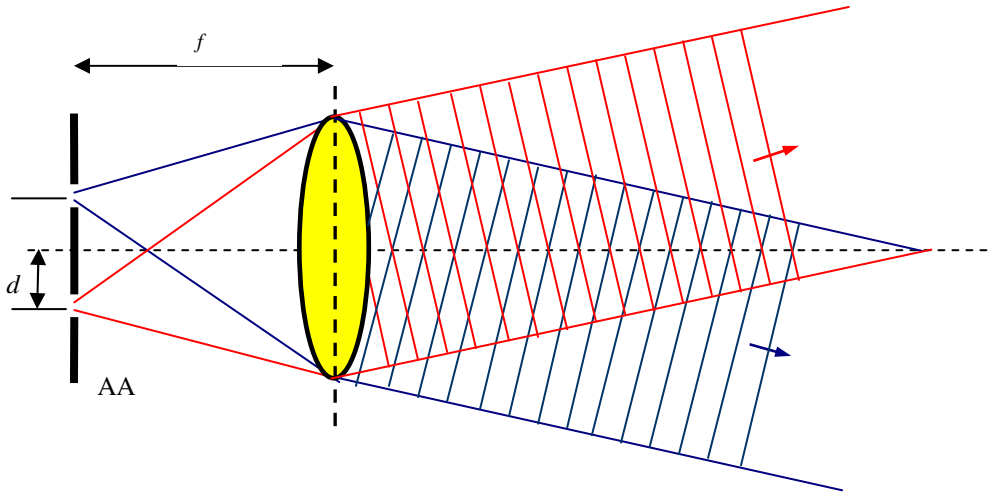

Figure 6.10 – Schematic of optical system used in original description of Bessel beams, consisting of an annular aperture AA with radius *d*, and a thin lens of focal length *f*.

From [BOR97] it can be shown that the Fraunhofer diffraction pattern generated by an annular aperture is proportional to the structure of a first order Bessel function. However, when the ratio of the central obscuration radius, a_0, to the outer radius of the aperture, a, is small compared to the wavelength, the diffracted far-field pattern can be represented by a zeroth order Bessel function.

The field produced by this annular aperture form of generation is the closest approximation to an ideal truncated Bessel beam, for at the original plane of the non-diffracting field, i.e. just behind the lens, $z = 0$, both the amplitude and phase exist in the form required by the basic equation for a monochromatic non-diffracting field eq. (6.3). To a good approximation, the wavefront diffracted from annular aperture with similar inner and outer radii can be represented as the superposition of spherically diverging fields with their origin at the centre of the transmitting region (ring). This generates the amplitude profile of a zeroth order Bessel beam, while the wavefront is converted by the spherical surface of the lens according to

$$\exp\left(i\phi_{AA}(r)\right) = \exp\left(-i\frac{k\left(r+d\right)^2}{2f}\right)\exp\left(i\frac{kr^2}{2f}\right)$$

$$\rightarrow \phi_{AA}(r) = \frac{kd}{f}r$$

with d the radial position of the centre of the annular aperture $d = a_0+(a-a_0)/2$. This circularly symmetric linear variation of phase introduces a linear radial phase variation generating self-interference and subsequently the Bessel amplitude profile $J_0(k_r r)$. The Bessel beam generated then has the radial wavenumber $k_r = kd / f$.

The Laguerre-Gaussian Mode analysis of this optical arrangement, i.e. the expansion of an annular aperture, see Figure 6.11, suggests a strong relationship between individual higher order LG modes and the diffracted field.

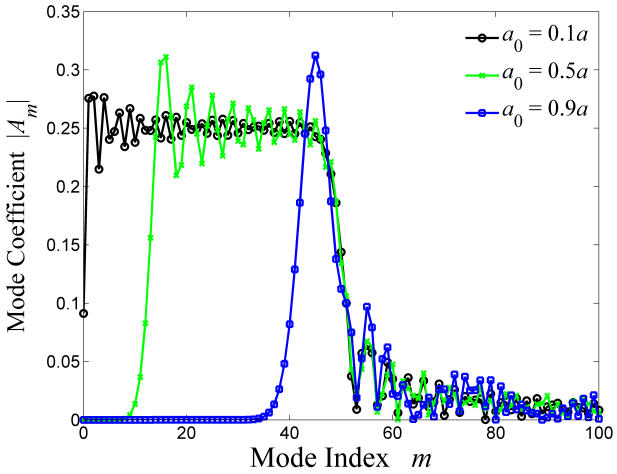

Figure 6.11 – The mode coefficients of an annular aperture for various values of the inner radius a_0. Calculated with $M = 100$.

The variation of the LG mode coefficients shown in Figure 6.11 for an annular aperture of inner radius a_0 show a shift in the dominant LG modes used to represent such a ring structure and a reduction in the number of modes with significant values of $|A_m|$. This decrease in the value of the lower order modes signifies a more oscillatory transverse diffraction pattern, which is again due to the similarity in spatial structure between the higher-order Laguerre-Gaussian modes and the zeroth order Bessel function representing the amplitude of the diffracted beam generated at the annular aperture.

A very simple experiment to verify this formation was arranged by the author using a 100GHz radiation source. Eccosorb™ was used to create a 18mm circular null in an aperture of radius 30mm, and a spherical lens made from HDPE with f =230mm. This would also establish the suitability of Gaussian beam mode decomposition for the simulation of non-diffracting beams and related fields. Shown in Figure 6.12 are predicted fields for the annular aperture method, and a measured field is compared with its simulated counterpart.

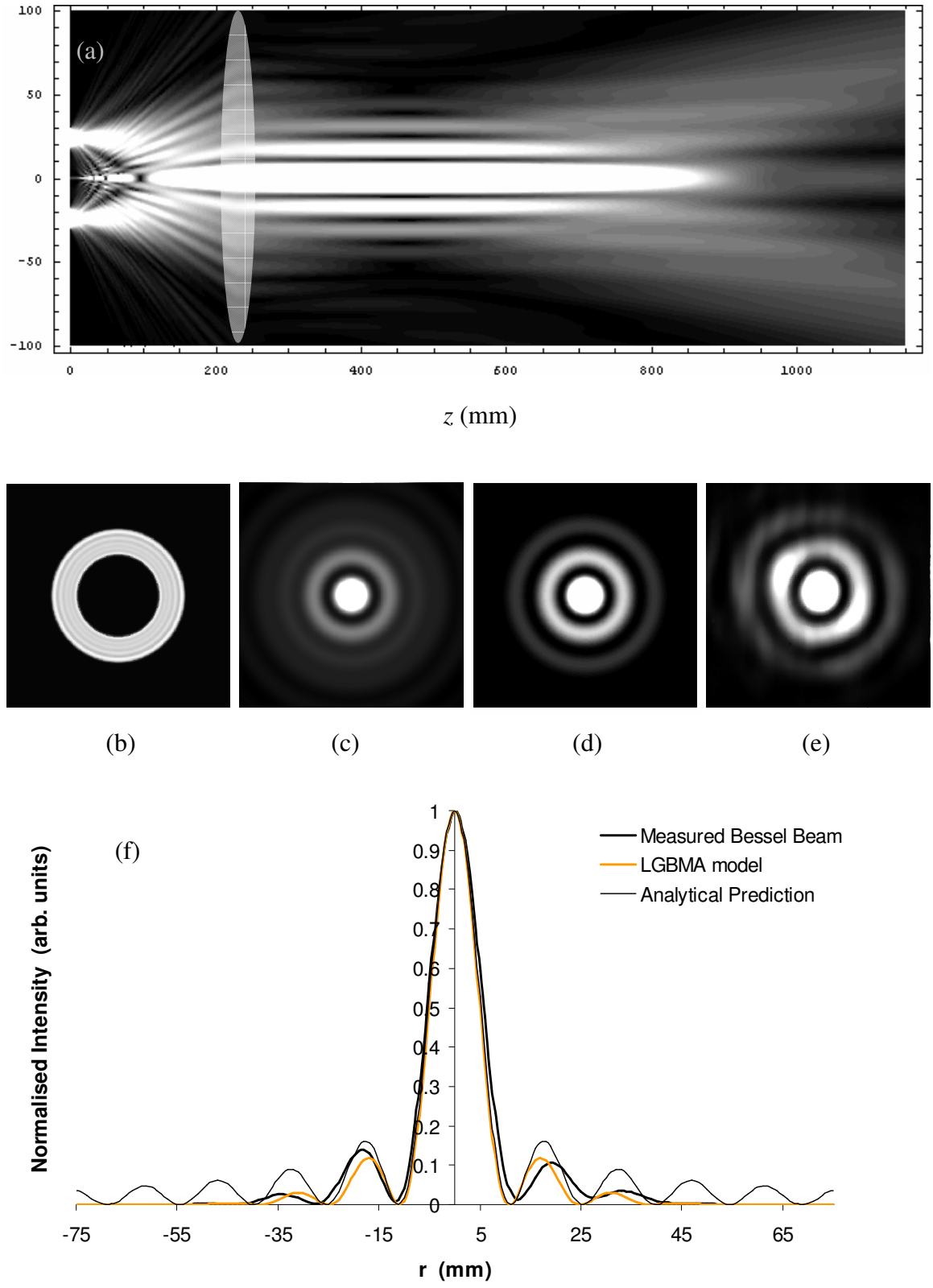

Figure 6.12 - Simulated fields for the production of a Bessel beam from an annular aperture of outer radius 30mm, inner radius 18mm, and f = 230mm. (a) The predicted field in the diffraction half-plane. Intensity at (b) $z = 0$, (c) $z = f / 2$, (d) $z = f$ from the lens. (e) experimental measurement at $z = 2f$, and (f) a comparison of models at the focal plane of the lens. Note that the upper limit of intensity scale in some cases is reduced to enhance less obvious diffraction features.

Apart from the purpose of demonstrating the propagation of non-diffracting beams, this method of BB creation has found little practical applications in optical systems as the power available to the Bessel beam formation is limited by the area of the transparent region of the annular aperture, which will inevitably be small.

6.7 - The conical lens

One method that overcomes the truncation and loss of energy in the annular aperture method, is through the application of the conical lens, or *axicon*, a transparent and conical element that produces a similar line focus to the apparatus in the previous section. This element is, as suggested by its name, a conical optically dense element that modifies the phase of an incoming wave according to the linear radial variation of the thickness of the lens. The term *axicon* has often been used generally for any optical method used in the generation of Bessel beams, but in this thesis this description will be reserved for this transparent and symmetric conical lens. The basic operation of a conical lens is seen in Figure 6.13, and describes the formation of a pseudo-Bessel beam by generating self-interference in a plane wave through a conical phase modulation.

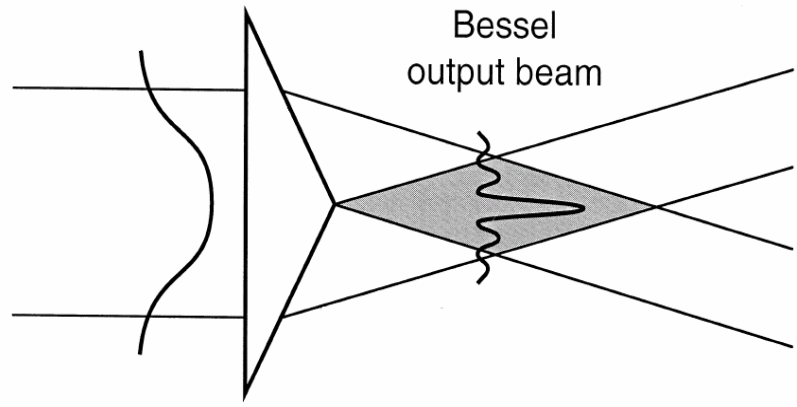

Figure 6.13 – The formation of a pseudo Bessel beam by conical lens. Reproduced from [MONK99].

A mathematical description of such a lens is achieved in a similar way to the method used to describe the thin spherical lens in Chapter two by assuming that diffraction effects in the axicon itself are negligible, and thus the axicon is represented as an infinitesimally thin phase modulation. Figure 6.14 below shows how a simple numerical portrayal of a conical lens of refractive index n can be obtained.

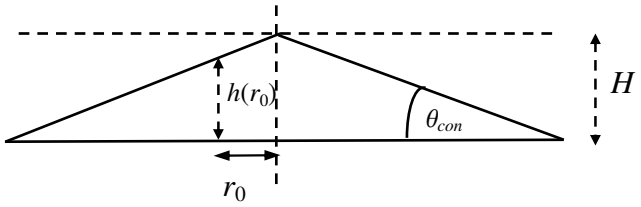

Figure 6.14 – Model for determining the planar phase transformation of a conical lens.

The physical height of the conical lens at a point r_0 is $h(r_0) = r_0 \tan\theta_{con}$, and by completely neglecting diffraction effects of the incident field within the conical lens, the phase variation imposed by the axicon is determined as $\phi(r_0) = nkh(r_0) + kH - kh(r_0)$. Eliminating the constant phase term kH, as it makes no contribution to the relative phase variations, we find the phase of a conical lens to be given by

$$\phi_{con}(r_0) = k(n-1)\, r_0 \tan\theta_{con}\,. \tag{6.10}$$

Now, in comparison with the phase variation of a thin lens, the conical lens produces a phase variation which causes a wavefront at each point on the surface to be directed at a constant angle to the optical axis, whereas for a spherical lens the angle of refraction at each point varies in direction toward a single point on the axis.

Before simulations are developed that show the diffraction characteristics of a beam propagated through such a conical phase variation, certain qualities of the conical lens can be estimated, for reference, using simple geometrical optics' rules such as Snell's law. The figure below shows the arrangement for predicting the axicon field's geometric behaviour.

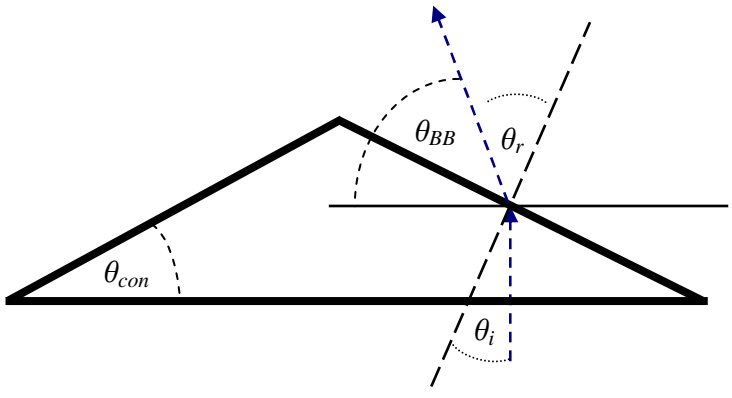

Figure 6.15 – Calculation of the Bessel beam angle of a conical lens.

Using Snell's law the angle of refraction of the conical wave with respect to the base of the axicon is given by

$$\theta_{BB} = \frac{\pi}{2} - \sin^{-1}\left(n \sin\theta_{con}\right) + \theta_{con}, \tag{6.11}$$

and from (6.11) the radial and longitudinal wave vectors of the resulting Bessel beam

$$k_r = k\cos\theta_{BB}, \tag{6.12(a))}$$

$$k_z = k\sin\theta_{BB.} \tag{6.12(b))}$$

and again the condition $k^2 = k_r^2 + k_z^2$ holds. Figure 6.16 shows the variation of the k_r and k_z values relative to the wavenumber k for a value of the refractive index n = 1.52. However, due to total internal reflection, not all values of k_r can be achieved.

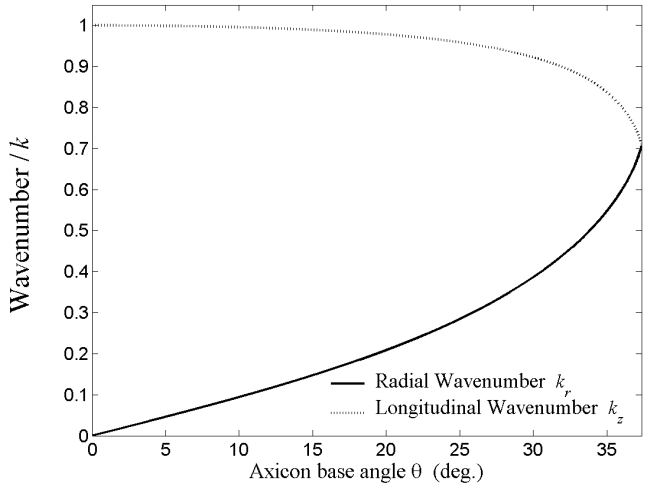

Figure 6.16 – Behaviour of the radial and longitudinal wavevectors created by refraction of a plane wave in a conical lens with n = 1.52.

The comparison of an axicon with its "equivalent" ideal truncated Bessel beam shows a similarity in the spatial frequency of both aperture functions. In the case of Bessel functions the transverse spatial frequency does not have a constant value, but the distances between its roots do rapidly converge upon a value of π/k_r with increasing r.

Unlike the BB's produced with the previous annular aperture method, and the ideal truncated BB's, the pseudo-Bessel beam produced by an axicon exhibits a non-uniform on-axis intensity distribution, due to the greater convergence of energy on the optical axis from more extreme parts of the axicon surface with increasing z.

Bessel functions $J_0(r)$ and the cosine function can be related using the asympototic expression

$$J_0(r) \cong \sqrt{\frac{2}{\pi r}} \cos\left(r - \frac{\pi}{4}\right),$$

which can be used as a reliable approximation with $r \gg 0$ where a central singularity occurs in the above description. Figure 6.17 compares the Bessel and axicon aperture functions for generation of fields with equal radial wavevectors k_r.

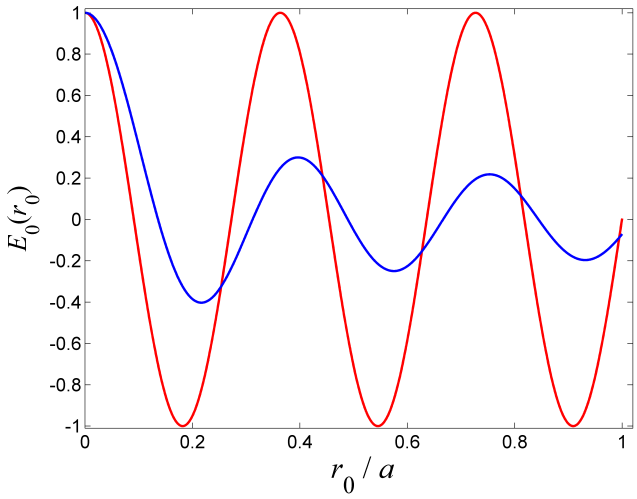

Figure 6.17 – A comparison, at $z = 0$, of Bessel beam (blue) and the real part of the axicon (red) aperture functions, $E_0(r_0)$ producing pseudo-Bessel beams with the same values of k_r. The axicon angle is 10°, the wavelength $\lambda = 3$mm, and the radius $a = 30\lambda$. $N_F = 2.83$.

The trend of mode coefficients of the aperture functions in Figure 6.17 also show strong similarity with each other, with the exception of a modulating envelope in the case of the Bessel function analogous to the transverse fall-off in the amplitude profile.

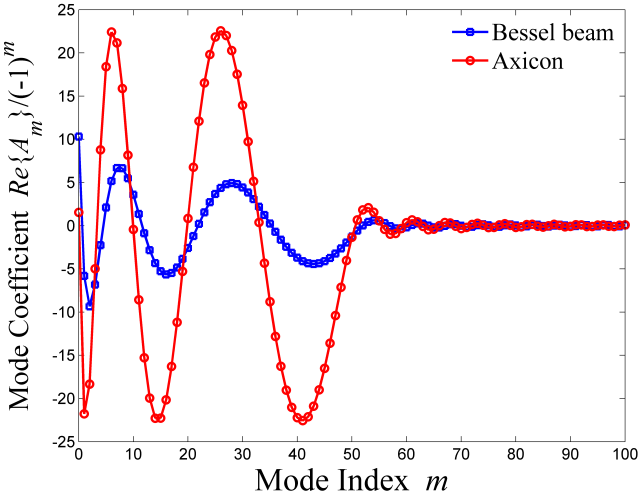

Figure 6.18 – The mode coefficients, with $M = 100$, of an axicon field and of the ideal Bessel beam that it attempts to approximate. The change in sign of the modes inherent in the integration of LG modes has been eliminated for a clearer description.

Zapata-Rodríguez et. al. [ZAP06] discussed the concept of a Fresnel number to represent the diffraction characteristics of a Bessel beam in the same manner as the Fresnel number of field focused by a spherical lens was mentioned in section 2.6.2 [ZAP06]. Here, the Fresnel number of a Bessel beam is given by

$$N_F = \frac{a^2}{\lambda Z_{\max}} \tag{6.13}$$

and yields the number of oscillations in the real part of the Bessel beam function. While it will not give an exact figure for the number of Fresnel zones contained in an axicon beam, it will give a useful approximation for quantifying the effects of such a lens.

The field produced by an axicon is obviously strongly dependent on the base angle of the conical surface and the refractive index of the material, and also the radius of the element affects the number of lobes in the Bessel-like output field. As shown in Figure 6.19 (a) with a very low value of N_F the field created by the axicon will not deviate greatly from that of a simple circular aperture, but with an increase of N_F the limitation in diffractive spreading of the central lobe becomes more apparent.

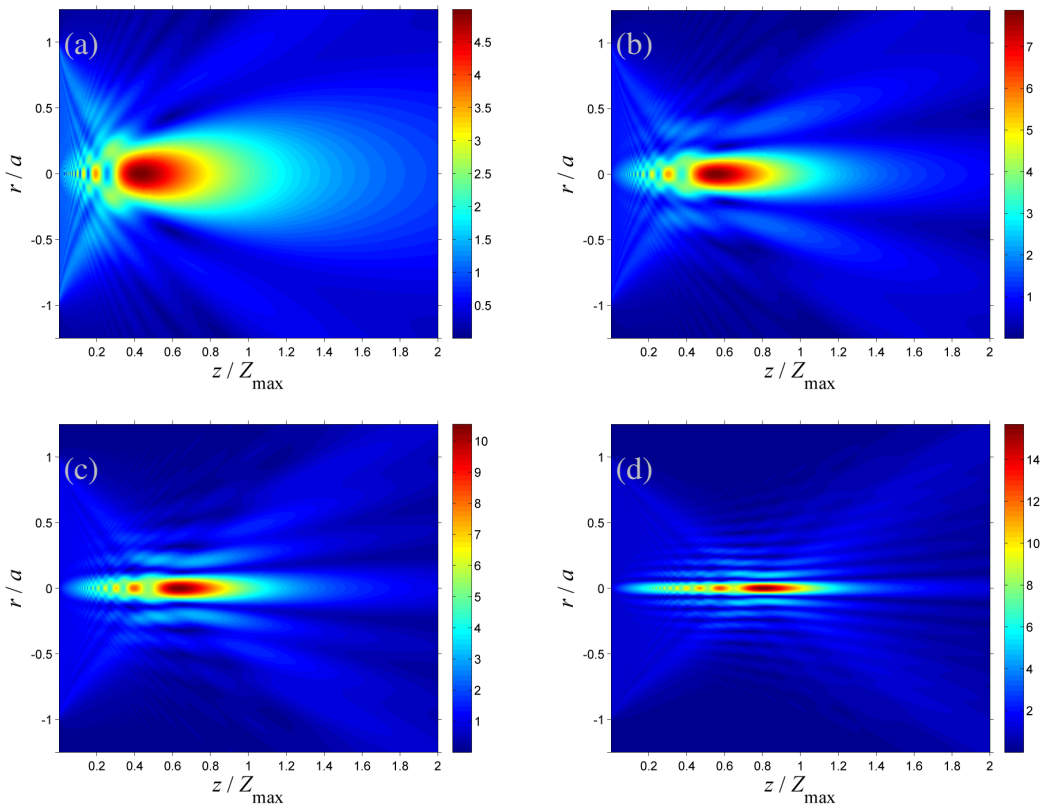

Figure 6.19 - The amplitude of the field from a conical lens illuminated by a plane wave. a = 30λ with the base angle of the axicon θ_{con} = (a) 3° (b) 6° (c) 10° (d) 20°, corresponding to N_F = 0.82, 1.65, 2.82, and 6.4 respectively.

The behaviour of the field of a conical lens is compared with an equivalent truncated Bessel beam in Figure 6.20. The plots show that for a conical lens there is only a limited region in which a field closely corresponds to a Bessel function with the greatest similarity in structure of the two fields occurring between $Z_{max}/2$ and Z_{max}.

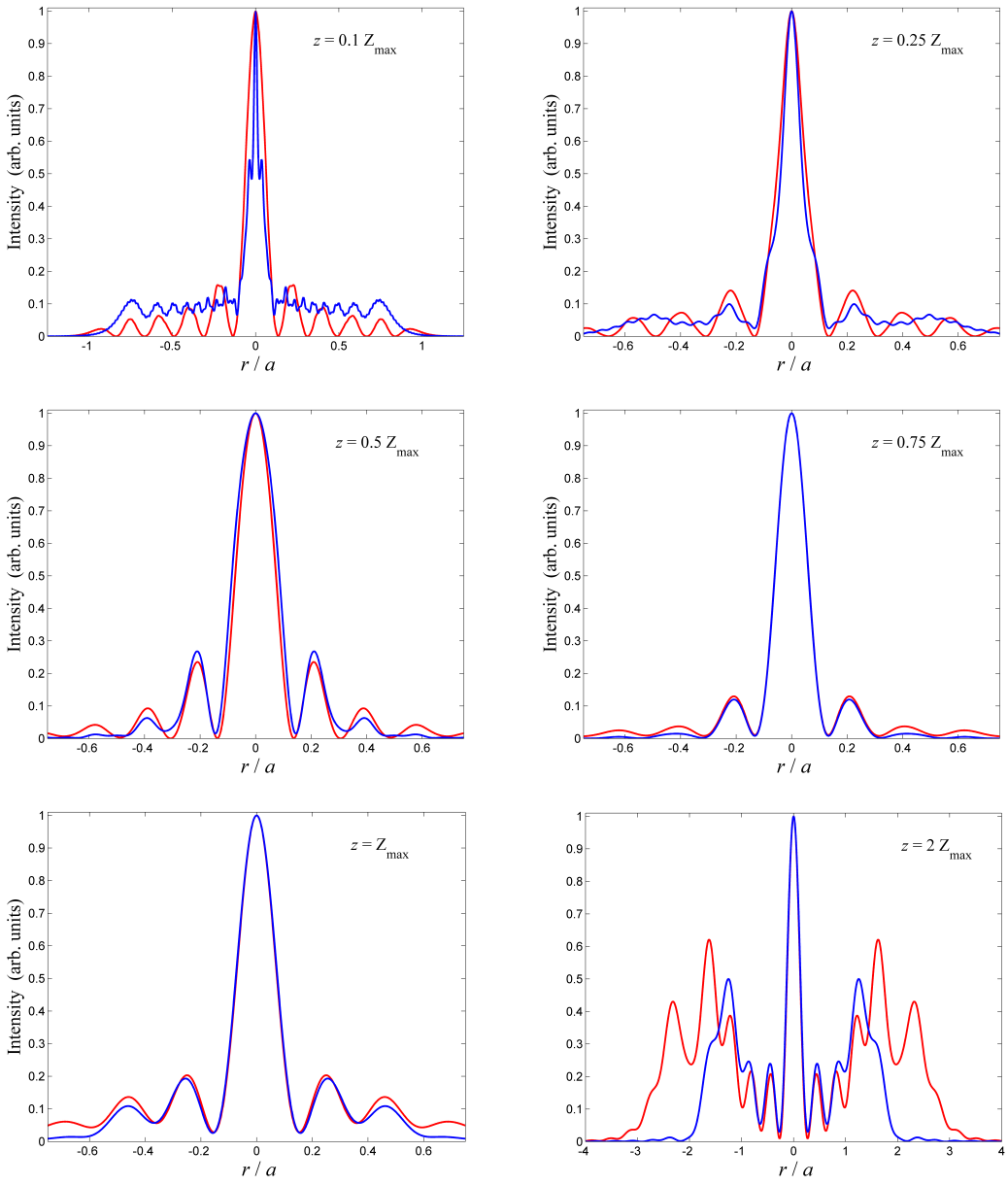

Figure 6.20 – Normalised diffraction patterns of a Bessel beam (red) compared with a corresponding conical lens (blue) producing the same radial wavevectors. The base angle of the axicon is 10°, with a radius a = 30 λ and refractive index of n = 1.52.

The formation of the beam from an axicon shows that as the central lobe begins to form, just in front of the element, its width is determined by the width of the central lobe of the sinusoidal aperture function, and is slightly narrower than that predicted from the radial wavenumber of an equivalent BB. However, with increasing z the median spot size of the axicon beam increases to a diameter that is consistent with the corresponding ideal truncated Bessel beam.

In terms of the phase structure of an axicon beam, see Figure 6.21, the phase profile of the field becomes inverted approximately beyond a distance of Z_{max} / 2 representing a divergence of the BB away from the optical axis.

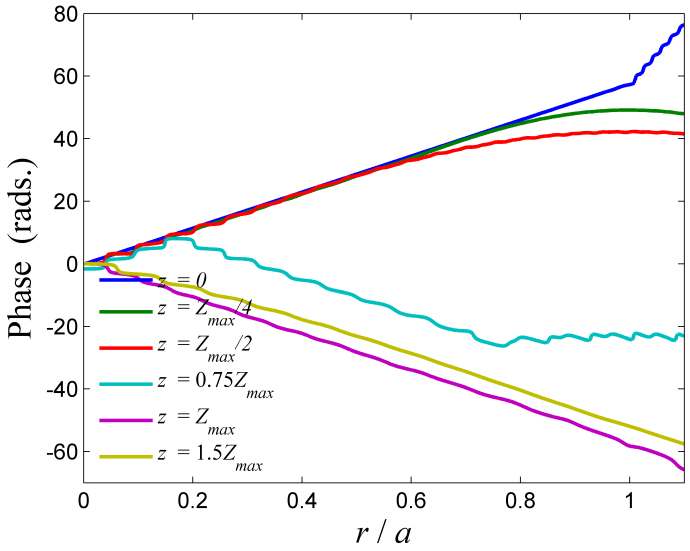

Figure 6.21 - A comparison of the variation in phase of an axicon beam and Bessel beam at various planes.

At the plane z = 0 the phase of the axicon beam is radially linear but as the field amplitude evolves into a more "Bessel-like" structure the phase develops a stepped structure with the phase effectively constant across each individual lobe of the amplitude pattern but varying from that of the adjacent lobe. The phase of the Bessel beam at the plane z = 0 is defined by a grating like structure of the Bessel function with phase values of $-\pi/2$ and $\pi/2$ corresponding to positive and negative values of $J_0(k_r r)$.

In the case of Bessel beam propagation, the on-axis amplitude oscillates about an average value of E_0. With a uniformly illuminated axicon, the elimination of the transverse amplitude decay seen in Bessel functions, asymptotically given as $\sqrt{2/\pi k_r r}$, produces a much different on-axis variation. When illuminated by a plane wave the

axicon generates a focal line which varies in intensity proportionally to z, as shown in Figure 6.22.

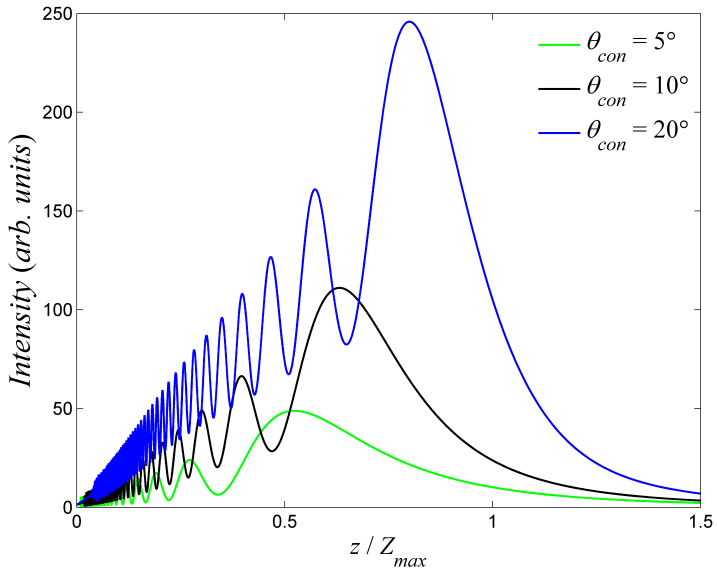

Figure 6.22 - The on-axis variation of the output field of a conical lens under plane wave illumination for three cone angles, with the axicon radius a = 30 λ.

Figure 6.22 also shows a limitation of the finite series Laguerre-Gaussian synthesis in the very near field of the diffraction plane, where the expected high frequency oscillations are eliminated by the truncation of the LG mode set to a finite number. However, calculating these fields using a diffraction integral technique actually gives spurious amplitude values in these regions due to a 1 / z factor of the integral. While the rapid on-axis oscillations in the extreme near-field of the element cannot be determined even when using a large M = 500 mode set, the calculation shows the field in these regions as an average of the expected oscillatory values, thus maintaining the general trend of the field variation.

The results of Figure 6.22 also show the limitations of the geometrical characterisation of the axicon lens. The value predicted by ray optics for the diffraction free range Z_{max} deviates from the actual point at which an on-axis intensity fall off occurs, as shown in Figure 6.23.

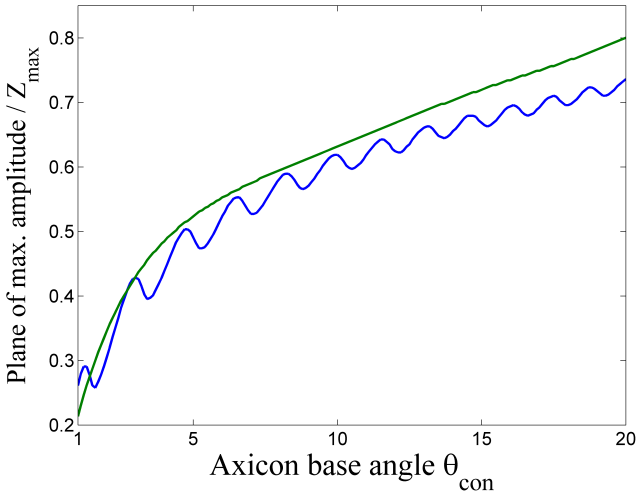

Figure 6.23 - The position of the maximum axial amplitude for a conical lens/axicon and the equivalent truncated Bessel beam. λ = 1, a = 30 λ.

To quantify the extent of the limitation of diffraction effects in the focal line of an axicon, one simple method is the calculation of the width of the focal line which will be defined, in this instance, by the full-width at half maximum of the intensity $|E(r,z)|^2$. Figure 6.24 compares the beam-widths of two axicon beams. The FWHM of the axicon beam intensity is compared with the same characteristic of the corresponding truncated Bessel beam, which is given for an ideal Bessel intensity $|E|^2$ as approximately 2.2513 / k_r.

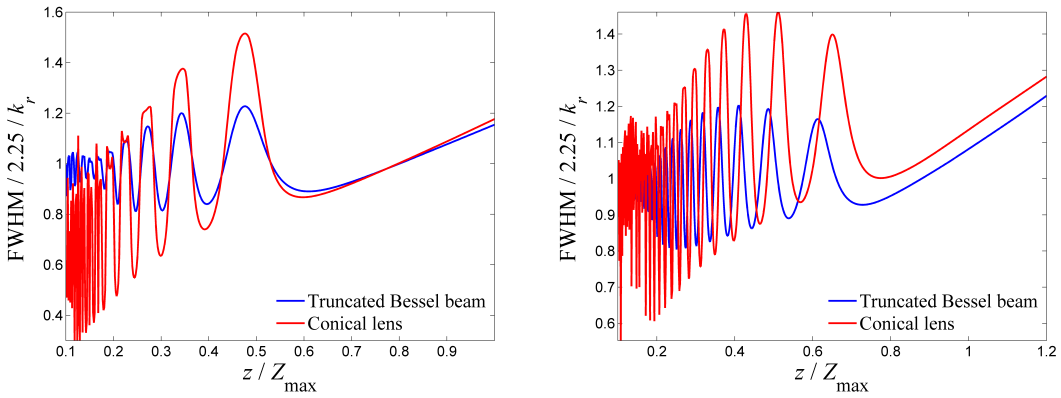

Figure 6.24 - The full width at half maximum for an axicon angle θ_{con} = (a) 10°, (b) 20°. Conical lens (red), compared with the truncated Bessel beam having equal value of k_r (blue), a = 30λ. The data in (a) corresponds to a Fresnel number N_F = 2.82, and in (b) N_F = 6.44. See also [ZAP06].

Figure 6.24 exhibits the deviation of the diffractive model of Bessel beams from the ideal notion of a truly consistent field profile as given by a geometrical analysis. As can be seen from the plots, while both beams exhibit an oscillatory variation of the central

spot diameter, the FWHM of the truncated Bessel beam maintains a greater consistency about the predicted diameter than that of the axicon.

6.8 - Experimental investigation

In terms of practical usage of Bessel beams, in particular fields from conical lenses, the combination of the high intensity and depth of focus provided by axicons has the potential to have many applications in optimising the performance of terahertz imaging systems through development of novel axicon-coupled devices. For example, one could produce a compact Bessel-beam source by placing an axicon at the aperture of a large scalar horn for delivery of intense fields to a subject without the requirement of collimating optical systems. In [MAY09], the author described a system developed for near-field reflection imaging using mm-wave horn antennas transmitting and receiving reflected radiation from an object, as described in Figure 6.25.

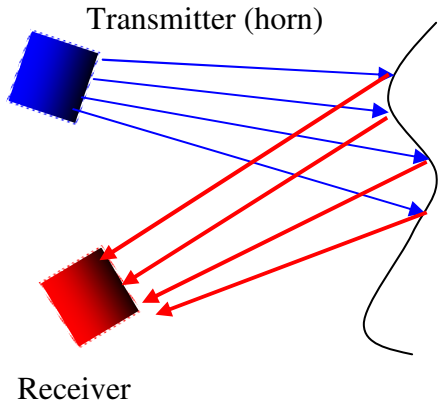

Figure 6.25 – Layout of near-field imaging technique applied in [MAY09].

An axicon coupled to a horn antenna may be a useful addition to such an arrangement creating an illuminating field on the object, with greater concentration of power than may be possible with a horn antenna alone.

To examine this, a low Fresnel number conical lens was manufactured from high-density polyethylene, with a radius of 30mm and axicon base angle of 20°, N_F = 2.133. To measure the beam, a Gunn diode with an operating frequency range of 95–105 GHz was employed. The operating frequency was set to 100 GHz and a profiled corrugated horn (aperture radius 10.5 mm, axial length 105 mm) was used as the radiating antenna. The measured and predicted farfield patterns of the horn exhibit low sidelobes and hence exhibit a high level of "Gaussicity" i.e. strong similarities with the

ideal Guassian function. The phase centre or waist position of the corrugated horn (with w_0 = 6.1 mm) lies a predicted distance of 18.6 mm behind the aperture and is placed to coincide with the focal point of an off-axis parabolic mirror (f = 500 mm), which collimates the beam incident on the axicon. The angle of throw of the parabolic mirrors was 45°. In this optical configuration, a corresponding Gaussian waist of 78mm is produced at the axicon with a flat phase front. The truncation of the field is therefore relatively slight. The field power was recorded by a Schottky-diode detector mounted on a computer-controlled XY scanner as used in chapter 3.

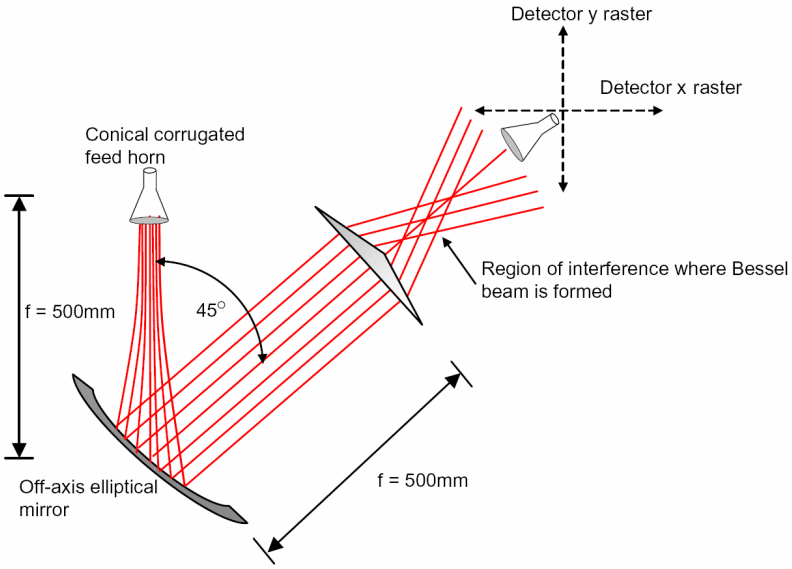

Figure 6.26 – Experimental setup for measurement of axicon field at millimetre wavelengths. Reproduced from [TRA04].

The conical lens tested in this arrangement is predicted to have a radial wavenumber of 0.473mm^{-1}, which with k = 2.0944, results in a BB spot radius of 5.5mm, and a diffraction free range of 140mm. The measured intensity patterns in this test are shown in Figure 6.27 with a comparison of an LG model of the conical lens.

For this particular axicon, the radius of 30mm (10λ) means that the maximum thickness at the centre of the lens is 10.91mm, which is small in relation to the free-space wavelength, and indeed to the wavelength in the lens of 1.97mm. With these dimensions, the analytical prediction of the axicon phase as a planar modulation given by eq. (6.10) is quite appropriate, and this is shown with agreement between the recorded and predicted diffraction patterns of Figure 6.27.

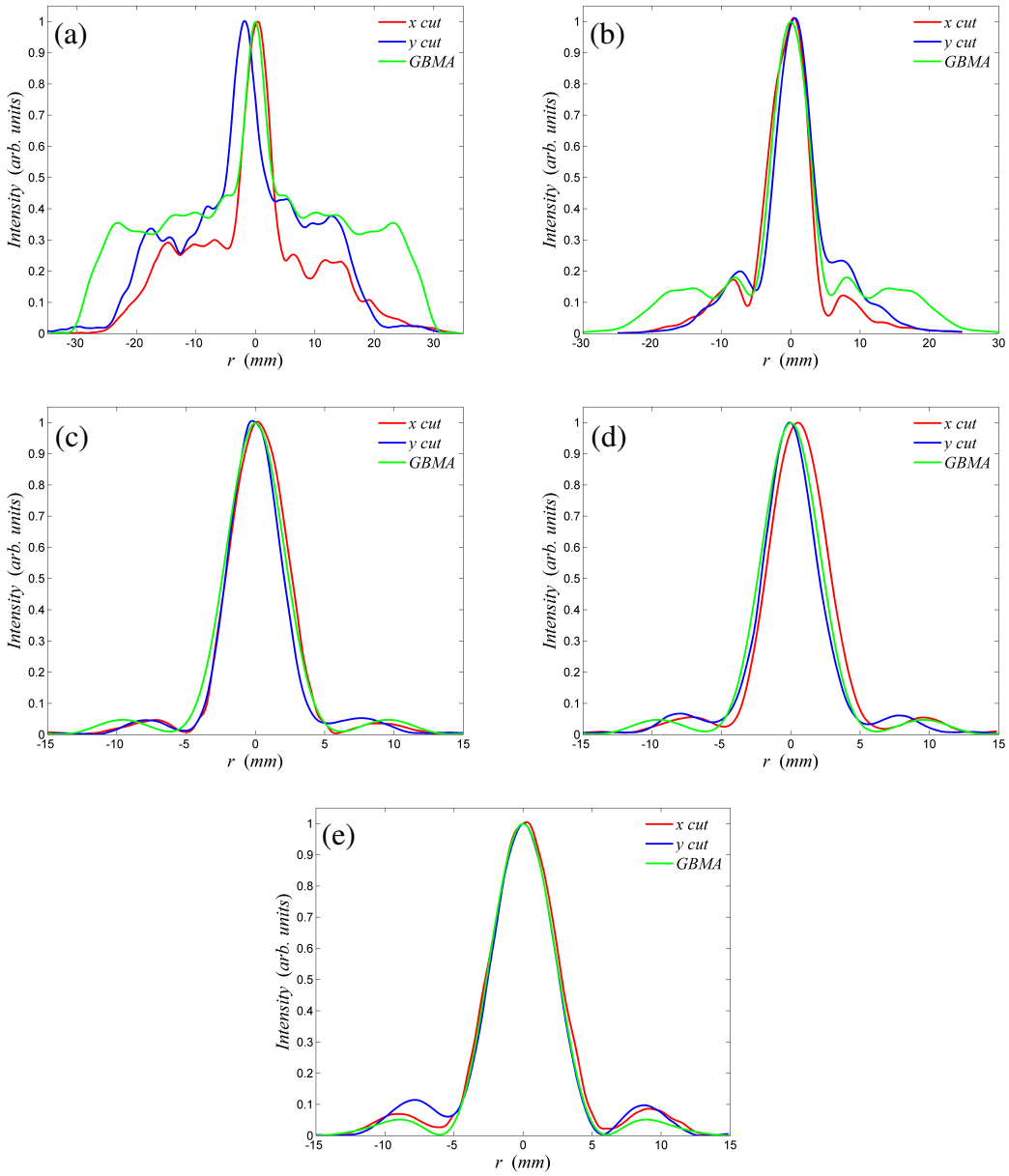

Figure 6.27 - Experimental measurement of the field generated by a conical lens at 100GHz. a = 30mm. z = (a) 0 mm (b) 25 mm, (c) 50 mm, (d) 80 mm, (e) 100 mm.

6.9 – Modal comparison of spherical and conical lenses

Due to the circular symmetry associated with most ideal radiation patterns, the occurrence of the Bessel function occurs widely in paraxial optics. As previously stated, the field at the focal plane of a uniformly illuminated thin lens is defined by a first order Bessel function and is given by eq. (5.1)

$$\left|E(r,f)\right|^2 \propto \left|\frac{J_1(kar/f)}{kar/f}\right|^2 .$$

The spherical lens provides an intense focus in the close vicinity of the defined focal distance and one advantage of the spherical lens over an axicon is the lower side lobe levels generated as defined by the equation above. As the axicon produces a much extended depth of field the peak amplitude is necessarily lower to conserve energy but the production of a relatively intense spot at multiple planes may be an advantage over the spherical lens in certain situations.

Shown below is the diffraction patterns of two axicons compared with the patterns of lenses with equal Fresnel numbers, i.e. the focal planes of the spherical lenses coincide with the diffraction free range Z_{max} of the corresponding conical lens.

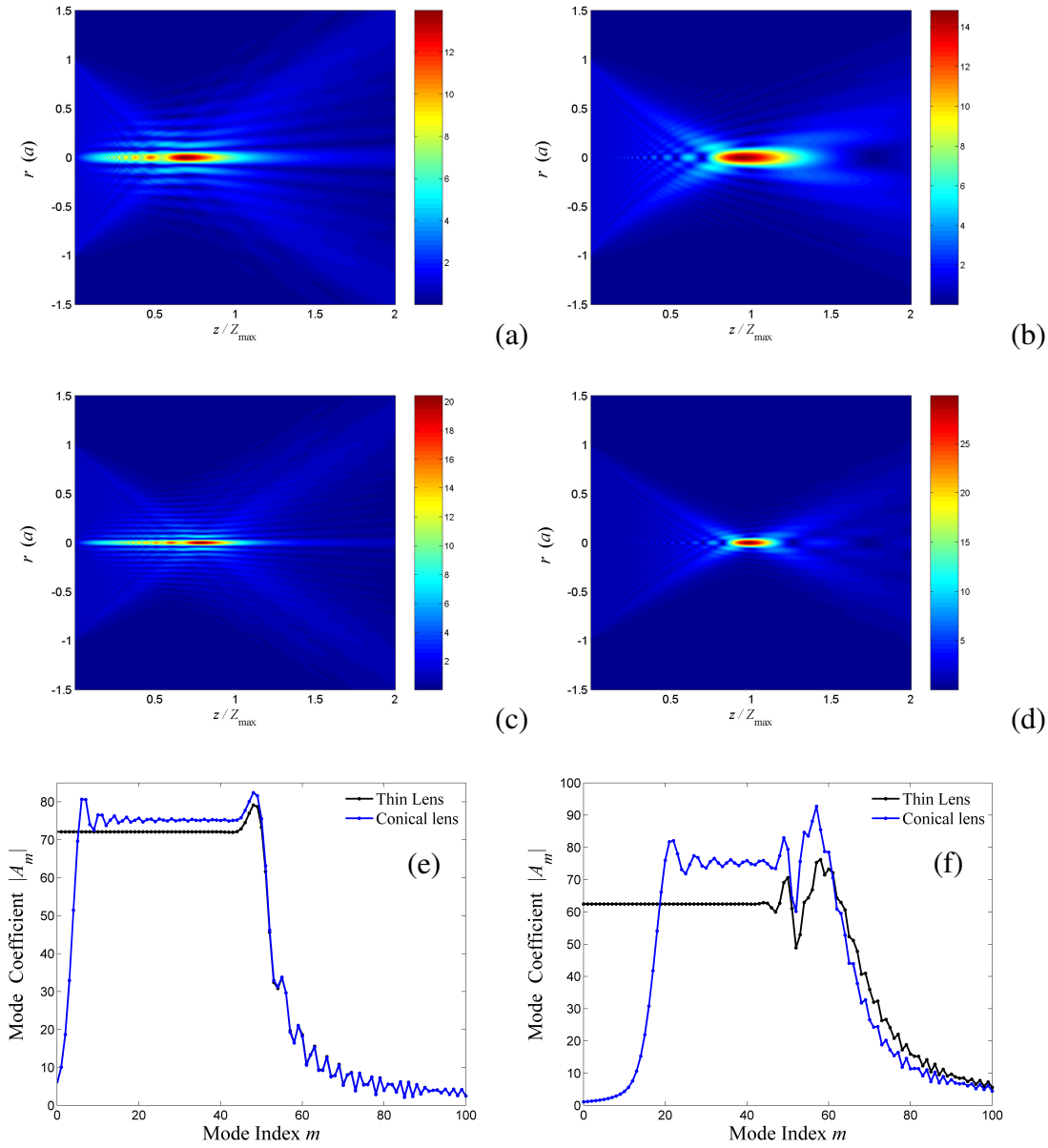

Figure 6.28 – Propagation of beams from conical (on left) and spherical lenses with equal Fresnel numbers. (a)-(b) θ=5°, N_F = 4.58. (c)-(d) θ=10°, N_F = 9.42. λ = 3, a = 100λ. The mode sets shown in (e) and (f) correspond to elements with N_F = 9.42 N_F = 21.5 respectively.

Comparison of the Laguerre-Gaussian mode coefficients of both lens types shows considerable deviations based on the structure of each function. When examined through their absolute value, representative of their individual importance to the overall diffraction effects, the most evident variation is a reduction in power of the lowest order modes, which corresponds to the formation of fields with similar oscillatory structures as the LG beam modes.

For a useful comparison of the LG mode structure of various types of lenses it is necessary to obtain a common mathematical description that can describe the two optical elements. A hyperbola can approximate both surfaces so we can describe the lens functions as

$$\exp\left(i\phi_{hyp}(r)\right) = \exp\left(iR_{hyp}\tan^2(\theta)\sqrt{1+\frac{r^2}{R_{hyp}^2\tan^2(\theta)}}\right) \tag{6.14}$$

which converges to a true conical function as $R_{hyp}\rightarrow 0$. Using this definition we can show how the deviation of a conical phase transformer from a spherical/hyperbolic form to a conical one generates a change in the dominance of the constituent LG modes of the optical field.

The above description of a hyperbola represents the surface of a cone of angle θ intercepted by at vertical plane a distance R_{hyp} from the apex of the cone. With increasing R_{hyp}, the structure changes from a cone (at $R_{hyp}\rightarrow 0$), to a hyperbola, and converges upon an approximate spherical function. In this manner this formulation can be used to examine the deviation of an axicon beam from that of the more conventional form of lenses.

As R_{hyp} is increased, there is an evident change in the surface of the wavefront from being completely conical with a well defined apex, to a hyperbola with a spherical-like surface near the centre and linear surface towards the outer edges. In this manner, the element then begins to behave as a lens/axicon hybrid. For the parameters λ = 1mm, θ = 10°, the mode coefficients and axial intensities of varying hyperbolic sections are depicted below.

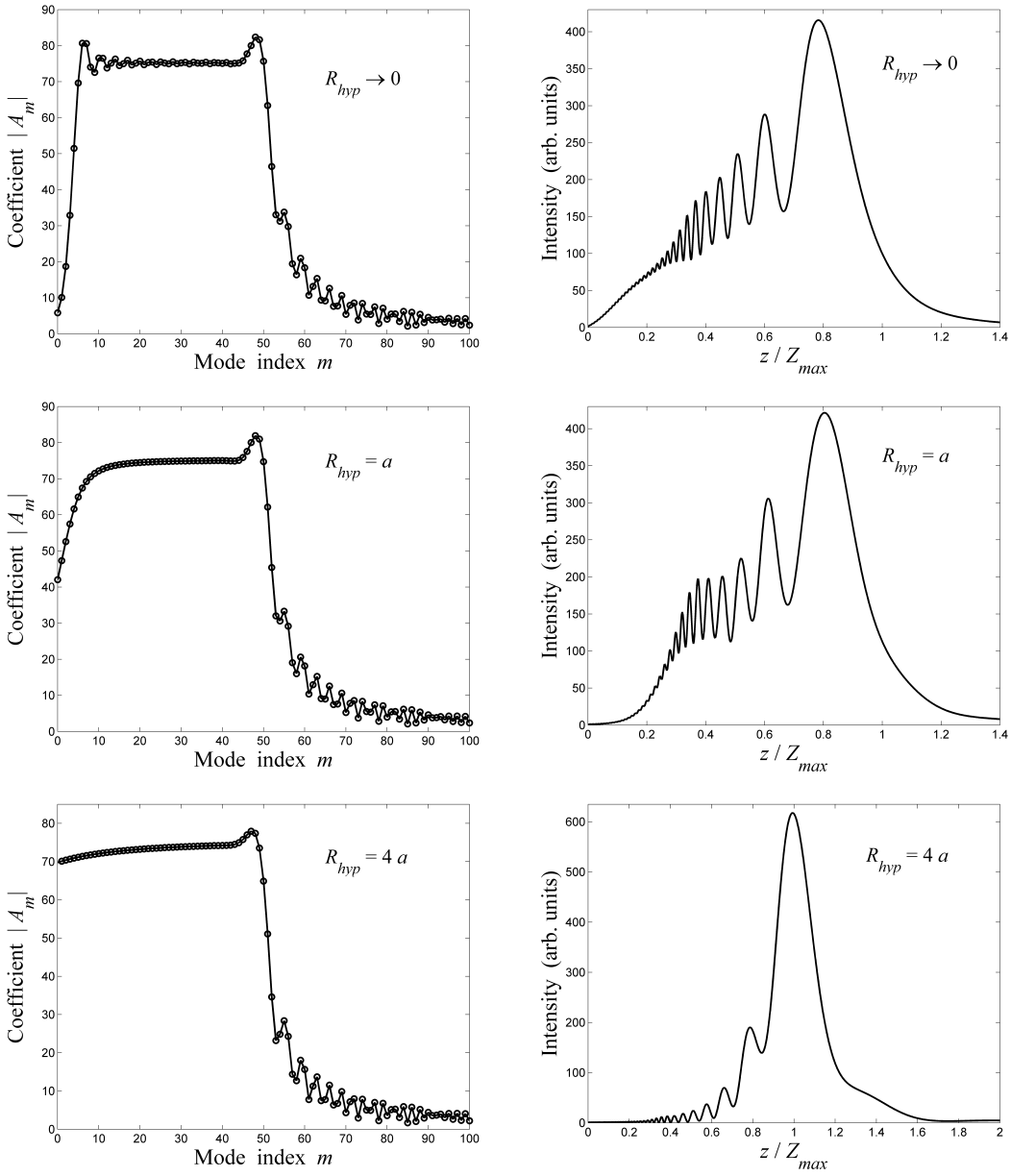

Figure 6.29 – The mode coefficients (left) of a hyperbolic lens for various values of R_{hyp}, with λ=1, a = 100λ, θ_{con} = 10°, and the corresponding axial intensity patterns on the right column.

The plots show an obvious increase in lower index mode coefficients with an increase in the value of R_{hyp}.

6.10 – Self-reconstruction in Bessel beams

The propagation of a Bessel beams show interesting properties when modulated by truncating aperture, and show the ability, referred to as self-healing, to maintain energy at a plane even when centrally obstructed at its source.

The Fresnel integral for the diffraction of a circularly symmetric wave field $E_0(r_0)$ is given by

$$E(r,z) = \frac{k}{i\,z}\exp\left(ikz + i\frac{kr^2}{2z}\right)\int_0^\infty E_0(r_0)J_0\left(\frac{k\,r_0\,r}{z}\right)\exp\left(i\frac{k\,r_0^2}{2z}\right)r_0 dr_0 . \tag{6.15}$$

If the calculation of the on-axis intensity only is desired, then this equation becomes

$$\left|E(r=0,z)\right|^2 = \left(\frac{k}{z}\right)^2\left|\int_0^\infty E_0(r_0)\exp\left(i\frac{kr_0^2}{2z}\right)r_0 dr_0\right|^2 . \tag{6.16}$$

To determine the propagation effects of a Bessel beam modulated by an aperture function $g(r_0)$, then $E_0(r)=g(r_0)J_0(k_r r_0)$, we can use the equation

$$\left|E(r=0,z)\right|^2 = \left(\frac{k}{z}\right)^2\left|\int_0^\infty g(r_0)J_0(k_r\,r_0)\exp\left(i\frac{kr_0^2}{2z}\right)r_0 dr_0\right|^2 . \tag{6.17}$$

Comparing this to (6.15), the reader should note that the two integrals are of the same form, with the exception of the r dependency in the argument of the Bessel function in (6.15). With a parameter change of $r = z\,k_r / k$ in (6.15), both equations have identical structure. This change of variable fundamentally represents a amplitude variation of the diffracted modulating field $g(r,z)$ measured along a line directed at an angle to the optical axis. Alternatively, this action represents a rotation of the field at an angle to the optical axis, and a measurement of the field distribution along z at $r = 0$, therefore we can say that the on-axis intensity variations of a Bessel beam modulated by a field $g(r)$ are directly related to the Fresnel diffraction properties of $g(r_0)$.

Due to the integration over an infinite range, the function $g(r)$ may have any form, such as, for example, the "top-hat" function which could be used to represent a hard aperture, a Gaussian amplitude profile, or perhaps a phase modulating thin spherical lens. To demonstrate this effect, the hypothetical propagation of a Bessel beam modulated by a circularly symmetric cosine function was calculated and compared with the diffraction of the tilted cosine beam.

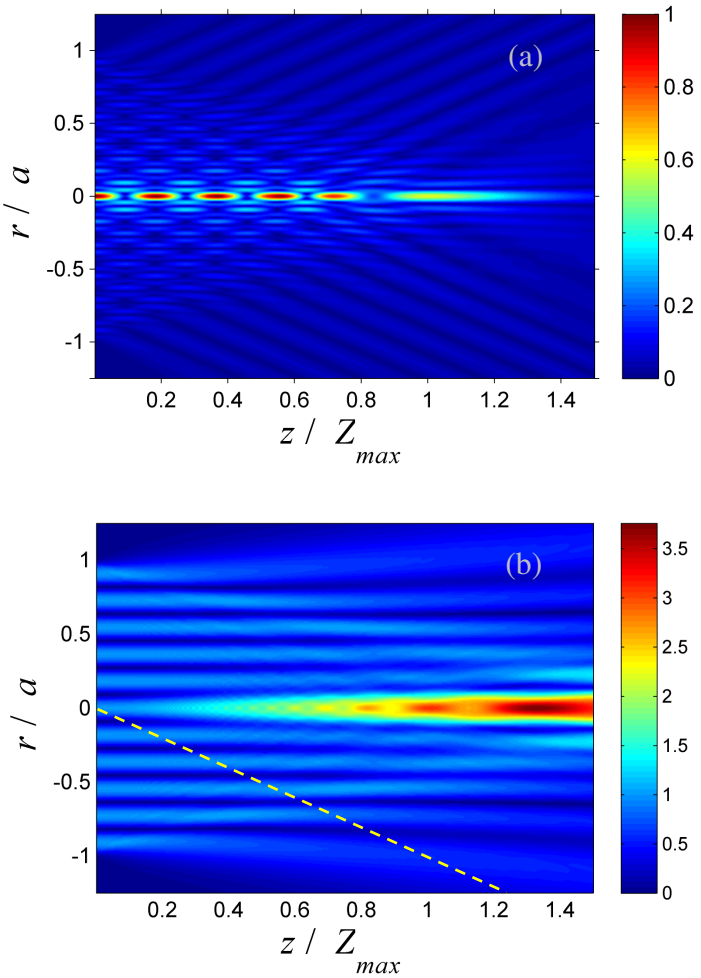

Figure 6.30 – Comparison of the propagation of (a) Bessel beam, and (b) the same Bessel beam modulated by cos(5.5π *r*/*a*). The on-axis (*r* = 0) amplitude of the field in (a) is identical to the amplitude along the diagonal line shown in (b).

This behaviour was previously studied in *Jiang et. al's* "*Propagation of apertured Bessel beams*" where the authors informally suggested that the on-axis intensity of a Bessel beam truncated by a hard aperture "looks very much like the Fresnel diffraction pattern of the straight edge", and this effect was shown for other modulating functions such as a truncated Gaussian beam, and an airy amplitude profile. However, the reasoning for such behaviour was not noted from the similarity in the above diffraction equations, and the study of the on-axis behaviour in axicons and Bessel beams has continued to maintain a significant number of publications. A notable example of this has been the publication *"Fractal conical lenses"* by *Monsoriu et. al.* [MON06], where the authors described the propagation of a beam from an axicon whose surface has been defined by the cantor function relating to fractal surfaces. This paper suggested that "these (Fractal, conical) lenses produce focal segments that are distributed along the

optical axis in a way that they reproduce the fractal profile of originating fractal conical lens", however this statement is true of any beam modulated by a conical lens.

Based on the preceding phenomenon, one of the most interesting properties of Bessel beams is the property known as self-healing or self-reconstruction, the ability of a BB to maintain its diffraction limited characteristics even after truncation by a small opaque screen. In Figure 6.31, the effects of an obscuration on an axicon beam is shown for the case of θ = 15°, a = 100 λ, λ = 3mm. The radius of the circular obscuration is 0.25 a, and 0.5 a.

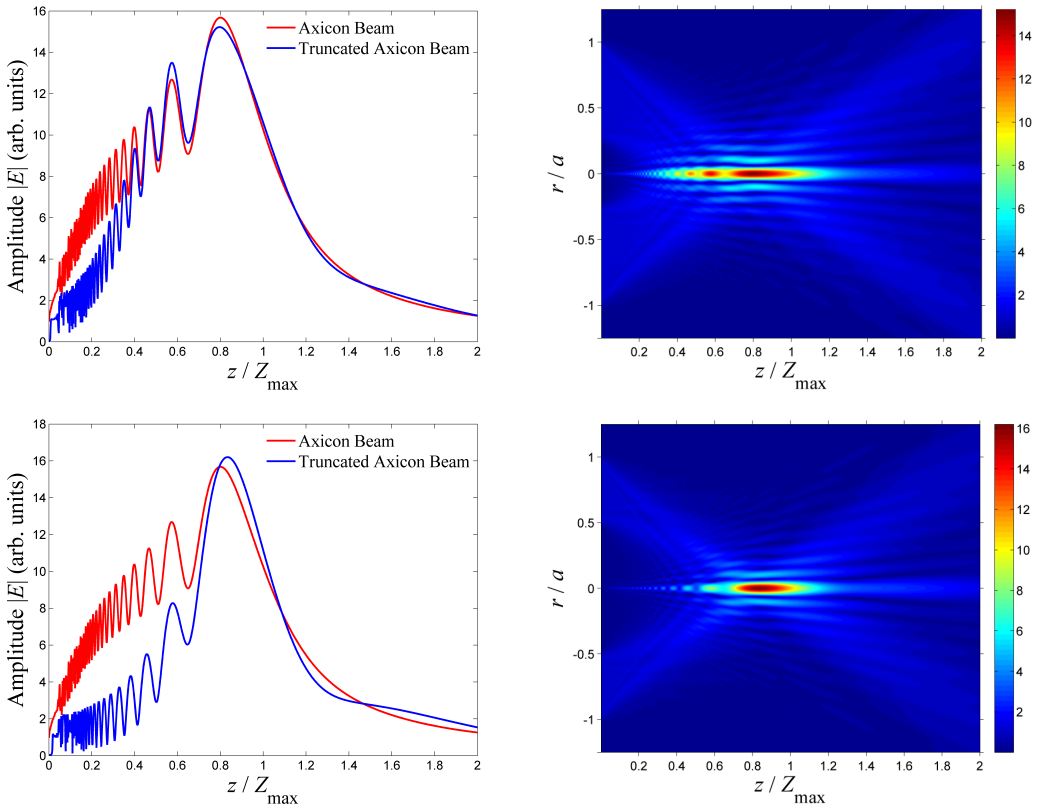

Figure 6.31- The self-reconstruction effects of an axicon beam under illumination by a plane wave. θ=20°, a = 30 λ. The first row shows the effects of obscuration by a circular disc of radius a/4, while in the second row its radius is a / 2.

Figure 6.31 shows the reconstruction of the on-axis amplitude, towards Z_{max}, even with truncation of the source field. This is due to the correspondence between a point on the optical axis and the points along a constant radius on the surface of the axicon lens. This is in contrast to the spherical lens, wherein the amplitude at the focal plane is dependent on amplitude contributions from all points on the lens surface.

This interesting property of Bessel beams may have applications in terahertz and mm-wave security screening where the self-reconstruction could allow for the

generation of a focal line even after obscuration by media composed of opaque and transparent regions.

6.11 - The influence of the input field on axicon beam characteristics

The characteristics of Bessel beams formed using an axicon illumination beam that has an infinite radius of curvature in its wavefront and a constant amplitude profile as described thus far is an ideal situation. Such fields do not occur in nature, and are far removed from realistic beams derived from lasers or diode oscillators. Especially at millimetre-wavelengths, a Gaussian structure is more evident from a waveguide field manipulated by a horn antenna. We thus need to examine how the geometrical predictions set out in earlier sections are altered by the deviation of a long wavelength field from the perfect source field of a plane wave.

Firstly, a variation in the width of a Gaussian input beam shows a decrease in the diffraction free range of the BB, and a reduction in its transverse extent. The presence of a Gaussian illuminating beam will affect the maximum on-axis intensity caused by the loss of off-axis power, and also the radial extent of the Bessel field due to the loss of energy at the edges of the optical element. Analytically, the LG decomposition of an ideal Bessel beam subject to an amplitude modulating Gaussian envelope, can be predicted from [GRA07]

$$\int_0^{\infty} \exp\left(-\alpha r_0^2/2\right) L_m\left(\frac{1}{2}\beta r_0^2\right) J_0\left(k_r r_0\right) r_0 dr_0 = \frac{(\alpha-\beta)^n}{\alpha^{n+1}} e^{-\frac{1}{2\alpha}k_r^2} L_n\left(\frac{\beta k_r^2}{2\alpha(\beta-\alpha)}\right)$$

where we can represent a Gaussian influence through

$$\alpha = \frac{2}{w_0^2} + \frac{2}{w_{in}^2} \text{ and } \beta = \frac{4}{w_0^2}.$$

While this method can give a swift calculation of a finite Bessel-Gauss beam, the infinite extent of both the Bessel and Gaussian functions allow for a direct analytical determination of its characteristics. In the same manner that the propagation characteristics for Laguerre and Hermite Gaussian beams were derived in previous work [MUR93], the diffraction effects of a Bessel beam modulated by a Gaussian amplitude function can be written explicity.[GOR89] was the first publication to give an expression for the Bessel-Gauss beam as

$$E_{BG}(r,z) = \frac{w_{in}}{w(z)} J_0\left(\frac{k_r r}{1+iz/Z_c}\right) \exp\left(i\left[\left(k^2 - \frac{k_r^2}{2k}\right)z - \tan^{-1}\left(\frac{z}{Z_c}\right)\right]\right)$$

$$\times \exp\left(\left[-\frac{1}{w^2(z)}+\frac{ik}{2R(z)}\right]\times\left(r^2+\frac{k_r^2 z^2}{k^2}\right)\right). \tag{6.18}$$

There is a decrease in the on-axis amplitude of a Bessel-Gauss beam due to the first factor in the above equation, while the cross-sectional profile is maintained for a finite distance in accordance with apodised Bessel beams. The most notable difference between this form, and a typical Bessel beam is the dependence of the on-axis amplitude on the illuminating field, characterized by

$$E_{BG}(0,z)=\frac{w_{in}}{w(z)}\exp\left(-\frac{k_r^2 z^2}{k^2 w^2(z)}\right)=\frac{w_{in}}{w(z)}\exp\left(-\frac{z^2}{w^2(z)}\cos^2(\theta_{BB})\right)$$

which is an effect of the phenomenon discussed in the previous section. For a conical lens, a similar analytical prediction is not available, and thus the effect of such Gaussian illumination must be studied numerically. For this case, the LG mode coefficients are given by

$$A_m=\sqrt{\frac{8\pi}{w_0^2}}\int_0^a L_m\left(2\frac{r_0^2}{w_0^2}\right)\exp\left(-\frac{r_0^2}{w_0^2}-\frac{r_0^2}{w_{in}^2}+ik(n-1)\tan\theta\, r_0\right)r_0 dr_0 \tag{6.19}$$

where w_{in} is the waist radius of the illuminating Gaussian beam. Figure 6.32 shows the variation of the on-axis intensity variation as a function of the waist radius of the Gaussian illumination of the axicon.

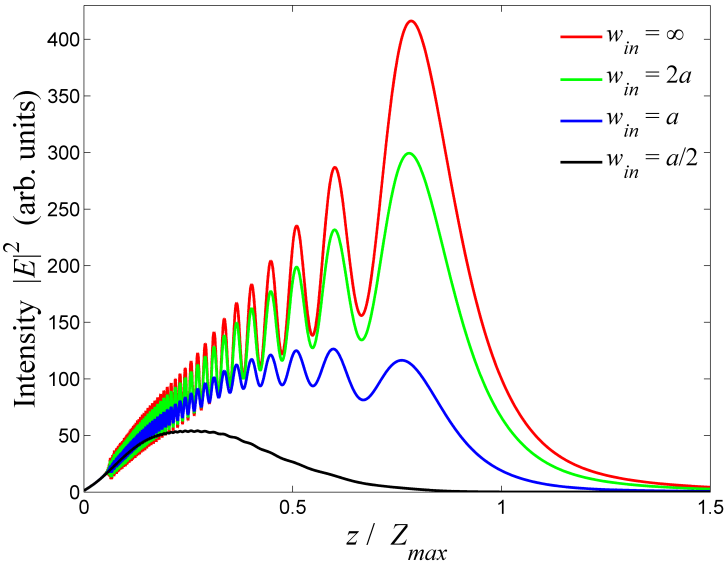

Figure 6.32 – On-axis behaviour of the axicon beam generated with a Gaussian beam of varying waist radius w_{in}. $\lambda = 1$, $a = 100$, $\theta = 10°$, $n = 1.52$. The phase of the illuminating field is assumed to be planar.

The transverse amplitude structures are naturally affected, and show a reduction in the total intensity, which is natural with illumination by Gaussian field structures with reduced power, see Figure 6.33.

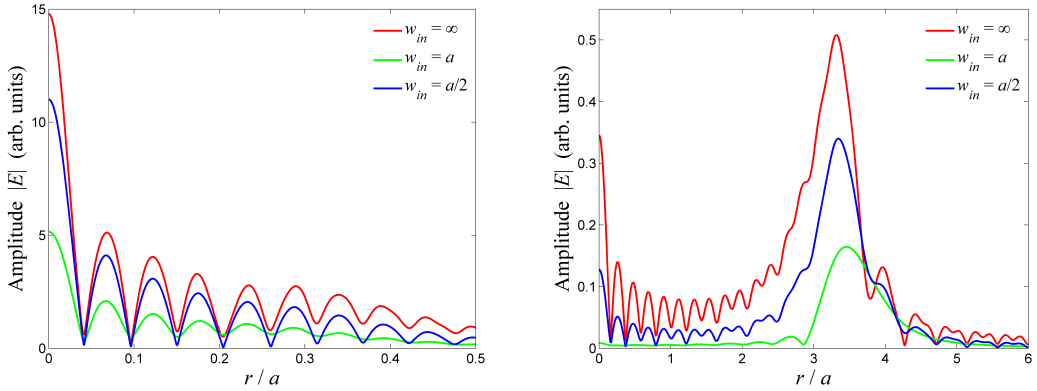

Figure 6.33 – The transverse amplitude at z = Z_{max}/2 (left) and z = 4 Z_{max} for a conical lens with a = 100 λ, and θ_{con}=10° with n = 1.52.

In Figure 6.32, it can be seen for Gaussian beams that have a beam width much less than that of the aperture radius a the on-axis intensity becomes a smoother and less oscillatory as diffraction caused by the edge of the axicon becomes less significant when truncating the beam at a lower amplitude value, i.e. with smaller values of w_{in}. Similarly in the far-field the transverse amplitude structure is also less oscillatory due to the same effect. However, the most important effect with Gaussian illumination is the reduction of overall energy in the system as can be seen in both plots of Figure 6.33.

So far, this study of axicons has concentrated on the ideal situation of the axicon being illuminated by a wave with an infinite radius of curvature, and this allows for the prediction of the radial wavenumber k_r, and diffraction free range Z_{max}. This is however an ideal scenario and it would now be advantageous to examine the focusing effects of conical illumination with a spherically diverging beam, typically characterised as being derived from an infinitesimal point source. In this case the behaviour of the field refracted by the axicon is altered by the presence of a curved wavefront. In this case, see Figure 6.34, the angle at which each point of the wavefront is refracted is not a constant across the element, and so the field at each z plane is, according to geometry, formed by the self-interference of radial wavevectors that increase with greater propagating distance, thus generating an expanding beam width.

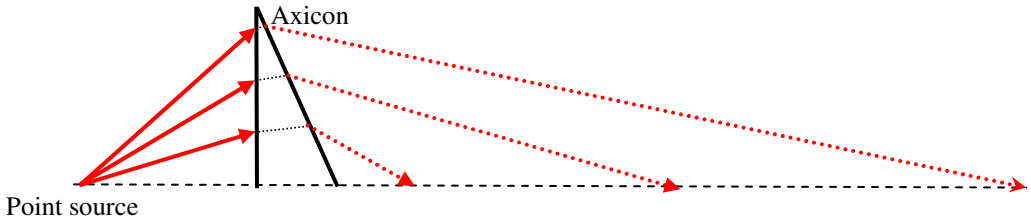

Figure 6.34 – The illumination of an axicon with a diverging wavefront causes varying angle of refraction across the element, and subsequently a variation of the angle of incidence to the optical axis.

At each point on the optical axis with the focal region the beam profile is still defined by a Bessel function, but with a decreasing radial wavenumber, causing a transverse broadening of the beam. The LG mode coefficients in this situation are obtained from

$$A_n = \sqrt{\frac{8\pi}{w_0^2}} \int_0^a L_n\left(2\frac{r^2}{w_0^2}\right) \exp\left(-\frac{r^2}{w_0^2}\right) \exp\left(i r k \left(-\frac{r}{2R_{in}} + (n-1)\tan\theta\right)\right) r dr \,. \qquad (6.20)$$

Publications on the study of axicon and lens characteristics are often based on the study of the axial/on-axis intensity variations calculated by the Fresnel integral. This calculation is much simplified in GBMA by the elimination of the transverse variation of each *LG* mode, and the complex quadratic phase factor, giving the complete variation as a simple sum:

$$E(r=0,z) = \sqrt{\frac{2}{\pi\, w(z)^2}} \exp(i k z) \sum_{m=0}^{M} A_m \exp\left(-i(2m+1)\tan^{-1}\left(\frac{k z}{2w_0^2}\right)\right).$$

Such a calculation is much faster than an equivalent Fresnel calculation, with only M integrations required.

We can exhibit the variations caused to the focal line of an axicon by the deviation of the wave's curvature from the ideal scenario of plane wave modulation, for λ = 1mm, aperture radius a = 100mm, and θ_{con} = 10°. See Figure 6.35.

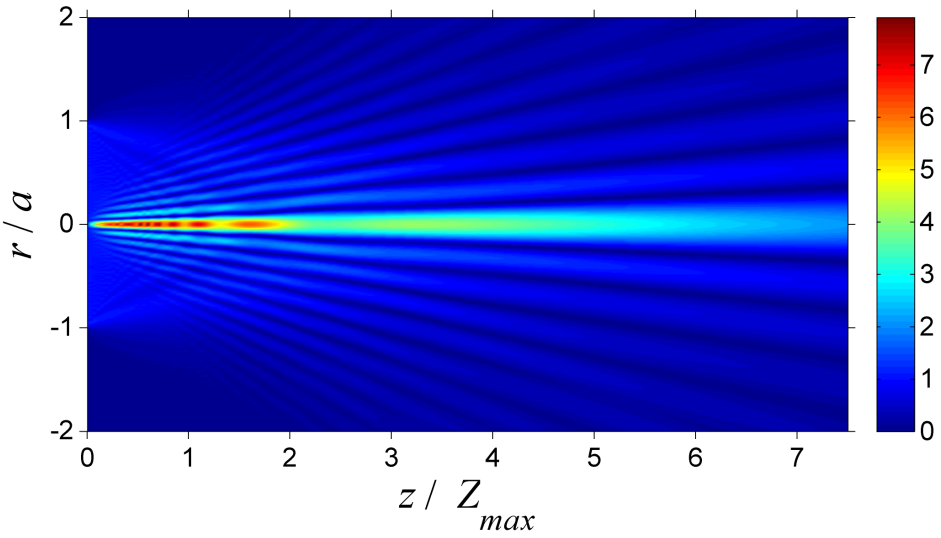

Figure 6.35 - The variation of the axial intensity of a conical lens through illumination by a diverging wavefront. Calculated for a conical lens with a = 100λ, and θ_{con}=10° with n = 1.52. The radius of curvature of the illuminating spherical wavefront is 10a while the amplitude variation is neglected across the conical lens at z = 0 to highlight the effect of the curved phase influence.

Along the optical axis, an increased radius of curvature of the input field creates a much longer focal line, but as can be seen in Figure 6.36 the amplitude of such a field is greatly reduced with increasing divergence of the lens illumination.

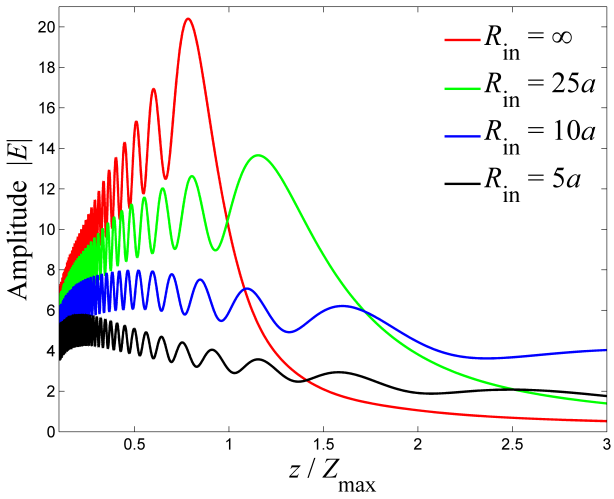

Figure 6.36 – The variation of the on-axis amplitude from an axicon by refraction of a spherically diverging field. Shown with the same optical parameters as Figure 6.35.

While the beams are shown to have increasingly larger spot sizes at greater distances from the axicon, the field does maintain an appreciable amplitude value along the axis for a considerable distance. Despite the larger beam widths, such focusing could be used

as a source of illumination in a terahertz imaging system without requiring collimating optics as was used in the section 6.8 this chapter.

6.12 - Focusing of Bessel beams

The plane wave solution to the wave equation can be considered as a special type of Bessel beam of radial parameter $k_r = 0$. The modulation of a plane wave by a spherical lens is known to give an intense central spot at the focal length f of the element, which can be expressed analytically. Generally, for the calculation of diffraction patterns of a field which has propagated through several optical elements or regions of higher refractive indices, several integrals would have to be solved numerically, which would make geometrical and paraxial techniques tolerable predictions for the properties of linear optical systems to compensate for the computation times of diffraction calculations.

A very useful variation of the Fresnel diffraction integral was introduced in [COLL70], which defined the propagation of optical waves through a circularly symmetric linear optical system defined through an ABCD matrix description. The complete form of this integral is

$$E(r,z) = \frac{ik}{B}\int_0^a E(r_0) J_0\left(\frac{kr_0 r}{B}\right) \exp\left(\frac{ik}{B}\left(A r_0^2 - 2r_0 r + D r_0^2\right)\right) r_0 dr_0 \qquad (6.21)$$

where all symbols have their usual meaning in relation to matrix optics. For the calculation of the diffracted field of a Bessel beam (at $z = 0$) of radial wavenumber k_r focused by a thin lens of focal length f, the appropriate $ABCD$ matrix is given by

$$\begin{pmatrix} A & B \\ C & D \end{pmatrix} = \underbrace{\begin{pmatrix} 1 & 0 \\ -\frac{1}{f} & 1 \end{pmatrix}}_{lens} \underbrace{\begin{pmatrix} 1 & f \\ 0 & 1 \end{pmatrix}}_{Free\ space} = \begin{pmatrix} 1 & f \\ -\frac{1}{f} & 0 \end{pmatrix}$$

and the associated diffraction integral for the focusing of a BB becomes given by

$$E(r,f) = \frac{ik}{f}\exp\left(-ik\left(f + \frac{r^2}{2f}\right)\right)\int_0^a J_0(k_r r_0) J_0\left(\frac{k\, r\, r_0}{f}\right) r_0 dr_0$$

and for a plane wave, $k_r = 0$, this equation is given by eq. 5.1. Here, we can simulate the focusing of Bessel beams without the requirement of analytically solving such integrals.

The LG mode coefficients for the focusing of Bessel beam at its source are predicted from

$$A_n = \sqrt{\frac{8\pi}{w_0^2}} \int_0^a L_m\left(2\frac{r_0^2}{w_0^2}\right) J_0(k_r r_0) \exp\left(r_0^2\left(\frac{-1}{w_0^2} + \frac{ik}{2f}\right)\right) r_0 dr_0 \,. \tag{6.22}$$

The behaviour of these fields in the focal region of a thin lens is shown in Figure 6.37 with a varying focal length.

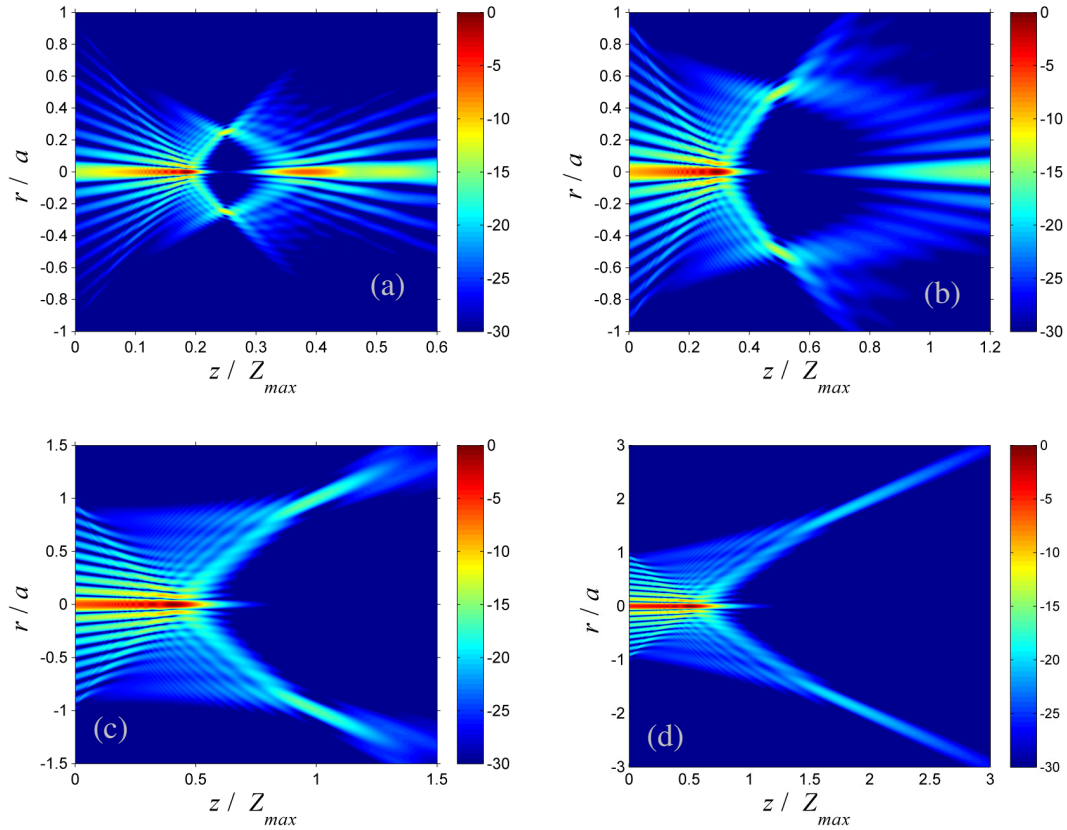

Figure 6.37 – The diffraction of Bessel beams focused by a thin lens with f = (a) $Z_{max}/4$, (b) $Z_{max}/2$, (c) Z_{max}, (d) $2Z_{max}$. λ = 3mm, a = 100λ, k_r = 0.096 (θ_{con}=5°).

Such properties of the focused axicon beams are important in the field of optical trapping where particles can be contained and manipulated in the hollow intense region of the field at the focal plane of the lens. In the above examples, with a laser wavelength of λ = 633nm the outer radius of the conical lens is 63μm, thus comparison of the diameter of the field at the focal plane to this radius depicts the microscopic dimensions of objects which can be manipulated, as was reported in [ZWI10] and [ARLT01].

6.13 – Synthesis of optical fields using Bessel beams

As shown earlier in this chapter Bessel functions and LG functions share certain similar characteristics in their oscillatory structure, namely rapid radial amplitude fall-offs and large central values at r = 0. Another important property shared

by both is that of orthogonality. Unlike the Laguerre-Gaussian functions which are orthogonal over $r = \{-\infty, \infty\}$, the zeroth order Bessel functions are orthogonal over range $\{0,a\}$, such that for a circularly symmetric function $E_0(r_0)$.

$$E_0(r_0) = \sum_{m=0}^{\infty} A_m J_0\left(\alpha_m \frac{r_0}{a}\right) \tag{6.23}$$

where,

$$A_m = \frac{2}{a^2 J_1^2(\alpha_m a)} \int_0^a J_0(\alpha_m r_0) E_0(r_0) r_0 dr_0 \tag{6.24}$$

and α_m is the m^{th} root of $J_0(r_0)$ [HOLM98]. Like the LG modes, these equations allow us to formulate any circularly symmetric function, which can be assumed to represent the transmittance function of an optical pupil. To account accurately for the entire field at $z > 0$, the optical propagation of each individual mode must be calculable, with diffraction angles and field strength dependent on waist parameters and radii of curvature for example. For Bessel beam analysis this becomes a trivial task: It is known that an ideal Bessel beam, (that described by a real Bessel function of infinite extent), propagates according to $J_0(k_r r)\exp(ik_z z - \omega t)$ with $k_r^2 + k_z^2 = k^2$, thus we can define that each individual Bessel beam mode of a expanded aperture will propagate according to eq. (6.3).

This is clearly a much simpler description of a mode than that of a LG mode, where several parameters are required for calculation of each mode. Also, and more importantly, Bessel beams are solutions to the complete wave equation and are therefore not restricted by the paraxial approximation, which could be a significant advantage over the conventional form of Gaussian beam mode analysis. BB mode analysis may be more useful in describing optical fields analytically, as Bessel functions are easily manipulated mathematically and are also more extensively described in the literature. Considering the illumination of a circular aperture with monochromatic radiation of wavenumber k, the diffracted field can be expressed using BB mode coefficients given by

$$\begin{aligned} A_m &= \frac{2}{a^2 J_1^2(\alpha_m r_2)} \int_0^a r_0 J_0\left(\frac{\alpha_m r_0}{r_2}\right) dr_0 \\ &= \frac{2}{\alpha_m a^2 J_1^2(\alpha_m a)} \end{aligned} \tag{6.25}$$

The infinite limit posed on the summation of Bessel modes in (6.23) poses little problem. As with LG synthesis, these series converge quickly with low values of M and

more accurate descriptions can be obtained using several thousand modes which is of little difficulty with modern computers.

As stated, Bessel functions are orthogonal only over a finite extent in contrast to the LG modes which exhibit orthogonality over all space. A field represented in this manner will be adequate only over the range $r_0=\{0, a\}$, with other undesired spurious features being reconstructed periodically outside this region. This means that the calculated diffracted field is valid over a finite longitudinal distance only as the undesired aliased transverse features will also "diffract" and will eventually overlap with the desired diffraction calculation. A solution to this is to define the function to be synthesised, $E_0(r_0)$ over a much larger extent r_2 with zero values between a and r_2. In this case the aperture function now includes the zero values between $r_0=a$ and $r_0=r_2$ which requires a much larger number of modes to expand the fine structure of the desired aperture function in $r_0 < a$. See Figure 6.38.

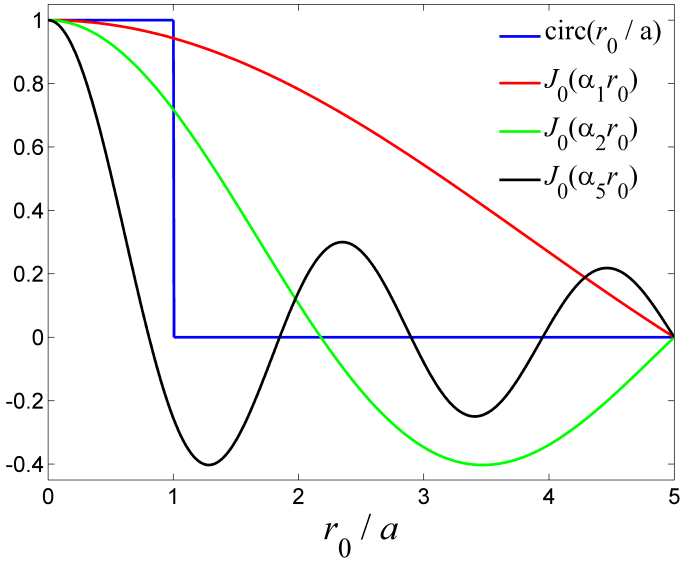

Figure 6.38 - The Bessel beam mode structure used in the Bessel expansion of the function circ(r_0 / a) with $r_2 = 5a$.

The diffraction effects the field in the diffraction half plane $z \geq 0$ can be calculated from

$$E(r,z) = \sum_{m=1}^{M} A_m J_0(\alpha_m r) \exp\left(i\sqrt{k^2 - \alpha_m^2}\, z\right) \tag{6.26}$$

in an identical manner to the use of the Gaussian beam mode methods used throughout this thesis.

The advantage of this simple technique is its complete independence from the Fresnel theory of diffraction and also it allows for calculation of diffraction effects with solutions of the *complete* wave equation without the paraxial approximation. However, the use of a Bessel mode calculation may only have validity in the near field due to the orthogonality properties of the Bessel functions, but even this is useful for modelling of low *F*-number systems which the Fresnel diffraction integral has difficulty predicting in the very near field. Also, this method predicts evanescent waves in the near field of the diffraction plane, with $\alpha_m > k$ in eq. (6.26) whereas the Fresnel diffraction model would predict these high frequency features as generating harmonic energy.

We can now demonstrate the use of Bessel functions in the modelling of diffraction effects, and as an example we will use the diffraction of a plane wave by a spherical thin lens. The calculation of BB mode coefficients for a thin spherical lens is given by

$$A_m = \frac{2}{r_2^2 J_1^2(\alpha_m r_2)} \int_0^a J_0\left(\alpha_m \frac{r_0}{r_2}\right) \exp\left(i \frac{k r_0^2}{2f}\right) r_0 dr_0 \qquad (6.27)$$

where again f is the focal length of the lens. For a lens with a low F-number the phase curvature at $z = 0$ is large, thus the number of modes used in a Fourier-Bessel synthesis is required to be high. Figure 6.39 shows the mode coefficients and the reconstruction of the diffracted fields using (6.26).

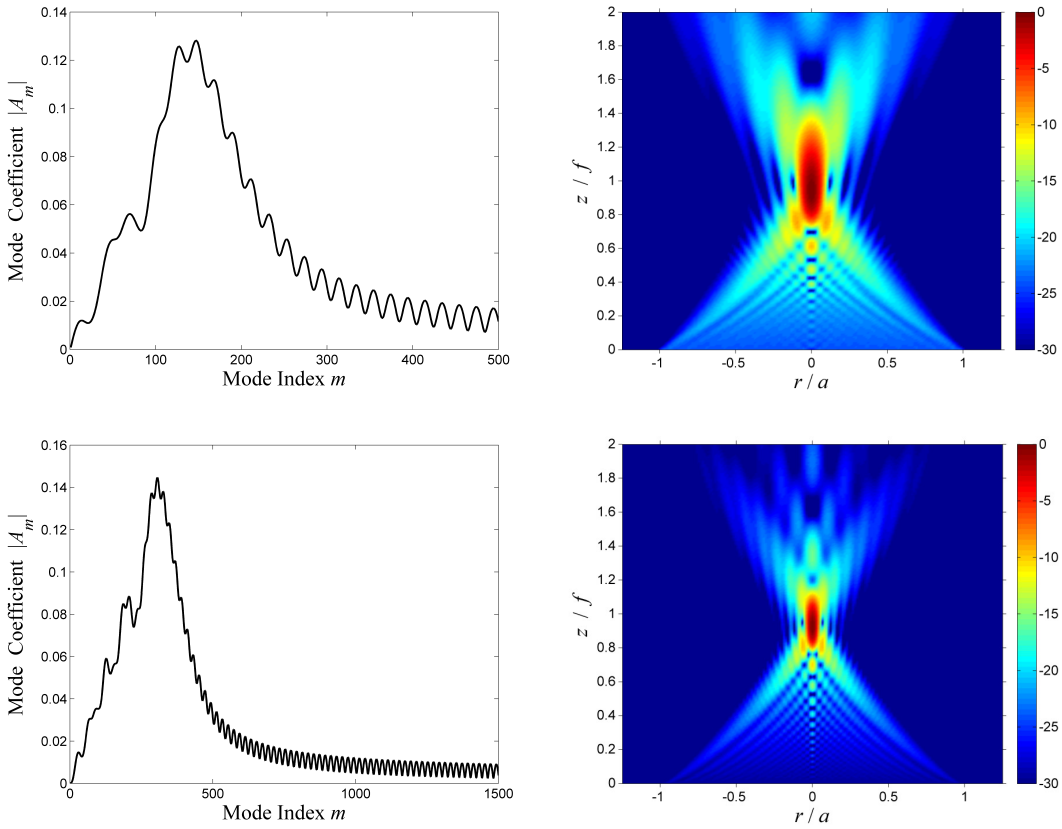

Figure 6.39 – Calculation of the modulation of a plane wave by a thin lens (top) *F*#2, and (bottom) *F*#1 as a superposition of Bessel beams using eq.(6.26) and eq.(6.27). $\lambda = 1$, $a = 20\,\lambda$, $r_2 = 20\,a$. The BB mode coefficients of each lens are shown in the left column.

Apart from their non-paraxial behaviour the application of ideal Bessel beam modes in this manner has a practical advantage over the Laguerre-Gaussian field modes when using software such as Matlab™ and Python as those languages contain a very efficient built-in function for the calculation of Bessel functions which allows for relatively swift generation of results. This is in contrast to the LG modes which have to be generated recursively in custom written functions.

6.14 – Pulsed Bessel beams

The resolution and depth of field shown with continuous wave Bessel beams and their generation using conical lenses is also desirable for temporal pulsed fields such as those used in THz spectroscopy. Such short field structures would be of benefit in terahertz time-domain systems where the use of a pulse that would maintain a narrow central spot could have useful applications in imaging at spectroscopy systems. The propagation of a time dependent zeroth order pulsed Bessel beam is defined by the integral

$$\psi^X(r,z,t) = \int_{-\infty}^{\infty} S(\omega) J_m\left(\frac{\omega}{V} r \sqrt{\frac{V^2}{c^2} - 1}\right) \exp\left(i\omega\left(\frac{z}{V} - t\right)\right) d\omega \qquad (6.27)$$

where V is the on-axis phase velocity ω/k_z [ZAM03], related to the propagation angle of the individual Bessel beams. One particular form of pulsed Bessel beam that has been given considerable attention particularly in the field of medical ultrasound, [LU90,LU92] is the field structure known as an X-wave. This term refers specifically to a pulsed Bessel beam with a frequency spectrum defined by $S(\omega) = \exp(-\beta\omega)$, where β is a real number. Inserting this spectral description into eq. (6.27), the integral can be solved explicitly to give the expression [ZAM03]

$$\psi^X(r,z,t) = \frac{V}{\sqrt{(\beta V - i(z - Vt))^2 + r^2\left(\frac{V^2}{c^2} - 1\right)}} \qquad (6.28)$$

with velocity $V = c \,/\, \cos(\pi/2 - \theta_{BB})$. In eq. (6.28) the field is generated by the integration of Bessel beams each with the same characteristic propagation angle θ_{BB}. The wavefront generated by this field has been the subject of some controversy due to a propagation of the pulse peak with apparent superluminal velocity. See Figure 6.40.

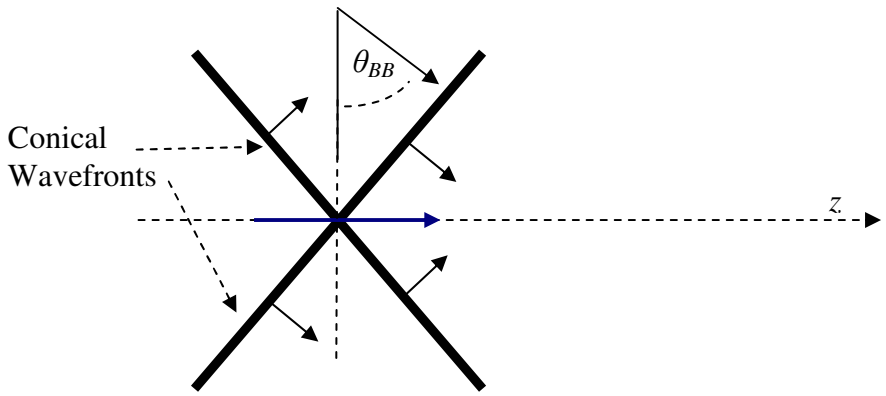

Figure 6.40 – Schematic of X-wave propagation.

The generation of the so-called X-waves is not possible with a real conical lens due to dispersion across the wide bandwidth of the function $\exp(-\beta\omega)$ which, depending on the value of β, is valid over all frequencies of the spectrum, and has more significant spectral components with lower frequencies. However, the conventional Gaussian spectrum used within this thesis does generate similar pulse effects as the X-waves.

Like several fields discussed in this thesis, the true description of Bessel pulses is again hypothetical due to its infinite extent and its realisation is performed by

physical approximations. Using the technique developed in chapter 4, we can describe the propagation of a temporal pulsed field refracted by a conical lens. In this model the assumption is made, for simplicity, that the refractive index of the hypothetical lens material is constant across the pulse spectrum with n = 1.51. For conical lenses with larger base angles, and therefore larger depths, the planar approximation may not be as suitable as it was the case in the discussion of dispersive diffractive lenses in chapter 5. Nevertheless, with a central frequency of ω_0 = 374.74 THz (λ_0 = 800nm), the propagation of a paraxial pulse with a relative bandwidth γ = 0.5 refracted by a borosilicate (BK7) conical lens with base angle 20° is described in the following section.

The mode coefficients of a conical lens in the paraxial regime are determined for each frequency from

$$A_m(\omega) = \sqrt{\frac{2}{\pi w_0^2}} \int_0^a L_m\left(2\frac{r_0^2}{w_0^2}\right) \exp\left(-\frac{r_0^2}{w_0^2}\right) \exp\left(i\frac{\omega}{c}(n(\omega)-1)\tan\theta\right) 2\pi r_0\, dr_0 \quad (6.29)$$

In the case of non-dispersive refraction, all values of the refractive index are equal thus $n(\omega) = n(\omega_0)$. Figure 6.41 illustrates the mode coefficients derived from this equation for an axicon beam. The values of the coefficients are modulated to account for the Gaussian spectrum of the pulse.

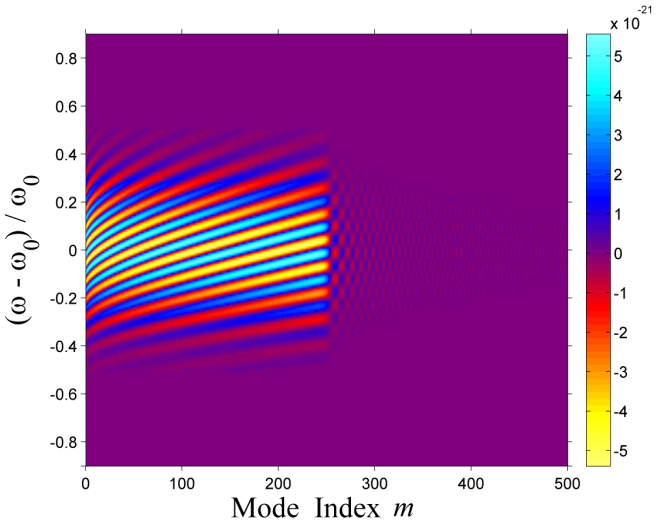

Figure 6.41 - The mode coefficients, Re{A_m} / $(-1)^m$ with M = 500, for each spectral component of a γ = 0.5 Gaussian shaped planar pulse focused by a non-dispersive axicon with a = 25 λ_0, λ_0 = 800 nm, θ_{con} = 20°, $w_0 = (a / 500)^{1/2}$, the refractive index n = 1.51 . The effect of the spectrum on each frequency has been included and accounts for the modulating envelope along the frequency axis.

The propagation of the pulse formed by the GBM modal description in eq.(6.29), using the mode coefficients of Figure 6.41, is shown in Figure 6.42. Note that the central spot size of the pulse again shows consistency.

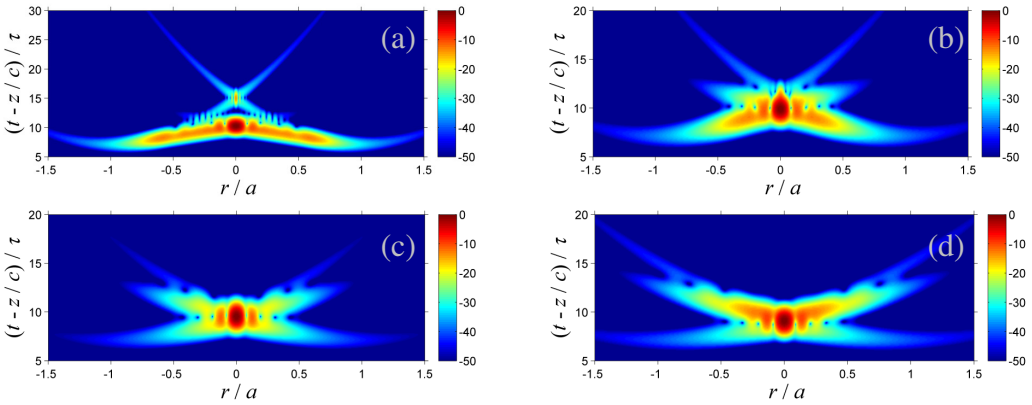

Figure 6.42 – Propagation of a plane wave pulse refracted by a dispersionless axicon with $\theta_{con} = 20^{\circ}$, $a = 25\lambda_0$. z = (a) Z_{max} / 4, (b) Z_{max} /2, (c) 0.75 Z_{max} , (d) Z_{max}.

6.15 - Conclusion

We have presented the properties of diffraction limited (Bessel) beams by use of the Laguerre-Gaussian synthesis. The transverse diffraction patterns shown in this chapter agree completely with the results determined directly from the Fresnel diffraction integral. However, in calculations of longitudinal on-axis amplitude variations a deviation between the two methods does become apparent, particularly in the near field, with the loss of high frequency oscillations on the optical axis which are dependent on higher order Gaussian modes. The transverse pattern, however, is not affected by this effect, and in fact a reduction of this oscillatory behaviour can help make on-axis amplitude trends more apparent, without any significant loss of useful information.

The results of the experimental measurement of a low Fresnel number conical lens have been presented, and similar elements may have potential applications in mm-wave imaging whereby a narrowly focused field can propagate over significant distances without the requirement of intensive collimating optical systems.

We have exhibited the structure of the pulsed fields refracted by conical lenses and showed that the pulsed form of pseudo-Bessel beam also maintains a diffraction free range of the central lobe.

The effect of non-uniform illumination of conical lenses has been illustrated with Gaussian beam illumination shown to reduce the overall amplitude of the field but also the diffraction free range. In the case of illumination by a diverging wavefront, the generated field no longer maintains an approximately constant beam radius over Z_{max} but creates a field that expands with increasing distance from the lens. However, this has been shown to maintain significant energy on the optical axis, and causes an increase in the length of the "focal line".

The author has also applied the description of ideal Bessel beam propagation as a method of non-paraxial field calculation. From the well-known Fourier-Bessel expansion of a circularly symmetric function, the diffraction at an aperture can be determined through a superposition of Bessel beams. This method as applied here is only valid in the near-field, but was shown to give very useful results in the simulation of spherical lenses.

Chapter Seven

Conclusion

This thesis has described the paraxial theory of Gaussian beam mode propagation and applied the associated techniques to modern areas of optical research such as ultrashort pulse propagation and digital holography, within the mm-wave and THz bands of the EM spectrum. Although rooted in the far-infrared band, the techniques used in the prediction of such long wavelength fields also have direct relevance in optical propagation in the near-infrared and visible regions of the spectrum.

While the primary concern of this thesis has been the paraxial diffraction of electromagnetic fields, the later sections of chapter 2 described methods that can be used for a more complete simulation of field propagation without paraxial restrictions. In particular, the author has demonstrated the more intensive method of the finite-difference time-domain algorithm in simulation of a 100GHz field in a dielectric lens antenna, a component which has evaded significant classification in the mm-wave band. The author considers FDTD to be the optimum model of electromagnetic field simulation for two reasons

(1) FDTD allows for modelling of electromagnetic effects based on the fundamental physical description given by Maxwell's equations.

(2) The method allows for simulation of arbitrarily shaped optical elements eliminating requirement of planar approximations conventionally used in scalar models.

Due to its computational complexity, FDTD has not become a standard simulation technique of electromagnetic effects in the mm-wave band. However, for the analysis of horn antennas and waveguides FDTD is a very useful supplement to conventional techniques in mm-wave research and can be used to obtain very realistic models without the requirement of complex and abstract mathematical theories.

The author has also suggested a novel method of Gaussian beam mode analysis using recently derived expressions for the propagation of Hermite-Gaussian modes allowing for application of the modal technique outside of the paraxial regime, which may be very useful in the analysis of mm-wave horn antennas.

The study and understanding of the dynamics of ultrashort pulses is a relatively new field of optical research. Throughout the literature, the methods of simulating

pulsed fields in the scalar theory rely primarily on diffraction integrals in both the paraxial and non-paraxial regimes. The inefficiency in numerically solving these integrals, one of the motivations of this work, is further exaggerated in the prediction of pulse diffraction due to the manner in which the short field is represented as a superposition of monochromatic fields with varying frequencies, requiring solution of a multitude of such diffraction integrals at each point in space.

The numerical simplification achieved with GBMA allows for very swift calculation of each monochromatic field with negligible deviation from the integral results and subsequently pulsed field calculations become much quicker. The GBM method calculates the monochromatic field at each point through a sum of $M+1$ modal terms while at each point in the diffraction half-plane the diffraction integrals require integration over an aperture function, which for oscillatory functions, such as lenses, have to be sampled at very large rates. While the aperture also has to be highly sampled in the Gaussian beam mode expansion, numerical integration is required only $M+1$ times. As well as this inherent optimisation of diffraction calculation, GBMA also combines well with the programming facility of vectorisation available in Matlab and Python which can accelerate the procedure even further. The GBMA method of pulse simulation allows for prediction of fields that, in comparison with similar examples in the literature, can have very high resolution and allow for examination of the fields on logarithmic scales.

From a physical viewpoint, the author has shown how GBM techniques can give an alternative view of the physical formation of optical pulses. The diffraction of a pulse by an aperture has been exhibited as a superposition of individual and independently propagating pulsed modes which gives an alternative explanation for the appearance of features such as boundary diffraction waves which propagate in a similar manner to the higher order ultrashort Gaussian beam modes.

The use of Gaussian beam mode analysis in pulsed simulations was also applied in the simulation of diffraction effects caused by quantised diffractive Fresnel lenses. Experimental continuous wave measurement of such a lens defined for operation at 100GHz showed excellent agreement with a finite term modal expansion in the focusing of a horn antenna beam.

Application of digital holography in millimetre wave imaging has been demonstrated through a simple optical arrangement. Images obtained using the system show very good resolution for objects that are only one order of magnitude greater than the wavelength. The technique has potential applications beyond those presented in the

context of imaging, for example, the use of a similar system as an interferometric method in the analysis of millimetre wave sources. Horn antennas have ambiguous phase centres, but by measurement of the phase of a generated beam using a similar system to that described, one could predict a radius of curvature of the detected field and subsequently determine the location of the horns phase centre which would be an important result in analysis of antennas with applications relating to astronomical radiotelescopes.

We have also exhibited the reconstruction of images from measurements of digital holograms using the Hermite-Gaussian expansion with complete independence from the conventional methods which involve fast Fourier transforms.

The properties of the conical lens, which is yet to gain widespread use in optics, have been described through the GBMA method. Through experimental testing of such a component at 100GHz, the generated Bessel beams suggest useful application in mm-wave imaging systems, possibly without the requirement of collimating optics, for generation of small focal spots.

The behaviour of individual Gaussian beam modes is well reported in the literature. However, the application of the orthogonal properties of these modes is rarely described. This thesis has shown that the efficiency and accuracy of Gaussian beam mode analysis can be an extremely useful addition to the more familiar diffraction techniques.

References

[ALDA06] J. Alda, J. M. Rico-Garcia, J. M. Lopez-Alonso, B. Lail, G. Boreman, "*Design of Fresnel lenses and binary-staircase kinoforms of low value of the aperture number*", Optics Communications, Vol. 260, pp. 454–461, (2006).

[ALL03] E. Allaria, S. Brugioni, S. De Nicola, P. Ferraro, S. Grilli, R. Meucci, "*Digital holography at* 10μm",Optics Communications, Vol. 215, pp. 257-262 (2003).

[ARLT01] J. Arlt, K. Dholakia, J. Soneson, E.M. Wright, "*Optical dipole traps and atomic waveguides based on Bessel light beams*", Physical Review A, Vol. 63, 063602, (2001).

[ASH03] R. Ashman and M. Gu, "*Effect of ultrashort pulsed illumination on foci caused by a Fresnel zone plate*", Applied Optics, Vol. 42, No. 10, (2003).

[BAN04] M. A. Bandres and J. C. Gutiérrez-Vega, "*Ince-Gaussian beams*", Optics Letters, Vol. 29, (2004).

[BER96] J. E. Bertie and Z. D. Lan, "*Infrared intensities of liquids: The intensity of the OH stretching band of liquid water revisited, and the best current values of the optical constants of H_2O(1) at 25 degrees C between 15 000 and 1 cm*", Applied Spectroscopy, vol. 50, no. 8, Aug. 1996.

[BIR92] J. R. Birch, ''*The far-infrared optical constants of polypropylene, ptfe and polystyrene*'', Infrared Physics, Vol. 33, 33–38, (1992).

[BOR89] Z. Bor, "*Distortion of femtosecond laser pulses in lenses*", Optics Letters, Vol. 14, No. 2, (1989).

[BORG96] R. Borghi, F. Gori, M. Santarsiero, "*Optimization of Laguerre-Gauss truncated series*", Optics Communications 125, pp. 197-203, (1996)

[BORK04] A. V. Borksin et al., "*Advanced design of an elliptical lens antenna for mm-wave and sub-mm wave receivers"*, European Microwave Conference, Vol. 3, Amsterdam, 2004.

[BORN97] M. Born and E. Wolf, "*Principles of Optics*", Cambridge University Press, (1997)

[BRE75] B. Brendan, "*Acoustical Holography*", Optical Engineering, Vol. 14, No. 5, (1975).

[BRYN76] O. Bryngdahl, and W.H. Lee, "*Laser beam scanning using computer-generated holograms*", Applied Optics, Vol. 15, Issue 1, (1976).

[BUD98] E. Budiarto, Nen-Wen Pu, S. Jeong, J. Bokor, "*Near-field propagation of terahertz pulses from a large-aperture antenna*", Optics Letters, Vol. 23, No. 3, (1998).

[BUR04] Anna Burvall, "*Axicon Imaging by Scalar Diffraction Theory*", PhD Thesis, Royal Institute of Technology, Kista, Sweden.

[CAR80] W. H. Carter, **"***Spot size and divergence for Hermite Gaussian beams of any order***",** Applied Optics, Vol. 19, No. 7.

[CHA07] W. L. Chan, J. Deibel and D. M. Mittleman, "*Imaging with terahertz radiation*", Reports in Progress in Physics, Vol. 70, (2007).

[CHE05] V.S. Cherkasskya, B.A. Knyazeva,, V.V. Kubarev, G.N. Kulipanov,G.L. Kuryshev, A.N. Matveenko, A.K. Petrov, V.M. Popik, M.A. Scheglov, O.A. Shevchenko, N.A. Vinokurov, "*Imaging techniques for a high-power THz free electron laser*", Nuclear Instruments and Methods in Physics Research A 543,pp. 102–109, (2005)

[CHEN10] Y. Chen, "*Broadband one-dimensional photonic crystal wave plate containing single-negative materials*", Optics Express, Vol. 18, No. 19, (2010).

[CHU95] S. T. Chu, and S. K. Chandhuri, "*Finite-difference time-domain method for optical waveguide analysis*", Progress In Electromagnetics Research, Vol. 11, pp. 255–300, (1995).

[CLA84] P. J. B. Clarricoats, "*Corrugated Horns for Microwave Antennas*", IEEE Press, 1984.

[CLE01] M. Clemens and T. Weiland, "*Discrete electromagnetism with the finite integration technique*", Progress In Electromagnetics Research, 32, (2001).

[COL02] T. Colomb, P. Dahlgren, D. Beghuin, E. Cuche, P. Marquet, and C. Depeursinge, "*Polarization imaging by use of digital holography*", Applied Optics, Vol. 41, No. 1, pp. 27-37, (2002).

[COLL70] S. A. Collins, "*Lens-System Diffraction Integral Written in Terms of Matrix Optics*", JOSA, Vol. 60, Issue 9, pp. 1168-1177 (1970)

[COO65] Cooley, J. W. and J. W. Tukey, "*An Algorithm for the Machine Computation of the Complex Fourier Series*", Mathematics of Computation, Vol. 19, (1965).

[DAO09] L. V. Dao, K. B. Dinh, and P. Hannaford , "*Generation of extreme ultraviolet radiation with a Bessel–Gaussian beam*", Applied Physics Letters, Vol. 95, (2009).

[DENG05] D. Deng, H. Guo, D. Han, M. Liu, C. Li, "*Effects of dispersion and longitudinal chromatic aberration on the focusing of isodiffracting pulsed Gaussian light beam*", Physics Letters A, 334, pp. 73–80, (2005).

[DHO06] Kishan Dholakia, Peter Reece, "*Optical micromanipulation takes hold*", Nano Today, Vol. 1, 1, (2006).

[DRE00] R. Drezek, A. Dunn and R. Richards-Kortum, "*A Pulsed Finite-Difference Time-Domain (FDTD) Method for Calculating Light Scattering from Biological Cells Over Broad Wavelength Ranges*", Optics Express, Vol. 6, No. 7, (2000).

[DUAN05] K. Duan, B. Wang, B. Lu, "*Propagation of Hermite–Gaussian and Laguerre–Gaussian beams beyond the paraxial approximation*", Journal of the Optical Society of America A, Vol. 22, No. 9, (2005).

[DUR87] J. Durnin, J. J. Miceli, Jr., and J. H. Eberly, "Diffraction-free beams" Phys. Rev. Lett. 58, 1499 (1987).

[EIS04] S. Eisebitt, J. Lüning, W.F. Schlotter, M. Lörgen, O. Hellwig, W.Eberhardt, and J. Stöhr, "*Lensless imaging of magnetic microstructures by X-ray spectro-holography*", Nature 432, (2004).

[FENG04] Di Feng, Yingbai Yan, Guofan Jin, Shoushan Fan, "*Beam focusing characteristics of diffractive lenses with binary subwavelength structures*", Optics Communications, Vol. 239, pp. 345–352, (2004).

[FIT06] A.J. Fitzgerald, V.P. Wallace, M. Jiminez-Linan, Bobrow L, R. J. Pye, A.D. Purushotham, and D. D. Arnone. "*Terahertz pulsed imaging of human breast tumors*", Radiology, Vol. 239, pp. 533–40, (2006).

[FRI96] A.T. Friberg, "*Stationary-phase analysis of generalized axicons*", Journal of the Optical Society of America A, Volume 13, pp. 743–750, (1996).

[GAB48] D. Gabor, "*A New Microscopic Principle*", Nature, Vol. 161, pp. 777-778, (1948).

[GAR08] J. Garcia-Sucerquia, W. Xu, S.K. Jericho, M.H. Jericho, H.J. Kreuzer, "*4-D imaging of fluid flow with digital in-line holographic microscopy*", Optik, Volume 119, Issue 9, pp. 419-423, (2008).

[GBUR02] Greg Gbur and Emil Wolf, "*Diffraction tomography without phase information*", Optics Letters, Vol. 27, No. 21, November 1, (2002).

[GER72] R. Gerchberg, O. Saxton, "*A practical algorithm for the determination of phase from image and diffraction plane pictures*", Optik, Vol. 35, pp.237-246, (1972).

[GOL98] P. Goldsmith, "*Quasioptical systems*", IEEE press, Wiley, (1998).

[GON00] S. González-García, B. García-Olmedo, and R. Gómez Martín, "*A time-domain near-to-far-field transformation for FDTD in two dimensions*", Microwave and optical technology letters, Vol. 27, No. 6, (2000).

[GOO92] P. M. Goorjian, A. Taflove, "*Direct time integration of Maxwell's equations in nonlinear dispersive media for propagation and scattering of femtosecond electromagnetic solitons*", Optics Letters, Vol. 17, No. 3, (1992).

[GOO05] J. W. Goodman, "*Introduction to Fourier Optics*", Roberts and Company (2005).

[GOR87] F. Gori, G. Guattari, and C. Padovani, "*Bessel–Gauss beams*", Optics Communications Vol. 64, (1987).

[GRA07] I. S. Gradshteyn and I. M. Ryzhik, "*Table of integrals, series, and products*", Academic press (2007).

[GRAD04] M. L. Gradziel, D. White, N. Trappe , R. J. Mahon, T. J. Finn , S. Withington, , J.A. Murphy, C. M. O'Sullivan, "*Modeling of millimetre-wave and*

terahertz imaging systems" in *Passive Millimetre-Wave and Terahertz Imaging and Technology*, Proceedings of SPIE Vol. 5619 (2004).

[GRAF01] U.U. Graf, and S. Heyminck, "*Fourier gratings as submillimeter beam splitters",* IEEE Transactions on Antennas and Propagation, Vol. 49, No. 4, pp.542-546, (2001).

[GRO10] E. Grossman, C. Dietlein, J. Ala-Laurinaho, M. Leivo, L. Gronberg, M. Gronholm, P. Lappalainen, A. Rautiainen, A. Tamminen, and A.Luukanen, "*Passive terahertz camera for standoff security screening"*, Applied Optics, Volume 49, No. 19, (2010).

[GUS04] M. Gustafsson, M. Sebesta, B. Bengtsson, S. G. Pettersson, P. Egelberg, T. Lenart, "*High-resolution digital transmission microscopy - a Fourier holography approach*", Optics and Lasers in Engineering, Volume 41, Issue 3, pp 553-563, (2004).

[GUR00] A. Gürtler, C. Winnewisser, H. Helm, and P. U. Jepsen, "*Terahertz pulse propagation in the near field and the far field*", J. Opt. Soc. Am. A, Vol. 17, No. 1, (2000).

[HAN07] P. Han, "*Spectrum Compression of a Short Pulse from a Central Obstructed Circular Aperture in the Far-field*", Progress in electromagnetics research online, Vol. 3, No. 3, (2007).

[HAR76] Hartwick T S, Hodges D T, Baker D H and Foote F B, "*Far infrared imagery*", *Appl. Opt.* **15** 1919–22, (1976).

[HAR02] P. Hariharan, "*Basics of Holography*", Cambridge University Press, (2002).

[HARR90] C. B. Harris, E. P. Ippen, G. A. Mourou and A. H. Zewail, (Editors), *Ultrafast Phenomena VII*, Springer-Verlag, Berlin-Heidelberg, 1990

[HOLM98] S. Holm, "*Bessel and conical beams and approximation with annular arrays*", IEEE transactions on ultrasonics, ferroelectrics, and frequency control, vol. 45, no. 3, (1998)

[HSI03] J. Hsieh, "Computed Tomography – Principles, Design, Artifacts, and Recent Advances", SPIE Press, 2003.

[HU02] W. Hu and H. Guo, "*Ultrashort pulsed Bessel beams and spatially induced group-velocity dispersion*", J. Opt. Soc. Am. A, Vol. 19, No. 1 (2002).

[HUA08] Yi Huang and Kevin Boyle, "*Antennas from theory to practice*", Wiley, (2008).

[JAH08] G. Jahnke, M. S. Thorne, A. Cochard and H. Igel, "*Global SH-wave propagation using a parallel axisymmetric spherical finite-difference scheme: application to whole mantle scattering*", Geophys. J. Int. 173, (2008).

[JEO05] Y. U. Jeong, G. M. Kazakevitch, H. J. Cha, S. H. Park, B. C. Lee, "*Application of a wide-band compact FEL on THz imaging"*, Nuclear Instruments and Methods in Physics Research A, 543, (2005).

[JHA09] K.R. Jha, G. Singh, "*Dual-frequency terahertz rectangular microstrip patch antenna on photonic crystal substrate*", Applied Electromagnetics Conference, (2009).

[JIA95] Zhiping Jiang, Qisheng Lu, and Zejin Liu,Applied Optics, "*Propagation of apertured Bessel beams*", Vol. 34, Issue 31, pp. 7183-7185 (1995).

[JOS91] Rose M. Joseph, Susan C. Hagness, and Allen Taflove, "*Direct time integration of Maxwell's equations in linear dispersive media with absorption for scattering and propagation of femtosecond electromagnetic pulses*", Optics Letters, Vol. 16, No. 18, (1991).

[KAM97] I P. Kaminow, T. L. Koch (editors), "*Optical fiber telecommunications III, Volume 1*", Academic Press (1997).

[KAN06] Nikolaos V.Kantartzis, Theodoros D. Tsiboukis, "*Higher order FDTD schemes for waveguide and antenna structures*", Morgan & Claypool, (2006).

[KAR05] N. Karpowicz, H. Zhong, C. Zhang, Lin K-I, Hwang J-S, Xu J and X-C Zhang, "*Compact continuous-wave subterahertz system for inspection applications*", Applied Physics Letters, Vol. 86, (2005).

[KEL08] D. P. Kelly, B. M. Hennelly, A. Grün, and K. Unterrainer, "*Numerical sampling rules for paraxial regime pulse diffraction calculations*", J. Opt. Soc. Am. A**,** Vol. 25, No. 9, September, (2008).

[KHE08] M. Khelladi, O. Seddiki, F. T. Bendimerad, "Time-Frequency Decomposition of an Ultrashort Pulse: Wavelet Decomposition", Radioengineering, Vol. 17, No. 1, (2008).

[KIN96] J.T. Kindt, C.A. Schmuttenmaer, "*Far-infrared Dielectric Properties of Polar Liquids probed by Femtosecond Terahertz Pulse Spectroscopy*", Journal of Physical Chemistry, Vol. 100, pp.10373-10379, (1996).

[KRE97] T. M. Kreis and W.P.O. Jüptner, "*Suppression of the dc term in digital holography*", Optical Engineering, Vol. 36, (1997).

[KUNZ93] K.S. Kunz, R.J. Leubbers, "*The finite-difference time domain method for electromagnetics*", CRC press (1993).

[KUNG05] F. Kung, and H.-T. Chuah, "*A finite-difference time-domain software for simulation of printed circuit board assembly*", Progress In Electromagnetics Research, Vol. 50, pp. 299–335, (2005).

[LAK88] V. Lakshmikantham and D. Trigiante, "*Theory of difference equations numerical methods and applications*", Academic Press, Boston, (1988).

[LAN98] William Lanigan, "*Development of a Fourier Optics Test Facility for the Testing of Phase Gratings*", NUI Maynooth M.Sc. Thesis, (1998).

[LAV08] J. Lavelle, "*The Design and Optimisation of Quasioptical Telescopes*", PhD Thesis, NUI Maynooth, (2008).

[LAV10] J. Lavelle and C. O'Sullivan, "*Beam shaping using Gaussian beam modes*", *Journal of the Optical Society of America A, Vol. 27, Issue 2,* (2010).

[LAW67] R.W. Lawrence, J. W. Goodman, "*Digital image formation from electronically detected holograms*", Applied Physics letters, Vol. 11, No.3 (1967).

[LEE98] J.W.H. Lee, A.K.Y. Lai, "*FDTD analysis of indoor radio propagation*", Antennas and Propagation Society International Symposium, (1998).

[LEE04] W.M. Lee, X.-C. Yuan, K. Dholakia, "*Experimental observation of optical vortex evolution in a Gaussian beam with an embedded fractional phase step*", Optics Communications 239 (2004).

[LEE09] Y-S. Lee, in "*Principles of Terahertz Science and Technology*", Springer Science and Business Media, LLC, New York, (2009).

[LEI64] E. N. Leith and J. Upatneiks, "*Wavefront Reconstuction with Diffused Illumination and Three-Dimensional Objects*", Journal of the Optical Society of America, Vol. 54, pp. 1295-1301, (1964).

[LES90] J. C. G. Lesurf, "*Millimetre–wave optics, devices and systems*", Adam Higler, (1990).

[LEU90] R. Luebbers, F.P. Hunsberger, Karl. S. Kunz, R. B. Standler, M. Schneider, "*A Frequency-Dependent Finite-Difference Time-Domain Formulation for Dispersive Materials*", IEEE Transactions on Electromagnetic Compatability, Vol. 32, No. 3, (1990).

[LI81] Y. Li and E. Wolf, "*Focal Shifts in Diffracted Converging Spherical Waves*", Optics Communications, Vol. 39, 211 (1981).

[LIU06] Y Liu, B. Lü, "*Truncated Hermite–Gauss series expansion and its application*", Optik 117 (2006).

[LLO03] J. Lloyd, K. Wang, A. Barkan, D. M. Mittleman, "*Characterization of apparent superluminal effects in the focus of an axicon lens using terahertz time-domain spectroscopy*", Optics Communications, 219, (2003).

[LOH68] A.W. Lohmann and D.P. Paris, *"Binary Fraunhofer Holograms Generated by Computer"*, Applied Optics, Vol. 7, (1968).

[LOU73] R. Loudon, "*The Quantum Theory of Light*", Clarendon Press, Oxford. (1973).

[LU90] J.Y. Lu, J. F. Greenleaf, "*Ultrasonic Nondiffracting Transducer for Medical Imaging*", IEEE Transaction on Ultrasonics, Ferroelectrics and Frequency control, Vol. 37**,** No. 5, (1990).

[LU92] J.-Y. Lu and J. F. Greenleaf, "*Nondiffracting X waves - exact solutions to free-space scalar wave equation and their finite aperture realizations*", IEEE Transactions on Ultrasonics, Ferroelectrics, and Frequency control, Vol. 39, No. 1 (1992).

[MAC96] R.P. MacDonald, S.A. Boothroyd, T. Okamoto, J. Chrostowski, B.A. Syrett, "*Interboard optical data distribution by Bessel beam shadowing*", Optics Communications Vol. 122, pp. 169-I77 (1996).

[MAH06] R. J. Mahon, J. A. Murphy, and W. Lanigan, "*Digital holography at millimetre wavelengths*", Optics Communications, Vol. 260, No.2, (2006).

[MAY08] R. May, J. A. Murphy, C. O'Sullivan, M. Gradziel, N. Trappe, "*Gaussian beam mode analysis of phase gratings*", Proceedings of the SPIE, Terahertz Technology and Applications, Vol. 6893 (2008).

[MAY09] R.K. May, "*The development of quasi-optical techniques for long-wavelength imaging*", Ph.D. Thesis, NUI Maynooth (2009).

[MCK07] J. Mckenna, et. al., "*Observing time-dependent vibrational quantum dynamics in deuterium hydride molecular ions*", Journal of Modern Optics, Vol. 54, No. 7, (2007).

[MEL03] J. Meltaus, J. Salo, E. Noponen, M. M. Salomaa, V. Viikari, A. Lönnqvist, T. Koskinen, J. Säily, J. Häkli, J. Ala-Laurinaho, J. Mallat, and A. V. Räisänen. *"Millimeter-Wave Beam Shaping Using Holograms*", IEEE Transactions on Microwave Theory and Techniques, Vol. 51, No. 4, pp. 1274-1280, (2002).

[MEN07] O. Mendoza-Yero, G. Mínguez-Vega, J. Lancis, M. Fernández-Alonso, and V. Climent, "*On-axis diffraction of an ultrashort light pulse by circularly symmetric hard apertures*", Optics Express, Vol. 15, No. 8, (2007).

[MIC86] A.G. Michette, "*Optical systems for soft X-rays*", Plenum Press, (1986).

[MIT96] D. M. Mittleman, R. H. Jacobsen, and M. C. Nuss, "*T-Ray Imaging*", IEEE Journal of selected topics in quantum electronics, Vol. 2, No. 3, (1996).

[MIT97] D. M. Mittleman, S. Hunsche, L. Boivin and M. C. Nuss, "*T-ray tomography*", Optics Letters, Vol. 22**,** (1997).

[MIY07] N. Miyamoto, S. Nisiyama, S. Tomioka, T. Enoto, *"Numerical reconstruction of an infrared wavefront utilizing an optical phase modulation device",* Optics Communications, Volume 272, Issue 1, pp. 67-72, April (2007).

[MON06] J. A. Monsoriu, W. D. Furlan, P. Andrés, and J. Lancis, "*Fractal conical lenses*", Optics Express, Vol. 14, Issue 20, pp. 9077-9082, (2006).

[MONK99] S. Monk, J. Arlt, D.A. Robertson, J. Courtial, M.J. Padgett, "*The generation of Bessel beams at millimetre-wave frequencies by use of an axicon*", Optics Communications 170, (1999).

[MUR93] J A Murphy and A Egan, "*Examples of Fresnel diffraction using Gaussian modes*", European Journal of Physics,Vol. 14, pp. 121-127, (1993).

[NAU02] T. J. Naughton, Y. Frauel, B. Javidi, and E. Tajahuerce, "*Compression of digital holograms for three-dimensional object reconstruction and recognition*", Applied Optics, Vol. 41, No. 20, pp. 4124-4132 (2002).

[OKS10] A.F. Oskooi, D. Roundy, M. Ibanescu, P. Bermel, J. D. Joannopoulos, and Steven G. Johnson, "*MEEP: A flexible free-software package for electromagnetic simulations by the FDTD method*", Computer Physics Communications 181, (2010).

[OSU02] C. O'Sullivan, E. Atad-Ettedgui, W. Duncan, D. Henry, W. Jellema, J. A. Murphy, N. Trappe, H. van de Stadt, S. Withington, and G. Yassin, "*Far-infrared optics design and verification*", International Journal of Infrared and Millimeter Waves, Vol. 23, No. 7, (2002).

[PEA03] J. Pearce, D. M. Mittleman, "*Using terahertz pulses to study light scattering*", Physica B, 338, (2003).

[PED93] F. L. Pedrotti, L. S. Pedrotti, "*Introduction to Optics*", Prentice-Hall, (1993).

[PHI83] R. L. Phillips and L. C. Andrews, "*Spot size and divergence for Laguerre Gaussian beams of any order*", Applied Optics, Vol. 22, No. 5, (1983).

[PIC04] E. Pickwell, B. E. Cole, A. J. Fitzgerald, and V. P. Wallace, M. Pepper, "*Simulation of terahertz pulse propagation in biological systems*", Applied Physics Letters Vol. 84, No. 12, (2004).

[PIK07] P. Piksa, P, Cerny, "*Near-field Measurement of Gaussian Beam behind Dielectric Lens*", Radioelektronika 2007, 17th International Conference, (2007).

[PIN07] G.F. Pinton, "*Numerical Methods for Nonlinear wave propagation in ultrasound*", Ph.D Thesis, Duke University, (2007).

[POR98] M. A. Porras, "*Ultrashort pulsed Gaussian light beams*", Physical Review E, Vol. 58, No. 1, (1998).

[POR02] M.A. Porras, R.Borghi, M. Santarsiero, "*Superluminality in Gaussian beams*", Optics Communications 203, (2002).

[PRA99] D. W. Prather and S. Shi, "*Formulation and application of the finite-difference time-domain method for the analysis of axially symmetric diffractive optical elements*", Journal of the Optical Society of America, Vol. 16, No. 5, pp. 1131-1142, (1999).

[PRA01] D. W. Prather, D. Pustai, and S. Shi, "*Performance of multilevel diffractive lenses as a function of f-number*", Applied Optics, Vol. 40, No. 2, pp. 207-210, (2001).

[PRA07] B. Pradarutti, G. Matthäus, S. Riehemann, G. Notni, S. Nolte, A. Tünnermann "*Advanced analysis concepts for terahertz time domain imaging*", Optics Communications, Vol. 279, (2007).

[PRE07] W. H. Press, S. A. Teukolsky, W. Y. Vetterling, B.P. Flannery, "*Numerical recipes – The art of Scientific computing*", Cambridge press, (2007).

[QUE91] M. R. Querry, D. M. Wieliczka, and D. J. Segelstein, "*Water* (H_2O)", In *Handbook of Optical Constants of Solids II*, E. D. Palik, Ed., Boston, MA, Academic, pp. 1067–1077, (1991)

[RAH95] B. M. A. Rahman, "*Finite Element Analysis of Optical Waveguides*", Progress in Electromagnetics Research, Vol. 10, (1995).

[RAN04] A. Ranfagni, D. Mugnai, *"Superluminal behaviour in the near field of crossing microwave beams"*, Physics Letters A, 322, pp. 146–149, (2004).

[ROB04] Robertson, D.A., "*MISTM: Medical Imager for Sub-surface Temperature Mapping*", 29th Intl. Conf. Infrared & MM Waves, Karlsruhe, Germany (2004).

[SAC95] Z. S. Sacks, D. M. Kingsland, R. Lee, and J. F. Lee, "*A perfectly matched anisotropic absorber for use as an absorbing boundary condition*", IEEE Transactions on Antennas and Propagation, vol. 43, pp. 1460-1463, 1995.

[SALO97] J. Salo, "*Bulk-Wave Propagation and Non-Diffracting Waves in Anisotropic Elastic Media*", M.Sc. Thesis, Helsinki University of Technology, (1997).

[SAUL06] R. Sauleau, B. Barés, "*A Complete Procedure for the Design and Optimization of Arbitrarily Shaped Integrated Lens Antennas*", *IEEE Trans. on Antennas and Prop*, Vol. 54, No. 4, (2006).

[SCH94] U. Schnars, W. Juptner, "*Direct Recording of holograms by a CCD target and Numerical Reconstruction*", Applied Optics, Vol. 33, No. 2, pp.179-181, (1994).

[SCH04] U. Schnars and W. Juptner, "*Digital Holography: Digital Hologram Recording, Numerical Reconstruction, and Related Techniques*". Springer, (2004).

[SHE95] J. Shen, W. Shen, "*Image smoothing and edge detection by Hermite integration*", Pattern Recognition, Vol. 28, No. 8, (1995).

[SHE97] C.J.R. Sheppard, X. Gan, "*Free-space propagation of femto-second light pulses*", Optics Communications, Vol. 133, (1997).

[SHE01] D. M. Sheen, D. L. McMakin, and T. E. Hall, "*Three-dimensional millimeter-wave imaging for concealed weapon detection*", *IEEE Transactions on Microwave Theory and Techniques*, vol. 49, pp. 1581 – 1592, 2001.

[SHE09] P.M. Shearer, "*Introduction to Seismology*", Cambridge University Press, (2009).

[SHO93] M. Shoucri, R. Davidheiser, B. Hauss, P. Lee, M. Mussetto, S. Young, L. Yujiri, "*A passive millimeter wave camera for landing under low visibility conditions*", National Telesystems Conference, 'Commercial Applications and Dual-Use Technology', Conference Proceedings., (1993)

[SIE86] A. E. Siegman, "*Lasers*", University Science Books, (1986).

[STE73] G. Stephenson, "*Mathematical methods for science students*", Pearson education, (1973).

[TAF80] A. Taflove, "*Application of the finite-difference time-domain method to sinusoidal steady-state electromagnetic penetration problems*", IEEE Transactions on Electromagnetic Compatibility, vol. 22, (1980).

[TAF82] A. Taflove and K. R. Umashankar, "*A hybrid moment method / finite-difference time-domain approach to electromagnetic coupling and aperture penetration into complex geometries*", IEEE Transactions on Antennas and Propagation, vol. 30, (1982).

[TAF89] A. Taflove and K. R. Umashankar, "*The finite-difference time-domain* (*FD-TD*) *method for numerical modelling of electromagnetic scattering*", IEEE Transactions on Magnetics. Vol. 25, pp. 3086–3091, (1989).

[TAM08] A. Tamminen, Juha Ala-Laurinaho, Antti V. Räisänen, "*Indirect Holographic Imaging at* 310 GHz", Proceedings of the 5th European Radar Conference (2008).

[TAO03] X. Tao, N. Zhou, B. Lu, "*Recurrence propagation equation of Hermite-Gaussian beams through a paraxial optical ABCD system with hard-edge aperture*", Optik 114, No. 3, (2003).

[THO07] M. S. Thorne , T. Lay, E. J. Garnero, G. Jahnke, and H. Igel, *"Seismic Imaging of the Laterally Varying D Region Beneath the Cocos Plate*", Geophys. J. Int., Vol. 170, 635–48, (2007).

[TRA04] N. Trappe, R. Mahon, W. Lanigan, J. Anthony Murphy, S. Withington, "*The quasi-optical analysis of Bessel beams in the far infrared*", Infrared Physics and Technology (2004).

[VAS09] M.V. Vasnetsov, V.A. Pas'ko, "*Group velocity of Gaussian beams*", Ukranian Journal of Physics, Vol. 54, No. 1-2, (2009).

[VEE06] S.P. Veetil, H. Schimmel, F. Wyrowski, and C. Vijayan, "*Wave optical modelling of focusing of an ultra short pulse*", Journal of Modern Optics, Vol. 53, (2006).

[WANG04] S. Wang and X.C. Zhang, "*Pulsed terahertz tomography*", Journal of Physics D: Applied Physics, (2004).

[WANG07a] L. Wang, M. Dai, "*Application of a new type of singular points in fingerprint classification*", Pattern Recognition Letters, Vol. 28 (2007).

[WANG07b] L. Wang, Y. Wu and M. Dai, "*Some Aspects of Gaussian-Hermite Moments in Image Analysis*", Third International Conference on Natural Computation (2007).

[WANG08] M. Y. Wang and J. Xu, "*FDTD study on wave propagation in layered structures with biaxial anisotropic metamaterials*", Progress In Electromagnetics Research, Vol. 81, (2008).

[WAT04] Y. Watanabe, K. Kawase, T. Ikari, H. Ito, Y. Ishikawa, H. Minamide, "*Component analysis of chemical mixtures using terahertz spectroscopic imaging*", Optics Communications, Vol. 234, (2004).

[WEI02] E. Weisstein, "*Concise Encyclopedia of Mathematics*", CRC Press, (2002)

[WEN87] J.J. Wen, M.A. Breazeale, "*Gaussian beam functions as a base function set for acoustical field calculations*", IEEE Ultrasonics Symposium, (1987).

[WHI06] D. White, "*The development of Efficient CAD Software for Terahertz Optical Design and Analysis*", NUI Maynooth Ph.D. Thesis, (2006).

[WOO02] R. Woodward, B.E. Cole, V.P. Wallace, R.J. Pye, D.D. Arnone, E.H. Linfield and M. Pepper, "*Terahertz pulse imaging in reflection geometry of human skin cancer and skin tissue"*, Physics in Medicine and Biology, Vol. 47, pp. 3853–63, (2002).

[WUL93] T. Wulle and S. Herminghaus, "*Nonlinear optics of Bessel beams*", Physical Review Letters, Vol. 70, (1993).

[YAN07] Y. Yang, Y. Li, "*Spectral shifts and spectral switches of a pulsed Bessel–Gauss beam from a circular aperture in the far field*", Optics & Laser Technology, Vol. 39, (2007).

[YANG08] Z. Yang, Z. Yang, S. Zhang, "*Carrier-envelope phase of ultrashort pulsed Laguerre-Gaussian beam*", Chinese Optics Letters, Vol. 6, No. 3, pp. 189–191, (2008).

[YEE66] K. S. Yee, "*Numerical solution of initial boundary value problems involving Maxwell's equations in isotropic media*", IEEE Transactions Antennas and Propagation, Vol. 14, pp. 302–307, (1966).

[YUJ03] L. Yujiri, M. Shoucri, P. Moffa, "*Passive Millimeter-Wave Imaging*", IEEE Microwave magazine, Issue 9, (2003).

[ZAM03] M. Zamboni-Rached, K.Z. Nóbrega, H.E. Hernandez-Figueroa, E. Recami, "*Localized superluminal solutions to the wave equation in* (*vacuum or*) *dispersive media, for arbitrary frequencies and with adjustable bandwidth*", Optics Communications, 226, pp. 15–23, (2003).

[ZAM04] Michel Zamboni-Rached, "*Stationary optical wave fields with arbitrary longitudinal shape by superposing equal frequency Bessel beams: Frozen Waves*", Optics Express, Vol. 12, No. 17, (2004).

[ZAP06] C. J. Zapata-Rodríguez and A. Sánchez-Losa, "*Three-dimensional field distribution in the focal region of low-Fresnel-number axicons*", Journal of the Optical Society of America A, Vol. 23, No. 12, (2006).

[ZIO92] R. W. Ziolkowski, J. B. Judkins, "*Propagation characteristics of ultrawide-bandwidth pulsed Gaussian beams*", J. Opt. Soc. Am. A, Vol. 9, No. 11, (1992).

[ZOUA07] Q. Zoua, B. Lü, "*Temporal and spectral properties of ultrashort pulsed Laguerre–Gaussian beams in dispersive media*", Optik 118, pp. 83–87, (2007).

[ZHA07] Y. Zhang, J. Chen, X. Yea, "*Multilevel phase Fresnel zone plate lens as a near-field optical element*", Optics Communications, Vol. 269, (2007).

[ZWI10] S. Zwick, C. Schaub, T. Haist, W. Osten, "*Light fields with an axially expanded intensity distribution for stable three-dimensional optical trapping*", Optics Express, Vol. 18, No. 19, (2010).